Design, Syntheses, and Magnetic Properties of Vanadium-Lanthanide Complexes

Zur Erlangung des akademischen Grades eines

DOKTORS DER NATURWISSENSCHAFTEN

(Dr. rer. nat.)

von der KIT-Fakultät für Chemie und Biowissenschaften

des Karlsruher Instituts für Technologie (KIT)

genehmigte

DISSERTATION

von

M.Sc. Xian-Feng Li

aus

Jiangxi, China

1. **Referentin: Prof. Dr. Annie Powell**
2. **Referentin: Prof. Dr. Karin Fink**

Tag der mündlichen Prüfung: 23.10.2023

Declaration

I hereby declare that:

1. This work was done wholly while in candidature for a research degree at the KIT.
2. The whole thesis was written by me, and no other sources other than the specified were used.
3. The rules for ensuring the good scientific practice of the Karlsruhe Institute of Technology (KIT) have been used, and the submission and archiving of the primary data, in accordance with section A(6) of the rules for ensuring the good scientific practice of KIT, has been ensured.
4. The electronic version of the work is consistent with the written version.
5. Where I have consulted the published work of others, this is always clearly attributed.
6. I have acknowledged all main sources of help.
7. Where the thesis is based on work done by myself jointly with others, I have made clear exactly what was done by others and what I have contributed myself.
8. Furthermore, I declare that I did not undertake any previous doctoral studies, and I am currently not enrolled in any other ongoing doctoral procedure

Xian-Feng Li

Deklaration

Ich erkläre:

1. Diese Arbeit
2. wurde vollständig während der Kandidatur für ein Forschungsstudium am KIT durchgeführt.

2. Die gesamte Arbeit wurde von mir verfasst und es wurden keine anderen Quellen als die angegebenen verwendet.

3. Es wurden Maßnahmen zur Sicherstellung einer guten wissenschaftlichen Praxis des Karlsruher Instituts für Technologie (KIT) angewendet und die Übermittlung und Archivierung der Primärdaten gemäß Abschnitt A(6) der Regeln zur Sicherstellung einer guten wissenschaftlichen Praxis des KIT sichergestellt.

4. Die elektronische Fassung des Werkes entspricht der schriftlichen Fassung.

5. Im Fall, dass ich die veröffentlichten Arbeiten anderer konsultiert habe, wird dies immer eindeutig zugeordnet.

6. Ich habe alle wichtigen Hilfsquellen zur kenntlich gemacht.

7. Wenn die Arbeit auf Arbeiten basiert, die ich gemeinsam mit anderen geleistet habe, habe ich kenntlich gemacht, was von anderen geleistet wurde und was ich selbst beigesteuert habe.

8. Des Weiteren erkläre ich, dass ich kein vorheriges Promotionsstudium absolviert habe und mich derzeit nicht in einem anderen laufenden Promotionsverfahren befinde.

Xian-Feng Li

Table of contents

Abstract 9

Zusammenfasung 11

Chapter 1. Introduction 14

1.1 Magnetic Properties of Matter 14

1.2 Types of Magnetism 14

1.2.1 Diamagnetism 15
1.2.2 Paramagnetism 15
1.2.3 Ferromagnetism 16
1.2.4 Antiferromagnetism 16
1.2.5 Ferrimagnetism 17

1.3 Magnetic Anisotropy 17

1.3.1 Lanthanide Ion Anisotropy 18

1.4 Introduction to Single Molecule Magnets 19

1.4.1 Research Progress of 3d SMMs 21
1.4.2 Research Progress of 4f SMMs 23
1.4.3 Research Progress of 3d-4f SMMs 26

1.5 Magnetic Refrigeration 31

1.6 Research Objectives 33

1.6.1 Motivation to study Vanadium-4f Complexes 33
1.6.2 The choice of ligands for vanadium-4f complexes 34

Chapter 2: Vanadium-Lanthanide Complexes as 3d-4f SMMs 36

2.1 Introduction 36

2.2 Results and Discussions 37

2.2.1 Butterfly Type II Compound of $V^{III}_2Ln^{III}_2$ (Ln = Tb-Yb, Y) 37
2.2.1.1 Crystal Structure of $[V_2Ln_2(\mu_3\text{-}OH)_2(^tBuDea)_2(piv)_6]\cdot 2MeOH$ [Ln = Tb-Yb (2.1-2.6) and Y (2.7) 37
2.2.1.2 Magnetic properties of complexes, $V^{III}_2Ln_2$ (Ln=Tb - Yb and Y) (2.1-2.7) 41
2.2.2 Butterfly Type I Compound of $V^{III}_2Dy_2$ 54
2.2.2.1 Crystal Structure of $[V^{III}_2Dy_2(\mu_3\text{-}OH)_2(L)_2(p\text{-}Me\text{-}PhCO_2)_6]\cdot 2MeOH$ (L=N-(2-Pyridylmethyl)iminodiethanol) (2.8) 54
2.2.2.2 Magnetic properties of complex $V^{III}_2Dy_2$ 2.8 56
2.2.3 $[V^{III}_5Dy_8]$ and $[V^{III}_4V^{IV}Dy_5]$ 3d-4f SMMs without Applied Field 58
2.2.3.1 Crystal Structure of $(Et_3NH)[V^{III}_5Dy_8(\mu_3\text{-}OH)_{12}(Bu^tDea)_4(NCC_6H_4CO_2)_{20}]\cdot 15MeCN$ 58
2.2.3 2 Magnetic properties of complex $V^{III}_5Dy_8$ 2.9. 60
2.2.3.3 Crystal Structure of $[V^{III}_3V^{IV}Dy_5(\mu_2\text{-}OH)(\mu_3\text{-}OH)_7(\mu_2\text{-}$

O)(^{t}BuDea)$_3$(piv)$_{12}$]·4MeCN (2.10) 65
2.2.3.4 Magnetic properties of complex $V^{III}_3V^{IV}Dy^{III}_5$ 2.10 67
2.3 Conclusion 71
Chapter 3. Ferromagnetic [$V^{III}_4Ln^{III}_4$] 3d-4f Complexes as Magnetic Refrigerants 72
3.1 Introduction 72
3.2 Results and Discussions 74
3.2.1 $V^{III}_4Ln_4$ compounds (Ln= La^{III}, Nd^{III}, Gd^{III}, Dy^{III} and Y^{III}) (3.1-3.9) 74
3.2.1.1 Crystal Structure of [$V^{III}_4Ln_4(\mu_3$-OH)$_4$(mDea)$_4$(*p*-Me-PhCO$_2$)$_{12}$] xMeCN·yCH_2Cl_2 [Ln = La^{III}, Nd^{III}, Gd^{III}, Dy^{III}, Y^{III} (3.1-3.5) and [$V^{III}_4Ln_4(\mu_3$-OH)$_4$(Htea)$_4$(*p*-Me-PhCO$_2$)$_{12}$]·xMeCN yCH_2Cl_2 [Ln = La^{III}, Gd^{III}, Dy^{III} and Y^{III} (3.6-3.9)] 74
3.2.2 2 Magnetic properties of complexes of $V^{III}_4Gd_4$ 3.3, $V^{III}_4Dy_4$ 3.4 and $V^{III}_4Y_4$ 3.5 76
3.2.2 3 Magnetic properties of $V^{III}_4Gd_4$ 3.7 and $V^{III}_4Dy_4$ 3.8. 79
3.2.2 4 Magnetocaloric properties of $V^{III}_4Gd_4$ 3.3 and $V^{III}_4Gd_4$ 3.7. 82
3.2.2 Complexes of $V^{III}_4Ln_4$ (Ln= La^{III} and Gd^{III}) (3.10-3.13) 83
3.3 Conclusion 86
Chapter 4: Magnetostructural Correlation between Ring-shaped Complexes of Vanadium and Lanthanide Ions 88
4.1 Introduction 88
4.2 Results and Discussions 89
4.2.1 Complexes of two types of $V^{III}_3Ln_2$ (Ln = Tb-Er, Yb and Y) 89
4.2.1.1 Crystal Structure of [$V^{III}_3Ln_2(\mu_3$-OH)(tea)$_4$(*p*-Me-PhCO$_2$)$_6$]·2MeCN [Ln = Tb-Er, Yb and Y] (4.1-4.6) 89
4.2.1.2 Magnetic properties of $V^{III}_3Ln_2$ (Ln=Tb, Dy, Er, and Y) 91
4.2.1.3 Crystal Structure of [$V^{III}_3Ln_2(\mu_3$-OH)(tea)$_4$(piv)$_6$]·xMeCN yCH_2Cl_2 (Ln = Tb - Tm) (4.7 - 4.11) 95
4.2.1.4 Magnetic properties of $V^{III}_3Dy_2$ 4.8. 96
4.2.2 $V^{III}_4Dy_3$, $V^{III}_4Y_3$, $V^{IV}_4Gd_3$ and $V^{III}_4Gd_5$ 98
4.2.2.1 Crystal Structures of [$V^{III}_4Ln_3(\mu_2$-OMe)$_2$(teaH)$_6$(*p*-Me-PhCO$_2$)$_7$]·MeOH 3MeCN (Ln = Dy and Y) (4.12-4.13), (Et_3NH)[$V^{IV}_4Gd_3$(O)$_3(\mu_3$-O)$(\mu_3$-OH)$_5$(teaH)$_3$(piv)$_6$](piv)·MeCN·CH_2Cl_2·H_2O (4.14), and [$V^{III}_4Gd_5(\mu_3$-OH)$_7$(teaH)$_4$(piv)$_{12}$]·4MeCN (4.15) 98
7.3.4 Synthesis of [$V^{III}_3V^{IV}Dy^{III}_5(\mu_3$-OH)$_7(\mu_2$-O)$_2$(^{t}BuDea)$_3(piv)_{12}$]·4MeCN (2.10) 102
4.2.2.2 Magnetic properties of complex $V^{III}_4Dy_3$ 4.12 102
4.2.3 $V^{IV}_4V^{III}Dy_6$, $V^{III}_2V^{IV}_4Dy_4$ and $V^{IV}_6Dy_4$ 104
4.2.3.1 Crystal Structure of [$V^{IV}_4V^{III}Dy_6(\mu_4$-O)$_4(\mu_2$-O)$_4(\mu_3$-OH)$_4$(Bu^{t}Dea)$_4$(NCC$H_2$COO)$_8$(MeOH)$_6$]Cl·8MeCN (4.16) 104

4.2.3 2 Magnetic properties of complex $V^{IV}_4V^{III}Dy_6$ 4.16. 106
4.2.4 $V^{III}_2V^{IV}_4Dy_4$ and $V^{IV}_6Dy_4$ 107
4.2.4 1 Crystal Structure of $[V^{III}_2V^{IV}_4Dy_4(\mu_2\text{-}O)_4(\mu_3\text{-}OH)_2(\mu_2\text{-}OMe)_2(\mu\text{-}N_3)(\mu\text{-}Cl)(mDea)_2(mDeaH)(piv)_{14}(H_2O)_4]^{3+}$ (4.17) and $[(V^{IV}{=}O)_4\{V^{V}O_3(OMe)\}_2Dy_4(\mu_4\text{-}O)_2(\mu_2\text{-}OMe)_4(OMe)_2(MeOH)_2(teaH)_2(piv)_4]$ (4.18) 107
4.2.5 $V^{III}_4V^{IV}_4Ln_4$ (Ln= Gd, Dy and Y) 110
4.2.5.1 Crystal Structure of $[V^{III}_4V^{IV}_4Ln_4(\mu_2\text{-}O)_4(mDea)_4(piv)_{18}(N_3)_6]\cdot nCH_2Cl_2$ MeCN (Ln = Gd (4.19), Dy (4.20) and Y (4.21)) 110
4.2.5 2 Magnetic properties of complex of $V^{III}_4V^{IV}_4Dy_4$ 4.20. 112
4.3 Discussion 115
4.4 Conclusion 119
5. Conclusion and Outlook 120
6. Materials and Equipment 123
7. Syntheses of ligands and complexes 125
7.1 General procedures 125
7.2 Preparation of organic ligands 125
7.2.1 N-(2-Pyridylmethyl)iminodiethanol (H_2L1) 125
7.3 Preparation of Complexes 126
7.3.1 Synthesis of $[V^{III}_2Ln_2(\mu_3\text{-}OH)_2(^tBuDea)_2(piv)_6]\cdot 2MeOH$ [Ln = Tb-Yb (2.1-2.6) and Y (2.7) 126
7.3.2 Synthesis of $[V^{III}_2Dy_2(\mu_3\text{-}OH)_2(L)_2(p\text{-}Me\text{-}PhCO_2)_6]\cdot 2MeOH$ (L=N-(2-Pyridylmethyl)iminodiethanol) (2.8) 128
7.3.3 Synthesis of $(Et_3NH)[V^{III}_5Dy_8(\mu_3\text{-}OH)_{12}(Bu^tDea)_4(NCC_6H_4CO_2)_{20}]\cdot 15MeCN$ (2.9) 128
7.3.5 Synthesis of $[V^{III}_4Ln^{III}_4(u_3\text{-}OH)_4(mDea)_4(p\text{-}Me\text{-}PhCO_2)_{12}]\cdot xMeCN$ y CH_2Cl_2 [Ln= La, Nd, Gd, Dy and Y (3.1-4.5)] 129
7.3.6 Synthesis of $[V^{III}_4Ln^{III}_4(u_3\text{-}O)_4(teaH)_4(p\text{-}Me\text{-}PhCO_2)_{12}]\cdot xMeCN\ yCH_2Cl_2$ [Ln = La^{III}, Gd^{III}, Dy^{III} and Y^{III} (3.6-3.9)] 130
7.3.7 Synthesis of $[V^{III}_4La^{III}_4(u_3\text{-}OH)_4(mdea)_4(piv)_{12}]\cdot 8MeCN$ (3.10) 132
7.3.8 Synthesis of $[V^{III}_4Gd_4(u_3\text{-}O)_4(L_1)_4(L_2)_{12}]\cdot 8MeCN$ (3.11-13) 132
7.3.9 Synthesis of $[V^{III}_3Ln_2(\mu_3\text{-}OH)(tea)_4(p\text{-}Me\text{-}PhCO_2)_2(p\text{-}Me\text{-}PhCOOH)_4]\cdot 2MeCN$ [Ln = Tb-Er, Yb and Y (4.1-4.6) 133
7.3.10 Synthesis of $[V^{III}_3Ln_2(\mu_3\text{-}OH)(tea)_4(piv)_6]\cdot xMeCN\ yCH_2Cl_2$ [Ln = Tb-Tm (4.7-4.11) 135
7.3.11 $[V^{III}_4Ln_3(\mu_2\text{-}OMe)_2(teaH)_6(p\text{-}Me\text{-}PhCO_2)_7]\cdot MeOH\ 3MeCN$ [Ln = Dy and Y (4.12-4.13)] 137
7.3.12 Synthesis of $(Et_3NH)[V^{IV}_4Gd_3(O)_3(\mu_3\text{-}O)(\mu_3\text{-}OH)_5(teaH)_3(piv)_6](piv)\cdot MeCN\cdot CH_2Cl_2\cdot H_2O$ (4.14) 138
7.3.13 Synthesis of $[V^{III}_4Gd_5(\mu_3\text{-}OH)_7(teaH)_3(piv)_{12}]\cdot 4MeCN$ (4.15) 138
7.3.14 Synthesis of $[V^{IV}_4V^{III}Dy_6(\mu_4\text{-}O)_4(\mu_2\text{-}O)_4(\mu_3\text{-}$

$OH)_4(Bu^tDea)_4(NCCH_2COO)_8(MeOH)_6]Cl\cdot 8MeCN$ (4.16) 139
7.3.15 Synthesis of $[V^{III}_2V^{IV}_4Dy_4(\mu_2\text{-}O)_4(\mu_3\text{-}OH)_2(\mu_2\text{-}OMe)_2(\mu\text{-}N_3)(\mu\text{-}Cl)(mDea)_2(mDeaH)(piv)_{14}(H_2O)_4]^{3+}$ (4.17) 139
7.3.16 Synthesis of $[(V^{IV}{=}O)_4\{V^VO_3(OMe)\}_2Dy_4(\mu_4\text{-}O)_2(\mu_2\text{-}OMe)_4(OMe)_2(MeOH)_2(teaH)_2(piv)_4]$ (4.18) 140
7.3.17 $[V^{III}_4V^{IV}_4Ln_4(\mu_2\text{-}O)_4(mDea)_4(piv)_{18}(N_3)_6]\cdot nCH_2Cl_2$ MeCN (Ln = Gd (4.19), Dy (4.20) and Y (4.21)) 140
8. Crystallographic Data 142
9. Bibliography 165
10. Appendix 183
10.1 Curriculum Vitae ..... **Error! Bookmark not defined.**
10.2 Publications ..... **Error! Bookmark not defined.**
10.3. Acknowledgements 184

Abstract

3d-4f coordination complexes have received considerable attention due to their potential applications in single molecule magnets (SMMs) and magnetic refrigerants. These complexes possess a combination of 3d ions and 4f ions, both individually renowned for their excellent magnetic properties. The intriguing properties of SMMs make them highly promising for a wide range of applications, including molecular spintronics, high-density information storage materials, and quantum computing. A total of forty-five V-Ln complexes with nuclearities ranging from tetranuclear to tridecanuclear were synthesized, some of which have localized heterovalent states of vanadium ions. The main work is divided into the following three parts:

Chapter 2 of this thesis provides a comprehensive description of the molecular structures and magnetic properties of two distinct types of V-Ln complexes synthesized using Schlenk techniques. Different combinations of ligands and solvents resulted in diverse V-Ln complexes. The magnetic behaviors of each complex are explored in detail. These butterfly-type $V^{III}_2Dy_2$ complexes exhibit slow relaxation of magnetization usually under an applied direct-current (dc) field. The magnetic properties of the complexes are quantified fitting the relaxation times. For the $V^{III}_2Dy_2$ **2.2** complex, the obtained parameters are $\tau_0 = 1.518\times10^{-5}$ s, $\tau_{QTM} = 1.15\times10^{-3}$ s, and $U_{eff} = 14(2)$ K. On the other hand the $V^{III}_5Dy_8$ **2.9** and $V^{III}_3V^{IV}Dy_5$ **2.10** clusters demonstrate SMM characteristics without the need for an applied magnetic field. In the case of the $V^{III}_5Dy_8$ **2.9** complex, the results of micro-SQUID experiments confirm the presence of SMM behavior below 0.3 K, as seen from the hysteresis. Furthermore, the fitting of the Arrhenius equation yields an energy barrier of 8 K and a relaxation time of 10^{-13} s for the $V^{III}_5Dy_8$ **2.9** complex. Compared with SMM complexes of other trivalent transition metal ions and lanthanide ions, this chapter confirms that V-Ln type complexes can also be candidates for SMMs,

and also significantly expands the scope of research in the field of 3d-4f SMMs.

Chapter 3 focuses on the crystal structures and magnetic properties of 14 $V^{III}_4Ln_4$ complexes, all of which share the same square-in-square topology but differ in their ligands and lanthanide ions. The results of dc magnetic susceptibility experiments reveal that these $V^{III}_4Ln_4$ complexes exhibit ferromagnetic properties. In contrast, the $V^{III}_4Y_4$ complexes containing diamagnetic Y ions exhibit antiferromagnetism. Therefore, it can be concluded that there is a ferromagnetic interaction between the lanthanide and vanadium ions. Furthermore, this section discusses the magnetocaloric properties of two isostructural $V^{III}_4Gd_4$ complexes with slight differences in the ligands. $V^{III}_4Gd_4$ **3.3** has an entropy change of 16.08 J kg^{-1} K^{-1} at 3 K for H = 7 T, while $V^{III}_4Gd_4$ **3.7** has an entropy change of 19.53 J kg^{-1} K^{-1} at 3 K for H = 7 T.

Chapter 4 delves into the magnetostructural correlations of a series of ring-shaped V^{III}-Ln complexes *via* dc susceptibility measurements. Additionally, this chapter examines the relationship between the metal-metal distances and the arrangement of vanadium and lanthanide ions in the ring. Furthermore, the effects of ligand changes on the dc magnetic susceptibility properties of these isostructural complexes are discussed. Notably, the alteration of the ligand does not significantly impact on the dc magnetic susceptibility properties. The findings contribute towards a better understanding of the magnetic behavior observed in these ring-shape V^{III}-Ln complexes.

Zusammenfasung

3d-4f-Koordinationskomplexe haben aufgrund ihrer potenziellen Anwendungen in Einzelmolekülmagneten (SMMs) und magnetischen Kühlmitteln große Aufmerksamkeit erregt. Diese Komplexe bestehen aus einer Kombination von 3d- und 4f-Ionen, die beide für ihre hervorragenden magnetischen Eigenschaften bekannt sind. Die faszinierenden Eigenschaften von SMMs machen sie vielversprechend für ein breites Spektrum von Anwendungen, darunter molekulare Spintronik, Materialien zur Speicherung von Informationen mit hoher Dichte und Quantencomputer. Insgesamt wurden fünfundvierzig V-Ln-Komplexe mit Nuklearitäten von tetranuklear bis tridekanuklear synthetisiert, von denen einige lokalisierte heterovalente Zustände von Vanadium-Ionen aufweisen. Die Hauptarbeit gliedert sich in die folgenden drei Teile:

Kapitel 2 dieser Arbeit enthält eine umfassende Beschreibung der molekularen Strukturen und magnetischen Eigenschaften von zwei verschiedenen Typen von V-Ln-Komplexen, die mit Schlenk-Techniken synthetisiert wurden. Verschiedene Kombinationen von Liganden und Lösungsmitteln führten zu unterschiedlichen V-Ln-Komplexen. Das magnetische Verhalten der einzelnen Komplexe wird im Detail untersucht. Diese $V^{III}_2Dy_2$-Komplexe vom Schmetterlingstyp zeigen eine langsame Relaxation der Magnetisierung unter einem angelegten Gleichstromfeld (ac). Die magnetischen Eigenschaften der Komplexe werden anhand der Relaxationszeiten quantifiziert. Für den Komplex $V^{III}_2Dy_2$ **2.2** lauten die erhaltenen Parameter $\tau_0 = 1{,}518\times10^{-5}$ s, $\tau_{QTM} = 1{,}15\times10^{-3}$ s und Ueff = 14(2) K. Die Cluster $V^{III}_5Dy_8$ **2.9** und $V^{III}_3V^{IV}Dy_5$ **2.10** zeigen dagegen SMM-Eigenschaften, ohne dass ein Magnetfeld angelegt werden muss. Im Fall des Komplexes $V^{III}_5Dy_8$ **2.9** bestätigen die Ergebnisse der Mikro-SQUID-Experimente das Vorhandensein von SMM-Verhalten unterhalb von 0.3 K, wie

aus der Hysterese ersichtlich. Außerdem ergibt die Anpassung der Arrhenius-Gleichung eine Energiebarriere von 8 K und eine Relaxationszeit von 10^{-13} s für den $V^{III}_5Dy_8$ **2.9**-Komplex. Im Vergleich zu den SMM-Komplexen anderer dreiwertiger Übergangsmetall- und Lanthanidionen bestätigt dieses Kapitel, dass auch Komplexe vom Typ V-Ln als SMM-Kandidaten in Frage kommen, und erweitert zudem den Umfang der Forschung auf dem Gebiet der 3d-4f-SMMs erheblich.

Kapitel 3 konzentriert sich auf die Kristallstrukturen und magnetischen Eigenschaften von 14 $V^{III}_4Ln_4$-Komplexen, die alle die gleiche Quadrat-in-Quadrat-Topologie aufweisen, sich aber in ihren Liganden und Lanthanidionen unterscheiden. Die Ergebnisse von Experimenten zur magnetischen Suszeptibilität bei Gleichstrom zeigen, dass diese $V^{III}_4Ln_4$-Komplexe ferromagnetische Eigenschaften aufweisen. Im Gegensatz dazu zeigen die $V^{III}_4Y_4$-Komplexe, die diamagnetische Y-Ionen enthalten, Antiferromagnetismus. Daraus lässt sich schließen, dass es eine ferromagnetische Wechselwirkung zwischen den Lanthanid- und Vanadium-Ionen gibt. Außerdem werden in diesem Abschnitt die magnetokalorischen Eigenschaften von zwei isostrukturellen $V^{III}_4Gd_4$-Komplexen mit leichten Unterschieden in den Liganden erörtert. $V^{III}_4Gd_4$ **3.3** hat eine Entropieänderung von 16,08 J kg^{-1} K^{-1} bei 3 K für H = 7 T, während $V^{III}_4Gd_4$ **3.7** eine Entropieänderung von 17,31 J kg^{-1} K^{-1} bei 3 K für H = 7 T hat.

Kapitel 4 befasst sich mit den magnetostrukturellen Korrelationen einer Reihe von ringförmigen V^{III}-Ln-Komplexen anhand von Gleichstrom-Suszeptibilitätsmessungen. Darüber hinaus wird in diesem Kapitel die Beziehung zwischen den Metall-Metall-Abständen und der Anordnung der Vanadium- und Lanthanid-Ionen im Ring untersucht. Darüber hinaus werden die Auswirkungen von Ligandenänderungen auf die magnetischen Suszeptibilitätseigenschaften dieser isostrukturellen Komplexe diskutiert. Bemerkenswert ist, dass die Veränderung des Liganden keinen signifikanten

Einfluss auf die gleichstrommagnetischen Suszeptibilitätseigenschaften hat. Die Ergebnisse tragen zu einem besseren Verständnis des magnetischen Verhaltens bei, das in diesen ringförmigen V^{III}-Ln-Komplexen beobachtet wird.

Chapter 1. Introduction

1.1 Magnetic Properties of Matter

One of the fundamental properties of matter is magnetism, ranging from elementary particles in the microcosm to macroscopic objects in the real world, and even celestial bodies in the vast universe. In ancient times, scientists and historians generally believed that magnetism was first discovered accidentally by a Greek shepherd who one day observed that a small stone could attract the cast iron end of a stick he was holding. At the same time, this stone and its attraction to iron substances were found in Asia Minor, in the region of Magnesia in Macedonia, and in the city of Magnesia in Ionia. Therefore, most of the later people believed that the word "Magnetism" (magnetism) was derived from the names of these areas.[1]

1.2 Types of Magnetism

Magnetism is a fundamental property of matter. The magnetism of a substance refers to the property that it will be affected by a magnetic force in an inhomogeneous magnetic field. The strength of the material's magnetism, also known as strong magnetism or weak magnetism, is defined by the strength of the magnetic force on a unit mass of matter in the same inhomogeneous magnetic field. An important physical quantity describing the magnetic strength of an object is the magnetization vector M, which is the vector sum of the magnetic moments of each magnetic domain in a unit volume. The relationship between magnetization M and magnetic field strength H is expressed as:

$$M = \chi H$$

χ is the magnetic susceptibility of the object. According to the size and sign of the material susceptibility χ, the source of material magnetism and the magnetic structure characteristics, material magnetism can be divided into five categories:

diamagnetism, paramagnetism, ferromagnetism, antiferromagnetism and ferrimagnetism. The five categories of magnetism are briefly described below.

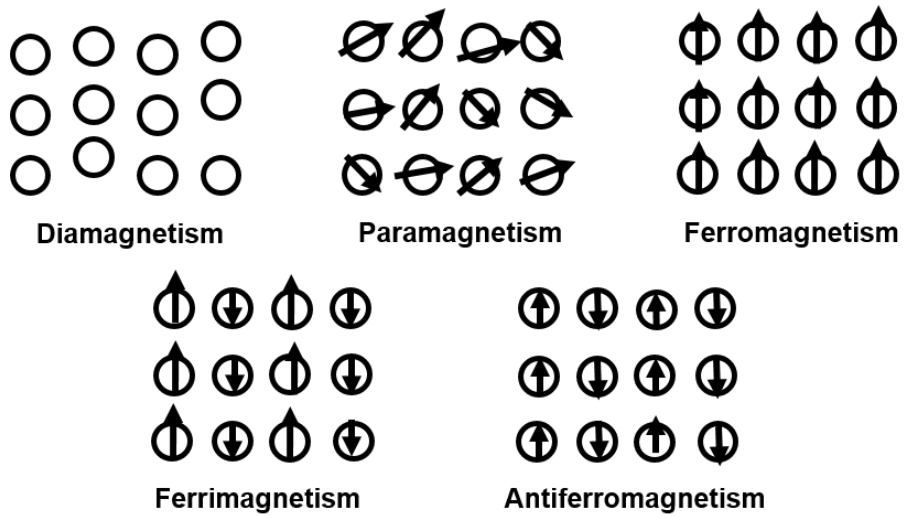

Figure 1.1: Schematic diagram of five different kinds of magnetism.

1.2.1 Diamagnetism

The magnetic moment of a free atom has three main sources: one is the spin of the electron, the second is the orbital angular momentum of the electron rotating around the nucleus, and the third is the change of the orbital magnetic moment induced by the rotation of the electron in an external magnetic field. The third source is the cause of diamagnetism, and the first two sources contribute to paramagnetism, ferromagnetism, antiferromagnetism and ferrimagnetism to varying degrees. It can be seen that there is a third source in all substances, so diamagnetism exists in all substances. The magnetization of diamagnetism is opposite to the direction of the external magnetic field.

1.2.2 Paramagnetism

The necessary condition for a substance to have paramagnetism is that the atoms, molecules or ions that make up the substance have an intrinsic magnetic moment. However, the interactions between these atomic magnetic

moments are very weak, and under the influence of thermal motion, they are basically in a randomly ordered state; the higher the temperature, the more disordered the arrangement. After the material is magnetized, the atomic magnetic moments tend to be arranged along the direction of the external magnetic field. The larger the external magnetic field, the more orderly the arrangement. It can be seen that the magnetization M of the paramagnetic substance is in the same direction as the external magnetic field H.

The magnetic susceptibility of paramagnetic substances is a function of temperature, obeying Curie-Weiss law.

$$\chi = \frac{C}{T \pm T_p}$$

χ is the magnetic susceptibility of the object. C is called the Curie constant, T_p is called the Curie paramagnetic temperature. Substances that obey the Curie-Weiss law show paramagnetism above a certain temperature, and show other properties below this temperature.

1.2.3 Ferromagnetism

There is an exchange interaction between the electrons of atoms or ions in ferromagnetic substances. Such a large magnetic field is enough to overcome the influence of thermal motion, so that the magnetic moments of atoms are aligned parallel to each other. The magnetic susceptibility of ferromagnetic substances is a function of temperature and also obeys the Curie-Weiss law.

1.2.4 Antiferromagnetism

Antiferromagnetism was first theoretically predicted by the French scientist Néel in 1936, discovered in 1938, and confirmed by neutron experiments in 1949. Substances that exhibit antiferromagnetism at low temperatures become paramagnetic after exceeding the magnetic transition temperature (commonly known as the Néel temperature), and their magnetic susceptibility temperature

relationship again obeys the Curie-Weiss law.

1.2.5 Ferrimagnetism

In 1948, after Néel created the theory of ferrimagnetism on the basis of antiferromagnetic theory, people realized the particularity of this kind of material. Ferrimagnetic substances generally have lower susceptibility and magnetization than ferromagnetic substances, but their resistivity is much higher. The magnetic susceptibility $\chi > 0$ of ferrimagnetic substances can be very large.

1.3 Magnetic Anisotropy

The phenomenon that the magnetization curves measured by the magnetization of a single crystal along different crystal axis directions and the difficulty of magnetization to saturation are different in the three directions is called magnetic anisotropy. The three main classifications include induced magnetic anisotropy, shape magnetic anisotropy and magnetocrystalline anisotropy.[2] Magnetic anisotropy plays a crucial role in the magnetic properties of single molecule magnet systems.[3] It affects the shape of the hysteresis loop, the magnitude of the coercive field of the magnet, and affects the occurrence of magnetic blocking of single molecule magnets (SMMs).[4]

For SMMs containing multiple paramagnetic metal centers these centers can be coupled in various ways.[5] Magnetic anisotropy can arise from spin-dipole and exchange coupling of electrons, hyperfine interactions between electrons and nuclei, and most notably electron spin-orbit coupling, all of which lead to anisotropic electron distribution in molecules.[6] Spin-orbit coupling results from the interaction of an electron's orbital angular momentum with its own spin angular momentum.[7] From the electron's point of view, this constitutes the orbital angular momentum. This type of coupling also exists between the

electron's spin and the nuclear magnetic field and is known as hyperfine coupling. For SMMs and lanthanide ions with relatively weak magnetic coupling, the magnetic anisotropy plays a decisive role in the properties of SMMs, directly affecting the magnetic relaxation switching barrier and blocking temperature of the system.[8]

1.3.1 Lanthanide Ion Anisotropy

Studies have shown that the magnetic properties of lanthanide-containing SMMs mainly come from the magnetic anisotropy of a single magnetic center, so the surrounding ligand field environment also plays important role in controlling the magnetic properties.[9-11] Therefore, the effective design of the ligand field environment around lanthanide metal ions is important for producing high-performance lanthanide based SMMs. Among them, lanthanide ion anisotropy and crystal field symmetry are the two most important design factors for optimizing the ligand field environment.

To clearly understand how to maximize the magnetic anisotropy for specific lanthanide ions, Long's research group proposed a theoretical model of the electron cloud distribution of lanthanide ions through theoretical calculations.[12] The model uses the method of quadrupole approximate calculation to describe the charge density distribution of the ground state of various lanthanide ions corresponding to the eigenstate. Due to the strong angle dependence of 4*f* orbitals, the 4*f* electron charge density distribution of lanthanide ions is usually not spherical, but anisotropic ellipsoidal.[13] By further drawing on the electrostatic model of effective point charge, it can be understood that for some lanthanide ions the charge density distributions are prolate (Pm^{3+}, Sm^{3+}, Er^{3+}, Tm^{3+}, Yb^{3+}), and for some they are oblate (Ce^{3+}, Pr^{3+}, Nd^{3+}, Tb^{3+}, Dy^{3+}, Ho^{3+}) or isotropic spherical (Gd^{3+}) from the Figure **1.3**.

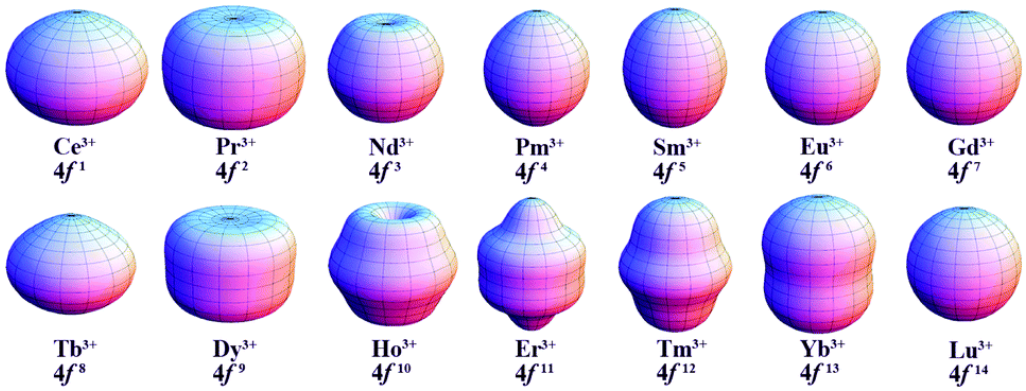

Figure 1.3: Anisotropy of the 4f charge density distribution of lanthanide ions.[13]

1.4 Introduction to Single Molecule Magnets

Magnetic materials have several applications making them an integral part of our lives. Magnetic materials can be found in technology ranging from small electronic products such as mobile phones to large maglev trains. In the current high-speed development of the information age, the requirements for higher storage capacity devices are also increasing. Due to the long-range ordering effect between molecules, traditional magnetic storage materials form magnetic domains after magnetization for information storage, which means that the amount of information stored is positively correlated with the size of the material.[14-16] Finding high-density storage and small-volume magnetic materials has become the focus of research in this area.

Since the slow magnetic relaxation phenomenon was first discovered in $[Mn_{12}O_{12}(O_2CCH_3)_{16}(H_2O)_4]$ (Mn_{12}) clusters by the Gatteschi group as shown in Figure **1.4**,[17] SMMs have made great progress over the past three decades and have become a research field that has attracted much attention integrating many disciplines such as chemistry, material sciences, and physics.[18-19] SMMs can be regarded as molecular scale nanomagnets, and each molecule is equivalent to a magnetic functional unit. Because of the unique molecular-level magnetism and the superparamagnetic behavior of SMMs, they exhibit many characteristics different from traditional magnetic materials. On the one hand,

unlike the traditional method of preparing magnets from large to small through mechanical processing, single molecule magnets are self-assembled in solution, forming magnetic materials from small to large molecular scales. The formed magnet has the characteristics of orderly arrangement, uniform size, low density, and good dispersion, which is more conducive to delocalization. Furthermore, quantum tunneling of magnetization (QTM) can be observed in SMMs exhibiting dual characteristics of classical mechanics and quantum mechanics in the same material.[20-22]

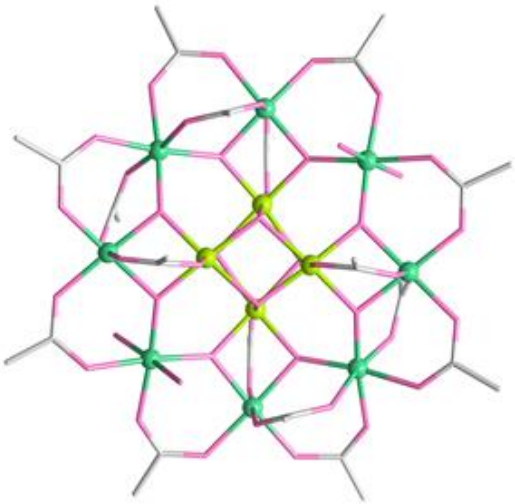

Figure 1.4: Molecular structure of Mn_{12} (light yellow: Mn^{IV}, light green: Mn^{III}).[14]

SMMs possess magnetic bistability at the molecular level and exhibit slow magnetic relaxation across the effective energy barrier below the blocking temperature. To better understand the origin of magnetism and analyze the key factors affecting magnetic behavior, microscopic relaxation can be analyzed by macroscopic models.[23] At zero applied magnetic field, the microscopic particles are evenly distributed in two degenerate states. When the external magnetic field is removed, the energy levels return to the degenerate state, but the number of microscopic particles occupying the two energy states are not the same. This results in remanence. Some microscopic particles then need to climb the energy barrier to return to an evenly distributed state, and the process of returning to an equilibrium state is called the magnetic relaxation process. As shown in Figure **1.5**, if the ambient temperature is low enough, the energy

provided by the thermal vibration is not enough to quickly cross the energy barrier, and some microscopic particles will be frozen in a specific orientation. This requires a long time to return to the equilibrium state, thus showing the phenomenon of slow magnetic relaxation.

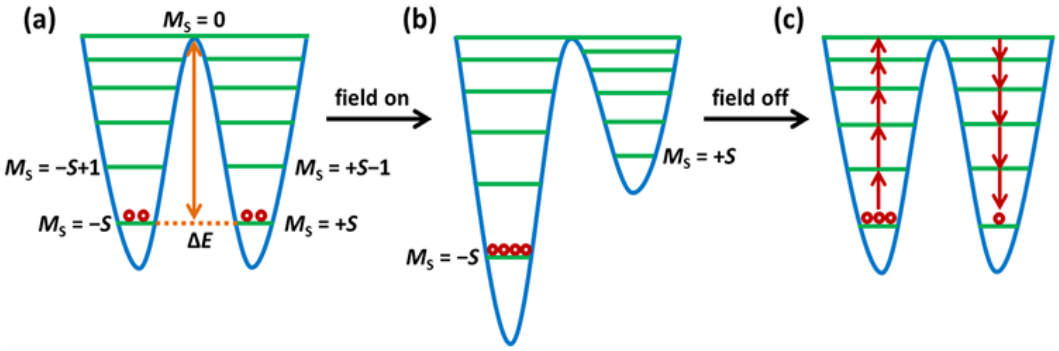

Figure 1.5: Schematic diagram of the generation process of the magnetic relaxation behavior of 3d SMMs.[14,23]

1.4.1 Research Progress of 3d SMMs

For 3d SMMs,[24-26] the relationship between the energy barrier *U* and the ground state spin value *S* and the zero-field splitting parameter *D* can be expressed as $U = |D|S^2$, if *S* is an integer number and as $U = |D|(S^2\text{-}1/4)$ if *S* is half integer number.[27] During the early studies on 3d SMMs, it was believed that increasing the ground-state spin value *S* could increase the energy barrier, so a large number of polynuclear manganese complexes were synthesized for example $[Mn_{19}]$,[24] $[Mn_{25}]$,[27] $[Mn_{31}]$,[28] and $[Mn_{84}]$.[29] For the complex $[Mn_{25}]$,[25] the ground state spin shows S = 61/2, and the enery barrier show U_{eff} = 9.3 K. Some scholars such as Waldmann *et al.* proposed that the ground state spin value *S* and the zero-field splitting parameter *D* show an inverse relationship, therefore the energy barrier cannot be increased by increasing the ground state spin value *S*.[31-32] In 2006, the research group of Powell reported that the ground state spin value S of the compound reached 83/2, but the anisotropy parameter was zero as shown in Figure **1.6**.[25]

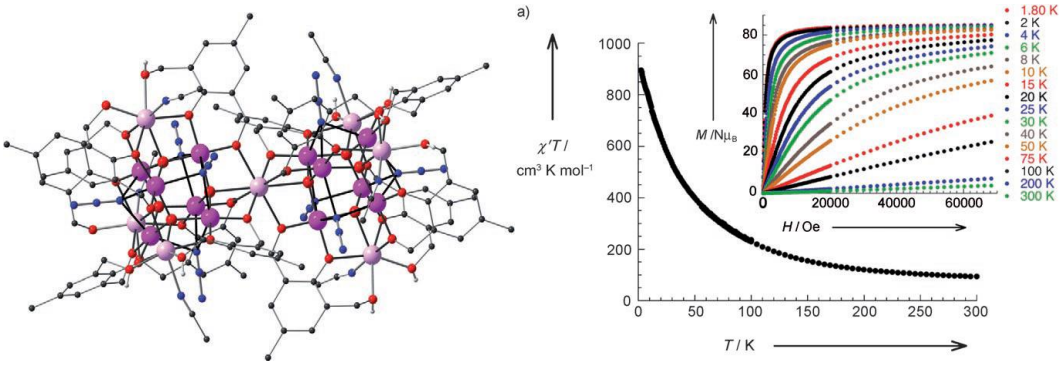

Figure 1.6: (a) Molecular structure of Mn_{19} in the crystal (Mn^{III} dark pink, Mn^{II} pale pink, O red, N blue, C gray, H white). (b) Temperature dependence of the χT product (where χ = dM/dH) measured in H_{dc} =0 Oe, H_{ac} =3 Oe, and v =1000 Hz (Inset: field dependence of the magnetization from 1.8 K to 300 K).[25]

In addition, SMMs based on transition metal clusters of Fe, Co, Ni, V, and Cr cations have also been reported.[33-48] In 2013, Long *et al.* reported a linear complex of $[K(crypt\text{-}222)][Fe^{I}(C(SiMe_3)_3)_2]$.[33] Magnetic experiments show that the complex exhibits slow magnetic relaxation at zero field, indicating that it is a single molecule magnet as shown in Figure **1.7**.[33] According to the fitting, its effective energy barrier is 325K (226 cm^{-1}), and the complex $[K(crypt\text{-}222)][Fe^{I}(C(SiMe_3)_3)_2]$ shows hysteresis loops below 6.5 K.

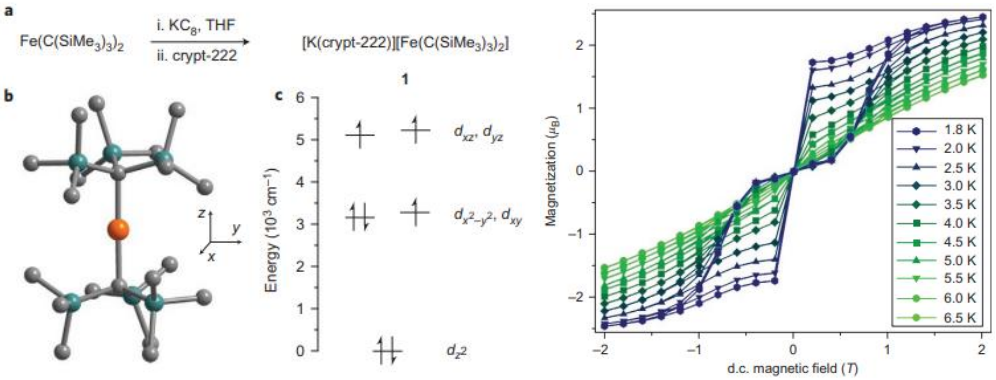

Figure 1.7: (a) Preparation, structure, and d-orbital splitting of the linear iron(I) complex $[K(crypt\text{-}222)][Fe(C(SiMe_3)_3)_2]$. (b) Variable-field magnetization data for $[K(crypt\text{-}222)][Fe(C(SiMe_3)_3)_2]$.[33]

To obtain SMMs with superior performance, molecules with high spin ground state and large uniaxial magnetic anisotropy must be obtained. Early researchers have been working on improving the spin ground state, focusing on the synthesis of high-nuclearity transition metal SMMs. For example in 2008, Ruiz and other researchers studied the magnetic anisotropy and magnetic

interaction of two Mn_6 clusters with similar structures shown in Figure **1.8**, and the results showed that the size of the anisotropy energy barrier was mainly dependent on the spin-orbit coupling intensity, not just by increasing the value of *S* and *D*.[29] Numerous results show that it is often difficult to obtain the spin ground state and large uniaxial magnetic anisotropy in the same system at the same time. So only increasing the spin value of the ground state cannot obtain a single molecule magnet with a higher energy barrier.

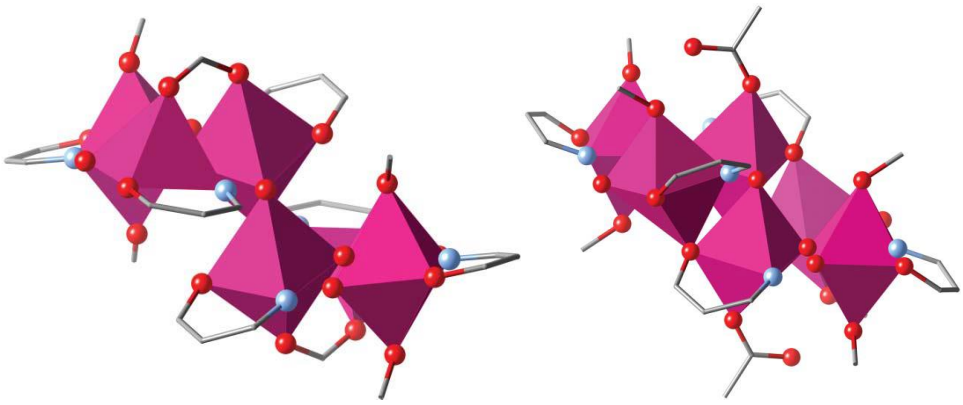

Figure 1.8: (a) Polyhedral representation of the structure of $[Mn_6O_2(sao)_6\text{-}(O_2CH)_2(MeOH)_4]$. (b) Polyhedral representation of the structure of $[Mn_6O_2(Etsao)_6\text{-}(O_2CPh(Me)_2)_2(EtOH)_6]$. (Mn, O and N atoms represented by pink polyhedral and red and blue spheres, respectively.).[32]

1.4.2 Research Progress of 4f SMMs

Compared with obtaining 3d SMMs with higher ground-state spin values, selecting metal centers with large magnetic anisotropy has been proven to be a more effective way to increase the effective energy barrier of SMMs.[49-51] The 4f electrons in the electron shell structure of the lanthanide ion have a large unquenched orbital angular momentum, resulting in a large magnetic moment and magnetic anisotropy. Since there is a shielding effect of the outer 5s and 5p electron shells, the crystal field effect and magnetic interactions between lanthanide ions are usually weak, so most lanthanide ions can still maintain their single-ion properties. Due to the above-mentioned advantages of lanthanide metal ions, they are ideal candidates for the construction of SMMs.[52]

In 2003, Ishikawa's research group introduced single lanthanide ions into the field of SMMs research for the first time, by reporting complexes based on

single Tb^{III} and Dy^{III} ions exhibiting SMM behavior.[53] Among them, the out-of-phase ac signals of the Tb^{III} complex correspond to peak temperatures of 15, 32, and 40 K at frequencies of 10, 100, and 997 Hz respectively, showing significant frequency-dependent behavior. This can be seen in Figure **1.9**. When diamagnetic Y^{III} is doped in this sample, the frequency-dependent behavior shifts slightly to higher temperatures, further verifying that the relaxation behavior of the complex comes from the magnetic anisotropy of the single Tb^{III}. The source of the magnetic properties of lanthanide complexes is obviously different from that of 3d metal clusters. In lanthanides the magnetic properties originate from the strong spin-orbit coupling of a single metal ion, the large J_Z value, and significant energy level splitting, resulting in the greater potential for the development of high-temperature SMMs.[54-56]

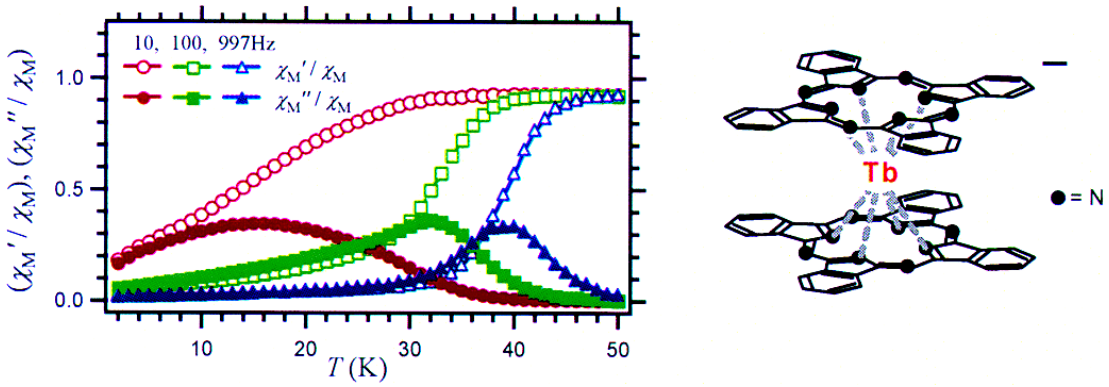

Figure 1.9: Temperature-dependent χ_M'/χ_M and χ''/χ_M ac magnetic susceptibility signals of the $[TbPc_2]^-$ complex and corresponding molecular structure diagrams.[53]

In recent years, there has been great progress in several research groups of scientists such as Mingliang Tong and Yanzhen Zheng research group from China and Ramaswamy Murugavel's and Mark Murrie's research groups from India and Scotland who have conducted a lot of studies on dysprosium based SMMs in the D_{5h} coordination environment.[57-60] Due to the high crystal field symmetry of this configuration, the quantum tunneling relaxation process under zero field can be suppressed. SMMs with D_{5h} symmetry exhibit excellent frequency-dependent behavior in ac magnetic susceptibility measurements and better coercive field in the hysteresis loop than previously reported for other

geometries of single ion lanthanide SMMs. Summarizing the bond length information of the first coordination layer of the listed complexes in Figure **1.10**, the longer the bonds in the pentagonal plane, the shorter the axial coordination bond.[57] It is beneficial to maintain the oblate ground state electron cloud density distribution of dysprosium ions, to obtain a significant single axial anisotropy. Thus, in this series of work the importance of single-ion anisotropy and crystal field symmetry for the construction of high-performance lanthanide SMMs has been demonstrated.

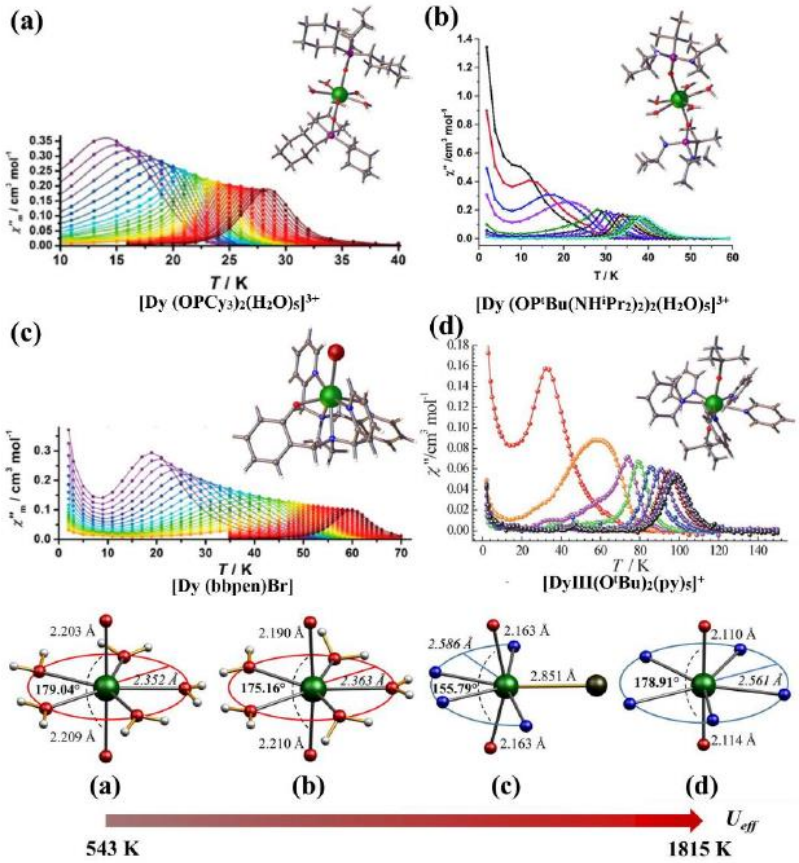

Figure 1.10: Molecular structures of representative pentagonal bipyramidal dysprosium complexes and the temperature-dependent imaginary part χ″ AC magnetic susceptibility signal plots for each complex.[57]

In 2017, the Mills' research group successfully used the hydrogenation reagent $[(Et_3Si)_2(\mu\text{-}H)][B(C_6F_5)_4]$, and dissociated the chloride ligand on the lanthanide ion, thereby obtaining the first lanthanide SMMs with only two cyclopentadienyl ligands forming a sandwich-type complex. The complex

exhibits outstanding relaxation behavior with a thermally activated Orbach relaxation process in the observable frequency range. The fitted relaxation energy barrier is 1837 K, and the hysteresis loops are still open at 60 K (Figure **1.11** top). Subsequently, in 2018, the Layfield research group optimized the residues on the cyclopentadienyl ligands, which made the axiality of the complex better, as the coordination distance between carbon and dysprosium ions became closer, promoting the effective energy barrier to 2216 K as shown in Figure **1.11** bottom. The maximum opening temperature of the hysteresis loops exceeds 80 K.[63] The complex was the SMM with the best performance reported at the time and it was the first SMM that exceeded the temperature of liquid nitrogen. The outstanding magnetic properties of this series of complexes benefit from the absence of transverse ligand fields and the π-electron coordination which is beneficial to weaken thermal vibrations and avoid the generation of fast relaxation pathways.[63]

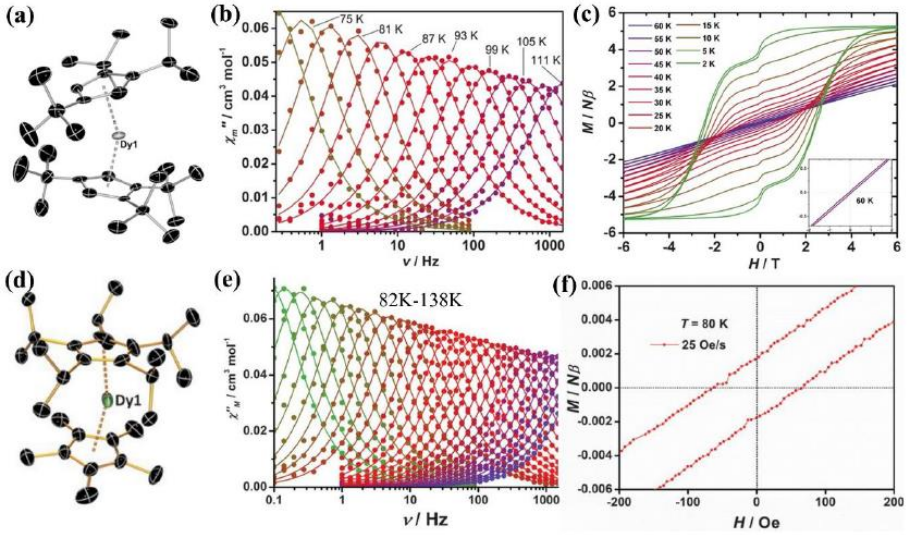

Figure 1.11: (a) Molecular structure of $[(Cp^{ttt})_2Dy]^+$; (b) frequency-dependent χ″ ac magnetic susceptibility signals; (c) hysteresis loops of $[(Cp^{ttt})_2Dy]^+$; (d) Molecular structure of $[(Cp^{iPr5})Dy(Cp^*)]^+$; (e) frequency-dependent out-of-phase ac susceptibility signals; (f) open hysteresis loop at 80 K.[63]

1.4.3 Research Progress of 3d-4f SMMs

Compared with lanthanide ions, the intrinsic crystal field effect of 3d metal ions is much stronger than the spin-orbit coupling effect, thus limiting the

effective orbital contribution of a single 3d metal ion, so that 3d metal ions generally exhibit weaker magnetic anisotropy.[64] Therefore, in 3d-4f SMMs, the magnetic anisotropy is still controlled by the strong magnetic anisotropy of lanthanide ions, and the absence of outer shielding orbitals in 3d metal ions promotes stronger 3d-4f exchange than 4f-4f exchange action. Meanwhile, 3d ions can be either anisotropic magnetic ions (such as Co^{II}, Mn^{III}, Cr^{II}),[65-68] isotropic magnetic ions (Mn^{II}),[69-70] or even diamagnetic ions (Zn^{II}, Co^{III}).[71-74] Using diamagnetic 3d metal ions will not directly affect the magnetic anisotropy of lanthanide ions, but the introduction of diamagnetic cations will indirectly polarize the charge density of bridging atoms and increase their electrostatic distribution. This may be beneficial for improving the magnetic anisotropy of lanthanide ions.[73] In addition, the introduction of diamagnetic ions will increase the volume of the entire molecule, which is conducive to increase the distance between Ln···Ln molecules and weakens the influence of the transverse crystal field caused by the dipole interaction between molecules. The introduction of 3d metal ions can play a positive role in improving the relaxation behavior of lanthanide ions.

In 2013, Murray's research group reported two cases of 3d-4f SMMs as shown in the Figure **1.12**. [75-76] The 3d metal ions were Co^{III} and Cr^{III}, and their effective energy barriers were 79 K and 77 K, respectively. However, since Co^{III} is a diamagnetic ion, it does not show exchange coupling to the Dy^{III} ions; whereas the paramagnetic Cr^{III} ions do. The data in the low temperature region in the dc magnetic susceptibility measurement shows an increase associated with ferromagnetic coupling. The difference in the 3d metal ions of the two complexes leads to the difference in the exchange effect, which makes the Cr^{III}-based complex exhibit a hysteresis loop and a good frequency-dependent behavior, while the Co^{III}-based complex does not show hysteresis or slow relaxation of the magnetization. It was shown through theoretical calculations that the exchange between Cr^{III} and Dy^{III} leads to a very small energy level gap

for tunneling, thus effectively inhibiting the quantum tunneling relaxation process. This work achieves the effective suppression of quantum tunneling by introducing 3d-4f exchange interactions, which proves that transition metal ions can play an important role in improving hysteresis performance.[77]

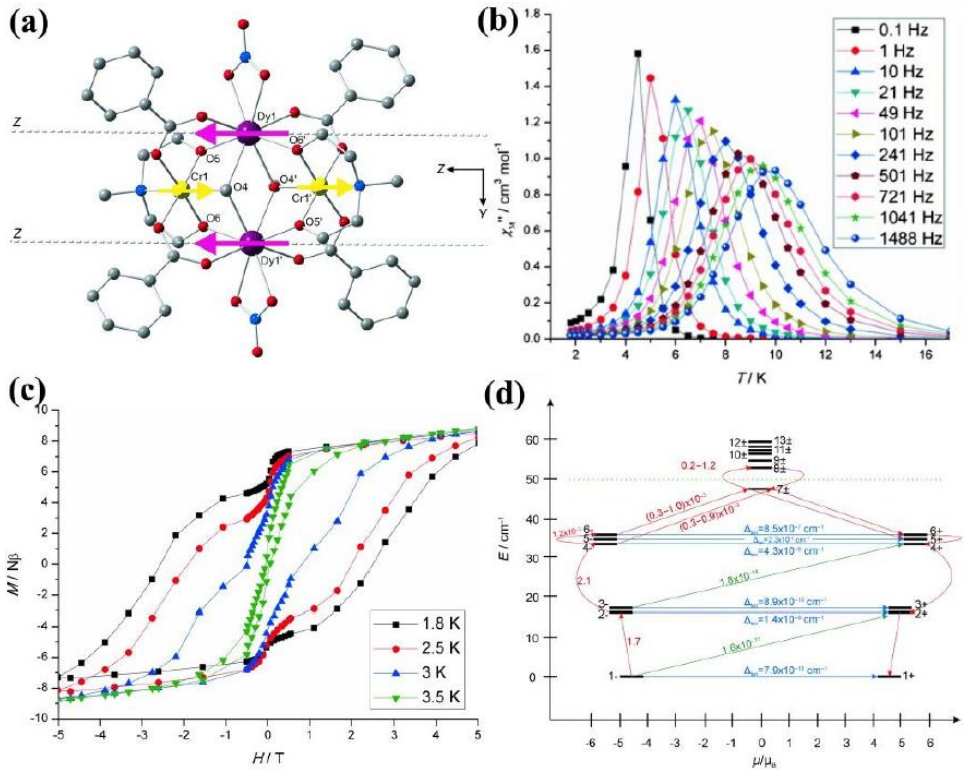

Figure 1.12: (a) Molecular structure of $\{Cr^{III}_2Dy^{III}_2\}$; (b) temperature-dependent χ'' ac magnetic susceptibility signal; (c) hysteresis loops; (d) low-lying excited states and the corresponding relaxation rates. [77]

In 2014, Tong's group synthesized an Fe^{II}-Dy^{III}-Fe^{II} SMM with a pentagonal-bipyramidal Dy^{III} ion, and two asymmetric and distorted Fe^{II} ions as shown in the Figure **1.13**.[78-79] *Ab initio* calculations suggest that the height of the barrier corresponds to the energy of the first excited Kramers doublet on the Dy^{III} site. This led to a record anisotropy barrier of 319 cm^{-1} (459 K) for 3d-4f SMMs at that time. The frozen magnetic moment of the Dy^{III} ion at low temperatures is responsible for slowing down the magnetic relaxation of Fe^{II} moments which is observed in the Mößbauer spectrum at zero applied field.

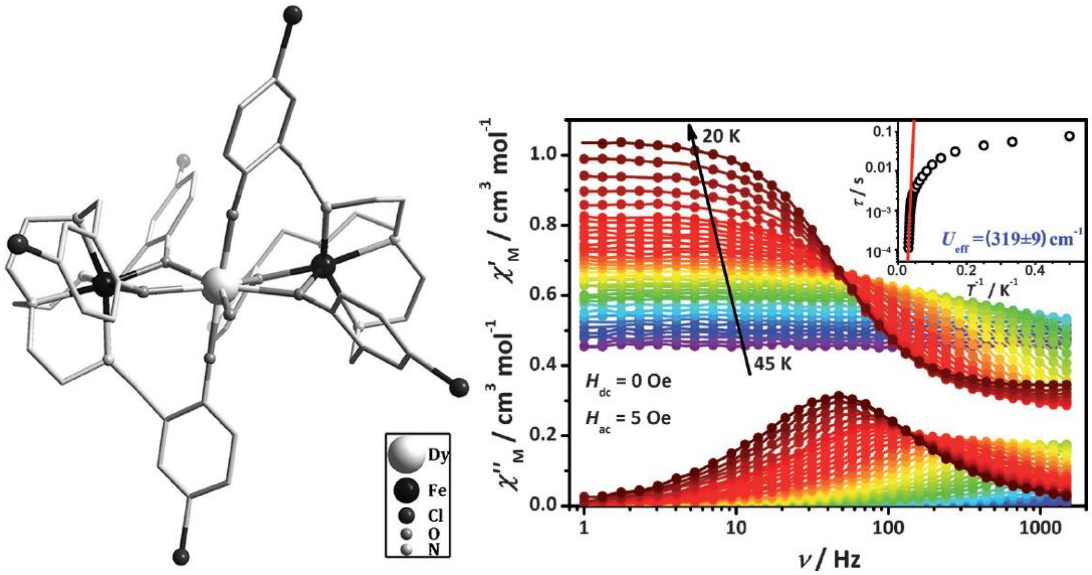

Figure 1.13: (a) Molecular structure of {$Fe^{II}_2Dy^{III}$}; (b) Plot of susceptibility versus frequency in the temperature range of 20-45 K at H_{dc} = 0 Oe (H_{ac}=5 Oe) for {$Fe^{II}_2Dy^{III}$}.[78]

In 2020, Tong's research group reported two Cu-Dy SMMs, the structures of which are shown in Figure **1.14**.[80] The molecular formula is $[Dy^{III}Cu^{II}_5(quinha)_5(sal)_2(py)_5](CF_3SO_3)py{\cdot}4H_2O$ and $[Dy^{III}_2Cu^{II}_{10}(quinha)_{10}(sal)_2(OH)(py)_9](CF_3SO_3)_3{\cdot}2py\ 2CH_3OH\ 2H_2O$, H_2quinha = quinaldihydroxamic acid, Hsal = salicylaldehyde. In the first structure, the Dy^{III} ion is located at the center of five Cu^{II} ions forming a planar shape. Above and below the pentagonal plane, pyridine and salicylaldehyde participate in coordination with the five-coordinate Cu^{II} ions. The Dy has five O atoms in the plane, and two O atoms of salicylaldehyde in the axial positions. The second compound has a double-layer structure, and two Cu_5Dy planes are bridged by Dy^{III} through OH^-. Figure **1.15** shows that the U_{eff} fitted to the ac data is 900 K and 838 K for the two complexes and the energy barrier value of 900 K is the largest recorded among 3d-4f SMMs.

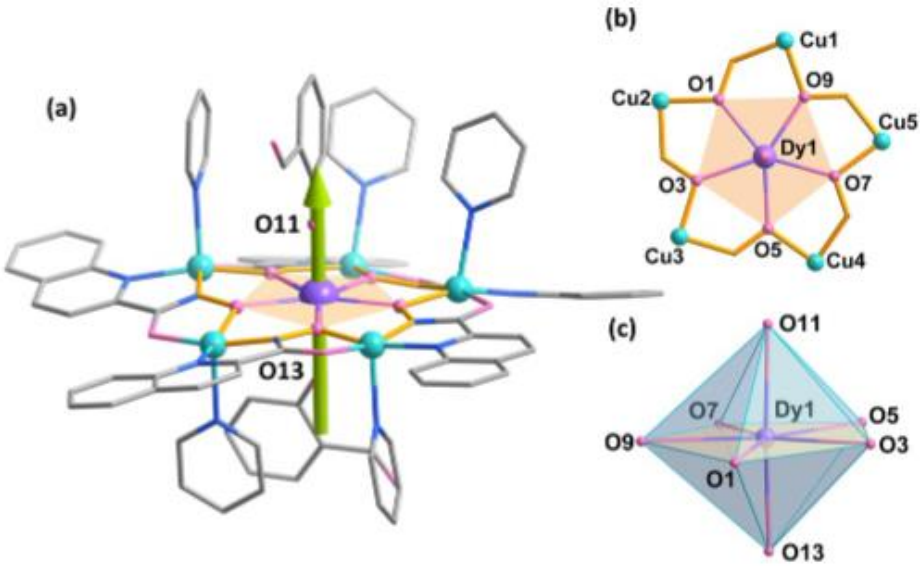

Figure 1.14: (a) Side view of $[Dy^{III}Cu^{II}_5(quinha)_5(sal)_2(py)_5]^+$; (b) Top view of the core; (c) Coordination environment of the Dy^{III} ion.

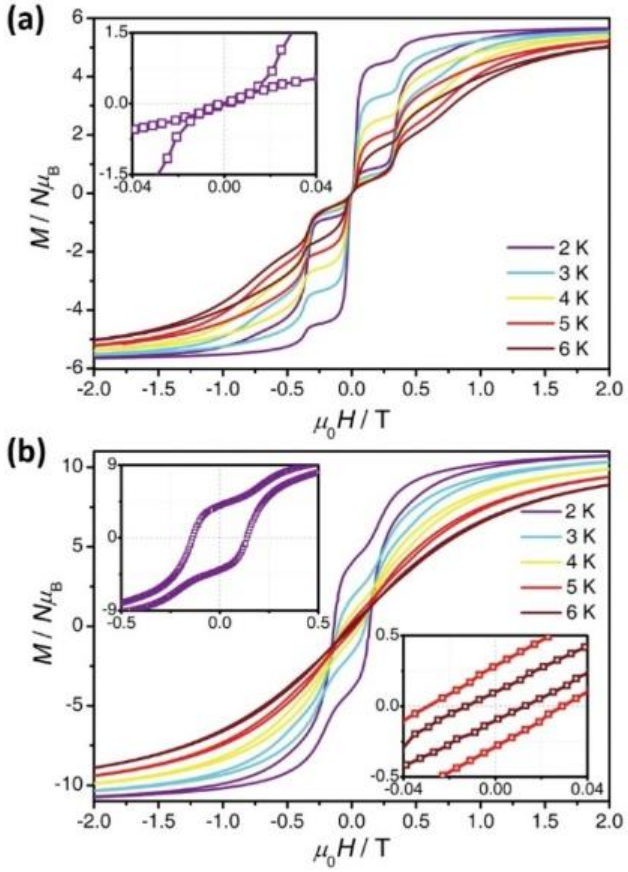

Figure 1.15: (a) Magnetic hysteresis loops for $[Dy^{III}Cu^{II}_5(quinha)_5(sal)_2(py)_5](CF_3SO_3)py{\cdot}4H_2O$ and $[Dy^{III}_2Cu^{II}_{10}(quinha)_{10}(sal)_2(OH)(py)_9](CF_3SO_3)_3{\cdot}2py\ 2CH_3OH\ 2H_2O$ (b) The data were collected with the field sweeping rate of 0.02 Ts^{-1} at various temperatures. Inset: the enlargement of magnetic hysteresis loops.

The examples given above are some of the best performing SMMs reported in the literature.

1.5 Magnetic Refrigeration

Magnetic refrigeration is a cooling technology based on the magnetocaloric effect. This technique can be used to attain extremely low temperatures, as well as the ranges used in common refrigerators.[81-86] The device operates as follows: a magnetocaloric material is exposed to an applied magnetic field, causing it to heat up. This temperature rise is a result of internal changes within the material that release heat. When the magnetic field is removed, the material reverts to its initial state, absorbing the previously released heat and returning to its original temperature. To achieve refrigeration, the material is allowed to dissipate its heat while in the magnetized, hot state. Subsequently, when the magnetism is removed, the material cools down, reaching a temperature lower than its original level. The effect was first observed in 1881 by a German physicist Emil Warburg, followed by French Physicist P. Weiss and Swiss physicist A. Piccard in 1917 as shown in the Figure **1.16**.[87-90]

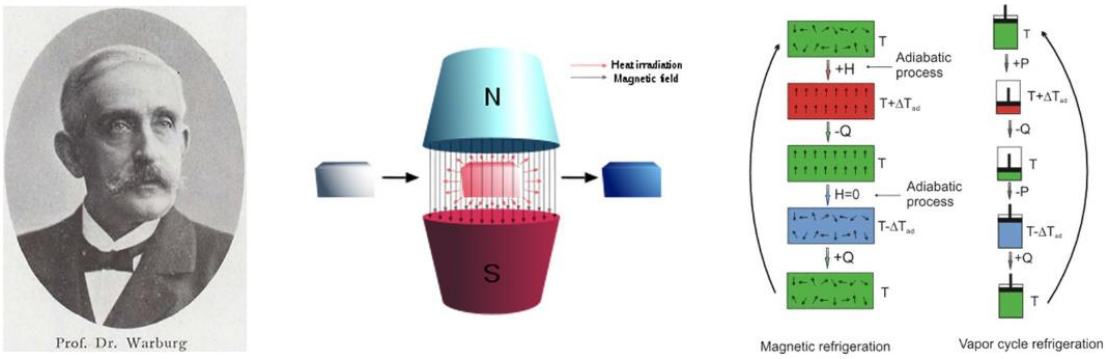

Figure 1.16: (a) Picture of Prof. Dr. Warburg; (b) Magnetic refrigeration thermodynamic cycle. (c) Schematic diagram of the isothermal magnetization and adiabatic demagnetization process of the magnetocaloric effect in a magnetic system when the magnetic field is applied or removed.

According to the Maxwell equation, $[\partial S_M (T, H) / \partial H]_T = [\partial_M (T, H)/\partial T]_H$, we can obtain the S_M by numerically integrating the derivative of magnetization with respect to temperature in practical terms.[91-93]

$$\Delta SM(T, \Delta H) = \int_{H_0}^{H_1} \frac{\partial M(T, H)}{\partial T} dH$$

As shown in the scheme above, the 1st deviation in the experimental magnetization (−ΔM/ΔT) represents the maxima at different temperatures for

different fields, the location of which indicate the greatest difference in magnetization from one temperature compared with its neighbor. The $-\Delta S_M$ values are obtained by integrating the area below the curve for $-\Delta M/\Delta T$ vs. H from H_0 to H_1. This scheme shows clearly that the magnetization data around the$-\Delta M/\Delta T$ vs. H peaks, which are typically 5–20 kOe for molecular coolants, play an important role during integration, thus a lack of detailed measurements for this region is likely to result in incorrect estimates of $-\Delta S_M$.[94-99]

For the heat capacity measurement, the total entropy can be established according to the equation below:

$$S_{Total}(T_0, H) = S_0 + \int_0^{T_0} \frac{C(T,H)}{T} dT$$

where S_0 is the zero temperature entropy (residual entropy), which is not relevant to the magnetic field for a condensed system, thus the changes in the isothermal magnetic entropy $\Delta S_M(T_0, \Delta H) = S_{Total}(T_0, H_1) - S_{Total}(T_0, H_0)$ and the adiabatic temperature $\Delta T_{ad}(T_0, \Delta H) = T_1(S_{Total}, H_1) - T_0(S_{Total}, H_0)$ are known as shown in the picture **1.17**. The errors in S_{Total} are highly dependent on the accuracy of the heat capacity measurements, as well as the thermometer used. The absolute error is used to calculate ΔS_M and ΔT_{ad} with a heat capacity technique, thus the relative error is smaller for materials with a larger MCE, or when applying a larger ΔH.[100-101]

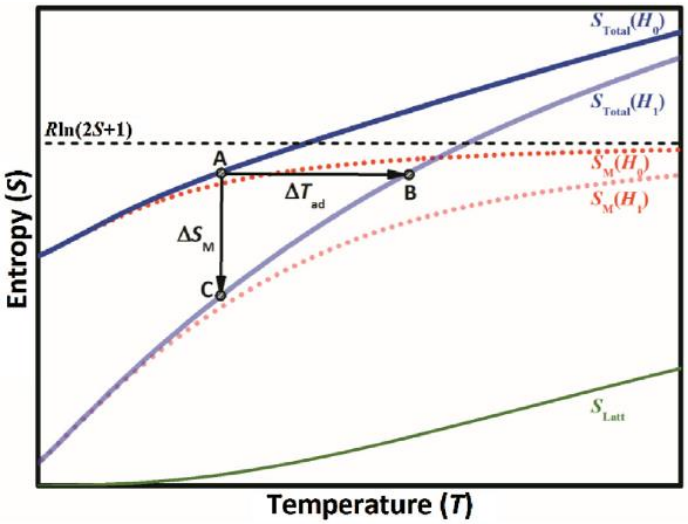

Figure 1.17: The schematic illustration of the typical S vs. T plot for molecular magnetic

coolants.

1.6 Research Objectives

1.6.1 Motivation to study Vanadium-4f Complexes

The work presented in this dissertation follows the design, synthesis, crystal structure and magnetic property characterization of vanadium-4f complexes.

As far as SMMs are concerned, the research on 3d-4f SMMs has developed rapidly in the past two decades. However, SMMs based on vanadium (III)- 4f complexes have not been reported so far because of the difficulty in obtaining stable V-Ln complexes with the desired oxidation state. Therefore, a series of vanadium-lanthanide complexes, some with SMM behavior, were synthesized for the first time by using Schlenk line technology, with the appearance of these vanadium-lanthanide complexes with SMMs properties filling this gap in the field of SMMs. Besides, it is well known that gadolinium ions are usually used as raw materials for magnetic refrigeration materials, some vanadium-gadolinium complexes synthesized are expected to be studied as magnetic refrigerants. Furthermore, some of our magnetic measurement results show that there may be ferromagnetic effects between vanadium-gadolinium complexes, so vanadium-gadolinium complexes are very likely to show magnetic refrigeration. As for the relationship between the crystal structure and the magnetic properties of ring-type vanadium-lanthanide complexes, it is known by summarizing the results of the magnetic properties of all the ring-type vanadium-lanthanide complexes. When the vanadium and lanthanide ions in the vanadium-lanthanide complexes are arranged in an alternating pattern, their direct-current susceptibility shows ferromagnetism, otherwise they are antiferromagnetic.

1.6.2 The choice of ligands for vanadium-4f complexes

Regarding the synthesis of 3d-4f complexes, the choice of ligands is very important. The difficulty of rationally designing and synthesizing 3d–4f complexes mainly results from the specific chemical nature of 3d and 4f ions and the complicated reaction systems. According to hard and soft acids and bases (HSAB), 3d and 4f metal ions have priority to coordinate with different donor atoms such as nitrogen and oxygen, respectively. In general cases, simply mixing 3d ions, or 4f ions with organic ligands would produce pure 3d or 4f complexes, respectively. Two main approaches, from the point of view of ligands, are widely adopted for rationally synthesizing 3d–4f complexes: (1) employing the ligands that are elaborately designed to possess different kinds of coordination pockets for both 3d and 4f metal ions; (2) introducing suitable co-ligands to assist the self-assembly processes in which lanthanide ions can combine transition metal ions at the presence of multidentate ligands. The two synthetic methods can be named as “designed assembly” approach and “assisted self-assembly” approach, respectively.

Alkylol amines, such as N-substituted diethanolamines, have multiple donor atoms and possess both chelating and bridging capabilities. They are often used to synthesize polynuclear 3d and 3d–4f complexes. For instance, methyldiethanolamine (H_2mdea) has resulted in a series of 3d–4f clusters with novel core topologies, such as $\{Mn^{III}_6Mn^{II}Ln\}$,[102] $\{Cr^{III}_4Dy_4\}$,[103] $\{Mn^{III}_4Mn^{IV}Ln_4\}$,[104] and$\{Fe^{III}_7Dy_3\}$.[105] For this reason, I chose these types of alkylamines as my ligands, as shown in the figure **1.18** below. Many vanadium-4f complexes were obtained with different structures and some of their magnetic properties were characterised.

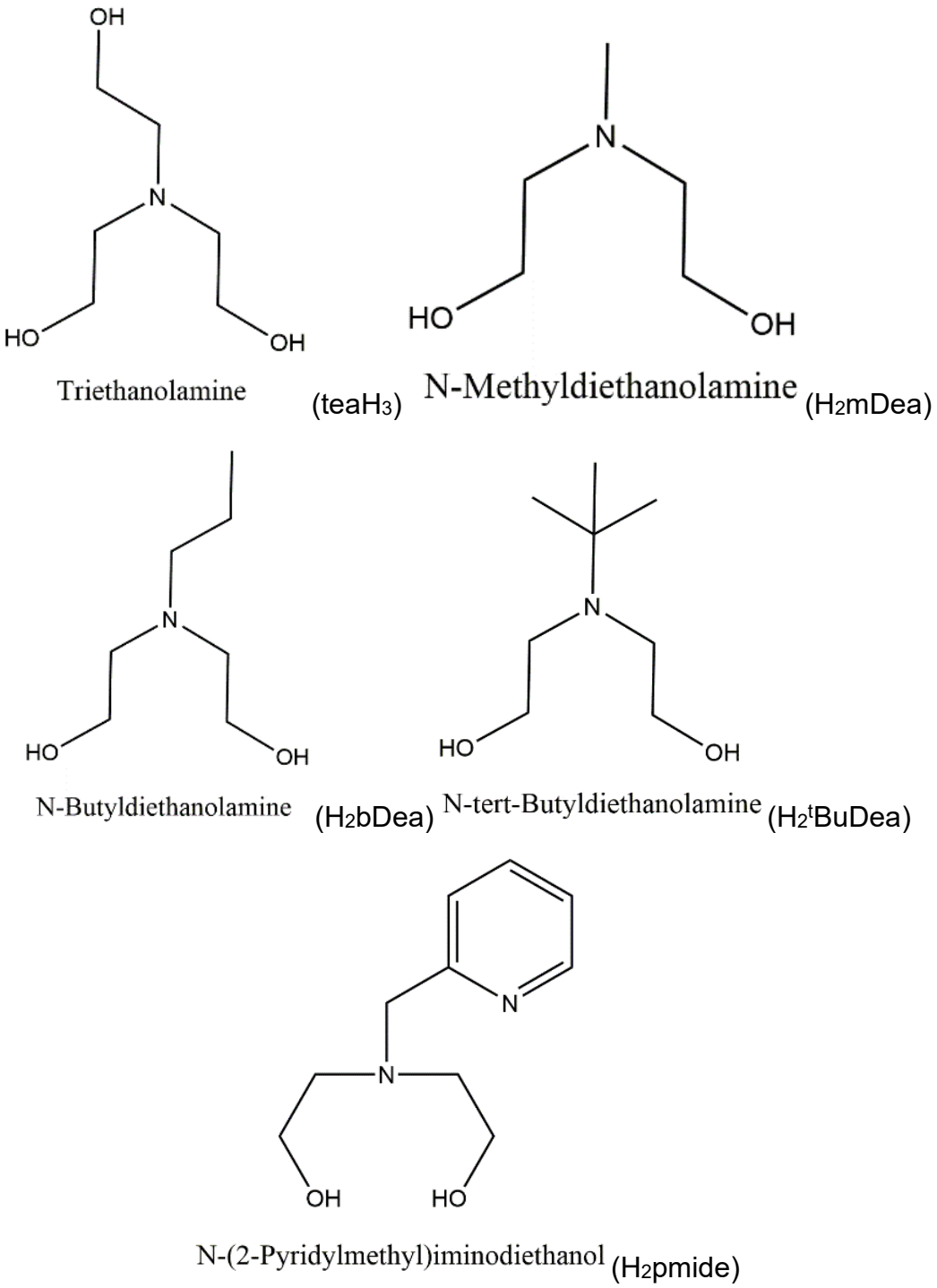

Figure 1.18: Schematic diagram of five different kinds of ligands.

Chapter 2. Vanadium-Lanthanide Complexes as 3d-4f SMMs

2.1 Introduction

Since the discovery of the phenomenon of slow relaxation of magnetization in the Mn_{12} coordination cluster by Sessoli and co-workers in 1993, and the subsequent characterization of these compounds as single-molecule magnets, it is expected that one day SMMs could be used in the field of ultra-high-density information storage, quantum information processing and molecular spintronics.[106-113] Many methods to improve the magnetic properties of coordination clusters have been investigated and regulating the magnetic coupling between paramagnetic ions to affect the magnetic relaxation behavior between 3d-4f complexes is one of the promising options for improving the performance of SMMs.[114-122]

Since the first 3d-4f SMM $[CuLTb(hfac)_2]_2$, where H_3L is 1-(2-hydroxybenzamido)-2-(2-hydroxy-3-methoxy-benzylideneamino)-ethane and Hhfac is hexafluoroacetylacetone, was reported by the Matsumoto group in 2004,[123] other 3d-4f SMMs have also been discovered.[124-146] For instance, Murray's group reported in 2013 two cases of 3d-4f SMMs ($Co^{III}_2Dy^{III}_2$ and $Cr^{III}_2Dy^{III}_2$) with similar effective energy barriers of 79 K and 77 K, respectively.[75] The $Cr^{III}_2Dy^{III}_2$ has a banana-shaped hysteresis loop and exhibits typical SMM behavior as a result of the magnetic coupling between Cr^{3+} and Dy^{3+} of *circa* 20 cm^{-1}, which shows that introducing transition metal ions can play an important role in improving the SMM performance. Most studies on 3d-4f complexes as SMMs so far have focused on mixing the transition metal ions Ti^{3+}, Cr^{3+}/Cr^{2+}, Mn^{3+}/Mn^{2+}, Fe^{3+}/Fe^{2+}, Co^{3+}/Co^{2+}, Cu^{2+} with lanthanide ions.[147-154] However, so far no SMM with vanadium(III)-lanthanide complexes have been reported.

According to previous literature reported, vanadium(III) ions with typically very large D can be used in the design of magnetic materials.[155-164] Only one

case of a vanadium-based SMM has been reported so far, [46-47] which may be due to the redox instability of vanadium(III) ion under ambient conditions. The introduction of lanthanide ions with large magnetic anisotropy into vanadium-based complexes could improve the magnetic relaxation process and facilitate the acquisition of SMM. Nonetheless, how to obtain stable vanadium(III)-lanthanide complexes is a challenge. Schlenk techniques are an excellent solution as they allow synthesis under inert conditions, eliminating the presence of oxygen to prevent the oxidation of vanadium(III) to vanadium(IV) or vanadium(V).

In this chapter, a series of stable vanadium-lanthanide complexes were synthesized under anaerobic conditions. Magnetic measurements were performed on these vanadium-lanthanide complexes. Some of these complexes behave as SMM in the absence of an applied magnetic field, while some others require an external magnetic field to exhibit SMM performance and some do not show SMM properties. Therefore, this chapter confirms for the first time that vanadium(III)-4f complexes can have SMM properties and expands the application of 3d-4f complexes in the field of SMMs.

2.2 Results and Discussions

2.2.1 Butterfly Type II Compound of $V^{III}_2Ln^{III}_2$ (Ln = Tb-Yb, Y)

2.2.1.1 Crystal Structure of $[V_2Ln_2(\mu_3\text{-}OH)_2(^tBuDea)_2(piv)_6]\cdot 2MeOH$ [Ln = Tb-Yb (2.1-2.6) and Y (2.7)

All crystallographic data of the compounds which will be discussed in this chapter can be found in the appendix.

Full structure determination was performed for compounds **2.1-2.7** using Single Crystal X-Ray Diffraction (SCXRD). All the seven complexes are isostructural and crystallize in the triclinic space group *P*-1. The phase purity of the samples was checked using powder XRD analysis. The structure of $V^{III}_2Dy_2$

2.2 is described as a representative and is illustrated in Figure **2.4**. The cluster core of **2.2** is of the butterfly type **II**,[166-167] with the V^{III} ions in the wingtip position and the Dy^{III} ions form the body which is what was also found for the $Cr^{III}_2Dy_2$ compound by Murray *et al.*.[75] The asymmetric unit contains half of the coordination cluster with one V^{III} and Dy^{III} ion and the whole molecule is generated through the inversion center. These metal sites are bridged by two μ_3-methoxide ligands lying one above and one below the plane of the metal atoms and bridging a wingtip transition metal ion of V^{III} to the two central Dy^{III} ions. Each $^{t}BuDea^{3-}$ ligand is coordinated to the wingtip V^{III} ion through the central N atom, and the two alkoxide arms of the ligand provide μ_2-O bridging to the central Dy^{III} ions. The body and wingtip ions are further bridged by four pivalate ligands. The remaining two pivalate ligands each chelate to a Dy^{III} ion. Each V^{III} ion has a distorted octahedral O5N-donor set with a V-N bond length of 2.228(3) Å and V-O bond lengths in the range 1.935(2) Å-2.051(2) Å.

Each Dy ion is found to be eight-coordinate with a square antiprismatic geometry through using a SHAPE 2.1 software with the Dy−O bond distances vary from 2.273(2) to 2.463(2) Å. The Dy···Dy, Dy···V and the closest intramolecular V···V distance are 4.150, 3.343, 5.242 Å, respectively. According to previous reports from our group, if the coordination cluster is the butterfly type **II** case, the V^{III}-Dy^{III} interaction dominates and since the positions of the Dy ions are in the body the single ion properties of the Dy^{III} ions are also important. This structure for $V^{III}_2Ln_2$ is similar to the $Cr^{III}_2Ln_2$ structure previously reported by our group, with the difference that apart from the change in transition metal ion from Cr^{III} to V^{III} the diethanolamine ligand has a ^{t}Bu in place of the ^{n}Bu residue.[165]

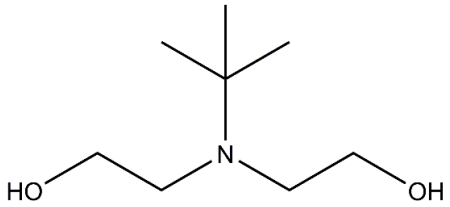

Figure 2.1: the ligand of $H_2{}^{t}BuDea$ in complex of **V_2Ln_2** (**Ln=Tb-Yb, Y**).

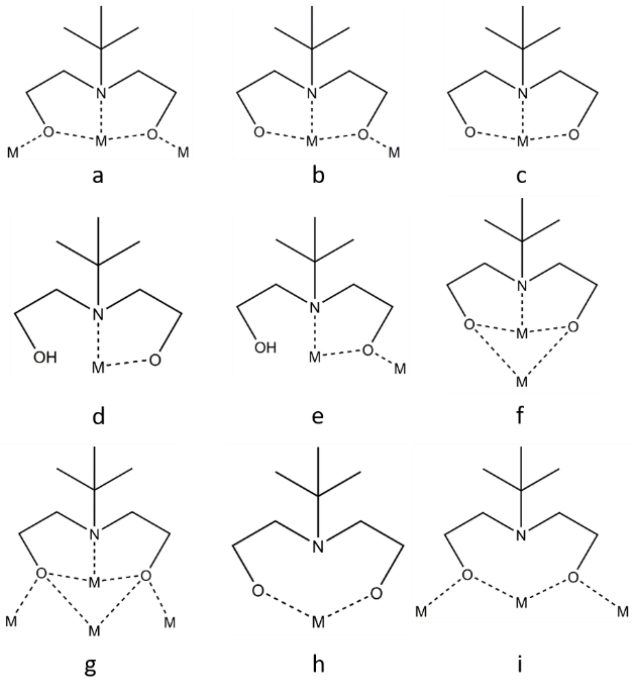

Figure 2.2: Most typical coordination modes of $H_2{}^tBuDea$ ligands according to the CSD.

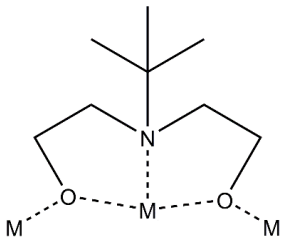

Figure 2.3: The non-chelating bridging coordination mode of the $H_2{}^tBuDea$ ligand in these complexes from **2.1-2.7**.

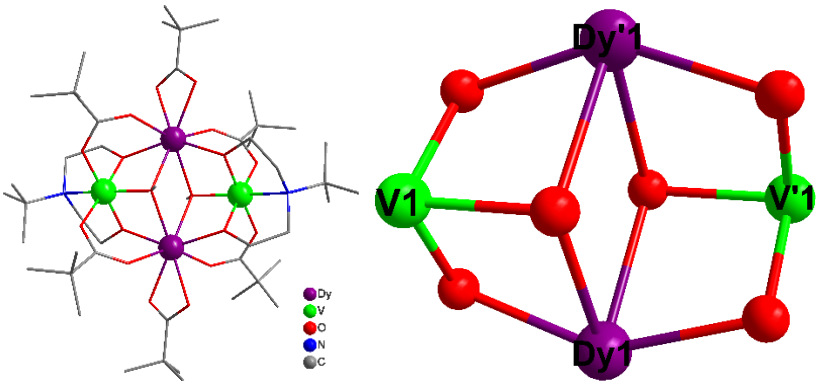

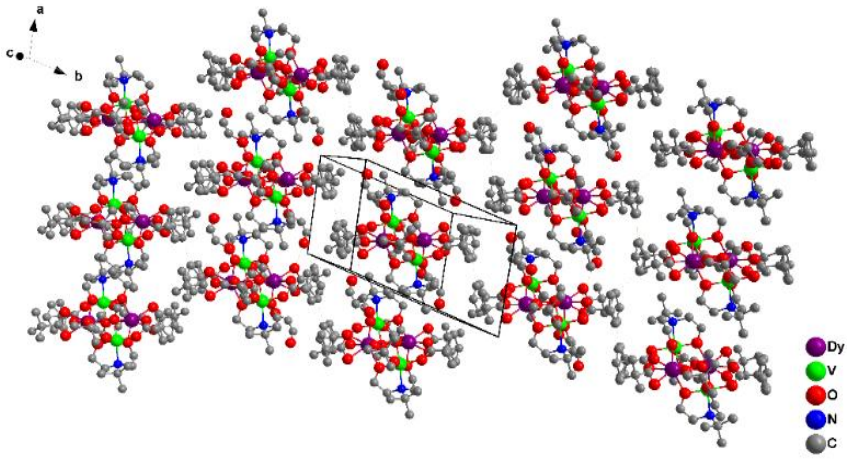

Figure 2.4: The molecular structures of complex, $V^{III}_2Dy_2$ **2.2** (top left). the core of complex $V^{III}_2Dy_2$ **2.2** (top right). the crystal packing of complex $V^{III}_2Dy_2$ **2.2** (bottom).

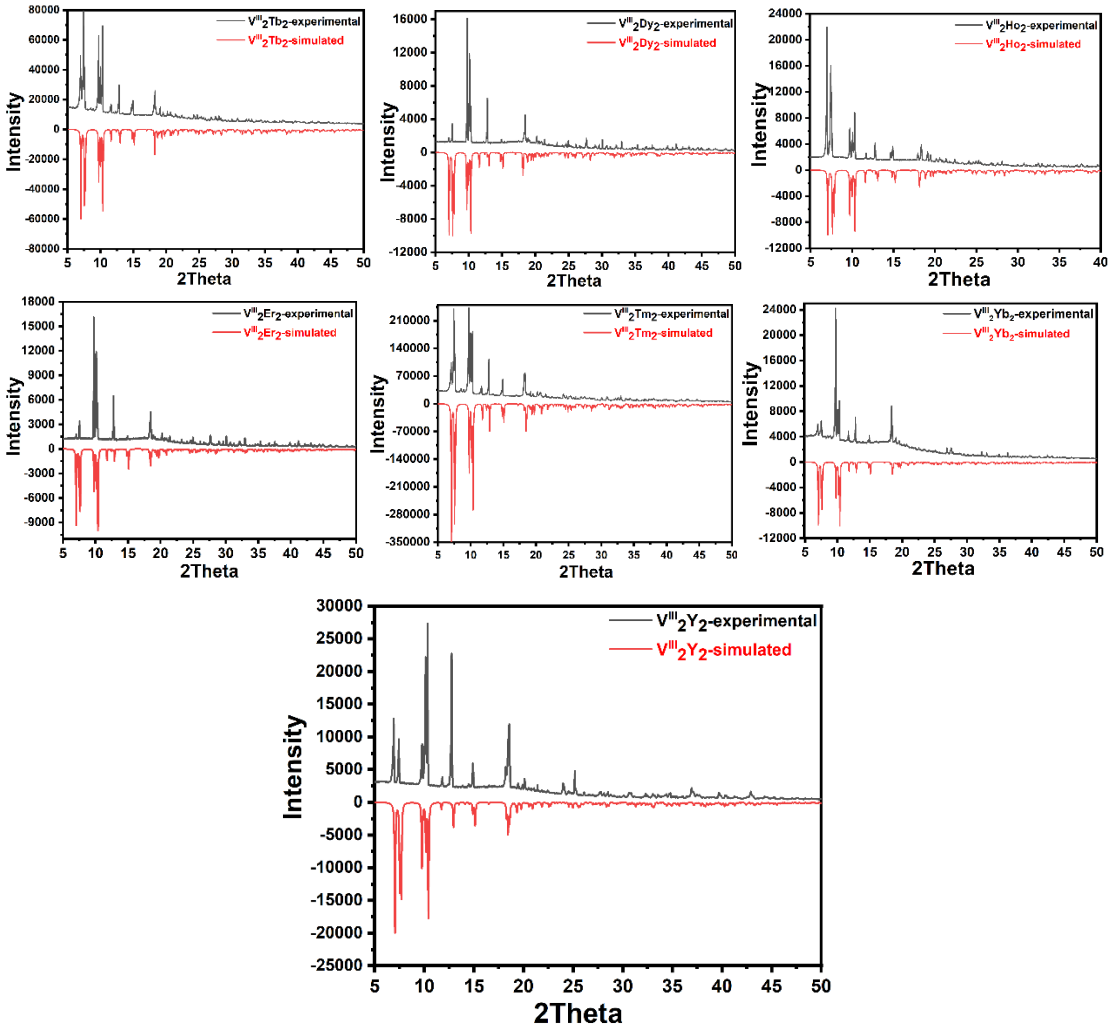

Figure 2.5: The PXRD for $V^{III}_2Tb_2$ **2.1**, $V^{III}_2Dy_2$ **2.2**, $V^{III}_2Ho_2$ **2.3**, $V^{III}_2Er_2$ **2.4**, $V^{III}_2Tm_2$ **2.5**, $V^{III}_2Yb_2$ **2.6** and $V^{III}_2Y_2$ **2.7**.

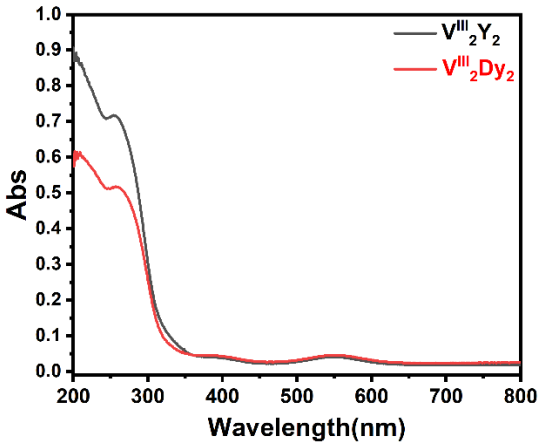

Figure 2.6: The solid-state UV/Vis spectrum for $V^{III}_2Dy_2$ **2.2** and $V^{III}_2Y_2$ **2.7**.

Table 2.1 The SHAPE 2.1 analysis for the M^{III} and Ln^{III} ions in complexes **2.1-2.6**.

	2.1-$V^{III}_2Tb_2$	**2.2-$V^{III}_2Dy_2$**	**2.3-$V^{III}_2Ho_2$**	**2.4-$V^{III}_2Er_2$**	**2.5-$V^{III}_2Tm_2$**	**2.6-$V^{III}_2Yb_2$**
Ln^{III}	**Tb^{III}**	**Dy^{III}**	**Ho^{III}**	**Er^{III}**	**Tm^{III}**	**Yb^{III}**
OP-8	23.915	24.164	24.568	24.556	24.489	24.840
HPY-8	22.444	22.417	22.463	22.443	22.604	22.596
HBPY-8	13.450	13.394	13.402	13.356	13.476	13.424
CU-8	11.377	11.313	11.310	11.249	11.275	11.271
SAPR-8	**1.751**	**1.727**	**1.722**	**1.738**	**1.708**	**1.731**
TDD-8	2.388	2.314	2.191	2.197	2.179	2.088
JGBF-8	11.238	11.195	11.279	11.186	11.219	11.151
JETBPY-8	26.454	26.628	26.381	26.621	26.614	26.665
JBTPR-8	2.600	2.602	2.534	2.518	2.499	2.472
BTPR-8	2.151	2.135	2.047	2.088	2.066	2.053
JSD-8	3.230	3.142	3.145	3.012	2.987	2.899
TT-8	12.205	12.108	12.147	12.065	12.084	12.079
ETBPY-8	22.633	22.764	22.842	22.941	22.959	23.089

OP-8 (D_8h) Octagon, HPY-8 (C_7v) Heptagonal pyramid, HBPY-8 (D_6h) Hexagonal bipyramid, CU-8 (Oh) Cube, SAPR-8 (D_4d) Square antiprism, TDD-8 (D_2d) Triangular dodecahedron, JGBF-8 (D_2d) Johnson gyrobifastigium J26, JETBPY-8 (D_3h) Johnson elongated triangular bipyramid J14, JBTPR-8 (C_2v) Johnson elongated triangular bipyramid J14, BTPR-8 (C_2v) Biaugmented trigonal prism, JSD-8 (D_2d) Snub diphenoid J84, TT-8 (Td) Triakis tetrahedron, ETBPY-8 (D_3h) Elongated trigonal bipyramid.

2.2.1.2 Magnetic properties of complexes, $V^{III}_2Ln_2$ (Ln=Tb - Yb and Y) (2.1-2.7)

Direct current (dc) magnetic susceptibility studies of compounds **2.1-2.7** were carried out using an applied magnetic field of 1000 Oe over the temperature range 1.8-300 K. The dc magnetic data of compounds **2.1-2.7** are summarized in **Table 2.2**. The χ_MT versus T plots for $V^{III}_2Dy_2$ **2.2** and its Y analogue $V^{III}_2Y_2$ **2.7** are shown in Figure **2.7**. As indicated in Figure **2.7**, the value of χ_MT at 300 K of 30.27 $cm^3 \cdot K \cdot mol^{-1}$ for $V^{III}_2Dy_2$ **2.2** is very close to the expected value (30.34 $cm^3 \cdot K \cdot mol^{-1}$) for two non-interacting V^{III} ions with S = 1, g = 2, and C = 1.000

$cm^3 \cdot K \cdot mol^{-1}$ and two Dy^{III} ions (S = 5/2, L = 5, $^6H_{15/2}$, g = 4/3, and C = 14.17 $cm^3 \cdot K \cdot mol^{-1}$). There is a rapid decrease in the $\chi_M T$ value on lowering the temperature from 300 to 33 K, reaching a minimum value for $\chi_M T$ of 25.70 $cm^3 \cdot K \cdot mol^{-1}$ at 33 K, below which it increases to the maximum value of 30.47 $cm^3 \cdot K \cdot mol^{-1}$ at 7.5 K. This type of behavior (increase below 33 K) suggests the presence of intramolecular ferromagnetic interactions between the V^{III} and Dy^{III} ions. The decrease in the $\chi_M T$ value in the high temperature range is likely due to the depopulation of the Stark sublevels of the Dy^{III} ions. For compound $V^{III}_2Y_2$ **2.7**, the $\chi_M T$ value of 1.72 $cm^3 \cdot K \cdot mol^{-1}$ at 300 K is much lower than for two non-interacting V^{III} ions. On lowering the temperature, the $\chi_M T$ decreases very quickly reaching 0.70 $cm^3 \cdot K \cdot mol^{-1}$ at 1.8 K. This behavior could indicate either antiferromagnetic coupling between the V^{III} ions or ZFS in compound **2.7**. The field dependence of the magnetization for $V^{III}_2Dy_2$ **2.2** at low temperatures (Figure **2.8**) reveals that the magnetization has a relatively rapid increase below 1 T and then follows a monotonic increase up to 7 T. The M value at 7 T is 10.22 Nβ (H = 7 T, at 1.8K), lower than the expected value of 15.4 Nβ, indicating a lack of saturation. Such behavior indicates the presence of magnetic anisotropy and/or low-lying excited states. Besides, the field dependence of the magnetization of $V^{III}_2Y_2$ **2.7** was performed at fields ranging from 0 to 14 T at 1.8, 3 and 5 K. Up to 7 T M increases without clear saturation reaching 2.69 Nβ (H = 7 T, at 1.8 K) for $V^{III}_2Y_2$ **2.7**. This lack of saturation of the magnetization for $V^{III}_2Y_2$ **2.7** suggests the presence of magnetic anisotropy. However, at fields beyond this of up to 14 T saturation is reached at a value of 3.889 Nβ.

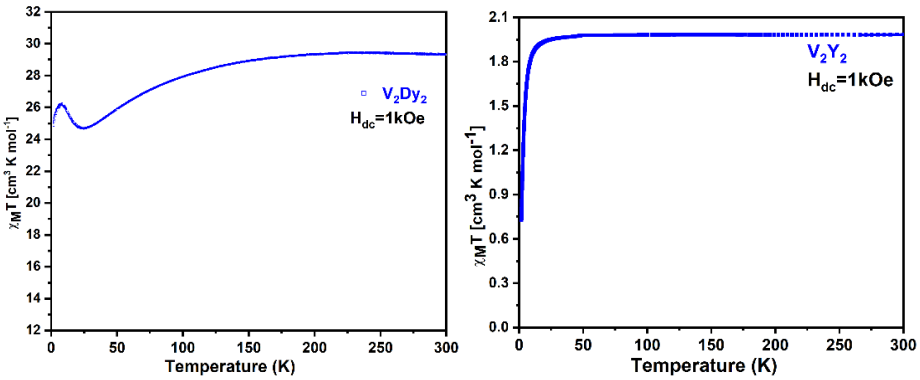

Figure 2.7: The plots of $\chi_M T$ vs T for $V^{III}_2Dy_2$ **2.2** and $V^{III}_2Y_2$ **2.7**.

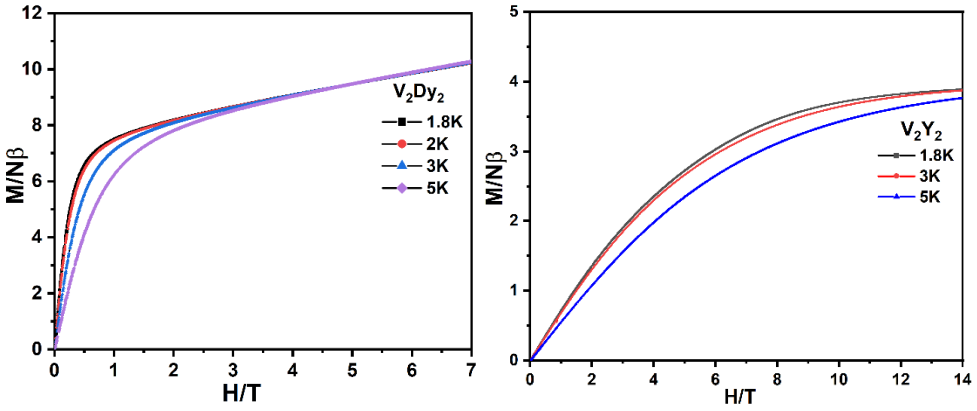

Figure 2.8: The plots of M vs H for $V^{III}_2Dy_2$ **2.2**. and $V^{III}_2Y_2$ **2.7**.

Table 2.2 Magnetic data of compounds **2.1-2.7** summarized from the dc measurements.

Compound	Ground state of Ln^{III} ion	χT expected for non-interacting ions per complex ($cm^3 \cdot K \cdot mol^{-1}$)	χT measured at 300 K per complex ($cm^3 \cdot K \cdot mol^{-1}$)	χT measured at 2.0 K per complex ($cm^3 \cdot K \cdot mol^{-1}$)	Magnetization at 3 K and 7 T(Nβ)
2.1-$V^{III}_2Tb_2$	$^7F_6$	25.64	23.62	20.84	8.10
2.2-$V^{III}_2Dy_2$	$^6H_{15/2}$	30.34	29.29	24.99	10.24
2.3-$V^{III}_2Ho_2$	$^5I_8$	30.14	28.16	25.05	9.90
2.4-$V^{III}_2Er_2$	$^4I_{15/2}$	24.96	24.88	15.85	9.77
2.5-$V^{III}_2Tm_2$	$^3H_6$	16.30	15.56	12.87	8.26
2.6-$V^{III}_2Yb_2$	$^2F_{7/2}$	7.14	7.11	0.84	3.65
2.7-$V^{III}_2Y_2$	---	2.00	1.72	0.70	2.64

The plot of $\chi_M T$ vs T is shown in Figure **2.9**. At 300 K, the $\chi_M T$ values are 23.62 $cm^3 \cdot K \cdot mol^{-1}$ for complex $V^{III}_2Tb_2$ **2.1**, which is slightly lower than the expected value of 25.64 $cm^3 \cdot K \cdot mol^{-1}$ for two uncoupled Tb^{III} ions (S = 3, $^7F_6$, g = 3/2, C = 11.82 $cm^3 \cdot K \cdot mol^{-1}$) and two non-interacting V^{III} ions with S = 1, g = 2, and C = 1.000 $cm^3 \cdot K \cdot mol^{-1}$. For complex $V^{III}_2Ho_2$ **2.3** the value of 28.16 $cm^3 \cdot K \cdot mol^{-1}$ is lower than the expected 30.14 $cm^3 \cdot K \cdot mol^{-1}$ for two uncoupled Ho^{III} ions (S = 2, $^5I_8$, g = 5/4, C = 14.07 $cm^3 \cdot K \cdot mol^{-1}$) and two non-interacting V^{III} ions (S = 1, g = 2, and C = 1.000 $cm^3 \cdot K \cdot mol^{-1}$). As the temperature is lowered, the $\chi_M T$ values decrease gradually and more dramatically below 100 K to reach minimum values of 20.14 $cm^3 \cdot K \cdot mol^{-1}$ and 20.40 $cm^3 \cdot K \cdot mol^{-1}$ at 32 K and 20 K

for complexes **2.1** and **2.3**, respectively. In both cases there is an increase to a maximum of 22.45 and 25.05 $cm^3 \cdot K \cdot mol^{-1}$ at temperatures of 9.6 K and 1.8 K. This indicates that in both compounds there are intramolecular ferromagnetic interactions between V^{III} and Tb^{III}/Ho^{III} ions. The lack of a superposition of the M vs H data of $V^{III}_2Tb_2$ **2.1** on to a single master curve and the low magnetization of 8.10 Nβ at 3.0 K and 7.0 T suggest the presence of a significant magnetic anisotropy and/or low-lying excited states. The almost linear increase of the M vs H data between 1 and 7 T indicates the presence of significant magnetic anisotropy.

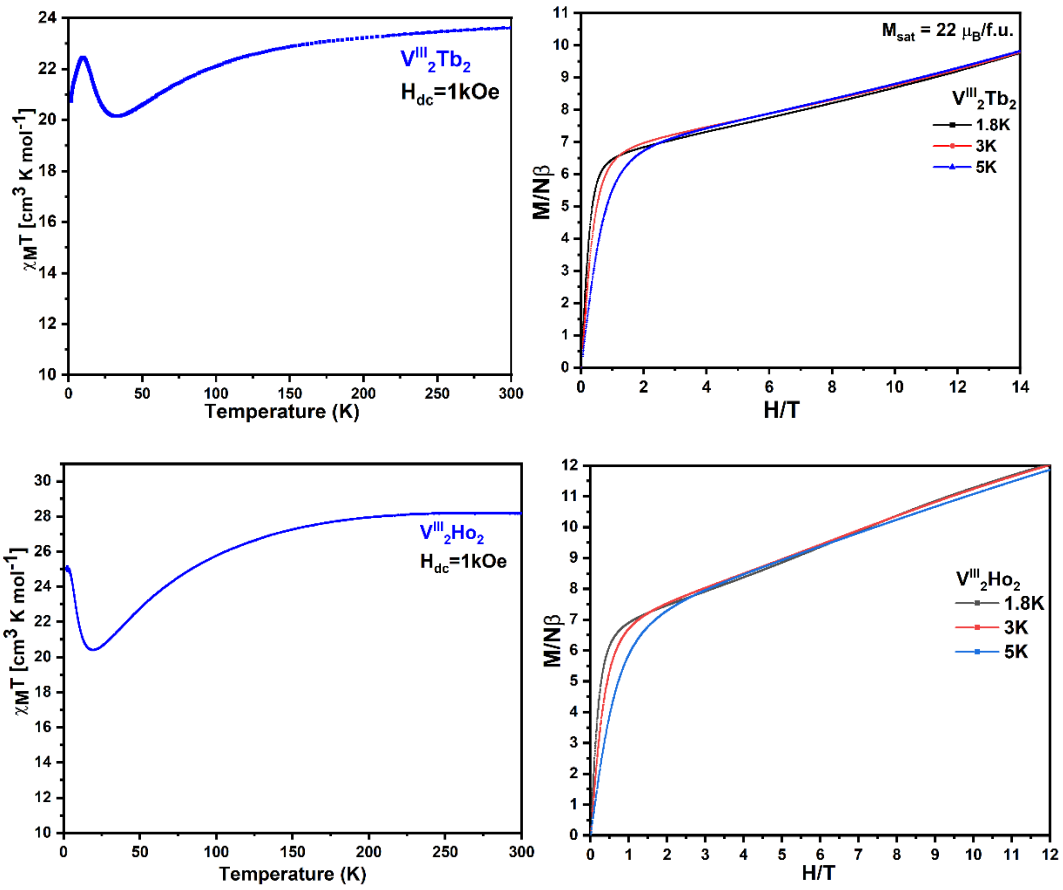

Figure 2.9: The plots of $\chi_M T$ vs T for $V^{III}_2Tb_2$ **2.1** and $V^{III}_2Ho_2$ **2.3** (left). The plots of M vs H for $V^{III}_2Tb_2$ **2.1** and $V^{III}_2Ho_2$ **2.3** (right).

The temperature dependence of the magnetic susceptibility for $V^{III}_2Er_2$ **2.4**, $V^{III}_2Tm_2$ **2.5** and $V^{III}_2Yb_2$ **2.6** performed in the temperature range from 2.0 to 300 K under a dc field of 1000 Oe are shown in Figure **2.10**. The dc data are summarized in Table **2.2** and show that the room temperature $\chi_M T$ values for

2.4-2.6, 24.88, 15.56 and 7.11 $cm^3 \cdot K \cdot mol^{-1}$, respectively, are in good agreement with the expected values of 24.96 $cm^3 \cdot K \cdot mol^{-1}$ ($V^{III}_2Er_2$ **2.4:** Er: S = 3/2, $^4I_{15/2}$, g = 6/5, C = 11.48 $cm^3 \cdot K \cdot mol^{-1}$ and V: S = 1, g = 2, C = 1.000 $cm^3 \cdot K \cdot mol^{-1}$), 16.30 $cm^3 \cdot K \cdot mol^{-1}$ ($V^{III}_2Tm_2$ **2.5:** Tm: S = 1, $^3H_6$, g = 7/6, C = 7.15 $cm^3 \cdot K \cdot mol^{-1}$ and V: S = 1, g = 2, C = 1.000 $cm^3 \cdot K \cdot mol^{-1}$), 7.14 $cm^3 \cdot K \cdot mol^{-1}$ ($V^{III}_2Yb_2$ **2.6:** Yb: S = 1/2, $^2F_{7/2}$, g = 8/7, C = 2.57 $cm^3 \cdot K \cdot mol^{-1}$ and V: S = 1, g = 2, C = 1.000 $cm^3 \cdot K \cdot mol^{-1}$). For complexes **2.4-2.6**, the $\chi_M T$ values decrease steadily with decreasing temperature down to 8 K due to the thermal depopulation of excited sub-levels of the lanthanide centers. For $V^{III}_2Er_2$ **2.4** the $\chi_M T$ value of $V^{III}_2Er_2$ **2.4** increases sharply again at temperatures below 8 K; this type of behavior suggests the presence of intramolecular ferromagnetic coupling in the complex $V^{III}_2Er_2$ **2.4**. Since such an upturn in the $\chi_M T$ curve was not observed for the $V^{III}_2Y_2$ **2.7**, the ferromagnetic interactions are either V^{III}-Er^{III} and/or Er^{III}-Er^{III} in nature. Besides, the field dependence of the magnetization of $V^{III}_2Er_2$ **2.4** was performed at fields ranging from 0 to 14 T at 1.8, 3 and 5 K (Figure **2.10**). At fields above 3 T, the magnetization increases linearly without clear saturation to ultimately reach 13.13 Nβ (H = 14 T, at 1.8 K) indicating the presence of magnetic anisotropy.

For $V^{III}_2Tm_2$ **2.5**, there is a steady decrease in the $\chi_M T$ value on lowering the temperature from 300 K reaching a minimum value for $\chi_M T$ of 12.38 $cm^3 \cdot K \cdot mol^{-1}$ at 13 K, below which it increases to a value of 13.20 $cm^3 \cdot K \cdot mol^{-1}$ at 4 K, followed by a further slight decrease to 12.83 $cm^3 \cdot K \cdot mol^{-1}$ at 2.0 K, suggesting intramolecular ferromagnetic interactions in complex **2.5**.

At 300 K, the experimental $\chi_M T$ value of $V^{III}_2Yb_2$ **2.6** (7.11 $cm^3 \cdot K \cdot mol^{-1}$) is very close to the expected value (7.14 $cm^3 \cdot K \cdot mol^{-1}$) for two V^{III} ions and two Yb^{III} ions. The $\chi_M T$ product remains basically unchanged on decreasing temperature to 100 K, followed by a sharp decrease and reaching a minimum value of 0.79 $cm^3 \cdot K \cdot mol^{-1}$ at 1.8 K. In this compound no increase of $\chi_M T$ is observed at low temperatures suggesting that in this compound there are no ferromagnetic interactions. The field dependence of the magnetization of $V^{III}_2Yb_2$ **2.6** was

performed at fields ranging from 0 to 14 T at 1.8, 3 and 5 K. M increases linearly, without the initial steep increase seen for the other compounds, without clear saturation to ultimately reach 5.70 Nβ (H = 14 T, at 1.8 K).

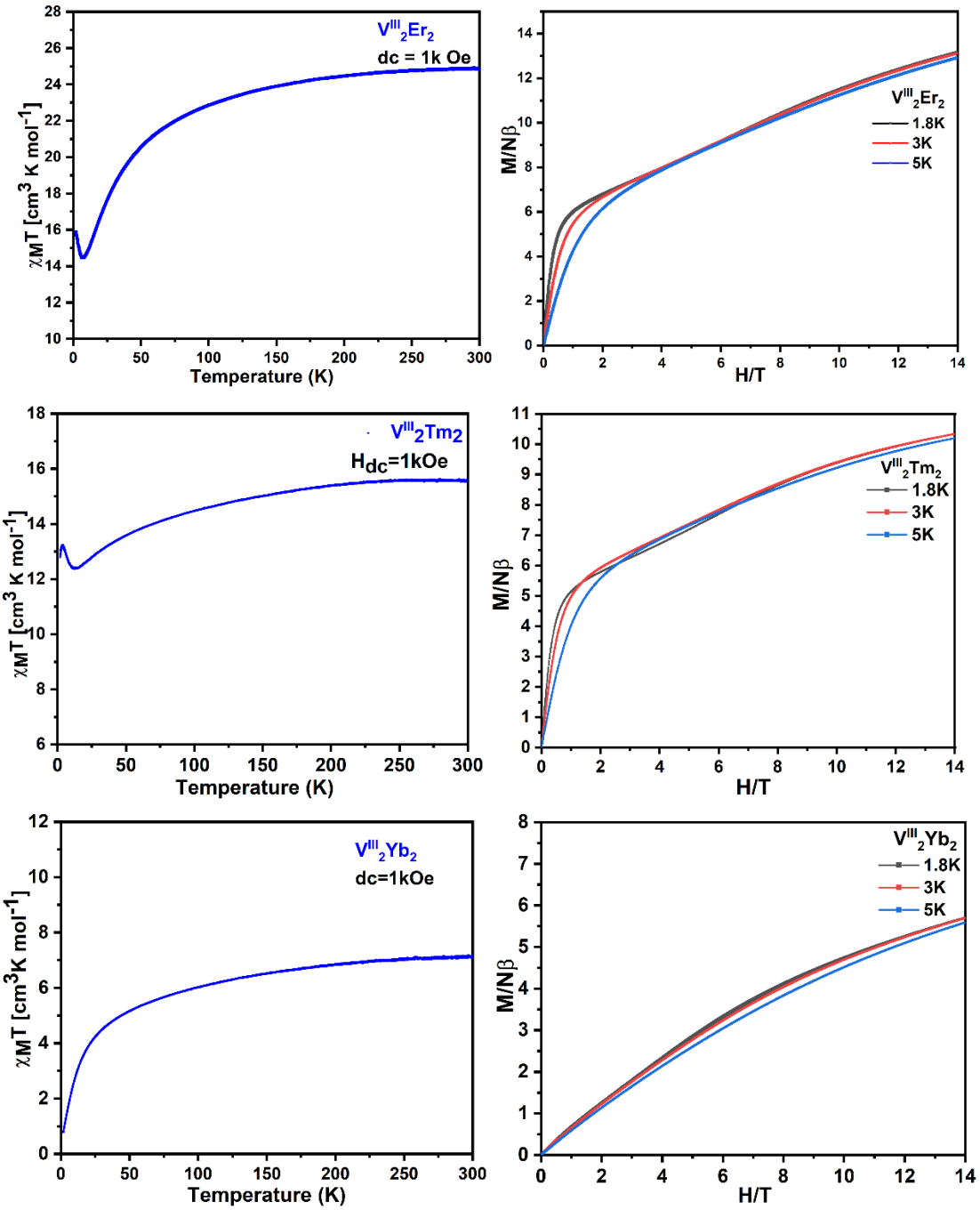

Figure 2.10: The plots of $\chi_M T$ vs T for $V^{III}_2Er_2$ **2.4**, $V^{III}_2Tm_2$ **2.5** and $V^{III}_2Yb_2$ **2.6** (left). The plots of M vs H for complexes, $V^{III}_2Er_2$ **2.4**, $V^{III}_2Tm_2$ **2.5** and $V^{III}_2Yb_2$ **2.6** (right).

To probe possible slow relaxation of the magnetization and quantum tunneling effects within compounds **2.1-2.7**, alternating current (ac) magnetic susceptibilities were investigated. For $V^{III}_2Dy_2$ **2.2** under zero applied dc field,

the out of phase signal (χ'') shows a peak at the edge of the measurement window, indicating the possible presence of SMM behavior (Figure **2.11**). Interestingly, applying a dc field suppresses the ac signal. To further analyze the possible SMM behavior of **2.2**, the ac susceptibility measurements were performed under zero dc applied field between 2.0 - 7.2 K. Hence, additional Micro-SQUID measurements were carried out to determine whether single crystal samples of $V^{III}_2Dy_2$ **2.2** show SMM properties.

As can be seen from Figure **2.12**, both the temperature and sweep-rate dependence are consistent with strong zero-field QTM (ZFQTM). The difference in normalized magnetization of d(M/Ms)/dH at 30 mK with different dc field scan rates shows a clear maximum (Figure **2.12**), confirms ZFQTM. The small peak that is only seen at positive fields in the derivative plot centered around 1.1 T is shown zoomed in Figure **2.12** bottom right.

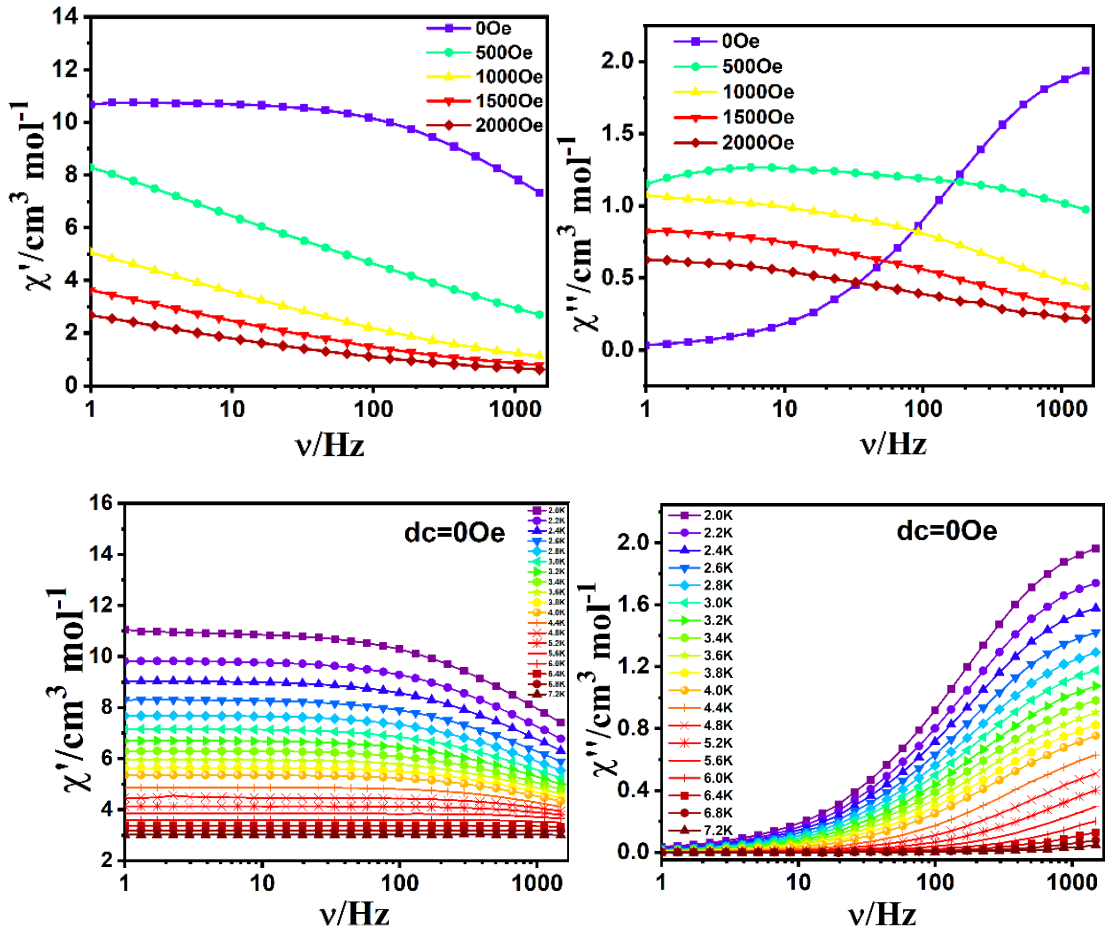

Figure 2.11: Plots of χ' (left top) and χ'' (right top) vs frequency range from 0 Oe to 2000 Oe at 2 K for complex of $V^{III}_2Dy_2$ **2.2**. Plots of χ' (left bottom) and χ'' (right bottom) vs temperature

range from 2 to 7.2 K for complex of $V^{III}_2Dy_2$ **2.2**.

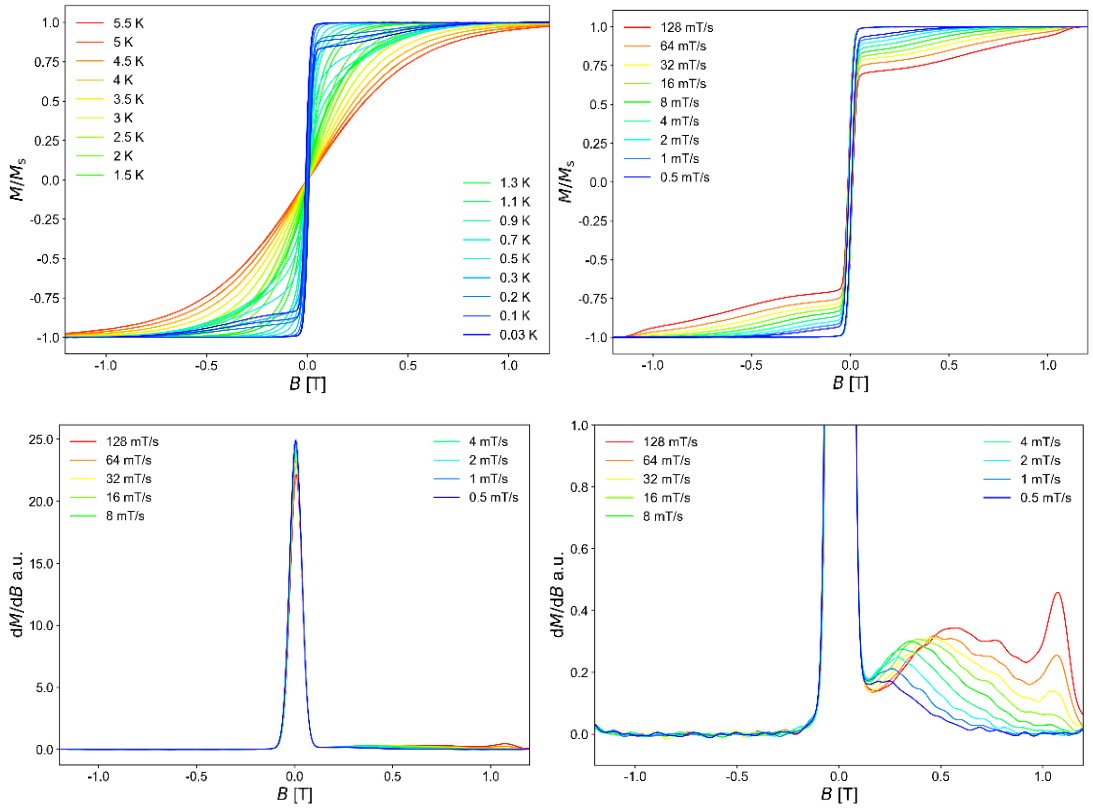

Figure 2.12: Micro-SQUID data of $V^{III}_2Dy_2$ **2.2** at different temperatures with a 8 mT/s sweep rate (top left), at 30 mK (top right) and the corresponding derivatives (bottom left and bottom right). The loops show a plateau between −0.5 and 0.5 T.

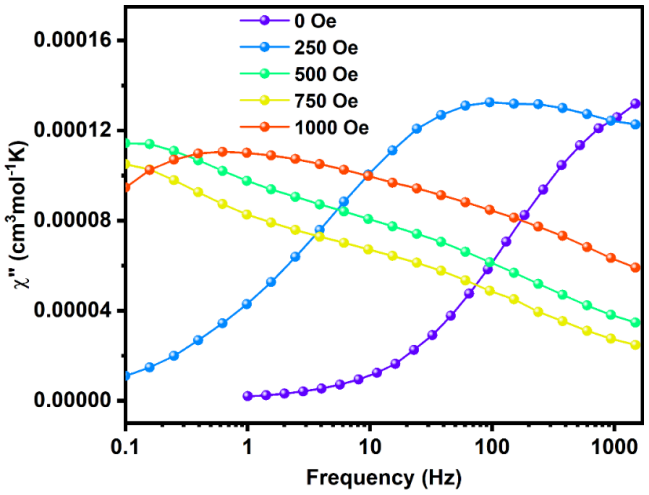

Figure 2.13: Frequency dependence under zero dc field of the out-of-phase for $V^{III}_2Dy_2$ **2.2**.

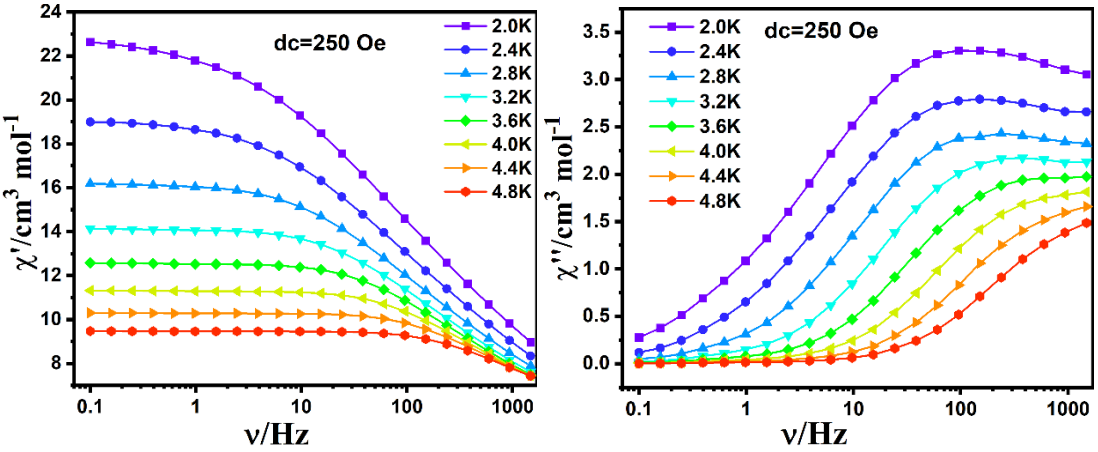

Figure 2.14: Plots of χ' (left) and χ'' (right) vs frequency under different temperature under 250 Oe fields for $V^{III}_2Dy_2$ **2.2**.

Additional ac susceptibility measurements were performed under further dc fields to include the missing 250 Oe field (Figure **2.13** and **2.14**). Although $V^{III}_2Dy_2$ **2.2** does not behave as an SMM under zero field, it can be seen from Figure **2.13** that $V^{III}_2Dy_2$ **2.2** may behave as an SMM under this applied magnetic field. As shown in Figure **2.14** out of phase signals were indeed observed for $V^{III}_2Dy_2$ **2.2**, revealing SMM behavior within the frequency window available.

Cole-Cole plots (χ'' vs χ' at different temperatures) can be used to study the distribution of relaxation processes, which are often characterized and discussed for SMMs or single chain magnets SCMs. The data of $V^{III}_2Dy_2$ **2.2** are presented in a Cole-Cole plot (**Figure 2.15**). The shape of the resulting curve is characteristic of more than one overlapping relaxation process. Therefore, it is only possible to fit these data using the generalized Debye model. The best fit that could be obtained between 2.0 and 4.8 K is shown in Figure **2.15**. Given this it was decided to not try to fit the relaxation dynamics to any of the current suggested models in the literature.[168-171]

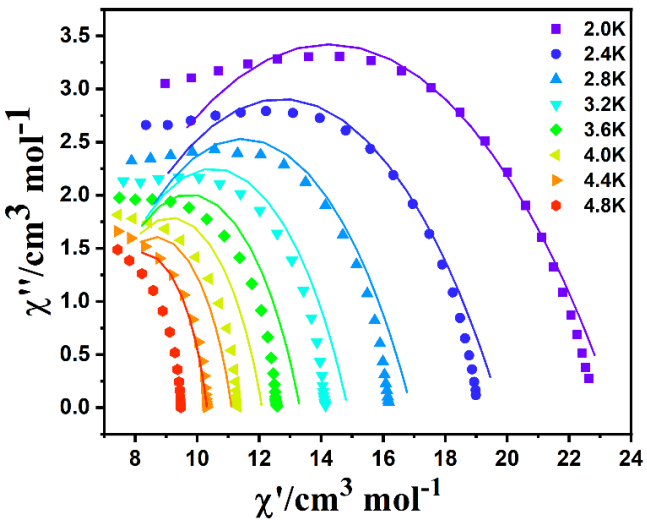

Figure 2.15: Cole-Cole plots for the complex of $V^{III}_2Dy_2$ **2.2** (solid lines for fit)

Ac susceptibility measurements were performed under a range of dc fields for complexes **2.3-2.7**. No out-of-phase signals (χ") were observed for the $V^{III}_2Yb_2$ (**2.6**) and the $V^{III}_2Y_2$ (**2.7**). This result for the Y^{III} compound is useful because it verifies that any SMM behavior comes from the 4f ion. To underline this fact not only was this measurement done at 2 K but also at 10 K (Figure **2.16** - **2.17** $V^{III}_2Y_2$ 2K and 10K in-and out-of-phase). Indeed, for all of these compounds (Figure **2.18** - **2.19**, Figure **2.21** - **2.24**), the lack of out-of-phase signals indicates the absence of SMM behavior in zero field because of the very fast quantum tunneling of the magnetization. In ac measurements maxima were observed for the $V^{III}_2Ho_2$ (**2.3**) and $V^{III}_2Tm_2$ (**2.5**) compounds at applied dc fields of 1500 Oe and 1000 Oe, respectively, but only a very weak signal was observed for $V^{III}_2Er_2$ (**2.4**) at various applied fields (Figures **2.21**).

Application of a dc field minimized the QTM of $V^{III}_2Ho_2$ **2.3** revealing full peaks in the out of phase (χ") signals as shown in Figure **2.20**. The presence of peaks that shift to lower frequency as the temperature decreases is indicative of slow relaxation of the magnetization (Figure **2.20**). Since none of the maxima are discernible no Cole-Cole plots are shown.

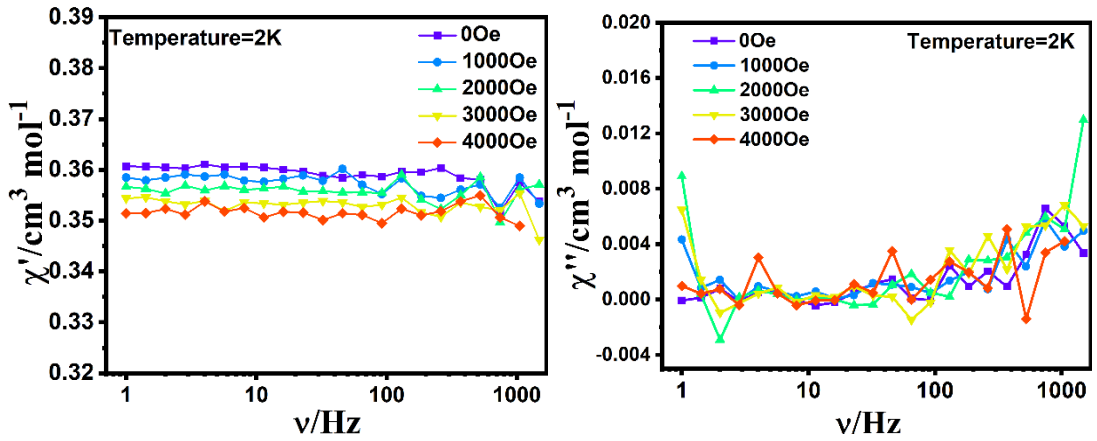

Figure 2.16: Plots of χ' (left) and χ'' (right) vs frequency range from 0 Oe to 3000 Oe at 2 K for complex of $V^{III}_2Y_2$ **2.7**.

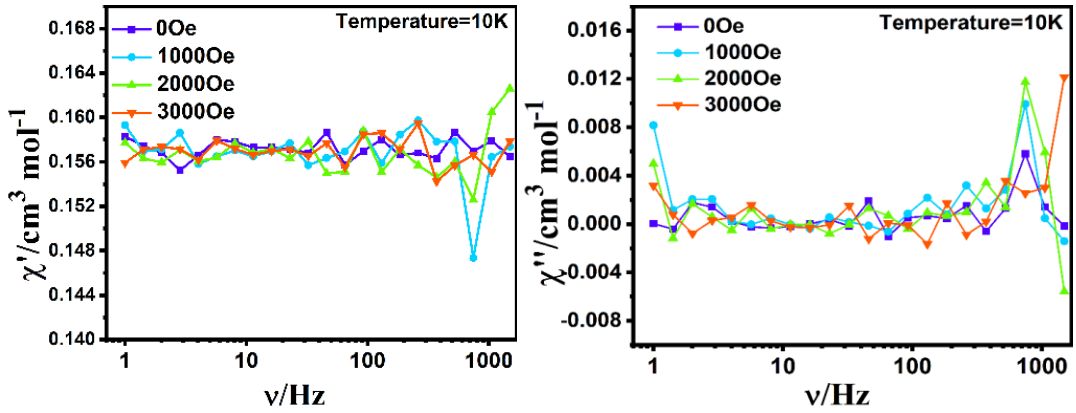

Figure 2.17: Plots of χ' (left) and χ'' (right) vs frequency under different frequencies at 10 K for complex of $V^{III}_2Y_2$ **2.7**.

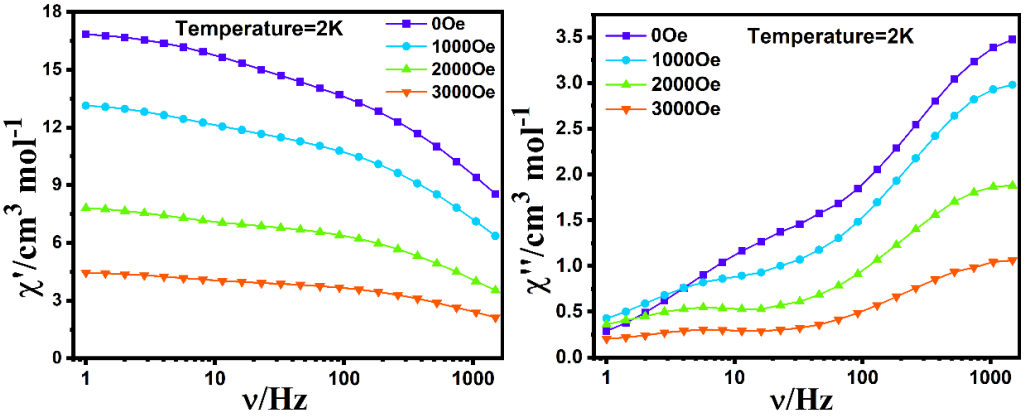

Figure 2.18: Plots of χ' (left) and χ'' (right) vs frequency range from 0 Oe to 3000 Oe at 2 K for complex of $V^{III}_2Ho_2$ **2.3**.

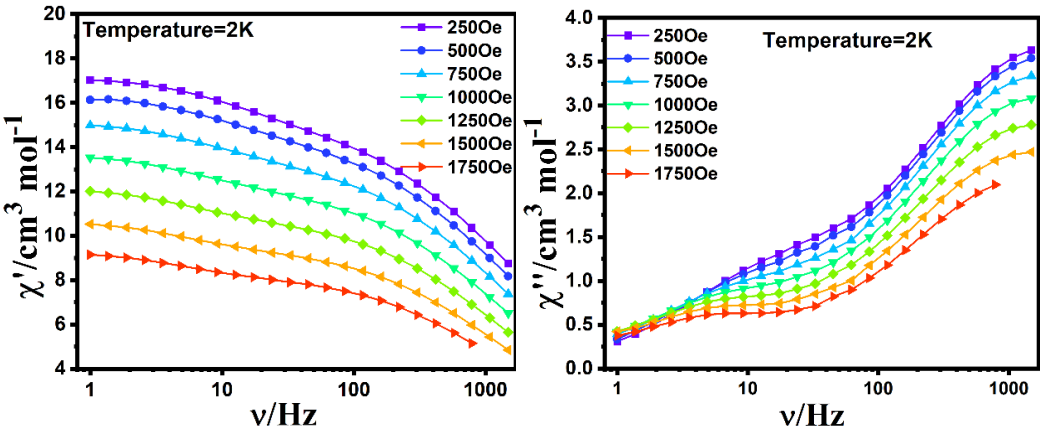

Figure 2.19: Plots of χ' (left) and χ'' (right) vs frequency under different frequencies at 2 K for complex of $V^{III}_2Ho_2$ **2.3**.

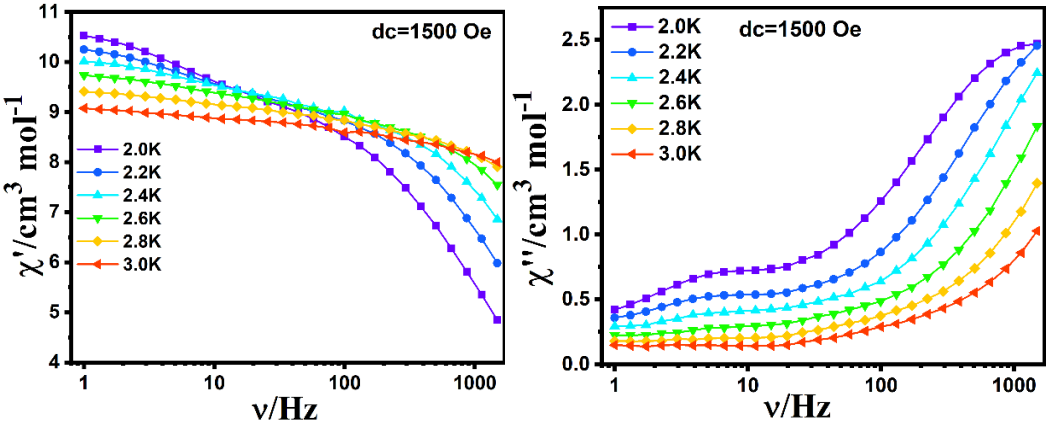

Figure 2.20: Plots of χ' (left) and χ'' (right) vs frequency under different temperature under 1500 Oe fields for complex of $V^{III}_2Ho_2$ **2.3**.

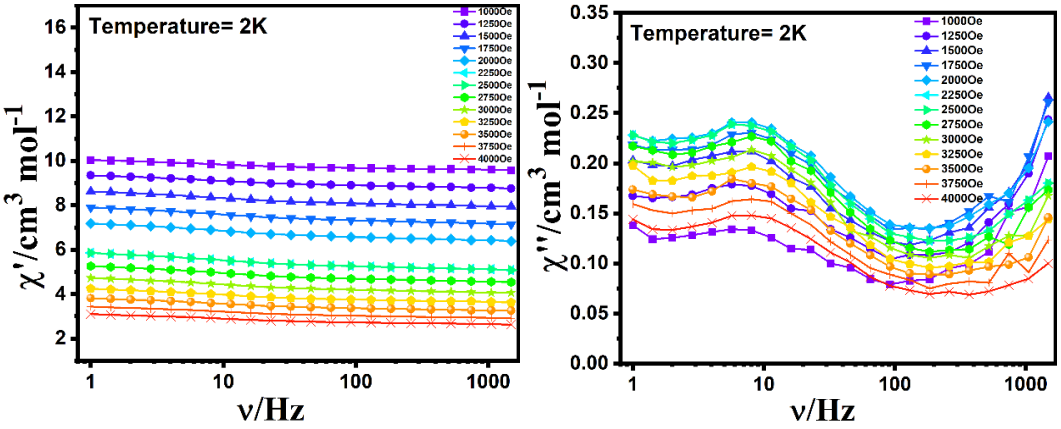

Figure 2.21: Plots of χ' (left) and χ'' (right) vs frequency under different frequencies at 2 K for complex of $V^{III}_2Er_2$ **2.4**.

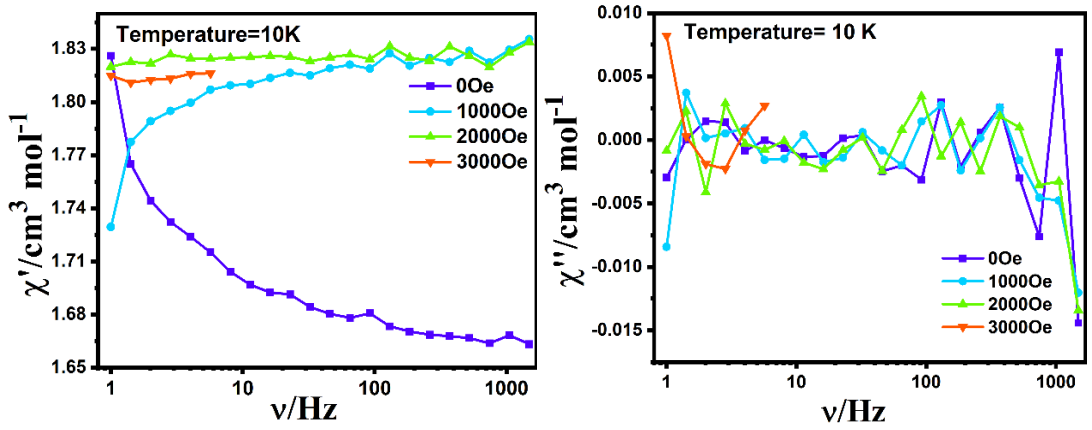

Figure 2.22: Plots of χ' (left) and χ'' (right) vs frequency under different frequencies at 10 K for complex of $V^{III}_2Er_2$ **2.4**.

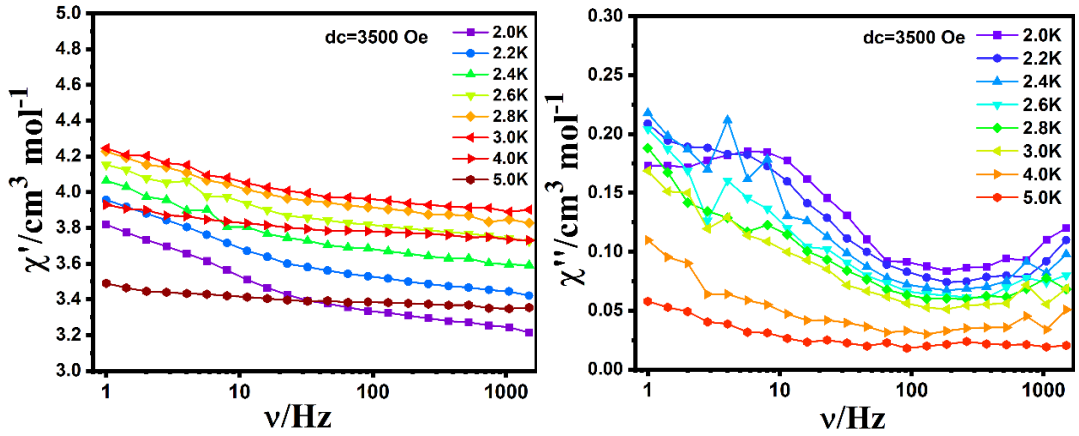

Figure 2.23: Plots of χ' (left) and χ'' (right) vs frequency under different temperature under 3500 Oe fields for complex of $V^{III}_2Er_2$ **2.4**.

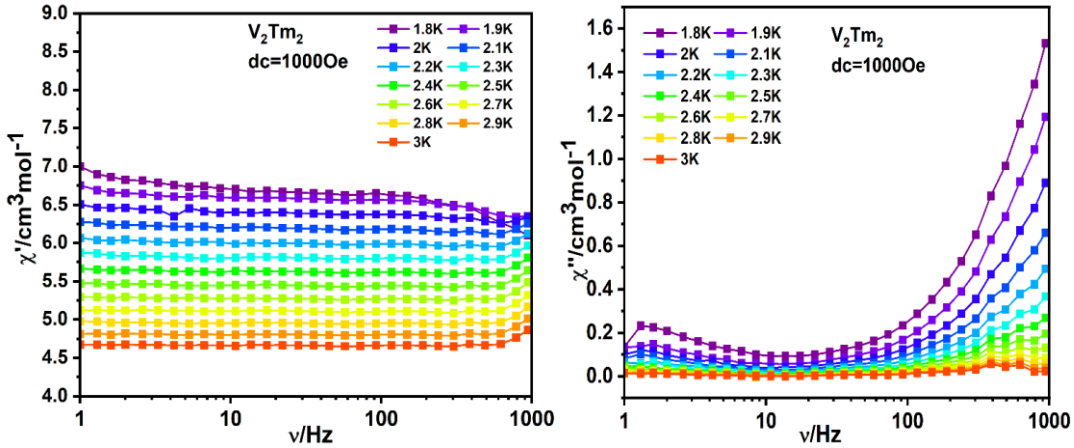

Figure 2.24: Plots of χ' (left) and χ'' (right) vs frequency under different temperature under 1000 Oe fields for complex of $V^{III}_2Tm_2$ **2.5**.

2.2.2 Butterfly Type I Compound of $V^{III}_2Dy_2$

2.2.2.1 Crystal Structure of $[V^{III}_2Dy_2(\mu_3\text{-}OH)_2(L)_2(p\text{-}Me\text{-}PhCO_2)_6]\cdot 2MeOH$ (L=N-(2-Pyridylmethyl)iminodiethanol) (2.8)

Complex $V^{III}_2Dy_2$ **2.8** crystallizes in $P2_1/c$ with $Z = 2$ with the formula $[V^{III}_2Dy_2(\mu_3\text{-}OH)_2(L)_2(p\text{-}Me\text{-}PhCO_2)_6]\cdot 2MeOH$ where H_2L is *N*-(2-pyridylmethyl)iminodiethanol (Figure **2.25**) abbreviated as H_2pmide. In contrast to the compounds described above the Dy^{III} ions are now at the wingtips of this butterfly type **I** complex. As shown in Figure **2.26**, each $pmide^{2-}$ ligand chelates a Dy^{III} center by the imino- and pyridyl nitrogens and with the deprotonated ethanol arms forming bridges to the V^{III} ions. The complex is exactly isostructural to the previously reported Mn^{III}/Fe^{III}/Cr^{III}/Al^{III} analogues with crystallographic inversion symmetry.[166-167]

SHAPE 2.1 analysis reveals that the two V^{III} ions have a distorted octahedral O_6 donor with V^{III}–O bond distances vary from 1.949 (2) Å to 2.048 (19) Å set which was established from the crystal data and through a SHAPE 2.1 analysis. These Dy^{III} ions with an O_7N_2 donor are best described as having a distorted spherical capped square antiprism geometry with deviation values of 0.952 by using SHAPE 2.1 software. Each Dy^{III} ion is found to be nine-coordinate with an average V^{III}–O/N bond length of 2.4402 Å. The Dy···Dy, Dy··· V^{III} and the closest intramolecular V^{III}··· V^{III} distance is 6.1055, 3.346, 3.1528 Å, respectively.

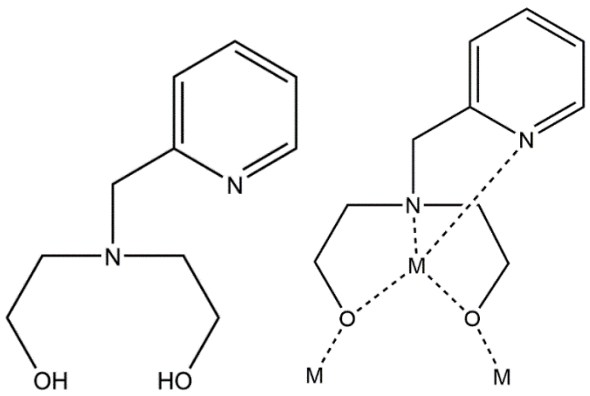

N-(2-Pyridylmethyl)iminodiethanol

Figure 2.25: the ligand and coordination mode of ligand in $V^{III}_2Dy_2$ **2.8**.

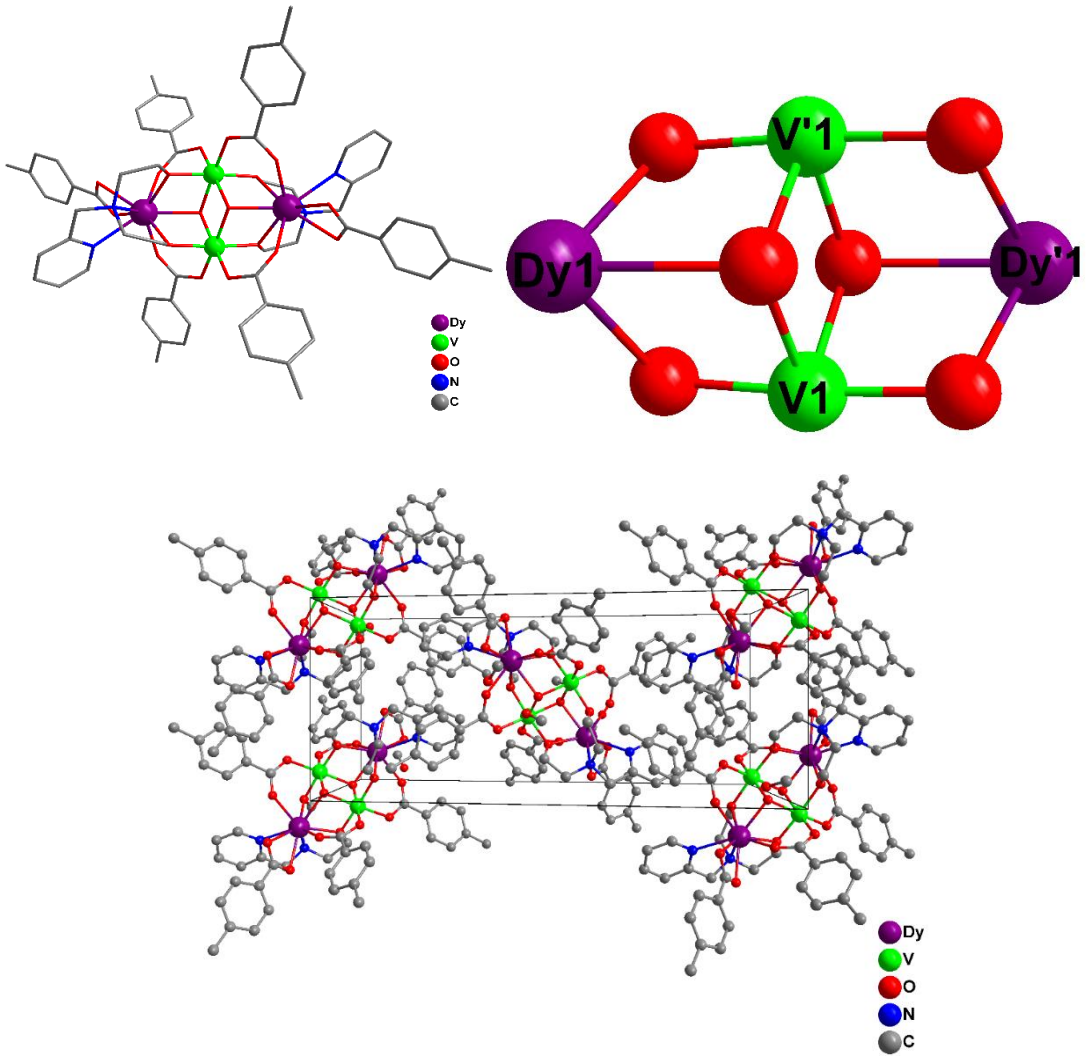

Figure 2.26: The molecular structures of $V^{III}_2Dy_2$ **2.8** (top left). the core of $V^{III}_2Dy_2$ **2.8** (top right). the coordination atmosphere of $V^{III}_2Dy_2$ **2.8** (bottom).

Table 2.3 The SHAPE 2.1 analysis for $V^{III}_2Dy_2$ **2.8**.

	2.8-$V^{III}_2Dy_2$
Ln^{III}	**Dy^{III}**
Enneagon (D_{9h})	33.471
Octagonal pyramid (C_{8v})	19.873
Heptagonal bipyramid (D_{7h})	18.436
Johnson triangular cupola J3 (C_{3v})	15.165
Capped cube J8 (C_{4v})	11.209
Spherical-relaxed capped cube (C_{4v})	10.088
Capped square antiprism J10 (C_{4v})	1.810
Spherical capped square antiprism (C_{4v})	**0.952**
Tricapped trigonal prism J51 (D_{3h})	2.869
Spherical tricapped trigonal prism (D_{3h})	1.611
Tridiminished icosahedron J63 (C_{3v})	10.619
Hula-hoop (C_{2v})	11.789
Muffin (C_s)	1.549

2.2.2.2 Magnetic properties of complex $V^{III}_2Dy_2$ 2.8

Dc magnetic susceptibility studies on complex $V^{III}_2Dy_2$ **2.8** were carried out in an applied magnetic field of 1000 Oe over the temperature range of 1.8-300 K. The $\chi_M T$ versus T plots for $V^{III}_2Dy_2$ **2.8** are shown in Figure **2.27**. As shown in Figure **2.27**, the value of $\chi_M T$ at 300 K of 31.73 $cm^3 \cdot K \cdot mol^{-1}$ for $V^{III}_2Dy_2$ **2.8** is close to the expected value (30.34 $cm^3 \cdot K \cdot mol^{-1}$) for two non-interacting V^{III} ions with S = 1, g = 2, and C = 1.000 $cm^3 \cdot K \cdot mol^{-1}$ and two Dy^{III} ions (S = 5/2, L = 5, $^6H_{15/2}$, g = 4/3, and C = 14.17 $cm^3 \cdot K \cdot mol^{-1}$). The $\chi_M T$ value remains essentially constant on lowering the temperature from 300 to 90 K, but then decreases to reach a minimum value for $\chi_M T$ of 29.86 $cm^3 \cdot K \cdot mol^{-1}$ at 20 K, followed by a rapid increase to a maximum value of 34.51 $cm^3 \cdot K \cdot mol^{-1}$ at 4.0 K. This type of behavior suggests the presence of intramolecular ferromagnetic interactions.

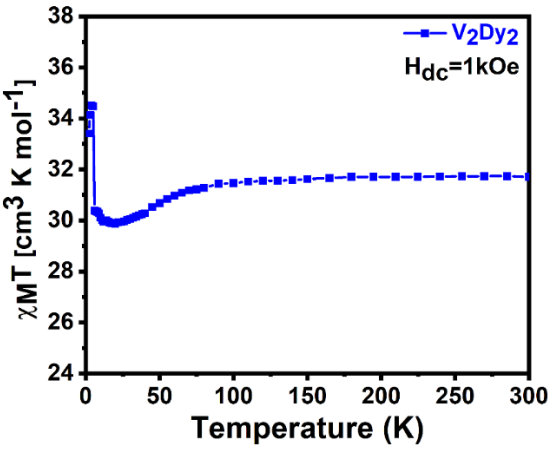

Figure 2.27: The plots of $\chi_M T$ vs T for $V^{III}_2Dy_2$ **2.8**.

Ac susceptibility measurements were obtained under applied dc fields at 2 K from 0 to 4500 Oe as shown in Figure **2.28**. These results indicate that $V^{III}_2Dy_2$ **2.8** shows SMM behavior with an applied dc field with the optimum field being 2000 Oe. Ac susceptibility measurements were carried out at this field between 2.0 and 5.6 K. As shown in Figure **2.29**, out-of-phase signals with clear maxima were observed for $V^{III}_2Dy_2$ **2.8**.

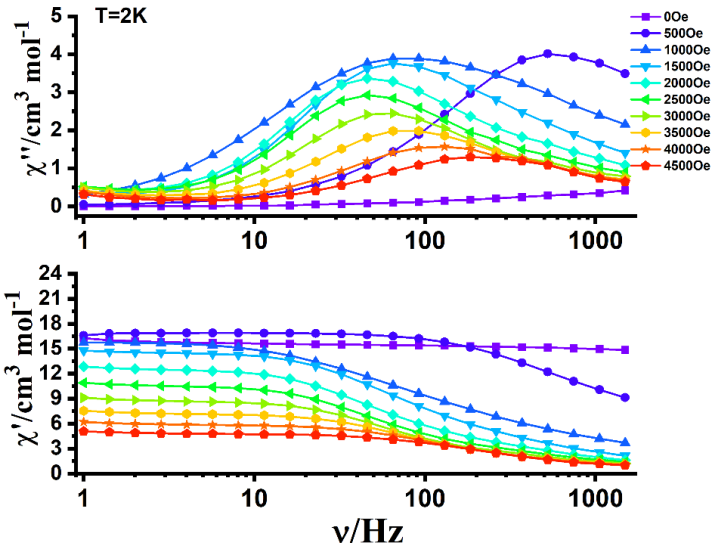

Figure 2.28: Plots of χ' (left) and χ'' (right) vs frequency range from 0 Oe to 4500 Oe at 2 K for complex of $V^{III}_2Dy_2$ **2.8**.

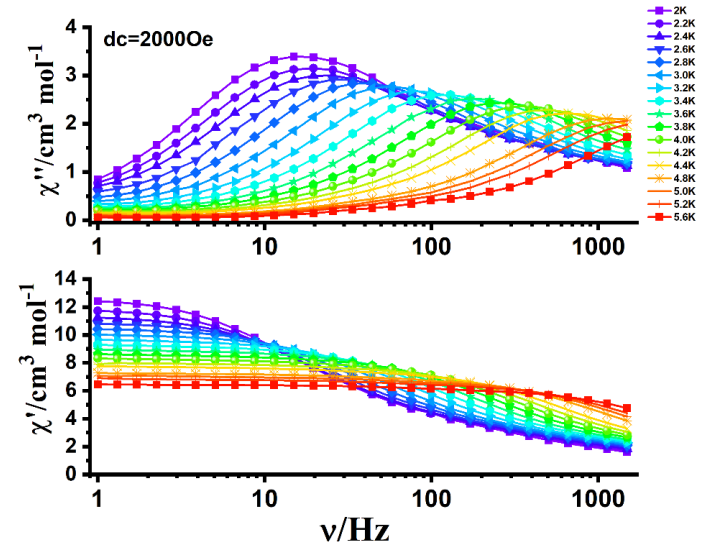

Figure 2.29: Plots of χ' (left) and χ'' (right) vs frequency at the shown temperatures under 2000 Oe field for $V^{III}_2Dy^{III}_2$ **2.8**.

As shown in Figure **2.30**, the normalized magnetization vs. H curve measured on a Micro-SQUID shows a slinky double-S shaped curve. It is interesting that the slow relaxation behavior indicative of SMM properties that is clearly observable in the ac SQUID data, is not obvious from the measured Micro-SQUID data.

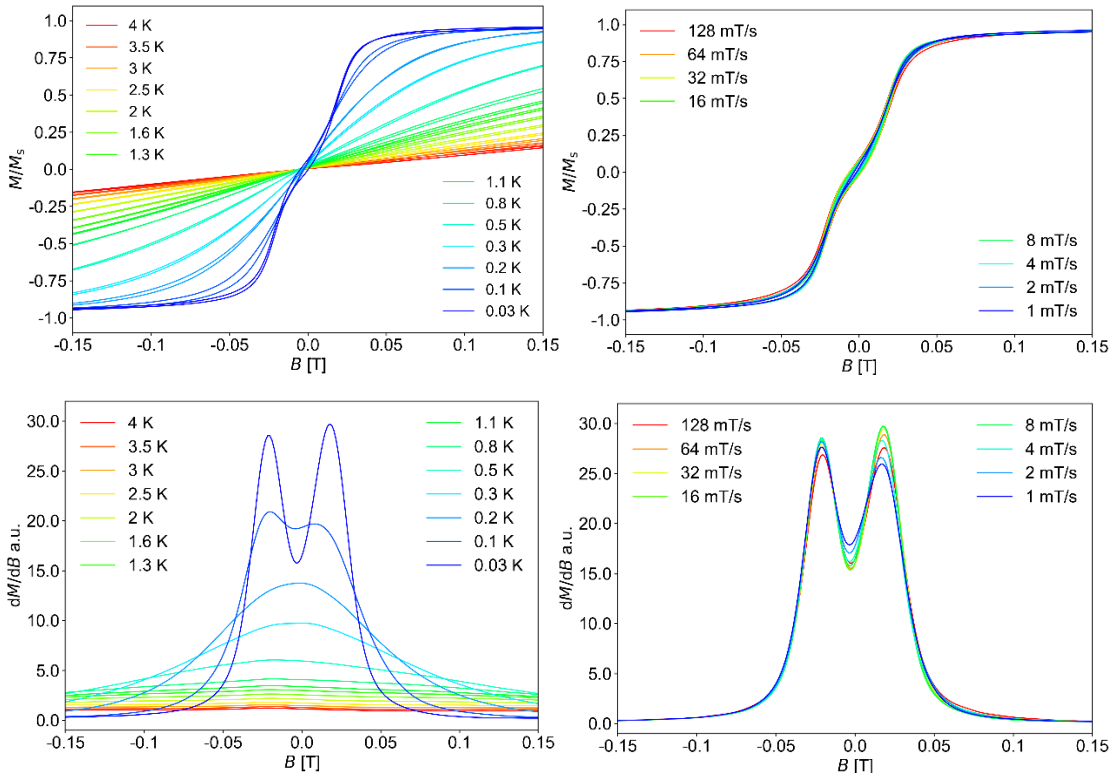

Figure 2.30: Micro-SQUID data for $V^{III}_2Dy_2$ **2.8** at different temperatures with 8 mT/s sweep rate (top left), at 30 mK (top right) and the corresponding derivatives (bottom left and bottom right).

2.2.3 $[V^{III}_5Dy_8]$ and $[V^{III}_4V^{IV}Dy_5]$ 3d-4f SMMs without Applied Field

2.2.3.1 Crystal Structure of $(Et_3NH)[V^{III}_5Dy_8(\mu_3\text{-}OH)_{12}(Bu^tDea)_4(NCC_6H_4CO_2)_{20}]\cdot 15MeCN$

The complex within $(Et_3NH)[V^{III}_5Dy_8(\mu_3\text{-}OH)_{12}(Bu^tDea)_4(p\text{-}CN\text{-}benz)_{20}]\cdot 15MeCN$ ($V^{III}_5Dy_8$ **2.9**) crystallizes in the triclinic space group *P*-1 with Z = 1 which is confirmed by single crystal X-ray diffraction and powder XRD patterns as shown in Figure **2.31**. This core structure is isostructural to the previously reported $Fe^{III}_5Ln_8$ and $Mn^{III}_5Ln_8$ compounds.[172-173] The complex $V^{III}_5Dy_8$ **2.9** consists of five V^{III} ions, eight Dy^{III} ions, four doubly deprotonated diethanolamine ligands (Bu^tDea^{2-}), twenty deprotonated 4-cyanobenzoic acids ($p\text{-}CN\text{-}benz^-$).

As shown in Figure **2.32**, four of the V^{III} ions are located at the corners of the core structure with the fifth lying on the inversion center. Six Dy^{III} ions are

arranged in a triangle above and below this central V^{III} ion forming an hourglass. This hourglass is capped on either side by a V-Dy-V linker unit. Each of the four Bu^tDea^{2-} ligands chelates one of the outer V^{III} ions via the amine N and the two deprotonated alcohol arms. Additionally, the alcohol arms provide two μ_2-O bridges to the nearest Dy^{III} ions forming the linker unit to either side of the central hourglass motif as well as connecting these units to the two Dy triangles. There are three kinds of eight-coordinate Dy^{III} ions. The Dy ions that make up the triangles forming the hourglass motif either have three μ_3-OH ligands and five carboxylate oxygens or four μ_3-OH, three carboxylates and an alkoxide. The two Dy^{III} ions either side of the hourglass are eight-coordinate and attached *via* μ_3-OH bridges to one of the triangles Dy ions as well as a corner V^{III} ion, respectively. The V^{III} ions also have two coordination environments. The O_5N coordination environment of the corner V^{III} ions is provided by a chelating Bu^tDea^{2-}, two carboxylate O atoms of two *p*-CN-benz$^-$ and a μ_3-OH. The central V^{III} ion is coordinated by six μ_3-OH ligands. The geometry around the eight-coordinated Dy^{III} atom is best described as biaugmented trigonal prism J50 geometry using the SHAPE 2.1 software. The Dy^{III}–O bond distances vary from 2.223(5) to 2.469(3) Å. For the V^{III} ions the SHAPE 2.1 analysis reveals a distorted octahedral geometry. The nearest intramolecular distance between Dy^{III} ions is 3.769 Å, the nearest $V^{III}\cdots Dy^{III}$ distance is 3.391 Å and the nearest intramolecular $V^{III}\cdot\cdot V^{III}$ distance is 6.291 Å. The core has almost exact mirror symmetry with V3, Dy4 and Dy4’ lying in the mirror plane.

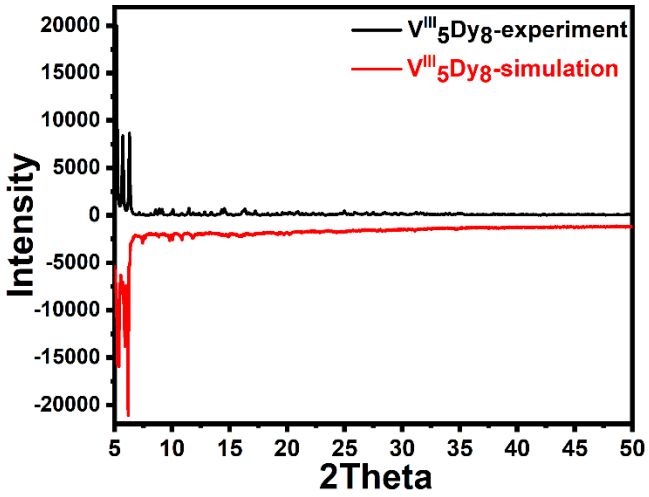

Figure 2.31: The PXRD of complex $V^{III}_5Dy_8$ **2.9**.

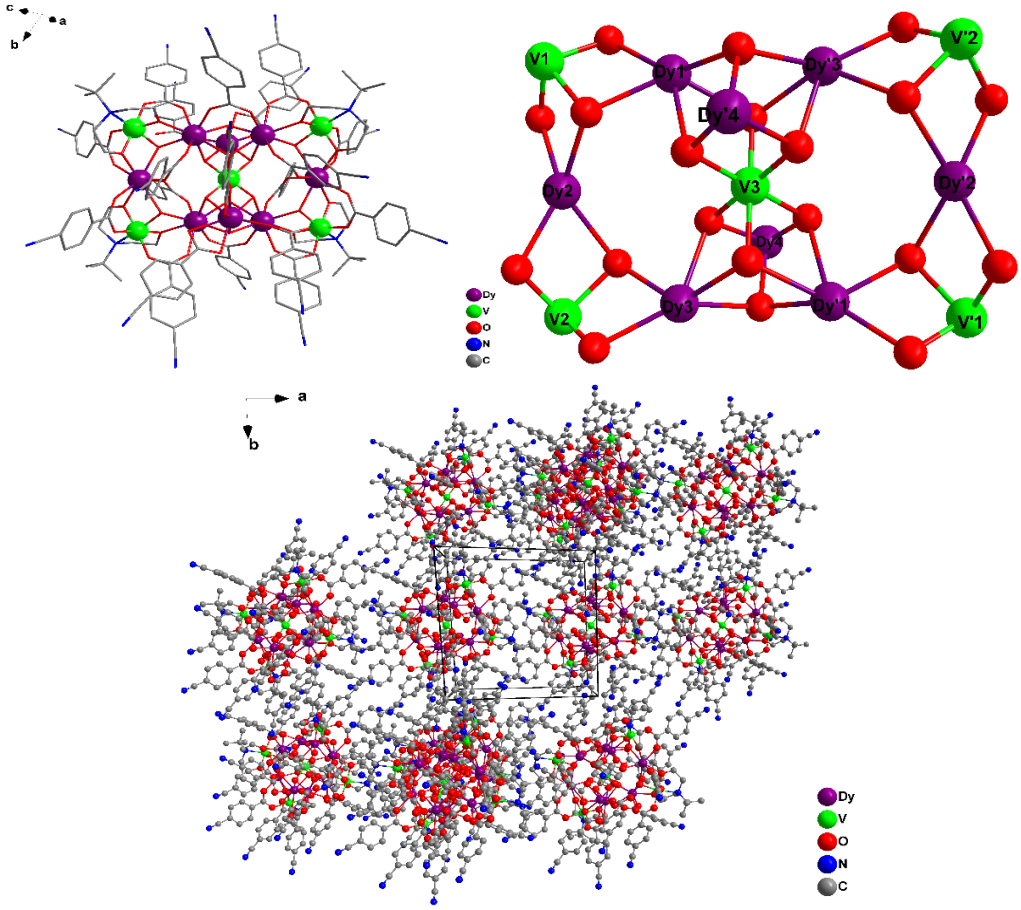

Figure 2.32: The molecular structure of complex, $V^{III}_5Dy_8$ **2.9** (top left). the core of complex $V^{III}_5Dy_8$ **2.9** (top right). the packing of complex $V^{III}_5Dy_8$ **2.9** (bottom).

2.2.3 2 Magnetic properties of complex $V^{III}_5Dy_8$ 2.9.

Dc magnetic susceptibility studies of complex $V^{III}_5Dy_8$ **2.9** were carried out under an applied magnetic field of 1000 Oe over the temperature range 1.8-300 K. The $\chi_M T$ versus T plot for $V^{III}_5Dy_8$ **2.9** is shown in **Figure 2.33**. The value

of $\chi_M T$ at 300 K of 107.42 $cm^3 \cdot K \cdot mol^{-1}$ for $V^{III}_5Dy_8$ **2.9** is less than the expected value (118.36 $cm^3 \cdot K \cdot mol^{-1}$) for five non-interacting V^{III} ions with S = 1, g = 2, and C = 1.000 $cm^3 \cdot K \cdot mol^{-1}$ and eight Dy^{III} ions (S = 5/2, L = 5, $^6H_{15/2}$, g = 4/3, and C = 14.17 $cm^3 \cdot K \cdot mol^{-1}$). The $\chi_M T$ value of complex $V^{III}_5Dy_8$ **2.9** remains almost constant down to about 50 K and then rapidly decreases reaching a minimum value of 67.79 $cm^3 \cdot K \cdot mol^{-1}$ at 1.8 K. This decrease could be explained a combination of intramolecular antiferromagnetic coupling plus the thermal depopulation of excited sub-states. At 2 K, the field dependence of magnetization of $V^{III}_5Dy_8$ **2.9** rapidly increases below 2 T, and at higher fields increases almost linearly and reaches the maximum value of 55.69 Nβ at 14 T and 2 K without saturation, which indicates the presence of anisotropy in the system.

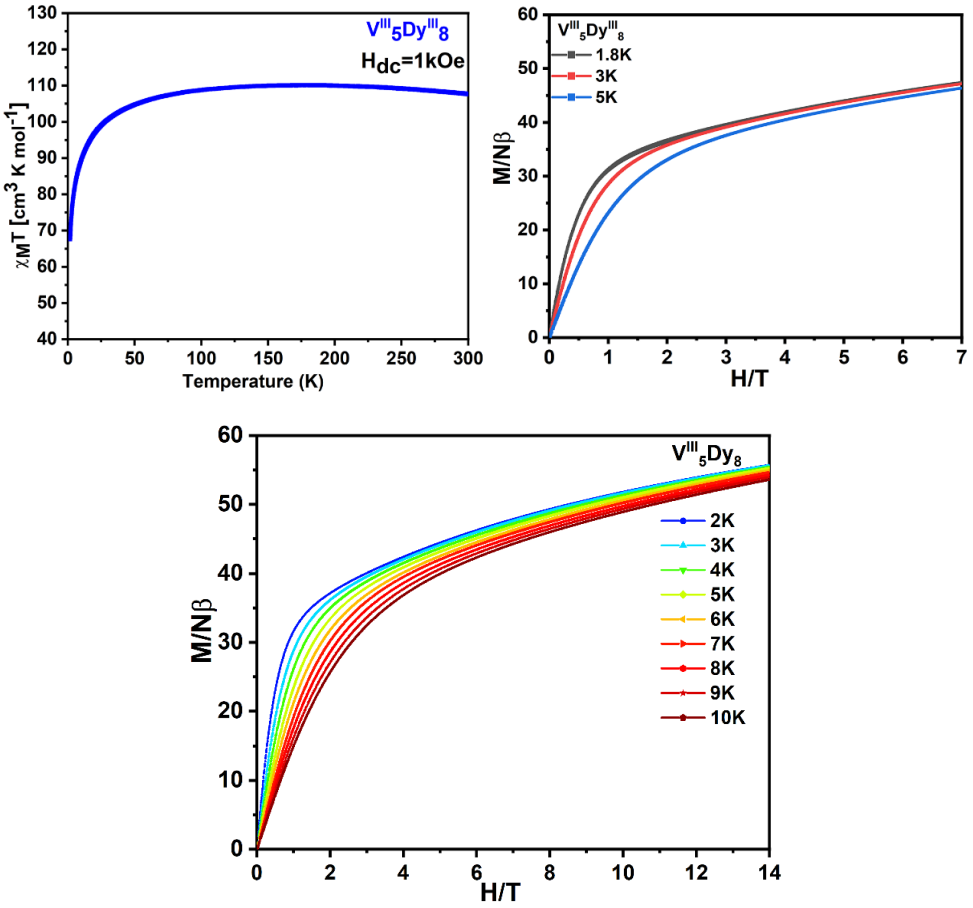

Figure 2.33: The plots of $\chi_M T$ vs T and M vs H for complex $V^{III}_5Dy^{III}_8$ **2.9**.

To check for slow magnetization relaxation and investigate the magnetic properties of $V^{III}_5Dy_8$ **2.9**, ac susceptibility measurements were conducted at

different temperatures. However, no maxima in the out-of-phase signals (χ”) were detected in the measuring window, indicating fast relaxation of the magnetization without applied magnetic fields. Nevertheless, the temperature dependence plots of the $V^{III}_5Dy^{III}_8$ **2.9** suggest the possibility of SMM behavior at low temperatures, as indicated in Figure **2.34**. Applying a range of dc fields did not improve the out-of-phase signals (Figure **2.35**).

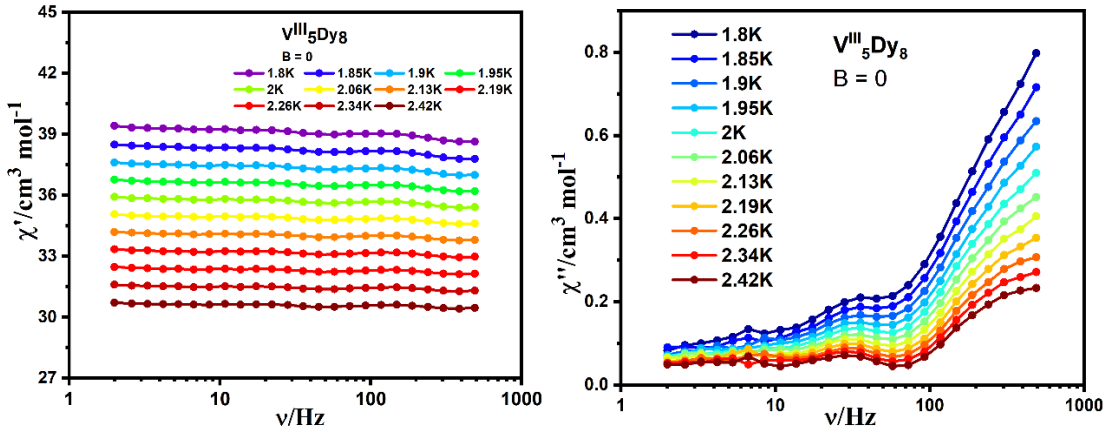

Figure 2.34: Plots of χ’ (left) and χ” (right) vs Frequency under different temperatures for complex of $V^{III}_5Dy^{III}_8$ **2.9**.

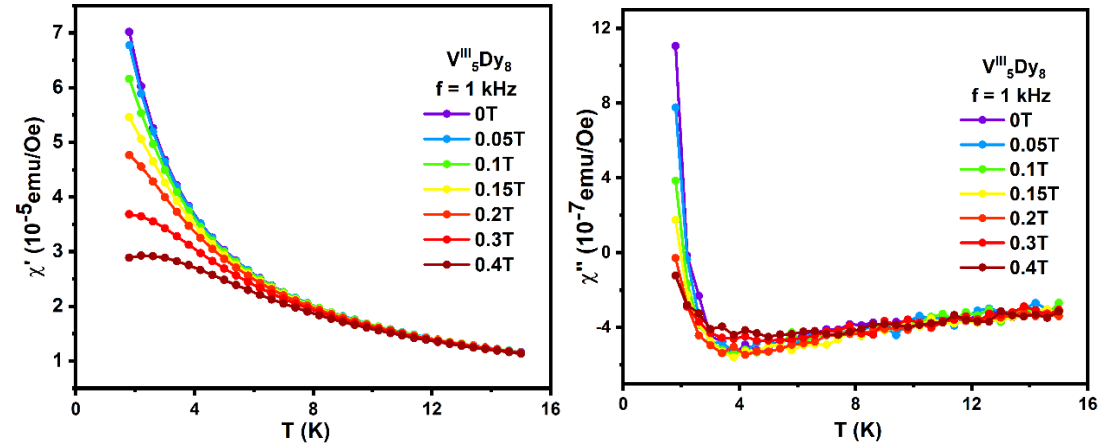

Figure 2.35: Plots of χ’ (left) and χ” (right) vs temperature under different applied fields for complex of $V^{III}_5Dy^{III}_8$ **2.9**.

To probe further the slow relaxation behavior, the magnetization of $V^{III}_5Dy^{III}_8$ was also measured using a Micro-SQUID. As shown in Figure **2.36**, the normalized magnetization vs. H curve shows open hysteresis at temperatures below 0.3 K with a coercive field of 106 mT at 0.03 K. To explore the hysteresis loop of $V^{III}_5Dy_8$ **2.9** further, the sweep-rate dependence at 30 mK was

established. The hysteresis loop phenomenon with obvious opening verifies that $V^{III}_5Dy^{III}_8$ **2.9** is the first confirmed V^{III}-based SMM without the need for an applied dc field. The relaxation data were plotted, and the data could be fitted with an Arrhenius law describing Orbach relaxation with a barrier to magnetization reversal of 8.01 K and a pre-exponential factor of 10^{-13} s (Figure **2.37**).

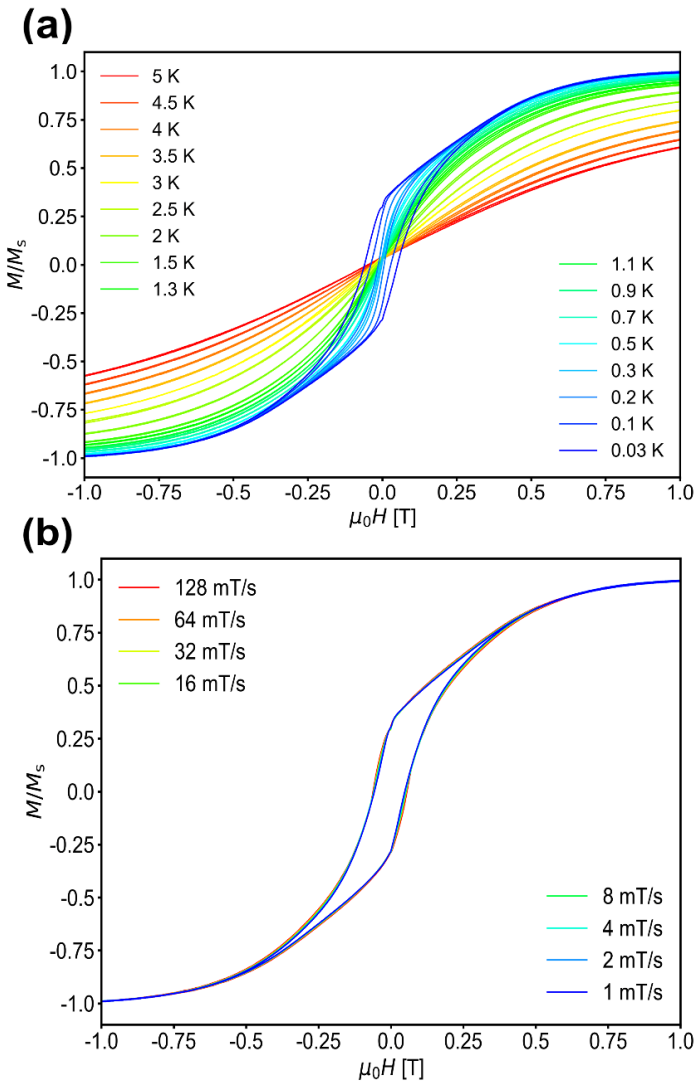

Figure 2.36. (a) micro-SQUID data of $V^{III}_5Dy_8$ **2.9** at different temperatures with 8 mT/s sweep rate; (b) micro-SQUID data of $V^{III}_5Dy_8$ **2.9** at different sweep rate at 30 mK.

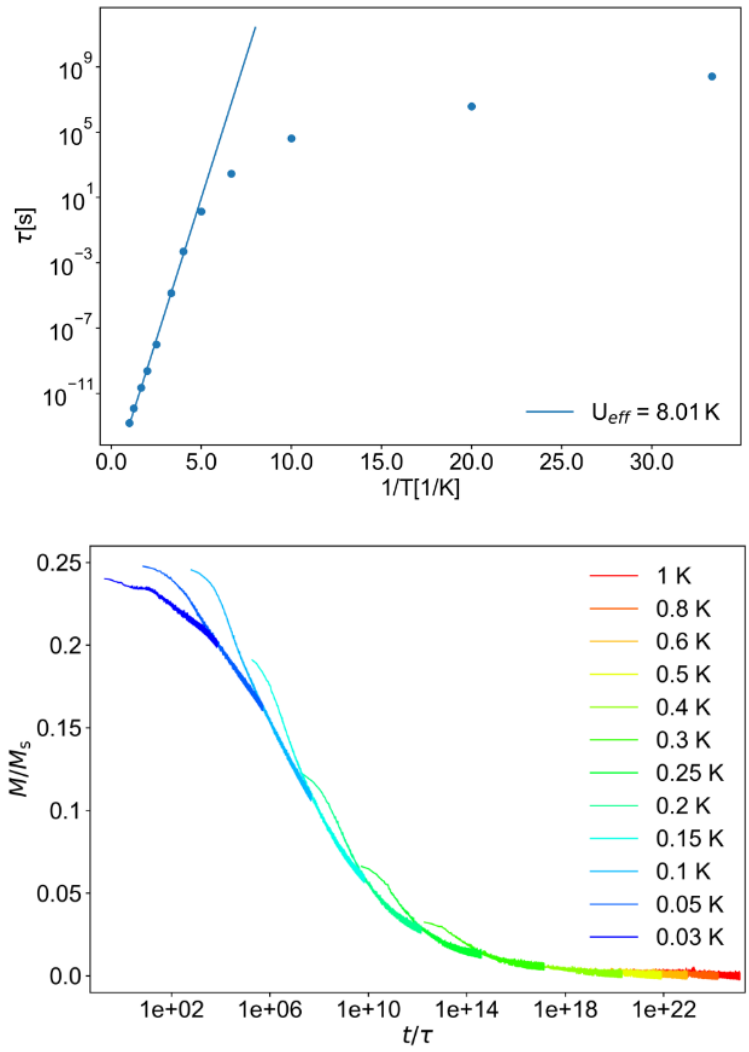

Figure 2.37. Relaxation data fitted with an Arrhenius law to extract the energy barrier as well as preexponential factor.

To explore the possibility of the magnetic anisotropic arrangement of Dy ions in $V^{III}_5Dy_8$ **2.9**, the anisotropy axes of the Dy^{III} ions were calculated using the MAGELLAN software, which uses a solely electrostatic model, and the results are shown in Figure **2.38**.[174] While such an analysis is not recommended for 3d-4f systems in the manual, the Powell group has previously found the axes to correspond well to those found from *ab initio* calculations.[175] In the triangles making up the hourglass motif, one Dy ion each has its anisotropy axis almost perpendicular to the plane of the Dy_3 triangle while the other two have their axes closer to becoming in-plane. The axes of the Dy ions in the V-Dy-V linker units are essentially parallel to the Dy_3 planes. Therefore, six of the eight Dy

ions have their axes almost co-parallel while the other two are essentially perpendicular to them.

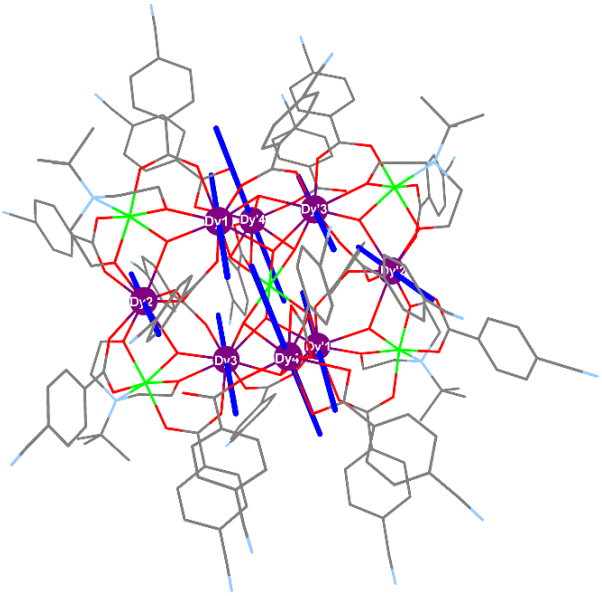

Figure 2.38. Anisotropy axes of the Dy^{III} ions in $V^{III}_5Dy_8$ **2.9** calculated using the MAGELLAN software.[172]

2.2.3.3 Crystal Structure of $[V^{III}_3V^{IV}Dy_5(\mu_2\text{-}OH)(\mu_3\text{-}OH)_7(\mu_2\text{-}O)(^tBuDea)_3(piv)_{12}]\cdot 4MeCN$ (2.10)

The compound $[V^{III}_3V^{IV}Dy_5(\mu_3\text{-}OH)_6(\mu_2\text{-}O)_2(^tBuDea)_3(piv)_{12}]\cdot 4MeCN$ ($V^{III}_3V^{IV}Dy_5$ **2.10**) crystallizes in the monoclinic space group $P2_1/c$ (No. 14). As shown in Figure **2.39**, each ^{t}BuDea^{2-} ligand is coordinated to one of three V ions through the central N atom and the two alkoxy O atoms. These all have an O_5N coordination sphere, whereas the remaining V ion has an O_6 coordination sphere. This in combination with charge balance as well as bond valence sum (BVS) is consistent with the unique V ion is in its +4-oxidation state. The BVS calculations gave oxidation states of 3.00, 3.04, 3.02 and 3.76 for V1, V2, V3 and V4, respectively, consistent with the localization of the charges. For V1-3 the V-N distances are in the range 2.265-2.275 Å and the V-O distances are in the range 1.890-2.062 Å. For V4 five of the V-O distances are in the range 1.895-2.070 Å but the sixth is significantly shorter at 1.779 Å. This is in line with a significant vanadyl character to this oxygen atom. The Dy-O distances range

between 2.284(11) Å-2.519(7) Å. SHAPE 2.1 analysis was used to investigate the coordination geometry of Dy atom. The biaugmented trigonal prism J50 with C_{2v} symmetry was found to be the best fit for $V^{III}_3V^{IV}Dy_5$ **2.10**. The PXRD pattern of $V^{III}_3V^{IV}Dy_5$ **2.10** is compared with the one simulated from the crystal structure in **Figure 2.40**.

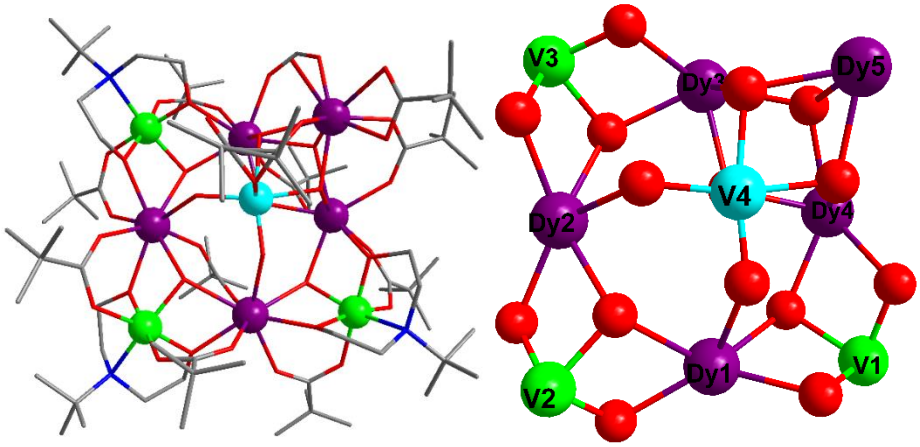

Figure 2.39: The molecular structures of complex $V^{III}_3V^{IV}Dy_5$ **2.10** (left). the core of complex $V^{III}_3V^{IV}Dy_5$ **2.10** (right).

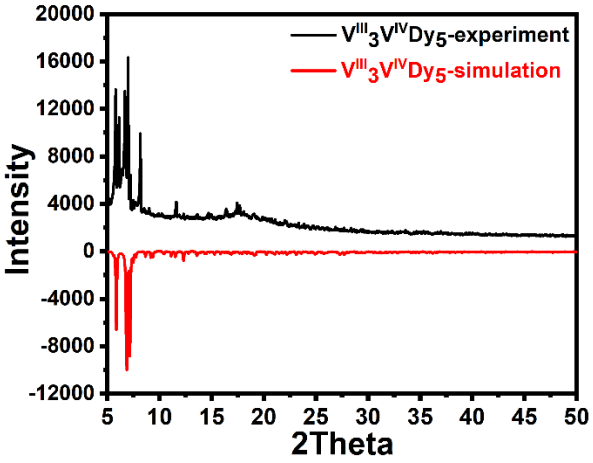

Figure 2.40: The PXRD of complex for $V^{III}_3V^{IV}Dy_5$ **2.10**.

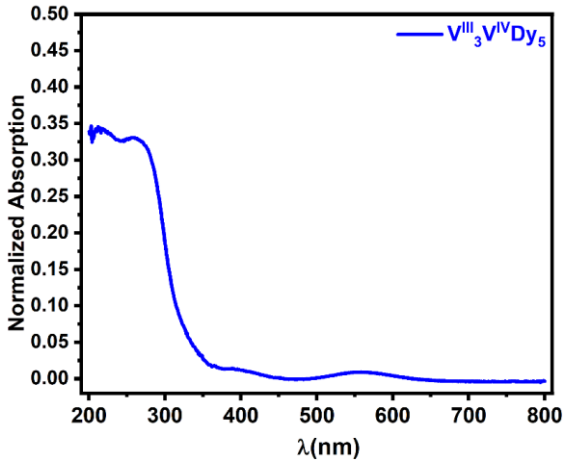

Figure 2.41: The solid-state UV/Vis spectrum of $V^{III}_3V^{IV}Dy_5$ **2.10**.

2.2.3.4 Magnetic properties of complex $V^{III}_3V^{IV}Dy^{III}_5$ 2.10.

The dc magnetic susceptibility of the complex $V^{III}_3V^{IV}Dy_5$ **2.10** was measured on a polycrystalline sample in the temperature range from 2 to 300 K under an applied magnetic field of 1000 Oe (Figure **2.42**). At room temperature, $\chi_M T$ is 74.11 $cm^3 \cdot K \cdot mol^{-1}$, which is in good agreement with the expected value of 74.85 $cm^3 \cdot K \cdot mol^{-1}$ calculated for three non-interacting V^{III} ions with S = 1, g = 2, and C = 1.000 $cm^3 \cdot K \cdot mol^{-1}$, one non-interacting V^{IV} ion with S = 1/2, g = 2, and C = 0.375 $cm^3 \cdot K \cdot mol^{-1}$, and five Dy^{III} ions (S = 5/2, L = 5, $^6H_{15/2}$, g = 4/3, and C = 14.17 $cm^3 \cdot K \cdot mol^{-1}$). Upon cooling, $\chi_M T$ decreases until 40 K, followed by a faster decrease to 6 K with a value of 56.43 $cm^3 \cdot K \cdot mol^{-1}$. After that, the value then increases again to 62.45 $cm^3 \cdot K \cdot mol^{-1}$ at 5 K. This type of behavior suggests the possibility of intramolecular ferromagnetic interactions.

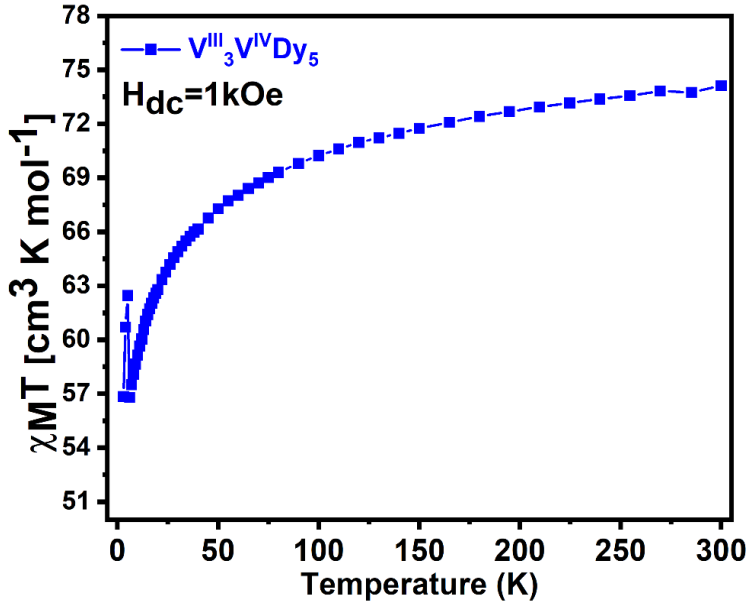

Figure 2.42: The plot of $\chi_M T$ vs T for $V^{III}_3V^{IV}Dy_5$ **2.10.**

Dynamic magnetic measurements were carried out in zero dc field to probe the magnetic relaxation behavior for $V^{III}_3V^{IV}Dy_5$ **2.10**. As indicated in Figure **2.43**, the frequency dependences of the in-phase (χ') and out-of-phase (χ'') ac susceptibility components show unusual behavior. In addition, ac measurements under 2000 Oe show atypical out-of-phase signals (Figure **2.44**).

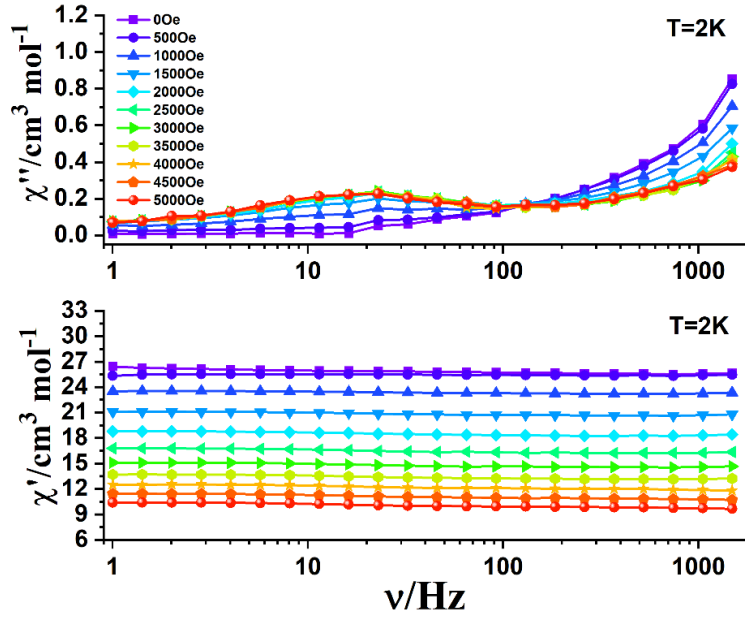

Figure 2.43: Plots of χ' (bottom) and χ'' (top) vs frequency from 0 Oe to 5000 Oe at 2 K for $V^{III}_3V^{IV}Dy_5$ **2.10**.

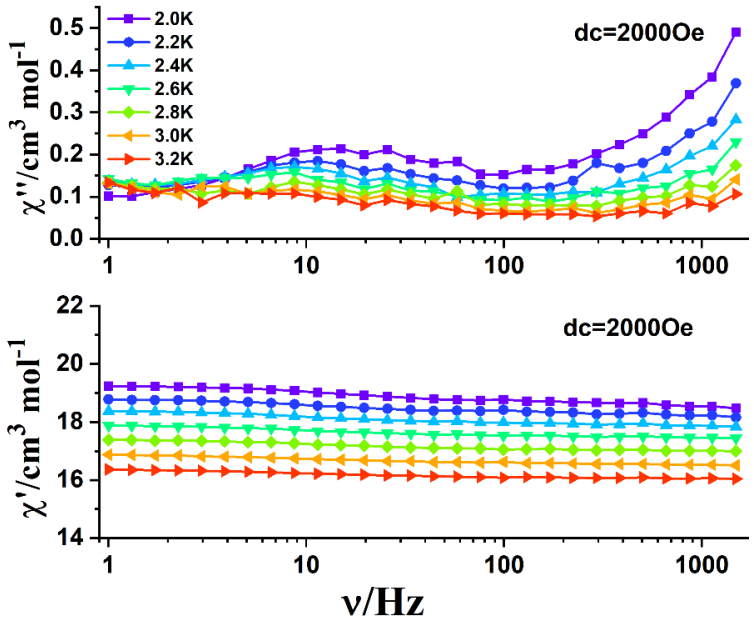

Figure 2.44: Plots of χ' (top) and χ'' (bottom) vs frequency under different temperature under 2000 Oe fields for $V^{III}_3V^{IV}Dy_5$ **2.10**.

To probe the slow relaxation behavior at lower temperatures, the magnetization of $V^{III}_3V^{IV}Dy_5$ **2.10** was measured using a Micro-SQUID (Figure **2.45**). Hysteresis loops are observed below 0.5 K. Only minor scan rate dependence was observed with slight QTM around zero field. The presence of the hysteresis loop with obvious opening confirms that $V^{III}_3V^{IV}Dy_5$ **2.10** exhibits SMM behavior with a coercive field of 140 mT at 30 mK (Figure **2.46**).

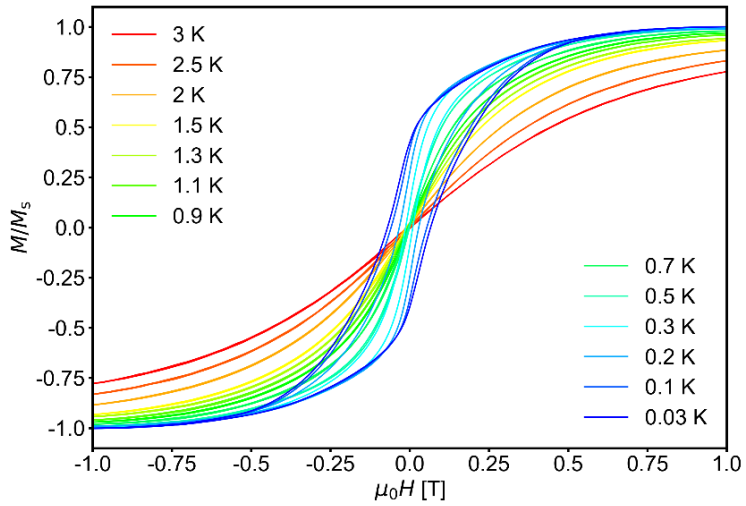

Figure 2.45. Micro-SQUID data of $V^{III}_3V^{IV}Dy_5$ **2.10** at different temperatures with a 8 mT/s sweep rate.

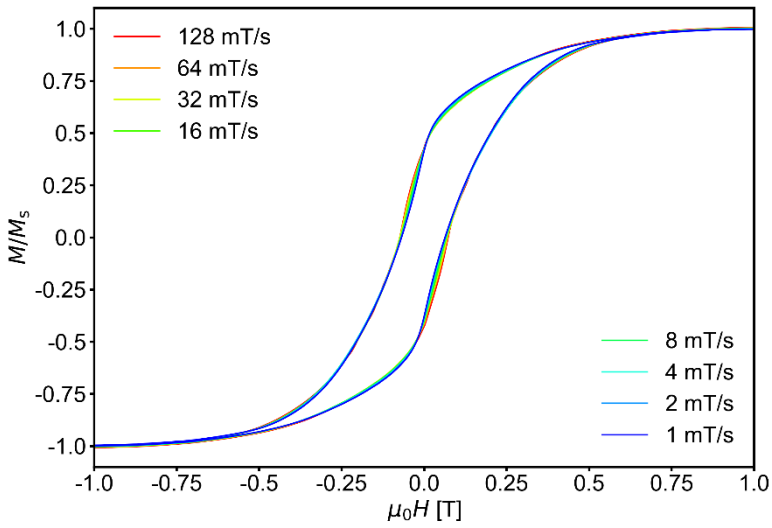

Figure 2.46. Micro-SQUID data of $V^{III}_3V^{IV}Dy_5$ **2.10** at different sweep rate at 30 mK.

2.3 Conclusion

In this chapter, four types of V-Ln complexes with SMM properties were comprehensively characterized both structurally and magnetically. The dc and ac magnetic properties of all complexes were measured.

Among these complexes, the butterfly-type V-Ln complexes are of particular interest. Based on the positions of 3d ions and 4f ions, these complexes were divided into butterfly type **I** V-Ln complexes and butterfly type **II** V-Ln complexes. A series of butterfly type V-Ln complexes were synthesized using Schlenk techniques. The study of their magnetic properties revealed that both butterfly-shaped V-Ln complexes exhibited SMM behavior under an external magnetic field. Additionally, the magnetic interactions between different lanthanide ions and vanadium ions in butterfly type **II** V-Ln complexes were investigated, and it was found that the ferromagnetic interaction gradually weakens until it disappeared with the increase of atomic number (Tb^{III}-Yb^{III}).

Both complexes, $V^{III}_5Dy_8$ **2.9** and $V^{III}_3V^{IV}Dy_5$ **2.10**, shared the characteristic of having a higher proportion of lanthanide ions compared to transition metal ions. The difference lies in the fact that the V ions of the latter exhibit two valence states, V^{III} and V^{IV}. However, at low temperatures, they both exhibit SMM behavior without an external magnetic field. The complex $V^{III}_5Dy_8$ **2.9** displays SMM behavior as evidenced by the open hysteresis loop with a coercive field of 106 mT at 30 mK and an energy barrier (U_{eff}) of 8.0 K. The complex $V^{III}_3V^{IV}Dy_5$ **2.10** also exhibited SMM behavior, as confirmed by the presence of an open hysteresis loop with a coercive field of 140 mT at 30 mK.

These results expand the scope of the field of 3d-4f SMMs to include vanadium-based examples and lay a solid foundation for further studying the magnetic interaction between vanadium and lanthanide ions.

Chapter 3. Ferromagnetic $[V^{III}_4Ln^{III}_4]$ 3d-4f Complexes as Magnetic Refrigerants

3.1 Introduction

Coordination chemistry has attracted more and more attention of chemists because of its structural diversity and architectural aesthetics. Transition metal ions and lanthanide metal ions with large coordination numbers have many structural types as a result of various coordination environment possibilities. This makes them useful in many fields, such as SMMs, magnetic refrigeration, molecular cages, catalysis and electrochemistry.[176-178] Among these potential applications, magnetic refrigeration is considered as a promising next-generation cooling technology based on the magnetocaloric effect (MCE).[179-186]

Magnetic refrigeration is a magneto-thermodynamic phenomenon where the magnetic coolant is heated or cooled according to the change in entropy as a result of an applied external magnetic field.[187-188] The requirements for a magnetic refrigeration material with excellent performance to display MCE are: 1) a high ground spin state, 2) high spin degeneracy (the presence of low-lying excited states between metal ions to achieve large entropy change), 3) preferably low anisotropy, 4) dominant ferromagnetic exchange, 5) a small relative molecular mass.[189-190]

Gadolinium has the largest theoretical magnetic entropy value of 110 J kg^{-1} K^{-1} among all lanthanide ions due to its f^7 electronic configuration.[191-192] For this reason it has been widely chosen to make magnetic refrigeration materials. One promising pathway for molecular materials is to combine transition metal ions with lanthanide ions because of the possibility of ferromagnetic 3d-4f interactions. [193-194]

It is likely that the type and strength of magnetic interactions determine the

way in which the entropy is steered by the system as shown in Figure **3.1**.

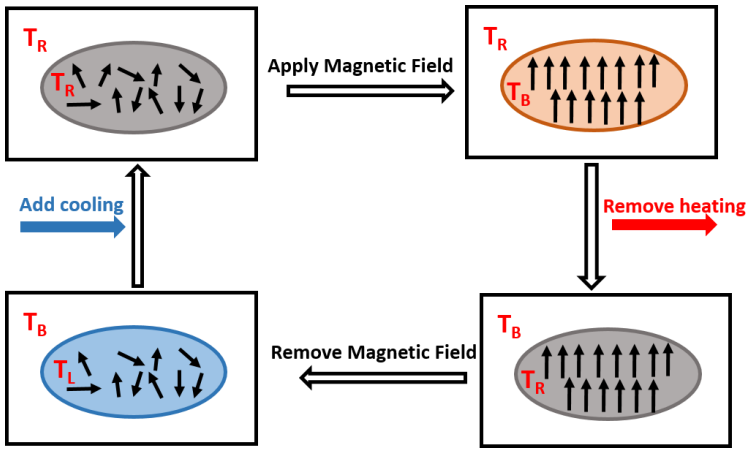

Figure 3.1: Magnetocaloric effect: Application of magnetic field leads to heating and removed of magnetic field casue cooling in the system under study (T_R=room temperature, T_B= more than room temperature, T_L= less than room temperature).

Most of the work so far on 3d-4f polynuclear complexes as magnetic refrigerants have focused on mixing transition metal ions (Cr^{3+}, Mn^{2+}/Mn^{3+}, Fe^{3+}, Co^{2+}/Co^{3+}, Cu^{2+}) with lanthanide ions.[195-209] For instance, Bendix's group synthesized a series of fluoride-bridged, trigonal bipyramidal $[Gd_3M^{III}_2]$(M=Cr, Fe, Ga) complexes, which are smaller in $[Gd_3Fe^{III}_2]$ than in $[Gd_3Cr^{III}_2]$ for the entropy change, that reveals the importance of intramolecular Fe–Gd ferromagnetic interactions;[210] Murray's group reported an isostructural $Cu^{II}_5Ln_4$ cluster based copper ion with comprising a series of vertex- and face-sharing $[GdCu^3]$ tetrahedra, which exhibits a record value of $-\Delta S_m$ = 31 J kg^{-1} K^{-1} at 3 K for 9 T at the time;[211] Winpenny's group found a series of Co^{II}–Ln grids and cages, which show very large values for the MCE as considered potential molecular magnetic refrigerants;[212] Tong's group found a oxydiacetate-bridged Mn^{II}–Gd material that gives rise to the maximum magnetic entropy changes of 50.1 J kg^{-1} K^{-1} for ΔH=70 kG, which was the largest reported magnetic entropy value in 3d-4f complexes.[213] As the smallest paramagnetic ion in the periodic table, vanadium (III) ions participate in ferromagnetic interactions in binuclear species and typically exhibit considerable magnetic anisotropy with negative axial zero field splitting parameter. However, up to now there are no reported studies of the MCE based on combining vanadium ions with gadolinium ions as

new magnetic refrigerants.

3.2 Results and Discussions

3.2.1 $V^{III}_4Ln_4$ compounds (Ln= La^{III}, Nd^{III}, Gd^{III}, Dy^{III} and Y^{III}) (3.1-3.9)

3.53.2.1.1 Crystal Structure of $[V^{III}_4Ln_4(\mu_3\text{-}OH)_4(mDea)_4(p\text{-}Me\text{-}PhCO_2)_{12}]$ $xMeCN{\cdot}yCH_2Cl_2$ [Ln = La^{III}, Nd^{III}, Gd^{III}, Dy^{III}, Y^{III} (3.1-3.5) and $[V^{III}_4Ln_4(\mu_3\text{-}OH)_4(Htea)_4(p\text{-}Me\text{-}PhCO_2)_{12}]{\cdot}xMeCN$ yCH_2Cl_2 [Ln = La^{III}, Gd^{III}, Dy^{III} and Y^{III} (3.6-3.9)]

Single crystals of $V^{III}_4Ln_4(\mu_3\text{-}OH)_4(mDea)_4(p\text{-}Me\text{-}PhCO_2)_{12}$ $xMeCN$ yCH_2Cl_2 (**3.1-3.5**) were grown on a Schlenk Line under anaerobic condition. The experimental powder X-ray diffraction patterns of these complexes **3.1-3.5** and the calculated ones based on SCXRD analysis of complexes **3.1-3.5** were obtained (Figure **3.2**). Here, complex $V^{III}_4Dy_4$ **3.4** is used as a representative for the crystal structure description. $V^{III}_4Dy_4$ **3.4** crystallizes in the centrosymmetric triclinic space group *P*-1 with Z = 2 as shown by SCXRD. As illustrated in Figure **3.3**, the central core of the octanuclear complex is based on two squares of four Dy ions and four V^{III} ions with the average Dy⋯ Dy distance of 4.54 Å and the average V^{III}⋯ V^{III} distance of 6.81 Å. Each pair of adjacent Dy centers are bridged by a μ_3-OH to a V^{III} cation with V^{III}(1)-O(1) bond length of 2.012(2), Dy(1)-O(1) bond length of 2.436(2), and a mean V^{III}⋯ Dy distance of 3.416 Å. Each Dy ion was found to be eight-coordinate with a distorted triangular dodecahedron geometry as the best fit using the SHAPE 2.1 software. The Dy−O bond distances vary from 2.295(2) to 2.447(2) Å. As illustrated in Figure **3.3**, the Dy ⋯ V edges are also each bridged by a deprotonated *p*-Me-$PhCO_2^-$ ligand. All V^{III} ions have a distorted octahedral O_5N donor set. The V^{III}−O bond distances are in the range 1.906(2) – 2.056(2) Å and the V^{III}−N bond distances vary from 2.146(3) to 2.161(3) Å. Each V^{III} is chelated by a doubly-deprotonated $mDea^{2-}$ ligand, one μ_3-OH and two oxygen atoms from two deprotonated *p*-Me-

$PhCO_2^-$ ligands forming bridges to the adjacent Dy ions.

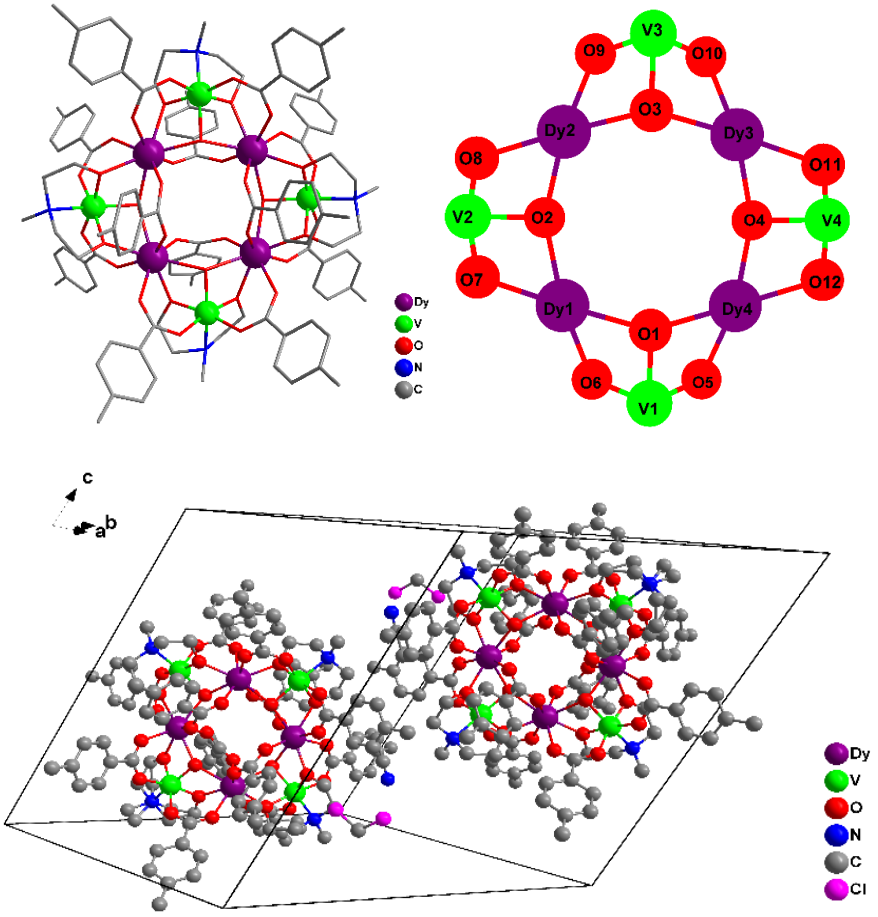

Figure 3.2: The molecular structures of $V^{III}_4Dy_4$ **3.4** (top left). the core of complex $V^{III}_4Dy_4$ **3.4** (top right). the packing of complex $V^{III}_4Dy_4$ **3.4** (bottom).

Both $V^{III}_4Dy_4$ **3.4** and $V^{III}_4Dy_4$ **3.8** are isomorphous and obtained under the same reaction conditions. The only difference lies in the ligands used (H_2mdea and H_3tea). Regarding $M^{III}_4Ln_4$ square-in-square type complexes, the Powell group has previously reported such structures with different ligands and transition metal ions.[214-215] However, most of the magnetic refrigeration properties of $M^{III}_4Ln_4$ complexes have not been reported before, and this chapter will describe the MCE of $V^{III}_4Ln_4$ complexes in detail.

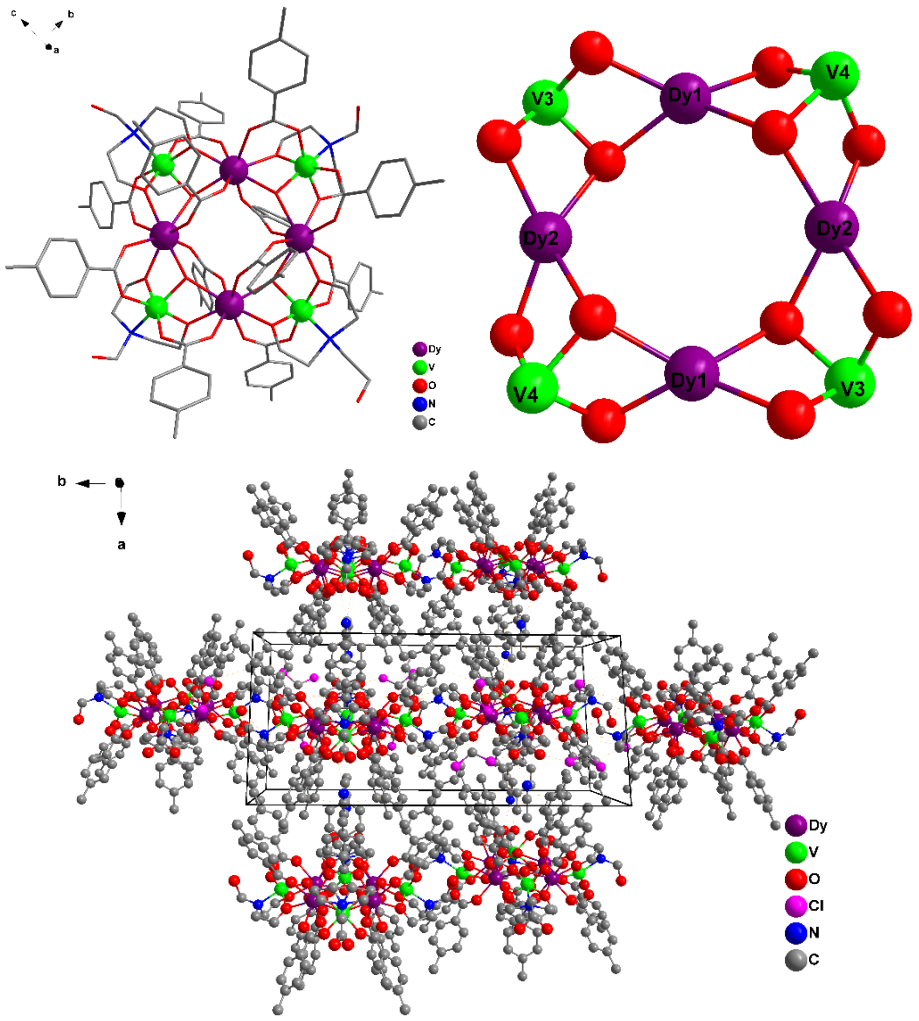

Figure 3.3: The molecular structure of $V^{III}_4Dy_4$ **3.8** (top left). the core of complex $V^{III}_4Dy_4$ **3.8** (top right). the packing of complex $V^{III}_4Dy_4$ **3.8** (bottom).

3.2.2 2 Magnetic properties of complexes of $V^{III}_4Gd_4$ 3.3, $V^{III}_4Dy_4$ 3.4 and $V^{III}_4Y_4$ 3.5

The temperature dependence of dc magnetic susceptibility data for $V^{III}_4Gd_4$ **3.3**, $V^{III}_4Dy_4$ **3.4** and $V^{III}_4Y_4$ **3.5** was evaluated in the temperature range 2–300 K under an external magnetic field of 1000 Oe (Figure **3.4**). The experimental $\chi_M T$ value of complex $V^{III}_4La_4$ **3.1** is 1.30 $cm^3 \cdot K \cdot mol^{-1}$ at 300 K, which is less than the theoretical value of 4 $cm^3 \cdot K \cdot mol^{-1}$ for four isolated V^{III} ions (S = 1, g = 2, and C = 1.000 $cm^3 \cdot K \cdot mol^{-1}$). The $\chi_M T$ value of $V^{III}_4La_4$ **3.1** decreases gradually in the temperature range between 300–6.0 K and then declines sharply to reach the minimum value of 0.88 $cm^3 \cdot K \cdot mol^{-1}$ at 1.8 K. The $\chi_M T$ versus T plots for $V^{III}_4Y_4$ **3.5** is shown in Figure **3.4**. The value of $\chi_M T$ at 300 K

of 3.99 $cm^3 \cdot K \cdot mol^{-1}$ for $V^{III}_4Y_4$ **3.5** is in excellent agreement with the expected value (4.00 $cm^3 \cdot K \cdot mol^{-1}$) for four non-interacting V^{III} ions with S = 1, g = 2, and C = 1.000 $cm^3 \cdot K \cdot mol^{-1}$. There is a rapid decrease in the $\chi_M T$ value upon lowering the temperature from 300 to 1.8 K, reaching a minimum value for $\chi_M T$ of 1.83 $cm^3 \cdot K \cdot mol^{-1}$ at 1.8 K.

For $V^{III}_4Gd_4$ **3.3**, the $\chi_M T$ decreases steadily with decreasing temperature above 10 K due to the magnetic coupling between the V and Gd ions. The room temperature value of the $\chi_M T$ for $V^{III}_4Gd_4$ **3.3** (36.97 cm^3 K mol^{-1}) is slightly larger than the theoretical value for spin-only four Gd^{III} ions and spin-only four V^{III} ions (theoretical: 35.52 cm^3 K mol^{-1}, C = 7.88 cm^3 K mol^{-1} with S = 7/2, L = 0, $^8S_{7/2}$, g = 2.0; C = 1.00 cm^3 K mol^{-1} with S = 1; g=2.0). Upon cooling, the $\chi_M T$ value of $V^{III}_4Gd_4$ **3.3** decreases to reach a minimum at 10 K with a $\chi_M T$ value of 23.8 cm^3 K mol^{-1}. Below this temperature the $\chi_M T$ values increase to reach 36.63 cm^3 K mol^{-1} at 2 K.

The $\chi_M T$ versus T plot for $V^{III}_4Dy_4$ **3.4** is shown in Figure **3.4**. The experimental room temperature $\chi_M T$ value is 60.43 $cm^3 \cdot K \cdot mol^{-1}$ in accordance with the theoretical value for four isolated V^{III} ion (S = 1, g = 2, and C = 1.000 $cm^3 \cdot K \cdot mol^{-1}$) and four isolated Dy^{III} ion (14.17 $cm^3 \cdot K \cdot mol^{-1}$, J = 15/2, g = 4/3) of 60.68 $cm^3 \cdot K \cdot mol^{-1}$. There is a rapid decrease in the $\chi_M T$ value on lowering the temperature from 120 to 6.0 K, reaching a minimum value for $\chi_M T$ of 42.77 $cm^3 \cdot K \cdot mol^{-1}$ at 6.0 K, below which it increases to the maximum value of 51.28 $cm^3 \cdot K \cdot mol^{-1}$ at 2.0 K. Since $V^{III}_4Y_4$ **3.5** shows antiferromagnetic interactions and/or a not insignificant D of the V^{III} ions at low temperatures, this suggests the presence of ferrimagnetism in $V^{III}_4Gd_4$ **3.3** and $V^{III}_4Dy_4$ **3.4**.

The field dependences of the magnetization of $V^{III}_4Gd_4$ **3.3**, and $V^{III}_4Y_4$ **3.5** were evaluated at 1.8, 3 and 5 K in the magnetic field range 0 – 14 T, while the complex $V^{III}_4Dy_4$ **3.4** was evaluated at 2, 3 and 5 K in the magnetic field range 0 – 7 T (Figure **3.4**). The M vs H curve for $V^{III}_4Y_4$ **3.5** saturates at 1.8 K and 14 T suggesting low overall anisotropy.

In addition, the M vs H data of $V^{III}_4Dy_4$ **3.4** were collected at temperatures at 2, 3 and 5 K and show a rapid increase at low magnetic fields (Figure **3.4**). The saturation of magnetization was not observed at the maximum field of 7 T magnetic fields with a value of 27.79 Nβ. For $V^{III}_4Gd_4$ **3.3**, saturation of magnetization was not observed even at high magnetic fields with values of 32.55 Nβ at 1.8 K and 14 T. This could be the result of an antiparallel arrangement of the V^{III} and Gd^{III} spins which upon application of higher fields start to align parallel.

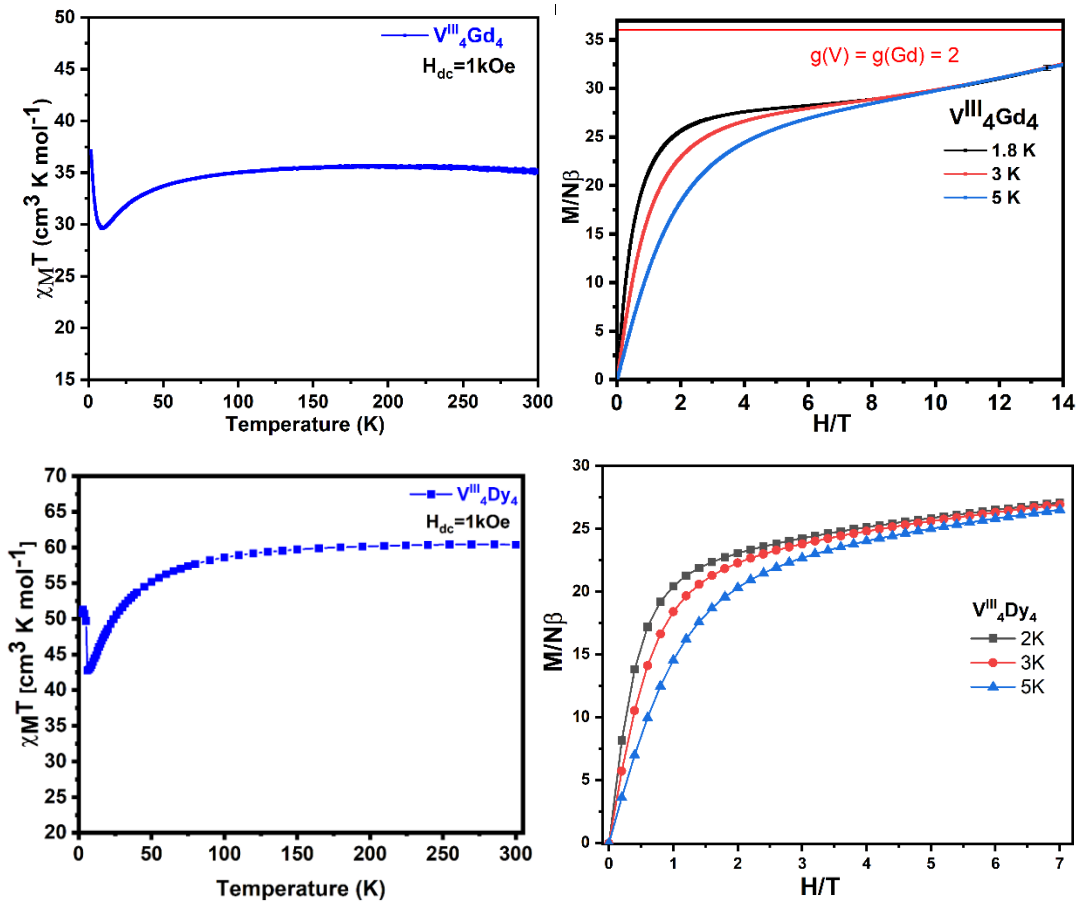

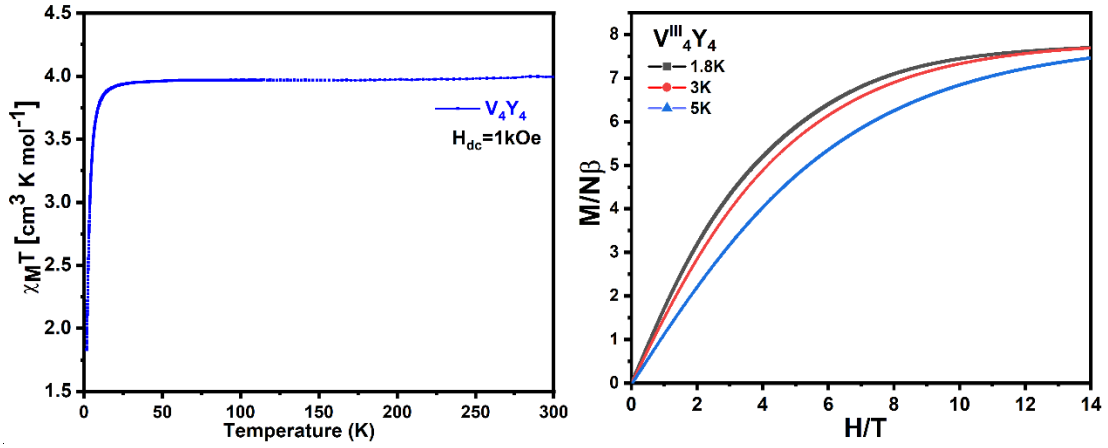

Figure 3.4: The plots of $\chi_M T$ vs T and magnetization for $V^{III}_4Gd_4$ **3.3**, $V^{III}_4Dy_4$ **3.4** and $V^{III}_4Y_4$ **3.5** (from top to bottom).

By investigating the temperature and frequency dependent ac magnetic susceptibility of $V^{III}_4Dy_4$ **3.4**, the typical characteristics of SMM behavior are not observed. As shown in Figure **3.5**, it is obvious that at 2 K the in-phase (χ') and out-of-phase (χ'') ac susceptibility signals of $V^{III}_4Dy_4$ **3.4** do not exhibit frequency dependence.

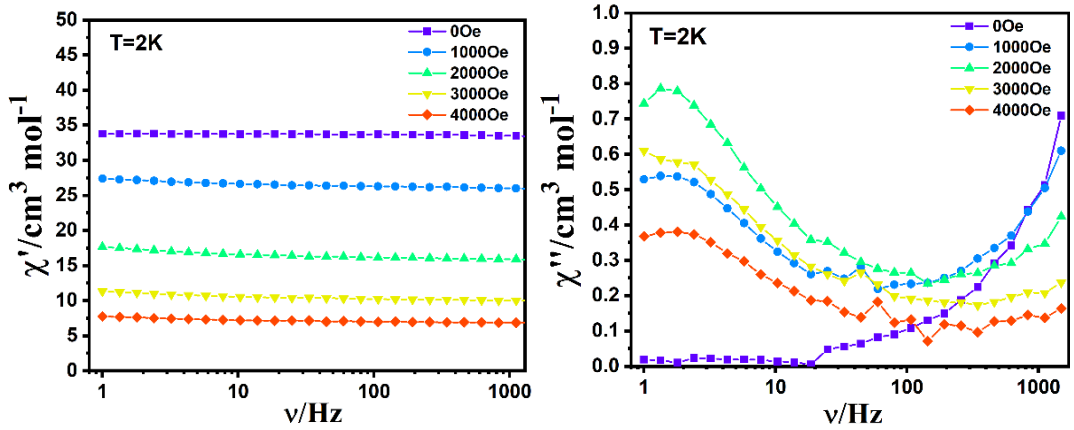

Figure 3.5: Plots of χ' (left) and χ'' (right) vs frequency at fields from 0 Oe to 4000 Oe at 2 K for $V^{III}_4Dy_4$ **3.4**.

3.2.2 3 Magnetic properties of $V^{III}_4Gd_4$ 3.7 and $V^{III}_4Dy_4$ 3.8.

Dc magnetic susceptibility measurements of $V^{III}_4Gd_4$ **3.7** and $V^{III}_4Dy_4$ **3.8** were carried out on polycrystalline samples under a 1 kOe applied dc field from 2 to 300 K. The $\chi_M T$ versus T plots for $V^{III}_4Gd_4$ **3.7** and $V^{III}_4Dy_4$ **3.8** are shown in Figure **3.6**.

The room temperature $\chi_M T$ value ($V^{III}_4Gd_4$ **3.7,** 35.88 cm^3 K mol^{-1}) is slightly larger than the theoretical value (35.52 cm^3 K mol^{-1}) for four non-interacting

Gd^{III} and four V^{III} ions. The $\chi_M T$ value for $V^{III}_4Gd_4$ **3.7**, decreases steadily with decreasing temperature down to 10 K, after which it increases again to reach a value of 37.18 at 2 K.

The $\chi_M T$ value of $V^{III}_4Dy_4$ **3.8** reaches 59.70 $cm^3 \cdot K \cdot mol^{-1}$ at 300 K, which is in good agreement with the theoretical value of 60.68 cm^3 K mol^{-1} for four isolated V^{III} ion (S = 1, g = 2, and C = 1.000 $cm^3 \cdot K \cdot mol^{-1}$) and four isolated Dy^{III} ions (14.17 $cm^3 \cdot K \cdot mol^{-1}$, J = 15/2, g = 4/3). The $\chi_M T$ value decreases upon lowering the temperature from *ca.* 120 to 7.0 K, reaching a minimum value for $\chi_M T$ of 39.74 $cm^3 \cdot K \cdot mol^{-1}$ at 7.0 K, below which it increases to the maximum value of 44.59 $cm^3 \cdot K \cdot mol^{-1}$ at 2.0 K.

The field dependence of magnetization of complexes $V^{III}_4Gd_4$ **3.7** and $V^{III}_4Dy_4$ **3.8** were evaluated at different temperatures in the different magnetic fields (Figure **3.6**). At high magnetic fields, the magnetization value is 31.15 Nβ for $V^{III}_4Gd_4$ **3.7** at 1.8 K and 14 T. For $V^{III}_4Dy_4$ **3.8**, the value of magnetization at 7 T and 2 K is 33.09 Nβ.

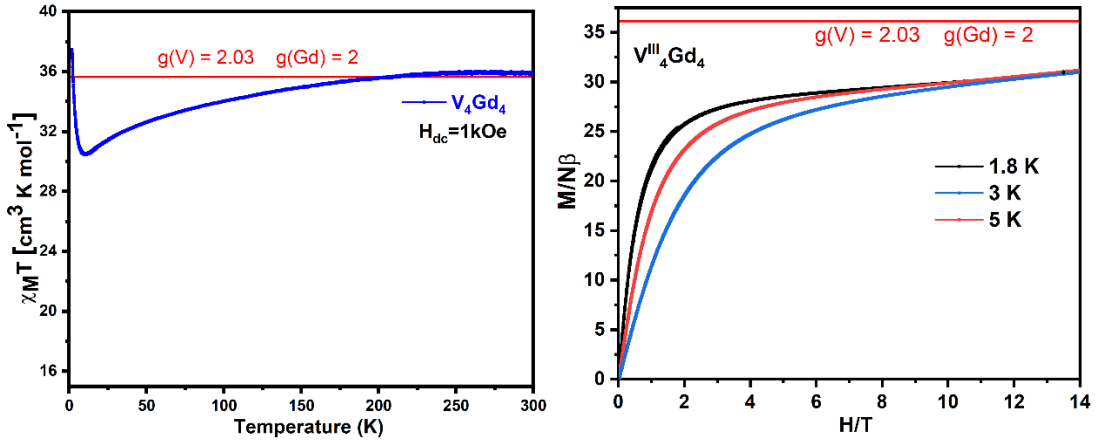

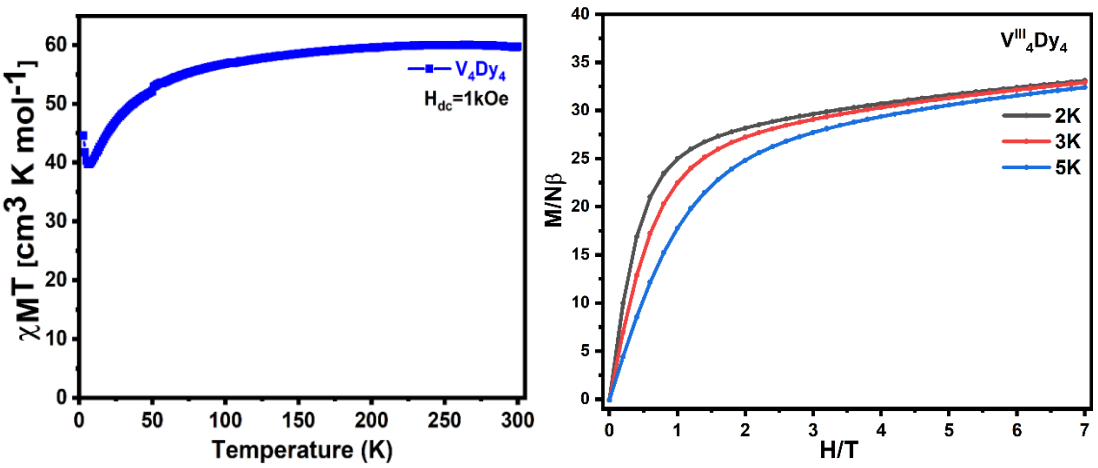

Figure 3.6: The plots of $\chi_M T$ vs T and magnetization for $V^{III}_4Gd_4$ **3.7** (top) and $V^{III}_4Dy_4$ **3.8** (bottom).

By investigating the temperature and frequency-dependent ac magnetic susceptibility of $V^{III}_4Dy_4$ **3.8**, the typical characteristics of SMM behavior are not observed (Figure **3.7**). It is obvious that, at 2 K, the in-phase (χ′) and out-of-phase (χ″) ac susceptibility signals of $V^{III}_4Dy_4$ **3.8** do not exhibit temperature and frequency dependence, and χ″ signals can be observed under applied fields from 0 to 2000 Oe (Figure **3.8**).

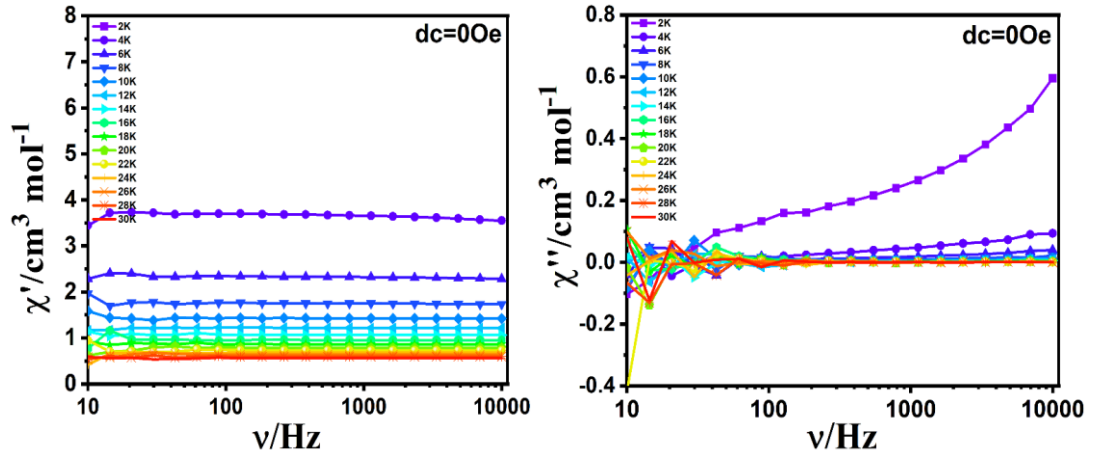

Figure 3.7: Plots of χ' (left) and χ'' (right) vs frequency at different temperatures in the absence of an applied field for $V^{III}_4Dy_4$ **3.8**.

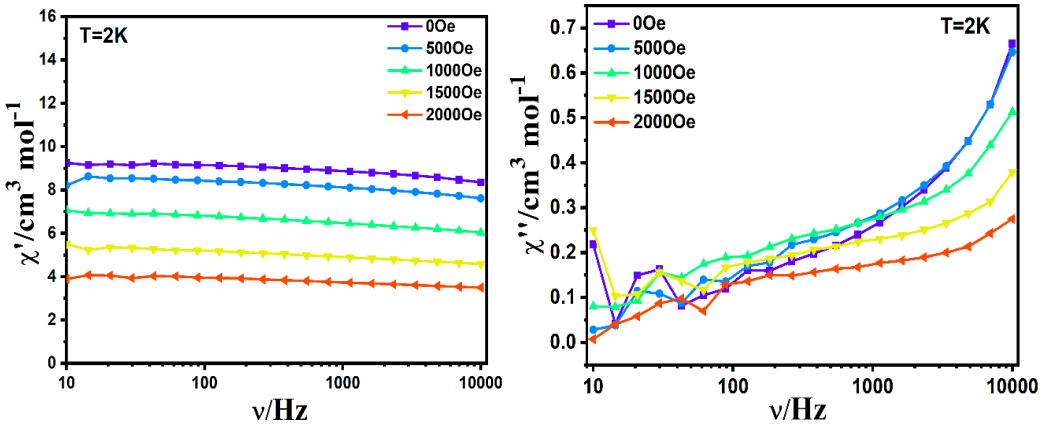

Figure 3.8: Plots of χ' (left) and χ'' (right) vs frequency under applied fields of 0 - 2000 Oe at 2 K for $V^{III}_4Dy_4$ **3.8**.

3.2.2 4 Magnetocaloric properties of $V^{III}_4Gd_4$ 3.3 and $V^{III}_4Gd_4$ 3.7.

Field-dependent isothermal magnetization measurements at low temperatures from 2.0 to 20 K between 0 and 7 T were also performed on polycrystalline samples of $V^{III}_4Gd_4$ **3.3** and $V^{III}_4Gd_4$ **3.7**. As shown in Figure **3.9**, the magnetization of $V^{III}_4Gd_4$ **3.3** and $V^{III}_4Gd_4$ **3.7** was measured against applied magnetic fields at different temperature from 2.0 - 20 K reveal a rapid increase at low magnetic fields. At high magnetic fields, the magnetization of $V^{III}_4Gd_4$ **3.3** increases gradually, finally reaching 30.00 Nβ at 2 K and H =7 T. This is lower than the theoretical saturation value for four Gd^{III} ions and four V^{III} ions. The magnetization of complex $V^{III}_4Gd_4$ **3.7** increases with the magnetic field and reaches 34.19 Nβ at 2.0 K and H =7 T, which almost achieving the theoretical saturation value of 36.00 Nβ (four Gd^{III} ions and four V^{III} ions).

The large magnetization values of $V^{III}_4Gd_4$ **3.3** and $V^{III}_4Gd_4$ **3.7** should enhance the MCE. The magnetic entropy change ΔS_m can be obtained from the Maxwell relation as follows: $\Delta S_m(T)_{\Delta H} = \int [\partial M(T,H) \partial T]_H \, dH$. As shown in Figure **3.9**, the value of $-\Delta S_m$ for $V^{III}_4Gd_4$ **3.3** is 16.08 J kg^{-1} K^{-1} at 3 K for H = 7 T. This is 55% of the calculated value for the spins of four uncorrelated Gd^{3+} (S_{Gd} = 7/2) and four V^{3+} (S_V = 1) ions using the equation $-\Delta S_m = nRln(2S+1)/M_w$ = (4Rln(8) + 4Rln(3))/M_w = 12.71R/M_w = 29.2 J kg^{-1} K^{-1} (R is the gas constant).

For $V^{III}_4Gd_4$ **3.7**, $-\Delta S_m$ value of 17.31 J kg^{-1} K^{-1} at 3 K and H = 7 T corresponds to 67% of the calculated value (29.2 J kg^{-1} K^{-1}) for $V^{III}_4Gd_4$ **3.7** of four uncorrelated Gd^{3+} (S_{Gd} = 7/2) and four V^{3+} (S_V = 1) ions. That the entropy changes of $V^{III}_4Gd_4$ **3.3** and $V^{III}_4Gd_4$ **3.7** are both smaller than the theoretical value of entropy, suggests the possibility of low-lying excited states, which might be the reason for the lower than expected entropy change.[194]

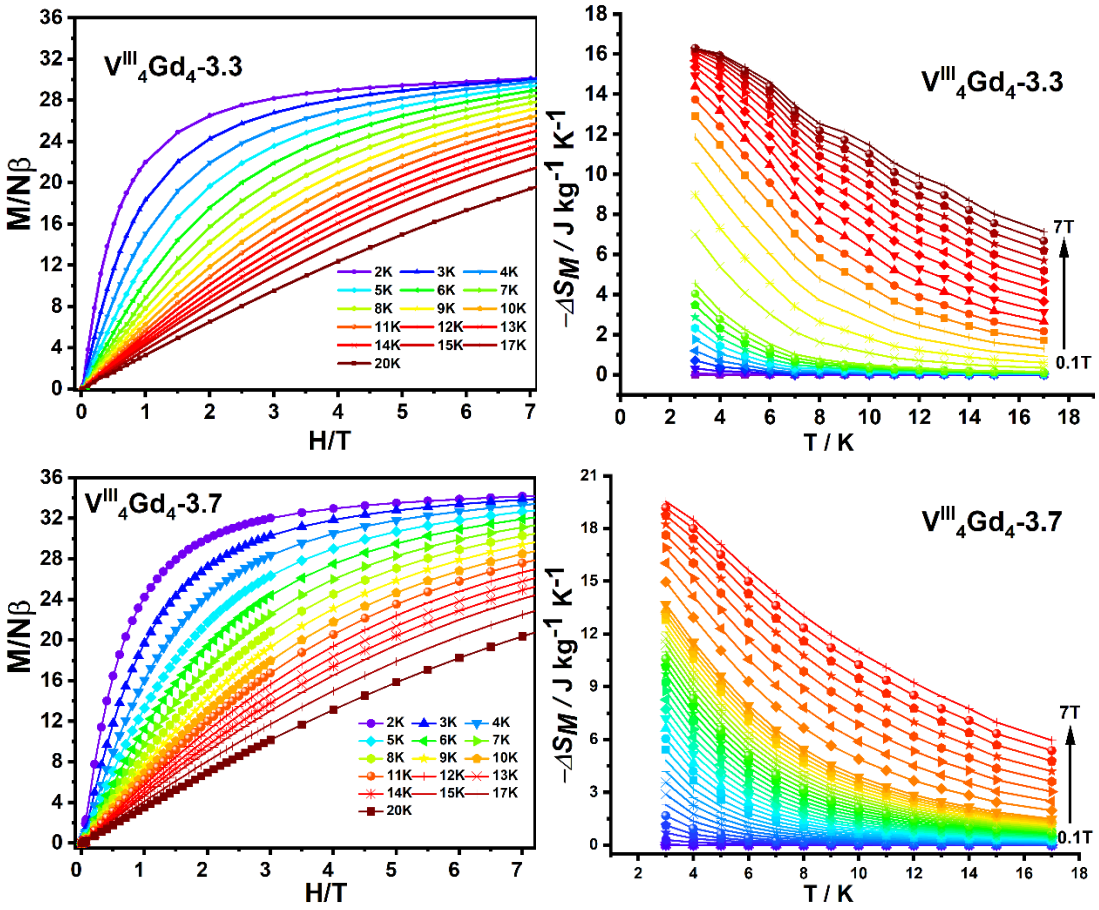

Figure 3.9: The plots of M versus H and magnetic entropy changes for $V^{III}_4Gd_4$ **3.3** (top) and $V^{III}_4Gd_4$ **3.7** (bottom).

3.2.2 Complexes of $V^{III}_4Ln_4$ (Ln= La^{III} and Gd^{III}) (3.10-3.13)

Here, the complexes $V^{III}_4Ln_4$ (with Ln = La^{III} and Gd^{III}) are described which are structurally similar to the above-mentioned complexes $V^{III}_4Ln_4$ (**3.1-3.9**), but using different ligand combinations (Table **3.1**). However, time did not permit for magnetic characterization to be performed.

Table 3.1 The space groups caused by different ligands in complexes **3.10 - 3.14**.

	Ln	Ligands	Space group
$V^{III}_4La_4$ **3.10**	La^{III}	H_2mDea and pivalates	*C*2/*c* (No. 15)
$V^{III}_4Gd_4$ **3.11**	Gd^{III}	H_2mDea and pivalates	*P*-1 (No. 2)
$V^{III}_4Gd_4$ **3.12**	Gd^{III}	teaH_3 and pivalates	$P2_1/c$ (No. 14)
$V^{III}_4Gd_4$ **3.13**	Gd^{III}	H_2^{t}BuDea and *p*-Me-PhCOOH	*P*-1 (No. 2)

As a representative, the structure of complex $V^{III}_4Gd_4$ **3.13** is discussed to illustrate the structural features common to the four complexes $V^{III}_4Ln_4$ ($V^{III}_4La_4$ **3.10**, $V^{III}_4Gd_4$ **3.11**, $V^{III}_4Gd_4$ **3.12**, $V^{III}_4Gd_4$ **3.13**). Compound $V^{III}_4Gd_4$ **3.13** crystallizes in the centrosymmetric triclinic space group *P*-1 (no. 2). The structure is shown in Figure **3.10**. In the octanuclear complex $V^{III}_4Gd_4$ **3.13**, the central core of the complex is based on two squares of four Gd ions and four V^{III} ions with the average Gd···Gd distance of 4.567 Å, the average V^{III}···V^{III} distance of 6.902 Å and the average Gd···V^{III} distance of 3.452 Å. Furthermore, it was found that the square formed by four Gd^{III} ions is surrounded by the square formed by four V^{III} ions. Each pair of adjacent Gd^{III} centers are bridged by a μ_3-OH to a V^{III} cation with V^{III}-O 2.022 Å, Gd-O 2.463 Å, and V^{III}···Gd^{III} 3.447 Å, respectively. Each Gd^{III} ion is found to be eight-coordinate with a distorted triangular dodecahedron geometry using a SHAPE 2.1 analysis with the Gd^{III}–O bond distances varying from 2.310 to 2.478 Å. As illustrated in Figure **3.10**, the Gd^{III} ··Gd^{III} edges are also bridged by two deprotonated *p*-Me-PhCO_2^- ligands that are on the opposite face of the Gd^{III}_4 square to four μ_3-OH ligands bridge. The V^{III} ions have a distorted octahedral O_5N donor set.

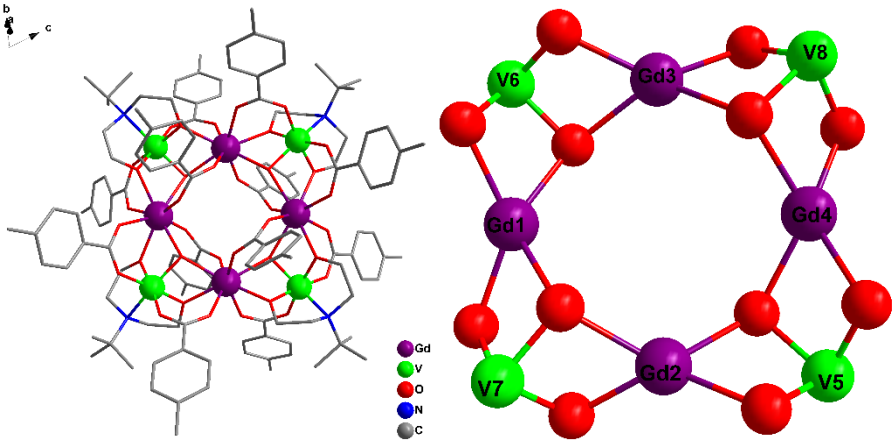

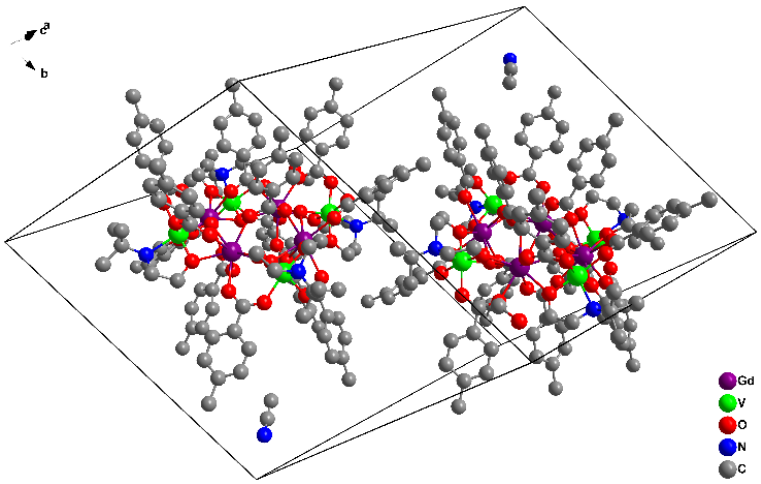

Figure 3.10: The molecular structure of $V^{III}_4Gd_4$ **3.13** (top left). the core of $V^{III}_4Gd_4$ **3.13** (top right). The crystal packing of complex $V^{III}_4Gd_4$ **3.13** (bottom).

3.3 Conclusion

In this chapter, a series of $V^{III}_4Ln_4$ complexes were characterized, both structurally and magnetically. These complexes are all $V^{III}_4Ln_4$ complexes of the same molecular structure and the difference between these complexes lies in the ligands and lanthanide ions. The main purpose is to understand the relationship between the magnetic properties of $V^{III}_4Ln_4$ complexes using different ligands and lanthanide ions. Furthermore, the dc, magnetization and ac magnetic properties of selected $V^{III}_4Ln_4$ complexes were measured by SQUID magnetometry.

The first series of $V^{III}_4Ln_4$ complexes described in this chapter have the following molecular formula $[V^{III}_4Ln_4(u_3\text{-}OH)_4(mDea)_4(O_2CPh\text{-}Me\text{-}p)_{12}]$ $xMeCN{\cdot}yCH_2Cl_2$ (Ln = La, Nd, Gd, Dy and Y). As a representative of this series of complexes, the crystal structure of $V^{III}_4Dy_4$ **3.4** complex was analyzed. It can be seen from the structure that these $V^{III}_4Ln_4$ complexes are square-in-square shaped, with four V^{III} ions in the outer square and four lanthanide ions in the inner square. The two squares are rotated by 45° to each other forming a ring-shaped structure. The dc measurement results of $V^{III}_4Gd_4$ **3.3** and $V^{III}_4Dy_4$ **3.4** show that as the temperature decreases, the value of χ_MT first decreases gradually in the high temperature area, and then drops sharply when it is lower than 50 K, reaching the lowest point, before increasing. For $V^{III}_4Y_4$ **3.5**, as the temperature decreases, the χ_MT values also decreases slowly in the high temperature range, and drops sharply below 10 K. Since Y^{III} is a diamagnetic ion these dc data show that the V^{III} ions could exhibit antiferromagnetic interactions, which also suggests that there may be ferrimagnetic interactions in $V^{III}_4Gd_4$ and $V^{III}_4Dy_4$. The ac measurement shows that $V^{III}_4Dy_4$ **3.4** does not have SMM properties even in an applied field.

Furthermore, the magnetocaloric properties of isostructural $V^{III}_4Gd_4$ **3.3** and $V^{III}_4Gd_4$ **3.7** complexes with two different ligands are discussed. Field-dependent isothermal magnetization measurements on $V^{III}_4Gd_4$ **3.3** and

$V^{III}_4Gd_4$ **3.7** complexes were also measured by SQUID magnetometry. The magnetization of $V^{III}_4Gd_4$ **3.3** increases gradually, finally reaching 30.00 Nβ at 1.9 K and H = 7 T, and $V^{III}_4Gd_4$ **3.7** reaching 34.19 Nβ at 1.8 K and H = 7 T. As for the entropy change of $V^{III}_4Gd_4$ **3.3** and $V^{III}_4Gd_4$ **3.7**, the value of $-\Delta S_m$ for $V^{III}_4Gd_4$ **3.3** is 16.08 J kg^{-1} K^{-1} at 3 K for H = 7 T, and the value of $-\Delta S_m$ is 19.53 J kg^{-1} K^{-1} at 3 K for H = 7 T for $V^{III}_4Gd_4$ **3.7**. These entropy values are 55% and 67% of the maximum theoretical entropy value.

Finally, this is the first reported V^{III}-Gd magnetic refrigeration material, and its performance is comparable to other similar 3d ions magnetic refrigerants expanding the scope of 3d-Gd magnetic refrigerant materials.[194]

Chapter 4. Magnetostructural Correlation between Ring-shaped Complexes of Vanadium and Lanthanide Ions

4.1 Introduction

Coordination chemists design new systems that exhibit desired physical or chemical properties,[216] such as magnetostructural correlations in copper-lanthanide complexes.[217-219] For ligand-bridged polymetallic complexes, some correlation must exist between the type and magnitude of magnetic interaction and the relative positions of the metal ions.[220-222]

The earliest of these correlations was established by Hatfield and Hodgson who showed a linear relationship between the magnetic parameter J and the Cu-O-Cu bridging angle φ in planar bis(μ-hydroxo) copper(II) dimers, with the Cu-O distance being less important. The crossover from ferromagnetic to antiferromagnetic exchange occurs at approximately 97.5°. [218] It is now established that when the Cu-O-Cu angle is greater than 90°, this type of complex exhibits ferromagnetism.[218]

In this chapter, a series of ring-shaped vanadium-lanthanide complexes were discussed with regard to magnetostructural correlation. Through the discussion in this chapter, we can understand some interesting phenomena of ring-shape vanadium-lanthanide complexes in terms of magnetic properties. It will also serve as a reference for researchers when studying similar materials. This is also the first time that ring-shaped vanadium-lanthanide complexes were shown to be ferrimagnetic.

4.2 Results and Discussions

4.2.1 Complexes of two types of $V^{III}_3Ln_2$ (Ln = Tb-Er, Yb and Y)

4.2.1.1 Crystal Structure of $[V^{III}_3Ln_2(\mu_3\text{-}OH)(tea)_4(p\text{-}Me\text{-}PhCO_2)_6]\cdot 2MeCN$ [Ln = Tb-Er, Yb and Y] (4.1-4.6)

Full structure determination was performed for compounds **4.1-4.6** using SC-XRD. All six complexes are isostructural and crystallize in the triclinic space group *P*-1 (no. 2) with Z = 2. These are also isostructural to a series of $Fe^{III}_3Ln_2$ compounds reported by Baniodeh *et al.*. [223] The structure of $V^{III}_3Dy_2$ **4.2** is described as a representative. As illustrated in Figure **4.1**, the pentanuclear complex $V^{III}_3Dy_2$ **4.2** consists of three V^{III} and two Dy^{III} ions. Each tea^{3-} ligand is coordinated to one Dy^{III} ion through three O atoms and the central N atom, and the two alcohol arms of the ligand provide μ_2-O bridging to the adjacent V^{III} ions. As for the vanadium ions, there are two ways of linking for coordination. The coordination environment of the first kind of vanadium ion is formed from four deprotonated alkoxides (derived from two tea^{3-} ligands) and two deprotonated *p*-Me-$PhCO_2^-$. The other two are coordinated identically by two deprotonated alkoxy groups derived from tea^{3-} and two deprotonated *p*-Me-$PhCO_2^-$. All three V^{III} ions have a distorted octahedral donor set. Each Dy ion is found to be eight-coordinate with a triangular dodecahedron geometry through using a SHAPE 2.1 analysis with the Dy−O bond distances varying from 2.273 to 2.463 Å. The Dy···Dy, Dy···V and the V···V distances are 5.622, 3.401 and 3.494 Å, respectively. The phase purity of these samples was checked using powder XRD analysis (Figure **4.2**).

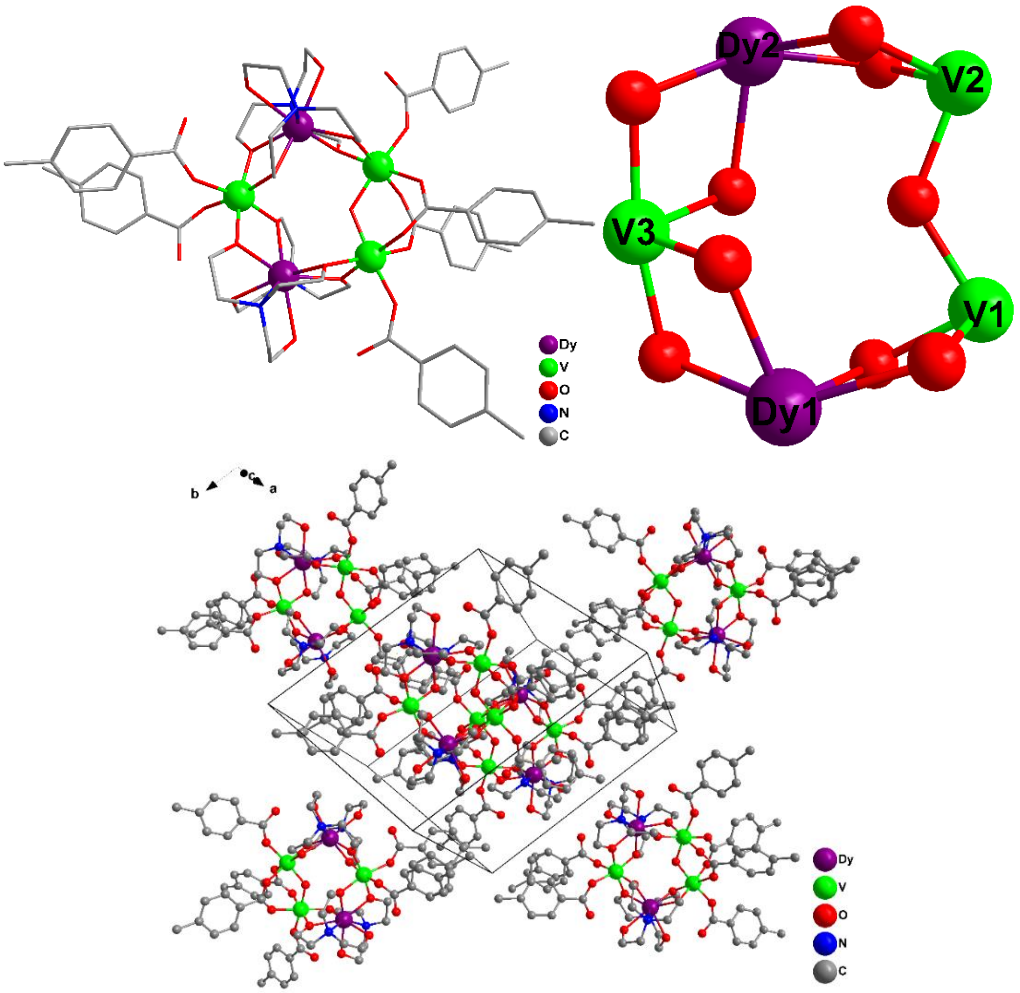

Figure 4.1: The molecular structure of $V^{III}_3Dy_2$ **4.2** (top left). the core of $V^{III}_3Dy_2$ **4.2** (top right). The crystal packing of complex $V^{III}_3Dy_2$ **4.2** (bottom).

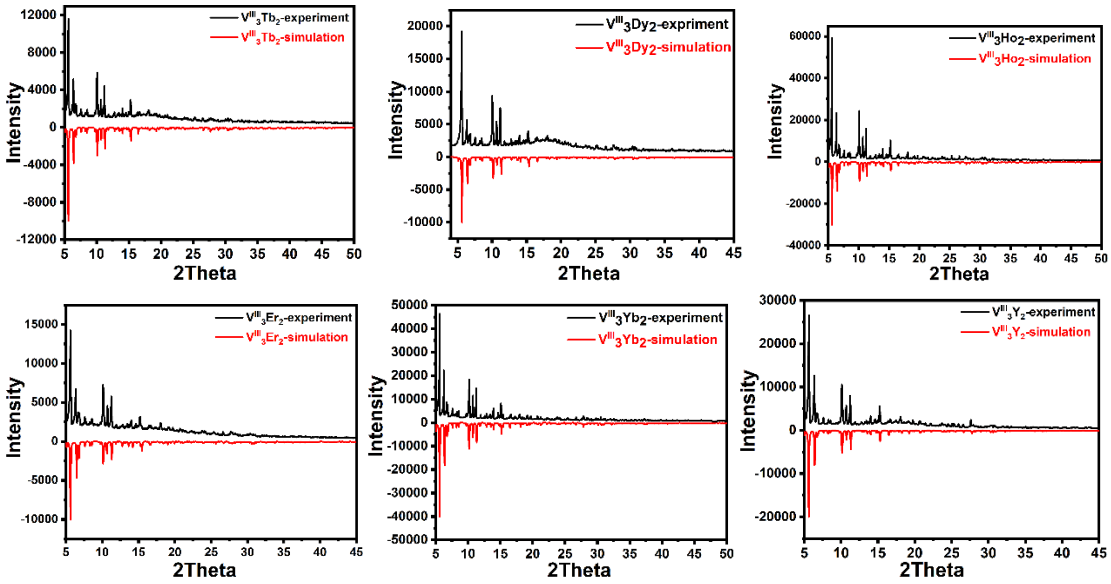

Figure 4.2: The PXRDs for $V^{III}_3Tb_2$ **4.1**, $V^{III}_3Dy_2$ **4.2**, $V^{III}_3Ho_2$ **4.3**, $V^{III}_3Er_2$ **4.4**, $V^{III}_3Yb_2$ **4.5**, $V^{III}_3Y_2$ **4.6**.

Table 4.1 The SHAPE 2.1 analysis Ln^{III} ions in complexes **4.1-4.6**.

	4.1-$V^{III}_3Tb_2$	**4.2-$V^{III}_3Dy_2$**	**4.3-$V^{III}_3Ho_2$**	**4.4-$V^{III}_3Er_2$**	**4.5-$V^{III}_3Yb_2$**	**4.6-$V^{III}_3Y_2$**
Ln^{III}	**Tb^{III}**	**Dy^{III}**	**Ho^{III}**	**Er^{III}**	**Yb^{III}**	**Y^{III}**
OP-8	31.349	31.178	31.292	31.295	31.371	31.183
HPY-8	22.185	23.072	22.433	22.042	23.328	23.231
HBPY-8	11.207	10.695	11.460	11.307	11.183	10.851
CU-8	8.580	6.944	8.805	8.651	7.446	7.154
SAPR-8	4.088	3.983	3.978	4.123	3.803	3.935
TDD-8	**3.238**	**3.853**	**3.061**	**3.248**	**3.530**	**3.718**
JGBF-8	10.543	11.283	10.544	10.544	11.180	11.187
JETBPY-8	21.428	21.188	21.674	21.203	21.435	21.225
JBTPR-8	4.098	4.066	3.937	4.128	3.936	4.007
BTPR-8	3.898	3.894	3.809	3.903	3.783	3.840
JSD-8	4.015	4.479	3.827	3.996	4.157	4.314
TT-8	9.390	7.765	9.613	9.472	8.273	7.981
ETBPY-8	19.500	19.600	19.895	19.371	19.859	19.697

OP-8 (D_8h) Octagon, HPY-8 (C_7v) Heptagonal pyramid, HBPY-8 (D_6h) Hexagonal bipyramid, CU-8 (*O*h) Cube, SAPR-8 (D_4d) Square antiprism, TDD-8 (D_2d) Triangular dodecahedron, JGBF-8 (D_2d) Johnson gyrobifastigium J26, JETBPY-8 (D_3h) Johnson elongated triangular bipyramid J14, JBTPR-8 (C_2v) Johnson elongated triangular bipyramid J14, BTPR-8 (C_2v) Biaugmented trigonal prism, JSD-8 (D_2d) Snub diphenoid J84, TT-8 (*T*d) Triakis tetrahedron, ETBPY-8 (D_3h) Elongated trigonal bipyramid.

4.2.1.2 Magnetic properties of $V^{III}_3Ln_2$ (Ln=Tb, Dy, Er, and Y)

Dc magnetic susceptibility studies of these compounds $V^{III}_3Ln_2$ were carried out under an applied magnetic field of 1000 Oe over the temperature range 1.8-300 K. $V^{III}_3Tb_2$ **4.1**, $V^{III}_3Dy_2$ **4.2,** $V^{III}_3Er_2$ **4.4** and $V^{III}_3Y_2$ **4.6** show a steady decrease of their $\chi_M T$ values on lowering the temperature from 300 K to 1.8 K. For $V^{III}_3Tb_2$ **4.1**, $V^{III}_3Dy_2$ **4.2,** $V^{III}_3Er_2$ **4.4** and $V^{III}_3Y_2$ **4.6**, the $\chi_M T$ values at 300 K are lower than the values expected for non-interacting metal ions including three vanadium ions and two lanthanide ions. Hence, the dc susceptibility studies of $V^{III}_3Dy_2$ **4.2** is described as a representative. As shown in Figure **4.3**, the value of $\chi_M T$ at 300 K of 30.73 $cm^3 \cdot K \cdot mol^{-1}$ for $V^{III}_3Dy_2$ **4.2** is in good agreement with the expected value (31.34 $cm^3 \cdot K \cdot mol^{-1}$) for three non-interacting V^{III} ions with S = 1, g = 2, and C = 1.000 $cm^3 \cdot K \cdot mol^{-1}$ and two Dy^{III} ions (S = 5/2, L = 5, $^6H_{15/2}$, g = 4/3, and C = 14.17 $cm^3 \cdot K \cdot mol^{-1}$). The $\chi_M T$ values of these complexes of $V^{III}_3Tb_2$ **4.1**, $V^{III}_3Dy_2$ **4.2,** $V^{III}_3Er_2$ **4.4** and $V^{III}_3Y_2$ **4.6** follow a similar trend, remaining almost constant down to about 100 K and then decrease reaching 18.76 $cm^3 \cdot K \cdot mol^{-1}$ $V^{III}_3Tb_2$ **4.1**, 23.98 $cm^3 \cdot K \cdot mol^{-1}$ $V^{III}_3Dy_2$ **4.2**, 17.74 $cm^3 \cdot K \cdot mol^{-1}$ $V^{III}_3Er_2$ **4.3** and 0.14 $cm^3 \cdot K \cdot mol^{-1}$ $V^{III}_3Y_2$ **4.6** at 1.8 K. This type of behavior suggests the possible presence of intramolecular

antiferromagnetic interactions in these $V^{III}_3Ln_2$ compounds.

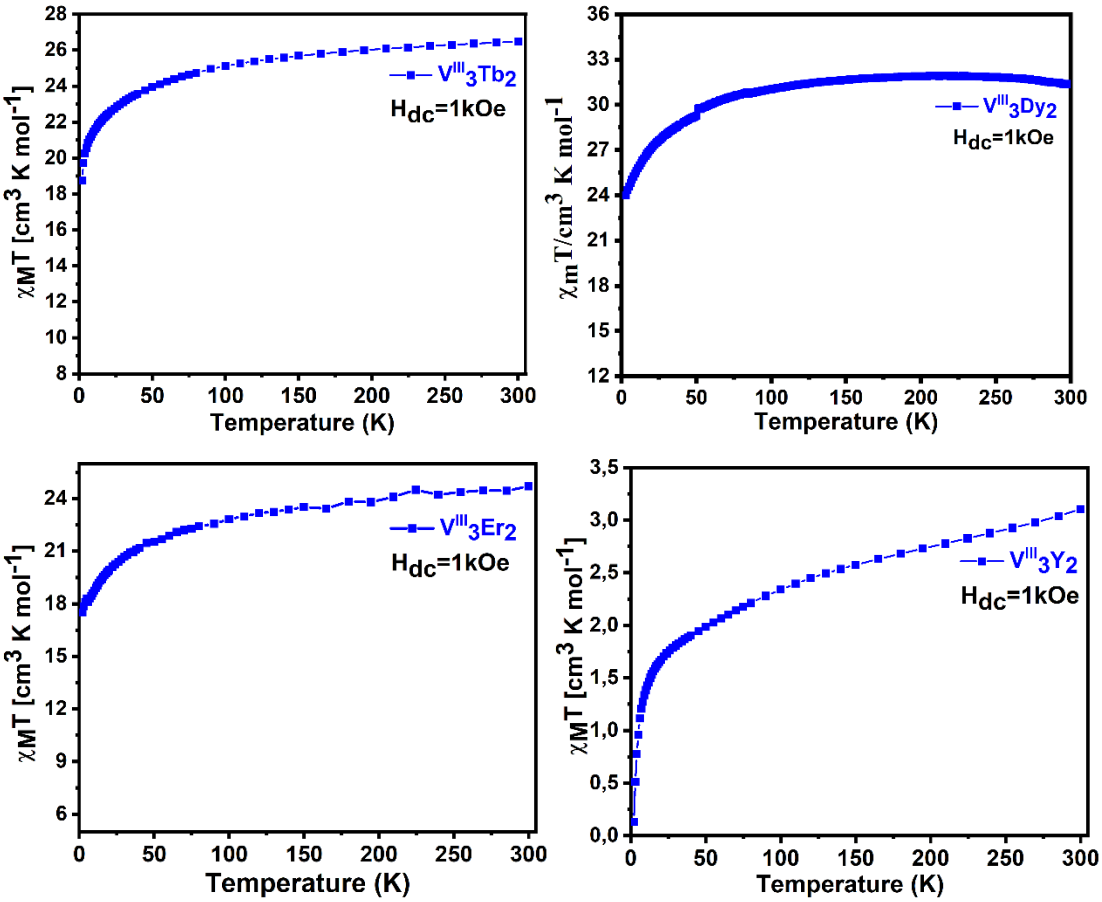

Figure 4.3: The plots of $\chi_M T$ vs T for $V^{III}_3Tb_2$ **4.1**, $V^{III}_3Dy_2$ **4.2**, $V^{III}_3Er_2$ **4.3** and $V^{III}_3Y_2$ **4.6**.

At 2 K, the field dependence of magnetization of $V^{III}_3Dy_2$ **4.2** rapidly increases below 1 T, and at higher fields increases almost linearly to a maximum value of 11.17 Nβ at 7 T without reaching saturation (Figure **4.4**). This indicates the presence of anisotropy in the system.

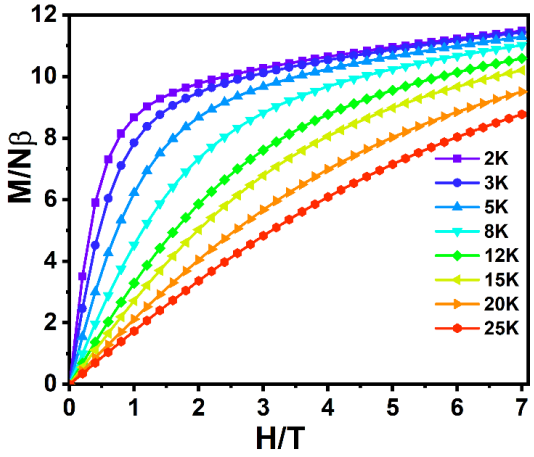

Figure 4.4: The plots of M vs H for $V^{III}_3Dy_2$ **4.2**.

Table 4.2 Magnetic data of compounds **4.1-4.6** summarized from the dc measurements.

Compound	Ground state of Ln^{III} ion	χT expected for non-interacting ions per complex ($cm^3 \cdot K \cdot mol^{-1}$)	χT measured at 300 K per complex ($cm^3 \cdot K \cdot mol^{-1}$)	χT measured at 2.0 K per complex ($cm^3 \cdot K \cdot mol^{-1}$)
4.1-$V^{III}_3Tb_2$	$^7F_6$	26.64	26.47	18.74
4.2-$V^{III}_3Dy_2$	$^6H_{15/2}$	31.34	31.38	24.01
4.3-$V^{III}_3Ho_2$	$^5I_8$	31.14	Not tested	Not tested
4.4-$V^{III}_3Er_2$	$^4I_{15/2}$	25.96	24.70	17.49
4.5-$V^{III}_3Yb_2$	$^2F_{7/2}$	8.14	Not tested	Not tested
4.6-$V^{III}_3Y_2$	---	3.00	3.10	0.14

To probe slow magnetization relaxation, ac susceptibility measurements were measured under different dc fields for $V^{III}_3Tb_2$ **4.1**, $V^{III}_3Dy_2$ **4.2,** $V^{III}_3Er_2$ **4.4** and $V^{III}_3Y_2$ **4.6**. No clear out of phase signal (χ") was observed in the dynamic susceptibility studies of the four complexes, indicating the absence of SMM behavior (Figure **4.5 – 4.8**).

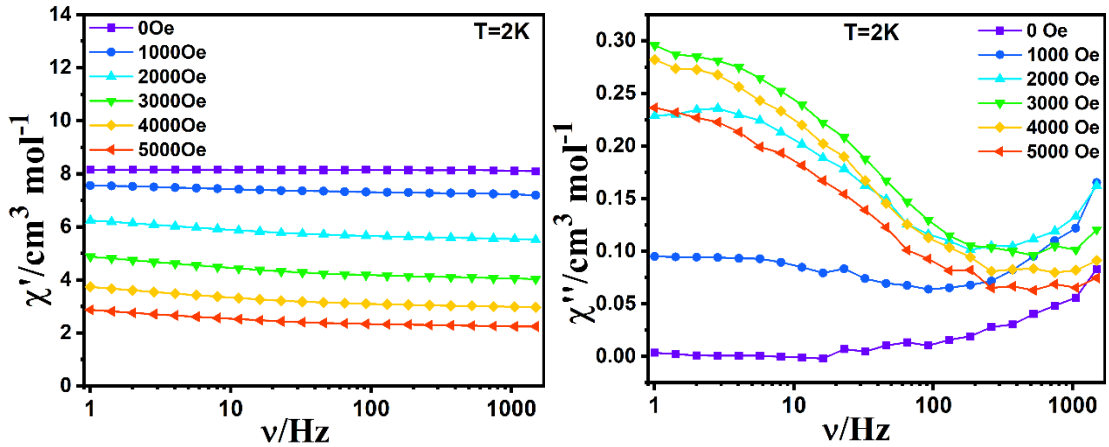

Figure 4.5: Plots of χ' (left) and χ'' (right) vs frequency under applied dc fields from 0 Oe to 5000 Oe at 2 K for $V^{III}_3Tb_2$ **4.1**.

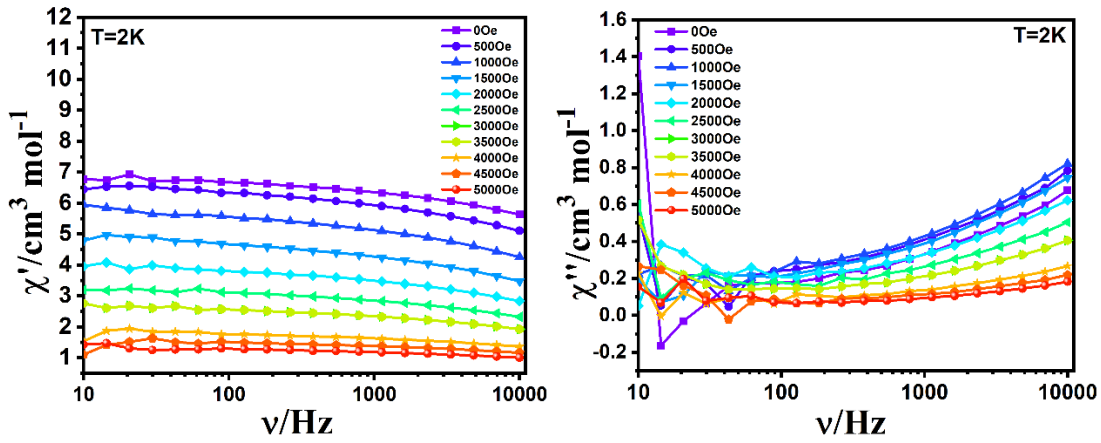

Figure 4.6: Plots of χ' (left) and χ'' (right) vs frequency under applied dc fields from 0 Oe to 5000 Oe at 2 K for $V^{III}_3Dy_2$ **4.2**.

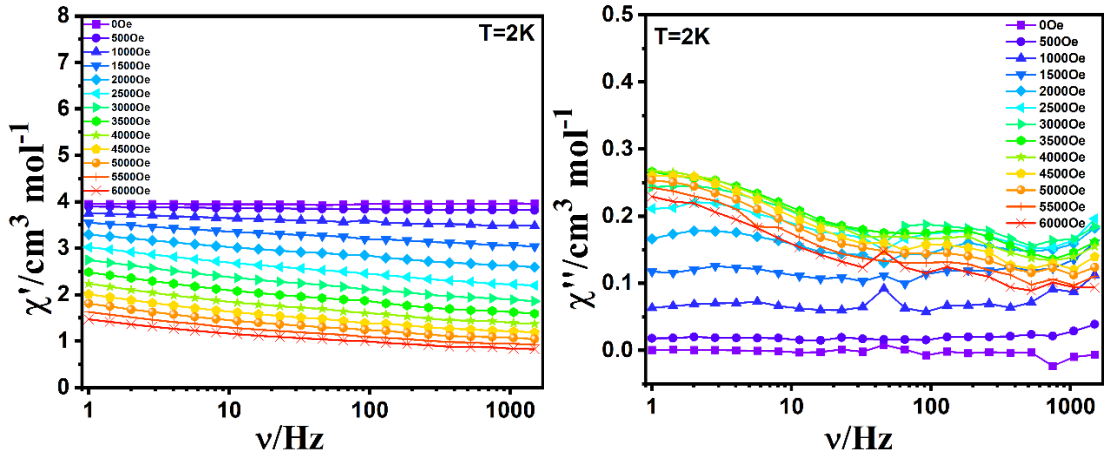

Figure 4.7: Plots of χ' (left) and χ'' (right) vs frequency under applied dc fields from 0 Oe to 5000 Oe at 2 K for $V^{III}_3Er_2$ **4.4.**

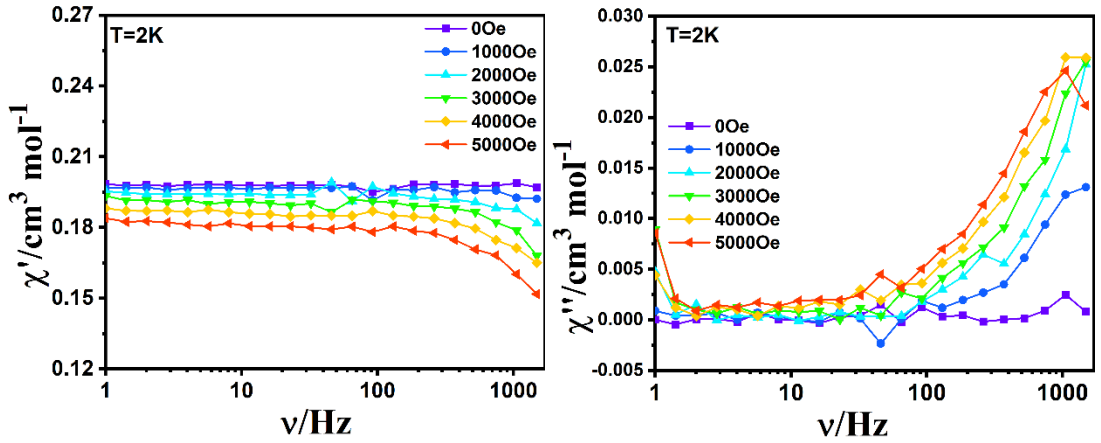

Figure 4.8: Plots of χ' (left) and χ'' (right) vs frequency under applied dc fields from 0 Oe to 5000 Oe at 2 K for $V^{III}_3Y_2$ **4.6**.

4.2.1.3 Crystal Structure of $[V^{III}_3Ln_2(\mu_3\text{-}OH)(tea)_4(piv)_6]\cdot xMeCN\ yCH_2Cl_2$ (Ln = Tb - Tm) (4.7 - 4.11)

These complexes **4.7 - 4.11** are isomorphous and the molecular structures are identical to the previously described compounds with the exception that the p-Me-$PhCO_2^-$ ligands are replaced by pivalates. $V^{III}_3Dy_2$ **4.8** crystallizes in the triclinic space group *P*-1 (No. 2) with Z = 2. The asymmetric unit contains three V^{III} ions, two Dy^{III} ions, four triply deprotonated $teaH_3$ ligands, six deprotonated pivalates, one μ_3-OH and one MeCN molecule (Figure **4.9**). The V^{III}-O distances range from 1.947(2) to 2.054(2) Å. Each Dy ion is found to be eight-coordinate with the Dy−N/O bond distances varying from 2.271(2) to 2.594(3) Å. The Dy···Dy distance is 5.650 Å. The $V^{III}\cdots V^{III}$ distances vary from 3.491 to 5.423 Å, while the intramolecular $Dy\cdots V^{III}$ distances vary from 3.427 to 5.579 Å. The phase purity of these samples of $V^{III}_3Dy_2$ **4.8**, $V^{III}_3Ho_2$ **4.9** and $V^{III}_3Er_2$ **4.10** was checked using powder XRD analysis (Figure **4.10**).

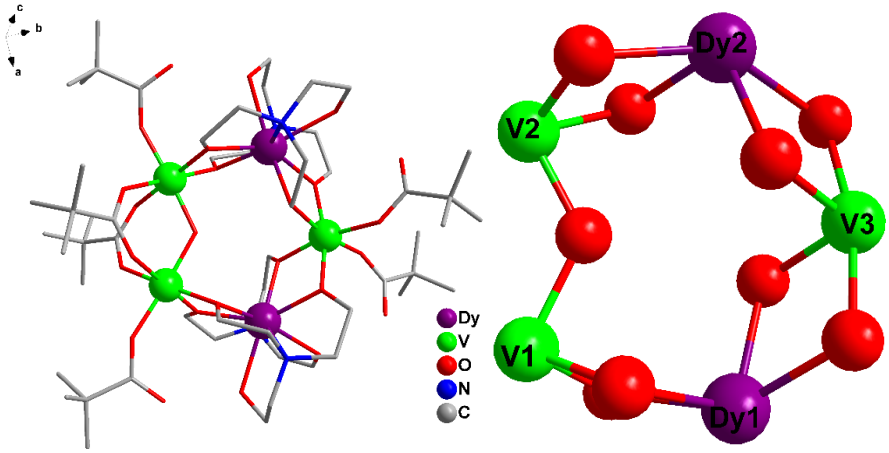

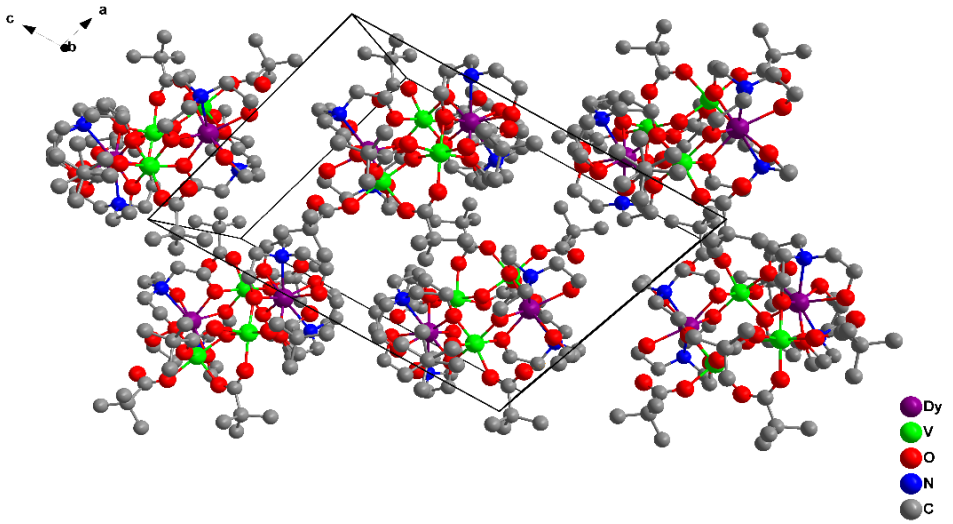

Figure 4.9: The molecular structure of $V^{III}_3Dy_2$ **4.8** (top left). The core of complex $V^{III}_3Dy_2$ **4.8** (top right). The crystal packing of complex $V^{III}_3Dy_2$ **4.8** (bottom).

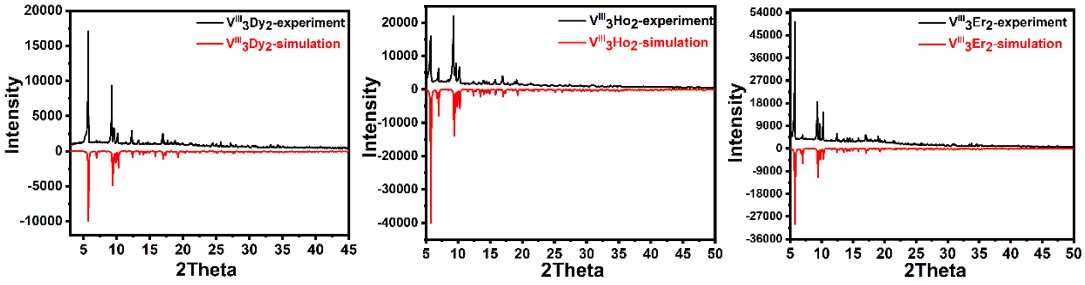

Figure 4.10: The PXRDs diffractograms of $V^{III}_3Dy_2$ **4.8**, $V^{III}_3Ho_2$ **4.9** and $V^{III}_3Er_2$ **4.10**.

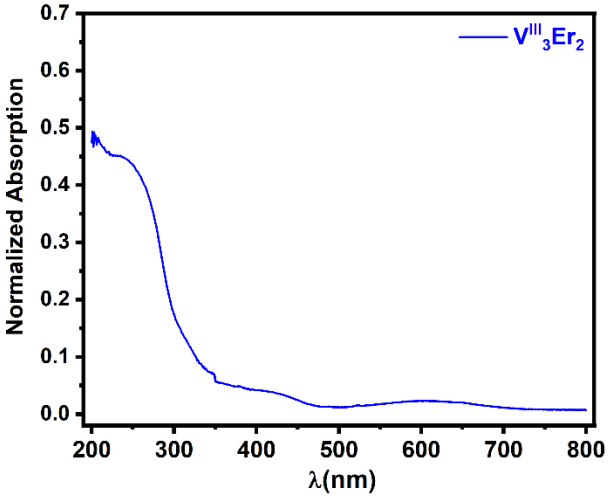

Figure 4.11: The solid state UV/Vis spectrum of $V^{III}_3Er_2$ **4.10**.

4.2.1.4 Magnetic properties of $V^{III}_3Dy_2$ 4.8.

Dc magnetic susceptibility studies of $V^{III}_3Dy_2$ **4.8** were carried out under an applied magnetic field of 1000 Oe over the temperature range 1.8 - 300 K. The $\chi_M T$ versus T plots for $V^{III}_3Dy_2$ **4.8** are shown in Figure **4.12**. The value of $\chi_M T$

at 300 K of 31.73 $cm^3 \cdot K \cdot mol^{-1}$ for $V^{III}_3Dy_2$ **4.8** is in good agreement with the expected value (31.34 $cm^3 \cdot K \cdot mol^{-1}$) for three non-interacting V^{III} ions with S = 1, g = 2, and C = 1.000 $cm^3 \cdot K \cdot mol^{-1}$ and two Dy^{III} ions (S = 5/2, L = 5, $^6H_{15/2}$, g = 4/3, and C = 14.17 $cm^3 \cdot K \cdot mol^{-1}$). There is a continuous decrease in the $\chi_M T$ value on lowering the temperature, reaching a minimum value for $\chi_M T$ of 21.86 $cm^3 \cdot K \cdot mol^{-1}$ at 2 K. This type of behavior could suggest the presence of intramolecular antiferromagnetic interactions.

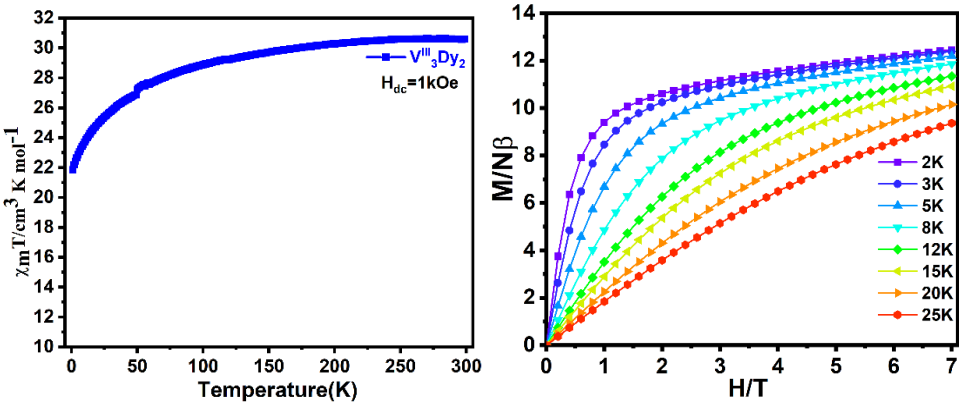

Figure 4.12: The plots of $\chi_M T$ vs T and M vs H for $V^{III}_3Dy_2$ **4.8**.

To probe slow magnetization relaxation, ac susceptibility measurements were performed at different applied fields for $V^{III}_3Dy_2$ **4.8**. No out-of-phase signals (χ") were observed (Figure **4.13 – 4.14**), indicating the absence of SMM behavior. Applying dc fields did not alter the observed behavior.

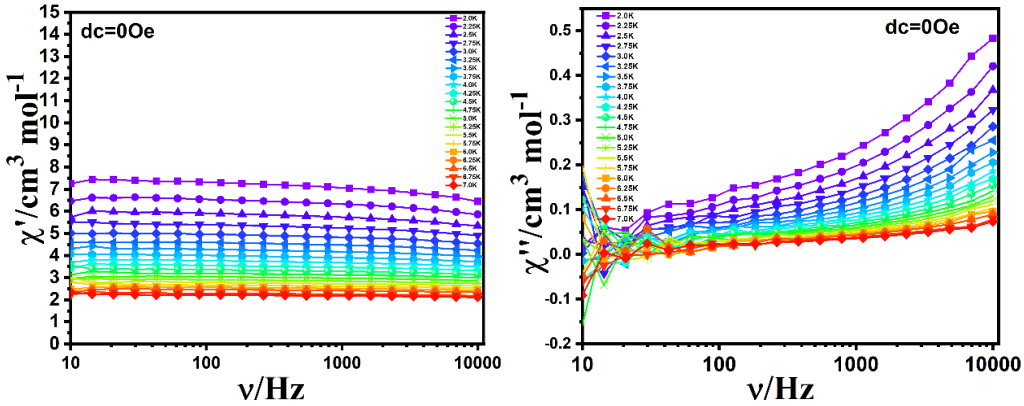

Figure 4.13: Plots of χ' (left) and χ" (right) vs frequency from 2 K -7 K under zero field for $V^{III}_3Dy_2$ **4.8**.

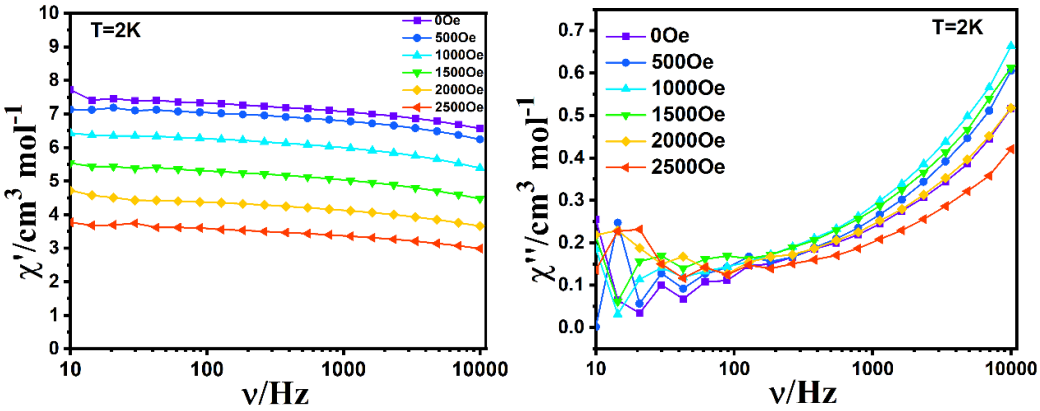

Figure 4.14: Plots of χ' (left) and χ'' (right) vs frequency under applied dc fields from 0 Oe to 2500 Oe at 2 K for $V^{III}_3Dy_2$ **4.8**.

4.2.2 $V^{III}_4Dy_3$, $V^{III}_4Y_3$, $V^{IV}_4Gd_3$ and $V^{III}_4Gd_5$

4.2.2.1 Crystal Structures of $[V^{III}_4Ln_3(\mu_2\text{-}OMe)_2(teaH)_6(p\text{-}Me\text{-}PhCO_2)_7]\cdot MeOH\ 3MeCN$ (Ln = Dy and Y) (4.12-4.13), $(Et_3NH)[V^{IV}_4Gd_3(O)_3(\mu_3\text{-}O)(\mu_3\text{-}OH)_5(teaH)_3(piv)_6](piv)\cdot MeCN\cdot CH_2Cl_2\cdot H_2O$ (4.14), and $[V^{III}_4Gd_5(\mu_3\text{-}OH)_7(teaH)_4(piv)_{12}]\cdot 4MeCN$ (4.15)

Full structure determination was performed for complexes **4.12-4.13** using SCXRD. $V^{III}_4Dy_3$ **4.12** was found to be isomorphous with $V^{III}_4Y_3$ **4.13**, crystallizing in the triclinic space group *P*-1 (No. 2). Therefore, only $V^{III}_4Dy_3$ **4.12** will be presented here in detail. The asymmetric unit contains four V^{III} ions, three Dy^{III} ions, five doubly deprotonated ligands ($teaH^{2-}$), seven p-Me-$PhCO_2^-$ ions and two doubly bridging MeO^- as shown in Figure **4.15**. Each Dy ion is chelated by two of the $teaH^{2-}$ ligands with the central N atom and three O atoms (derived from the alcohol oxygen groups of $teaH^{2-}$). The two deprotonated arms of each $teaH^{2-}$ ligand also provide μ_2-O bridging to the neighboring V^{III} ions. All Dy^{III} ions adopt an O_6N_2 coordination environment which can be best described as a biaugmented trigonal prism J50 geometry. The V^{III} ions have distorted six-coordinate O_6 octahedral environments. In this system, the $Dy^{III}\cdots Dy^{III}$ distances are 6.043 to 7.538 Å and the $Dy^{III}\cdots V^{III}$ distances vary from 3.098 to 7.628 Å.

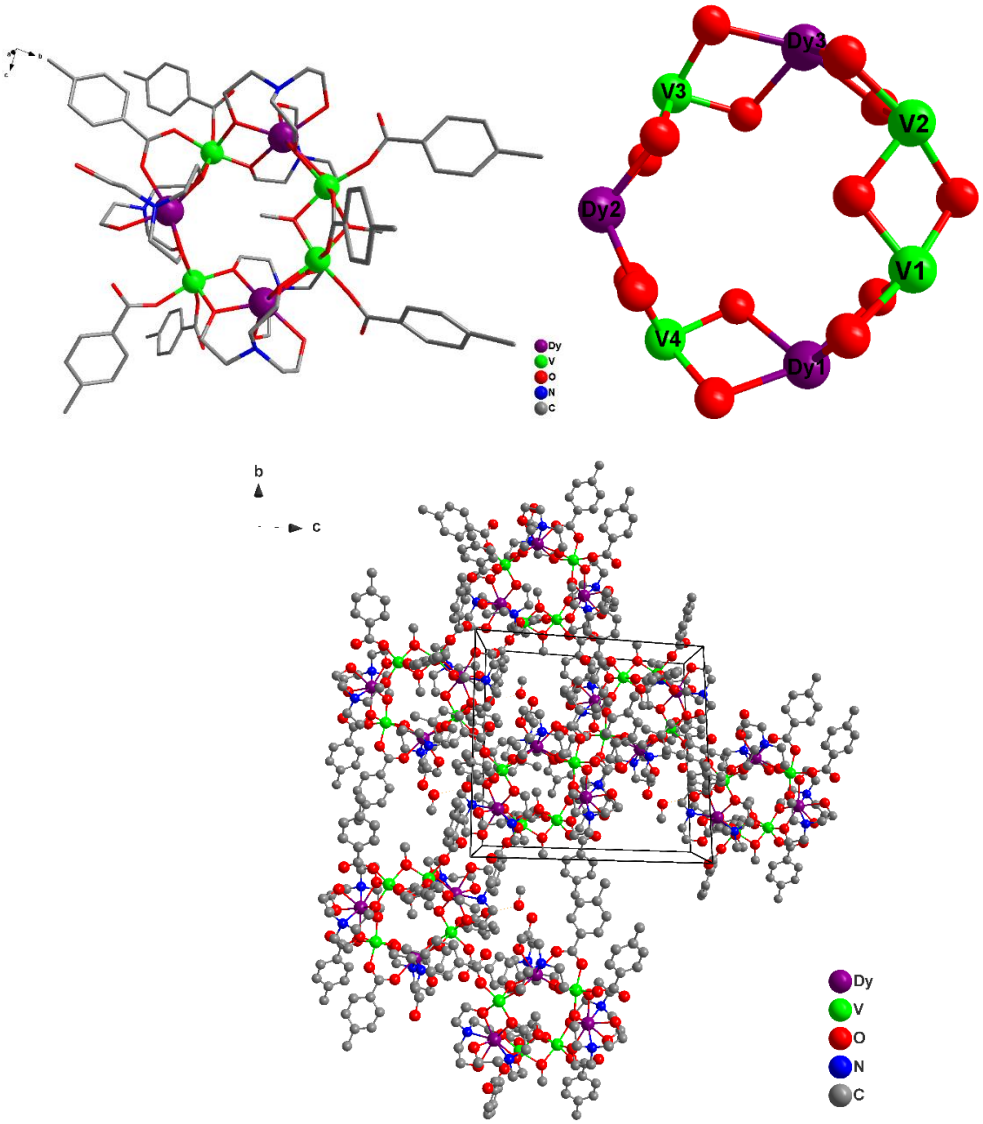

Figure 4.15: The molecular structure of $V^{III}_4Dy_3$ **4.12** (top left). The core of $V^{III}_4Dy_3$ **4.12** (top right). The crystal packing of $V^{III}_4Dy_3$ **4.12** (bottom).

Complex $V^{IV}_4Gd_3$ **4.14** crystallizes in the monoclinic space group $P2_1/c$ (No. 14). Unusually, the asymmetric unit contains one neutral cluster molecule, one triethylammonium cation, one uncoordinated pivalate anion as well as a mixture of lattice solvent molecules. As shown in Figure **4.16**, each ligand of $teaH^{2-}$ is coordinated to the Gd^{III} ion through the central N atom and three O atoms and the two deprotonated alcohol arms of $teaH^{2-}$ provide bridging to two neighboring vanadyl V^{IV} ions. All Gd^{III} ions adopt an O_8N coordination environment which can be best described as a spherical capped square antiprism geometry. The V^{IV}=O bond lengths of the three vanadyl ions V1, V2 and V3 are 1.590(4),

1.602(4) and 1.604(4) Å, respectively. The central V^{IV} ion V4 has its vanadyl oxygen coordinated to a Gd ion resulting in a longer V^{IV}=O bond length of 1.670(4) Å. The remaining V^{IV}-O bond lengths are in the range 1.918(4) to 2.066(3) Å. In this system, the $Gd^{III} \cdots Gd^{III}$ distances are 4.073 to 4.099 Å. The average $V^{IV} \cdots V^{IV}$ distance is 6.067 Å. The PXRD pattern of $V^{IV}_4Gd_3$ **4.14** is shown in Figure **4.17**.

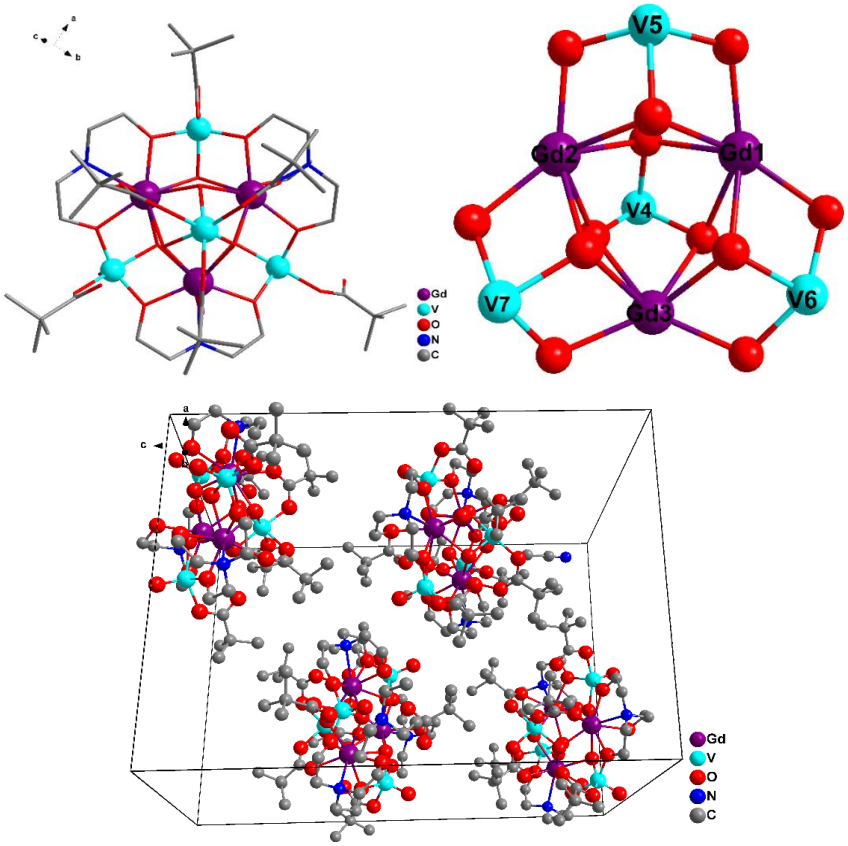

Figure 4.16: The molecular structures of $V^{IV}_4Gd_3$ **4.14** (top left). the core of complex $V^{IV}_4Gd_3$ **4.14** (top right).

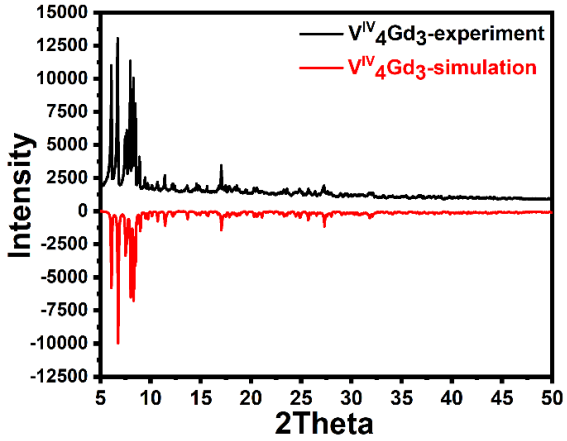

Figure 4.17: The PXRD for $V^{IV}_4Gd_3$ **4.14**.

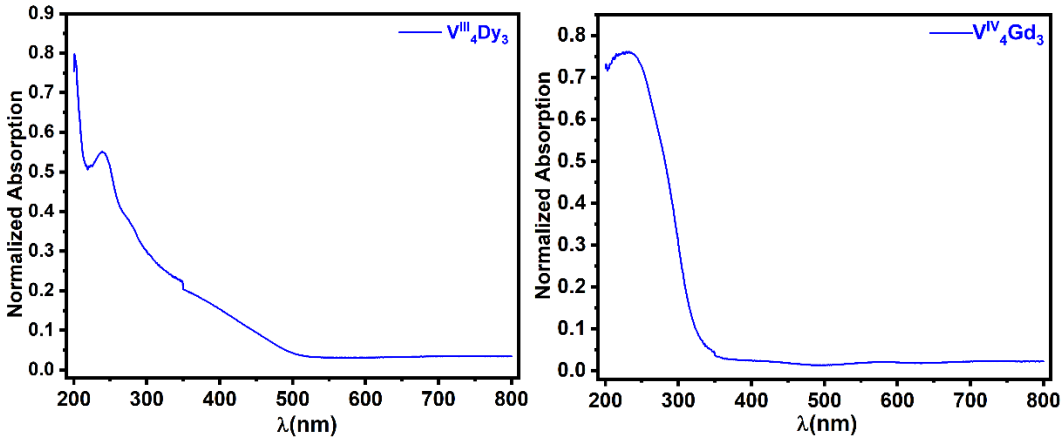

Figure 4.18: The solid-state UV/Vis spectrum of $V^{III}_4Dy_3$ **4.12** and $V^{IV}_4Gd_3$ **4.14**.

As shown in Figure **4.19**, In the complex $V^{III}_4Gd_5$ **4.15** each of the V^{III} ions is chelated by a $teaH^{2-}$ ligand through its nitrogen and two deprotonated ethanol arms, with the remaining ethanol arm not coordinated. The molecular structure of **4.15** is related to those of the $V^{III}_4Gd_4$ square-in-square complexes, however in **4.15** one of the four V^{III} corners (V4) of the square-in-square has been bent out of the V_4Gd_4 mean plane, so that the two deprotonated alkoxy oxygens of its $teaH^{2-}$ ligand bridge to the two Gd ions on the far side of the Gd_4 square. The fifth Gd (Gd5) is bridged to the back of this out-of-plane VGd_2 triangle by three $(\mu_3\text{-}OH)^-$ bridges.

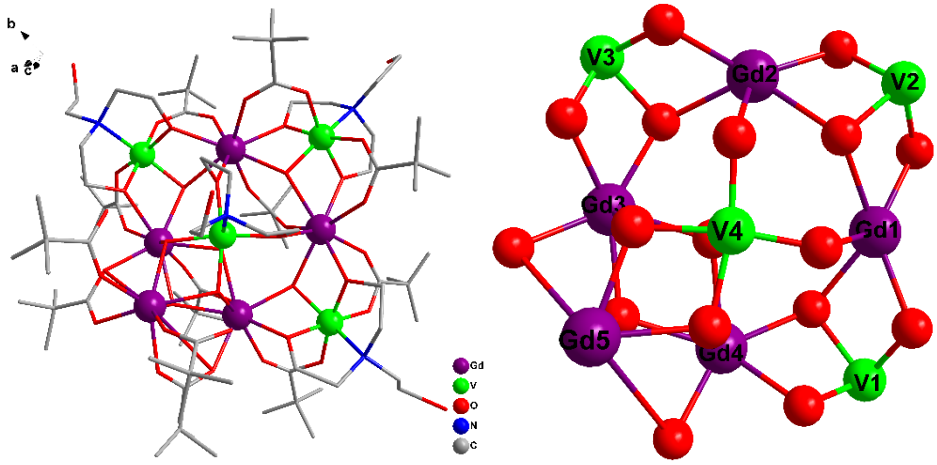

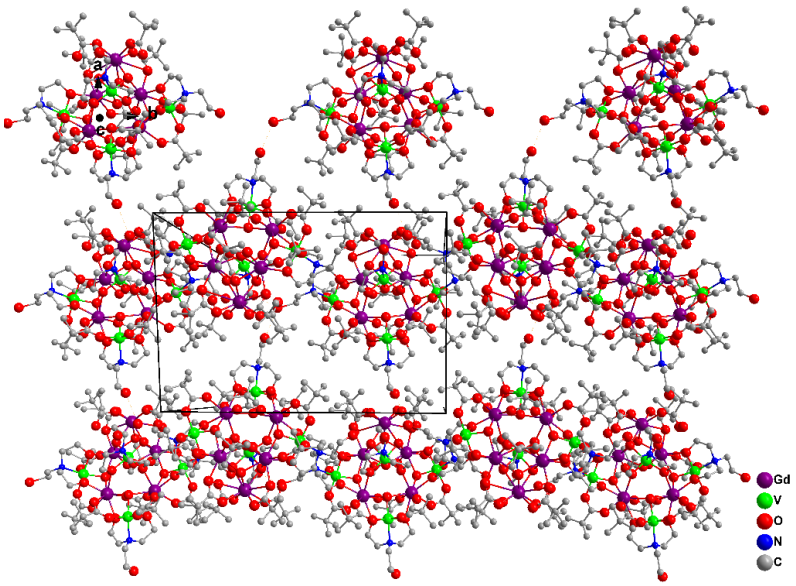

Figure 4.19: The molecular structure of $V^{III}_4Gd_5$ **4.15** (top left). The core of complex $V^{III}_4Gd_5$ **4.15** (top right). The crystal packing of complex $V^{III}_4Gd_5$ **4.15** (bottom).

7.3.4 Synthesis of $[V^{III}_3V^{IV}Dy^{III}_5(\mu_3\text{-}OH)_7(\mu_2\text{-}O)_2(^tBuDea)_3(piv)_{12}]\cdot 4MeCN$ (2.10)

A mixture of N-*tert*-butyldiethanolamine (483 mg, 3.3 mmol) was added to a solution of VCl_3 (314 mg, 0.5 mmol), $DyCl_3$ $6H_2O$ (566 mg, 1.5 mmol), and pivalic acid (400 mg, 3.9mmol) in mixture of MeOH and MeCN (10 mL/10 mL) in a Schlenk tube. After 10 min stirring, Et_3N (1 mL) was added, and the solution stirred for a further 24 h. The solution was then filtered under anhydrous and oxygen-free conditions and left undisturbed for crystallization. Yield: 42% (381.6 mg, based on Dy). Anal. Calc (found)% for $V^{III}_4Dy_5C_{84}H_{164}N_3O_{40}$ $4CH_3CN$: C, 36.39 (36.30); H, 5.84 (5.81); N, 3.22 (3.20). Selected IR data (KBr, cm^{-1}): 2961 (w), 2927 (w), 2868 (w), 1562 (s), 1482 (m), 1419 (m), 1376 (m), 1360 (m), 1329 (w), 1225 (w), 1102 (w), 601 (w), 502 (w).

4.2.2.2 Magnetic properties of complex $V^{III}_4Dy_3$ 4.12.

Dc magnetic susceptibility studies of $V^{III}_4Dy_3$ **4.12** were carried out under an applied magnetic field of 1000 Oe over the temperature range 1.8-300 K. The

$\chi_M T$ versus T plots are shown in Figure **4.20** and the $\chi_M T$ value at 300 K of 46.38 $cm^3 \cdot K \cdot mol^{-1}$ for $V^{III}_4Dy_3$ **4.12** is in excellent agreement with the expected value (46.51 $cm^3 \cdot K \cdot mol^{-1}$) for four non-interacting V^{III} ions with S = 1, g = 2, and C = 1.000 $cm^3 \cdot K \cdot mol^{-1}$ and three Dy^{III} ions (S = 5/2, L = 5, $^6H_{15/2}$, g = 4/3, and C = 14.17 $cm^3 \cdot K \cdot mol^{-1}$). Upon cooling, $\chi_M T$ decreases slightly until 40 K, followed by a rapid decrease to 2 K reaching a value of 30.64 $cm^3 \cdot K \cdot mol^{-1}$. This type of behavior suggests the possible presence of intramolecular antiferromagnetic interactions, although the decrease of the $\chi_M T$ values could also be ascribed to thermal depopulation of the excited sub-levels of the Dy^{III} ions. Furthermore, field-dependent magnetization measurements were performed (Figure **4.20**). The molar magnetization at 2 K reaches a value of 19.88 Nβ at 7 T. The theoretical saturation value for three Dy^{III} ions and four V^{III} ions is larger than the experimental observation. This, along with the decrease in the $\chi_M T$ value at low temperatures, could suggest the presence of low-lying excited states.

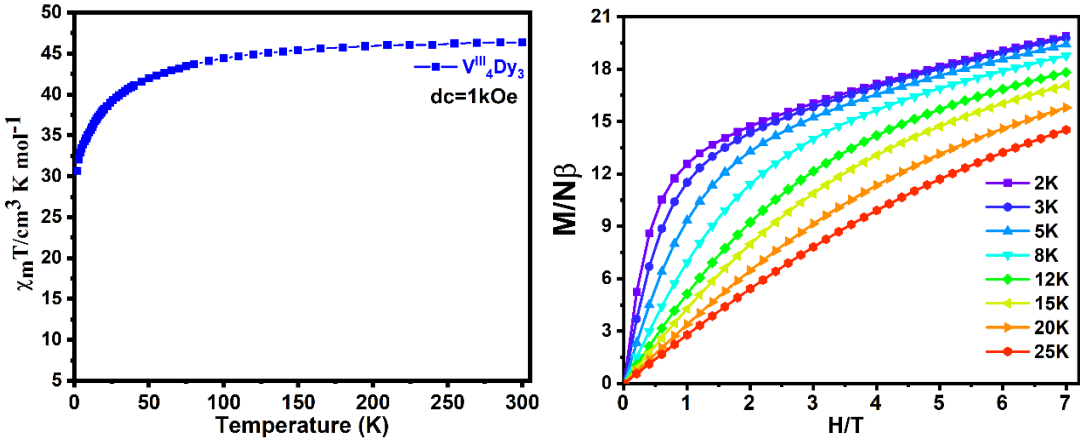

Figure 4.20: The plots of $\chi_M T$ vs T for $V^{III}_4Dy_3$ **4.12** and the plots of M vs H for $V^{III}_4Dy_3$ **4.12**.

To explore potential SMM behavior ac magnetic susceptibility studies were carried out on freshly filtered samples of $V^{III}_4Dy_3$ **4.12**. Under zero applied dc field, as indicated in Figure **4.21**, no obvious temperature dependent ac signals are detected, indicating that no slow relaxation of magnetization can be observed in the measuring frequency window. Applying a dc field did not improve the observed signals (Figure **4.22**).

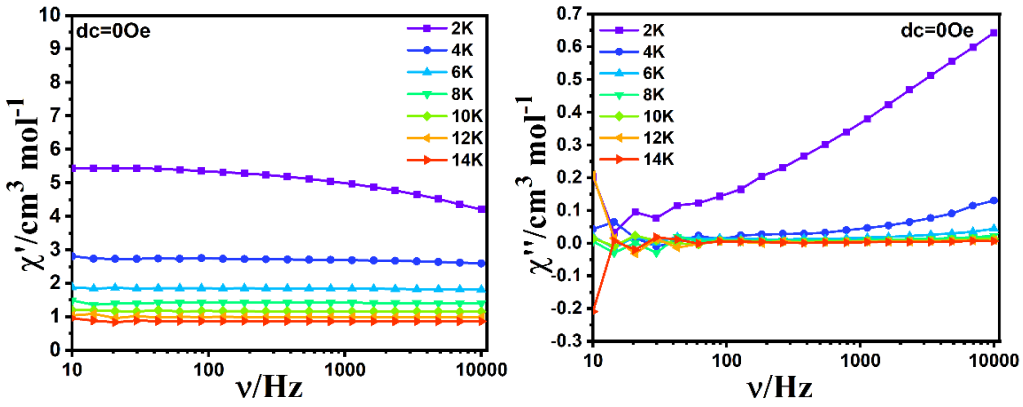

Figure 4.21: Plots of χ' (left) and χ'' (right) vs frequency from 2 K -14 K under zero field for $V^{III}_4Dy_3$ **4.12**.

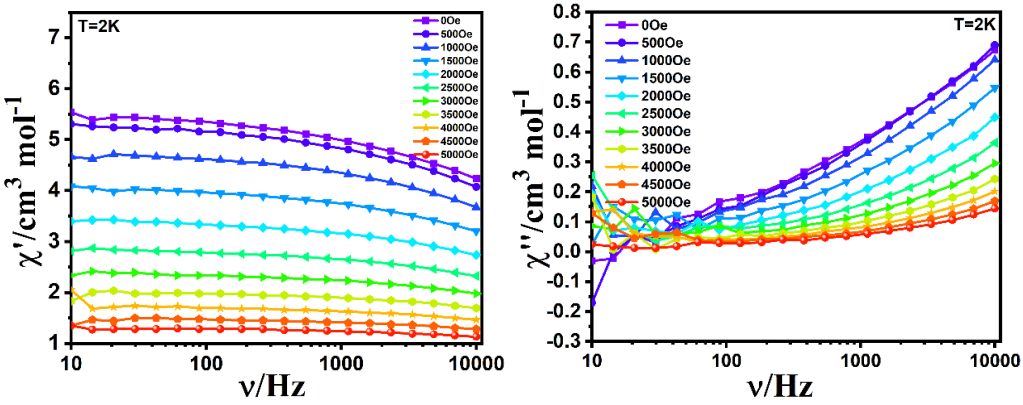

Figure 4.22: Plots of χ' (left) and χ'' (right) vs frequency under applied dc fields from 0 Oe to 5000 Oe at 2 K for $V^{III}_4Dy_3$ **4.12**.

4.2.3 $V^{IV}_4V^{III}Dy_6$, $V^{III}_2V^{IV}_4Dy_4$ and $V^{IV}_6Dy_4$

4.2.3.1 Crystal Structure of $[V^{IV}_4V^{III}Dy_6(\mu_4\text{-}O)_4(\mu_2\text{-}O)_4(\mu_3\text{-}OH)_4(Bu^tDea)_4(NCCH_2COO)_8(MeOH)_6]Cl\cdot 8MeCN$ (4.16)

The undecanuclear complex $V^{IV}_4V^{III}Dy_6$ **4.16** was characterized using SC-XRD and crystallizes in the monoclinic space group $P2_1/c$ (No. 14). As shown in Figure **4.23**, the molecules of complex $V^{IV}_4V^{III}Dy^{III}_6$ **4.16** consist of four V^{IV} ions, one V^{III} ion, six Dy^{III} ions, four Bu^tDea^{2-} ligands, eight deprotonated cyanoacetic acids and six methanol ligands. The core of the compound $V^{IV}_4V^{III}Dy_6$ **4.16** is a undecanuclear cluster formed by the five V^{III}/V^{IV} ions and six Dy^{III} ions, held together by oxo, hydroxo, bridging alkoxy and cyanoacetate ligands.

Each ligand of Bu^tDea^{2-} is coordinated to a V^{IV} ion through its O and N atoms

and the two deprotonated alcohol arms of the ligand provide μ_2-O bridging to the neighboring Dy^{III} ions. The central V^{III} ion is sandwiched by two Dy^{III}_3 triangles in a similar fashion to the $Cr^{III}Dy_6$ of Murray *et al.*.[224] The four vanadyl (V^{IV}=O) ions are each chelated by a doubly deprotonated Bu^tDea^{2-} and are arranged to either side of this core motif. The vanadyl oxygens are each also coordinated to a Dy ion and the V=O bond lengths, 1.649(6) and 1.651(6) Å are therefore longer than free V=O bonds. Each Dy^{III} ion is coordinated by eight oxygen donors. Using SHAPE 2.1 analysis, the geometry around the Dy ions is best described as a snub disphenoid J84 with the Dy^{III}–O bond distances varying from 2.299(6) to 2.473(7) Å.

The V^{III} ion has a distorted octahedral O_6 donor set composed of two μ_3-OH^- and four μ_4-O^{2-} ligands with an average V^{III}–O bond length of 1.968 Å. The V^{IV} ions are each five-coordinated with a distorted square pyramidal geometry in which the vanadyl oxygen occupies the apical position. Furthermore, the nearest intramolecular distances between Dy^{III} ions were found to be 3.725 Å and the closest intramolecular $V^{III}\cdots V^{IV}$ distance is 3.566 Å.

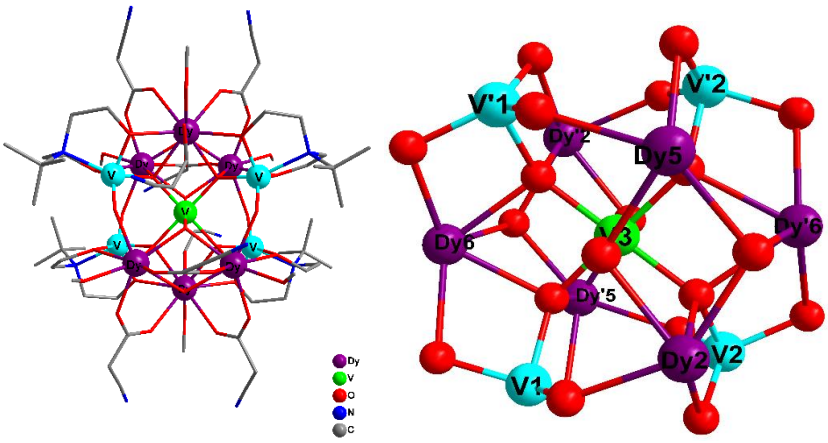

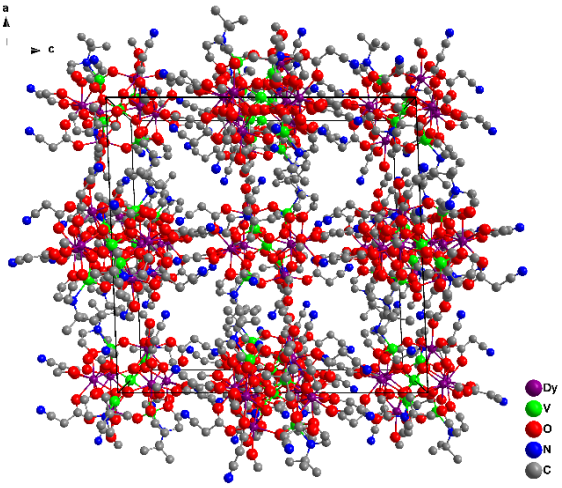

Figure 4.23: The molecular structures of complex, $V^{IV}_4V^{III}Dy_6$ **4.16** (top left). The core of complex $V^{IV}_4V^{III}Dy_6$ **4.16** (top right). The crystal packing of complex $V^{IV}_4V^{III}Dy_6$ **4.16** (bottom).

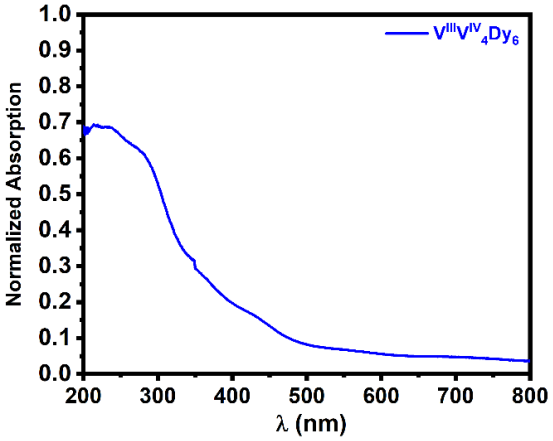

Figure 4.24: Solid state UV/Vis spectrum from 200-800 nm wavenumber for $V^{IV}_4V^{III}Dy_6$ **4.16**.

4.2.3 2 Magnetic properties of complex $V^{IV}_4V^{III}Dy_6$ 4.16.

Dc magnetic susceptibility measurements of $V^{IV}_4V^{III}Dy_6$ **4.16** were carried out on a polycrystalline sample under an applied magnetic field of 1000 Oe at T = 1.8 - 300 K. As shown in Figure **4.25**, the $\chi_M T$ value at 300 K of 87.21 $cm^3 \cdot K \cdot mol^{-1}$ for $V^{IV}_4V^{III}Dy_6$ **4.16** in good agreement with the expected value (87.52 $cm^3 \cdot K \cdot mol^{-1}$) for four non-interacting V^{IV} ions with (S = 1/2, g = 2, and C = 0.375 $cm^3 \cdot K \cdot mol^{-1}$), one V^{III} ion with (S = 1, g = 2, and C = 1.000 $cm^3 \cdot K \cdot mol^{-1}$) and six Dy^{III} ions (S = 5/2, L = 5, $^6H_{15/2}$, g = 4/3, and C = 14.17 $cm^3 \cdot K \cdot mol^{-1}$). The $\chi_M T$ value decreases on lowering the temperature to 73.12 $cm^3 \cdot K \cdot mol^{-1}$ at 12 K followed by an increase to 86.22 $cm^3 \cdot K \cdot mol^{-1}$ at 3 K before a final decrease to 81.90 $cm^3 \cdot K \cdot mol^{-1}$.

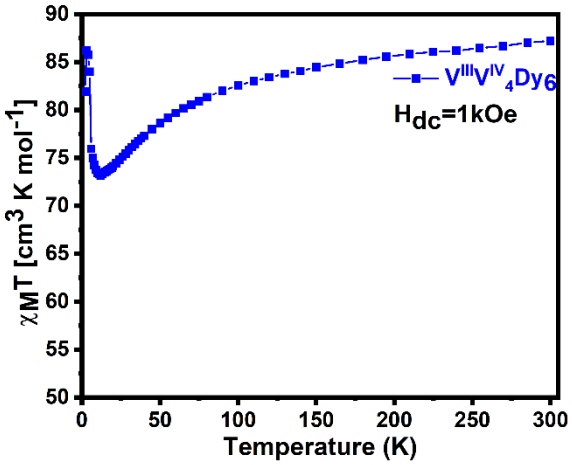

Figure 4.25: The plot of $\chi_M T$ vs T for $V^{IV}_4V^{III}Dy_6$ **4.16**.

To check for any slow relaxation of the magnetization in $V^{IV}_4V^{III}Dy_6$ **4.16**, variable-frequency (1–1700 Hz) ac magnetic measurements were carried out under a 3.5 Oe oscillating field with applied fields in the range 0 – 2000 Oe. No clear out-of-phase signal (χ") was observed as shown in Figure **4.26**. These results indicate the absence of SMM behavior of $V^{IV}_4V^{III}Dy_6$ **4.16**.

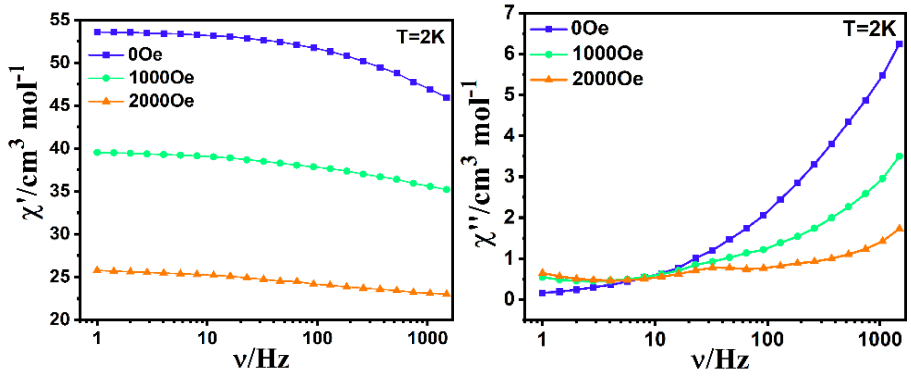

Figure 4.26: Plots of χ' (left) and χ" (right) vs frequency with applied dc fields in the range from 0 Oe to 2000 Oe at 2 K for $V^{IV}_4V^{III}Dy_6$ **4.16**.

4.2.4 $V^{III}_2V^{IV}_4Dy_4$ and $V^{IV}_6Dy_4$

4.2.4 1 Crystal Structure of $[V^{III}_2V^{IV}_4Dy_4(\mu_2\text{-}O)_4(\mu_3\text{-}OH)_2(\mu_2\text{-}OMe)_2(\mu\text{-}N_3)(\mu\text{-}Cl)(mDea)_2(mDeaH)(piv)_{14}(H_2O)_4]^{3+}$ (4.17) and $[(V^{IV}{=}O)_4\{V^{V}O_3(OMe)\}_2Dy_4(\mu_4\text{-}O)_2(\mu_2\text{-}OMe)_4(OMe)_2(MeOH)_2(teaH)_2(piv)_4]$ (4.18)

Two complexes (**4.17** and **4.18**) were measured using SC-XRD. The crystal data results indicate the two compounds crystallize in the same of monoclinic space group $P2_1/c$ (No. 14).

As shown in Figure **4.27**, the core of $V^{III}_2V^{IV}_4Dy_4$ **4.17** consists of V^{IV}_4/V^{III}_2 ions, four Dy^{III} ions. In addition the molecule is completed by two $mDea^{2-}$, one $mDeaH^-$, fourteen pivalates, two μ_3-OMe^-, four μ_2-O^{2-}, two μ_3-O^{2-}, two OH^- and two bridges which are a disordered mixture of N_3^- and Cl^-. There are eleven lattice MeCN molecules per cluster and three N_3/Cl counterions balancing the charge. In the structure of $V^{III}_2V^{IV}_4Dy_4$ **4.17**, the two $mDea^{2-}$ ligands are coordinated to the V^{III} and furthermore bridged to the Dy ions in similar manner as seen for other 3d-4f compounds. The $mDeaH^-$ ligand forms a strap across the two V^{IV}_2 units. The protonated N atom in the middle of this ligand does not coordinate. The coordination environments of the four Dy^{III} ions are identical, all of which are bridged to each other through O/N atoms. As shown in Figure **4.27**, vanadium ions of different valence states have different coordination environments.

The geometry around the eight-coordinated Dy^{III} atom of $V^{III}_2V^{IV}_4Dy_4$ **4.17** is best described as a distorted biaugmented trigonal prism with an O_7N donor set using SHAPE 2.1 analysis with the Dy^{III}–O bond distances varying from 2.223(5) to 2.469(3) Å. The V^{III} ions have distorted octahedral geometry with V^{III}–O/N bond lengths varying from 1.919(6) to 2.162(6) Å. All V^{IV} ions adopt an O_6 coordination environment which can be best described as distorted octahedral geometry with V^{IV}–O bond lengths varying from 1.668(4) to 2.129(5) Å, with one of the bond lengths being much shorter than the others, identifying this as the vanadyl oxygen. Furthermore, such oxygens form μ_2-O bridges to neighboring Dy ions. The two azide bridges are partially disordered with μ_2-Cl ligands.

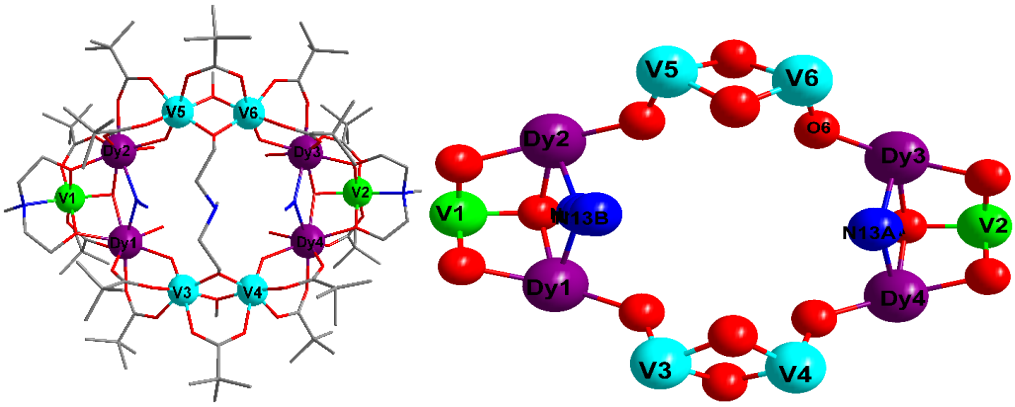

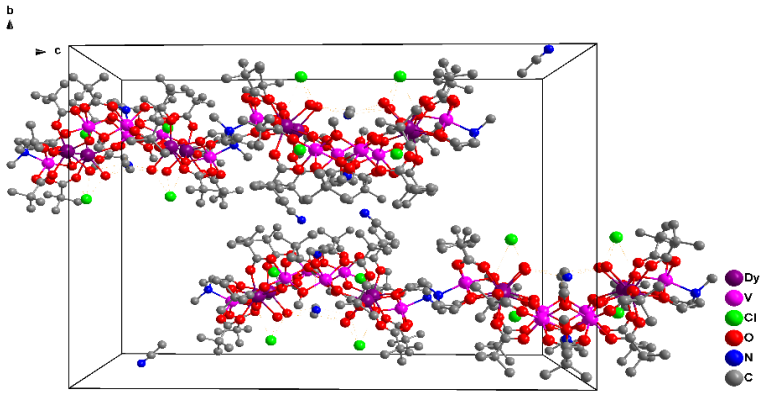

Figure 4.27: The molecular structure of $V^{III}_2V^{IV}_4Dy_4$ **4.17** (top left). The core of complex $V^{III}_2V^{IV}_4Dy_4$ **4.17** (top right). The crystal packing of complex $V^{III}_2V^{IV}_4Dy_4$ **4.17** (bottom).

As illustrated in Figure **4.28**, the core of the complex $V^{IV}_4V^{V}_2Dy_4$ **4.18** is based on a rectangle of Dy^{III} cations. Two opposite pairs of Dy are bridged by $(\mu_4\text{-}O)^{2-}$ bridges, which also coordinate to two V^{IV} centers, such that the geometries about these oxo ligands are distorted tetrahedral. The other two edges are bridged by chelating/bridging pivalates. Each of these four vanadiums can be has a square pyramidal geometry, with non-bridging vanadyl oxygens (V=O 1.591(6) and 1.596(6) Å) in the apical positions. Two of the Dy are chelated by $(teaH)^{2-}$ ligands, with the deprotonated oxygens forming bridges to neighbouring V^{IV} centers. Above and below the Dy_4 rectangle are two capping $\{V^{V}O_3(OMe)\}^{2-}$ units, with the three oxido oxygens bridging to the $Dy_4V^{IV}_4$ unit. This V^{V} center has a tetrahedral geometry, with V-O bond lengths to the three bridging oxo ligands of 1.668(4), 1.669(4) and 1.732(4) Å, and the terminal –OMe having a V-O bond length of 1.785(5) Å. Bond Valence Sum (BVS) calculations assign a valence to the capping V^{V} of 5.14, but the four "V^{IV}" have values of 4.41 and 4.21. It cannot be ruled out that these four vanadiums are better described as $V^{IV}_2V^{V}_2$, with all the terminal methoxy ligands deprotonated.

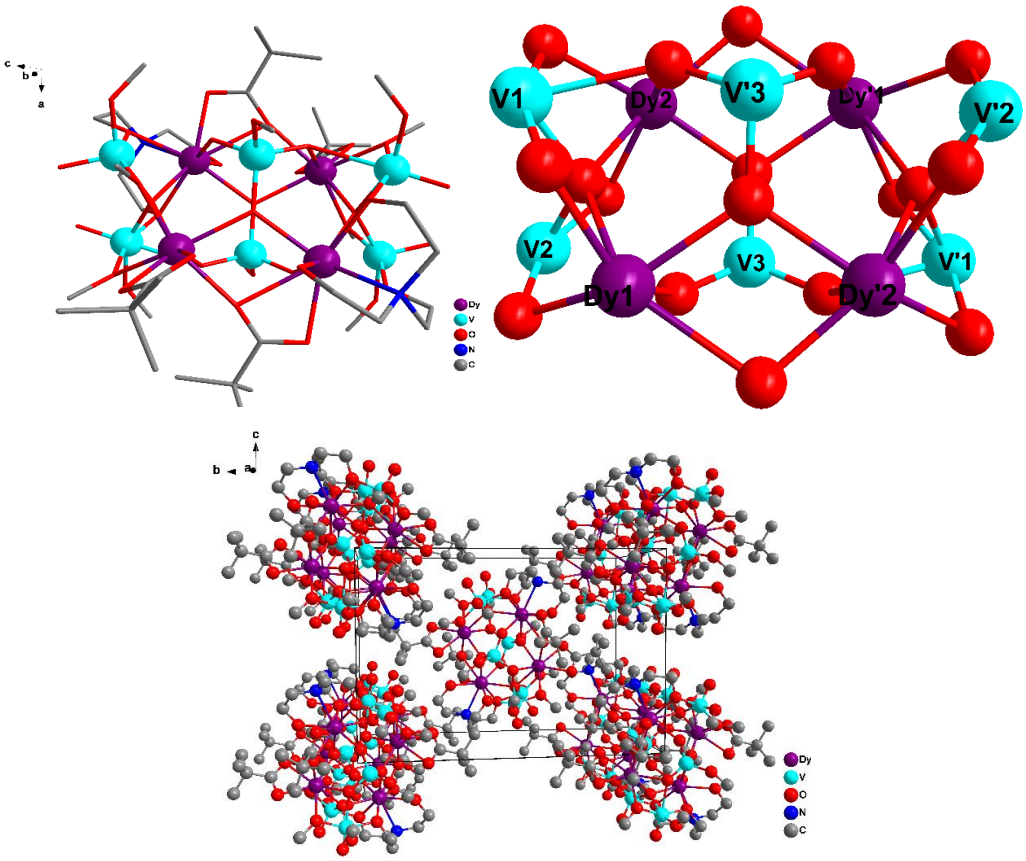

Figure 4.28: The molecular structure of complex, $V^{IV}_6Dy_4$ **4.18** (top left). The core of complex $V^{IV}_6Dy_4$ **4.18** (top right). The crystal packing of complex $V^{IV}_6Dy_4$ **4.18** (bottom).

4.2.5 $V^{III}_4V^{IV}_4Ln_4$ (Ln= Gd, Dy and Y)

4.2.5.1 Crystal Structure of $[V^{III}_4V^{IV}_4Ln_4(\mu_2\text{-}O)_4(mDea)_4(piv)_{18}(N_3)_6]\cdot nCH_2Cl_2$ MeCN (Ln = Gd (4.19), Dy (4.20) and Y (4.21))

The structures of **4.19-4.21** were determined using SC-XRD. All three complexes are isostructural and crystallize in the monoclinic space group $P2_1/c$ (No. 14). The structure of $V^{III}_4V^{IV}_4Dy_4$ **4.20** is used as a representative for all three compounds. The dodecanuclear core structure of $V^{III}_4V^{IV}_4Dy_4$ **4.20** consists of pairs of V^{III} ions linked to one of the Dy ions followed by a link to a pair of V^{IV} ions followed by another Dy ion. This is repeated to give the full cyclic core structure.

Each $mDea^{2-}$ ligand is coordinated to one V^{III} ion through its central N atom with the alkoxy groups chelating to the V^{III} and bridging to the Dy. This is similar

to the butterfly motif but in this case with the four bridging pivalates exclusively on the outside of the cycle. Additionally, the V^{III} pairs are connected by an azide bridge. The V^{IV} pairs are bridged by two azides as well as a pivalate. The connection to the neighboring Dy is via two pivalates and one μ_2-OH.

In this compound, the different valence vanadium ions have different coordination environments. The V^{III} ions have a distorted octahedral N_2O_4 environment provided by the central N atom of the $mDea^{2-}$ and an N from the azide bridge plus the oxygen atom provided by the $mDea^{2-}$ as well as the pivalate bridges. For the tetravalent V^{IV} ions the distorted octahedral N_2O_4 coordination is provided by two bridging azides, three bridging pivalates and one μ_2-vanadyl-O. Each Dy^{III} ion is eight-coordinate with a bicapped trigonal prism geometry using a SHAPE 2.1 analysis. The average Dy^{III}–O bond length is 2.317 Å. The Dy···Dy, Dy···V and the closest V···V distance are 5.622, 3.401, 3.494 Å, respectively.

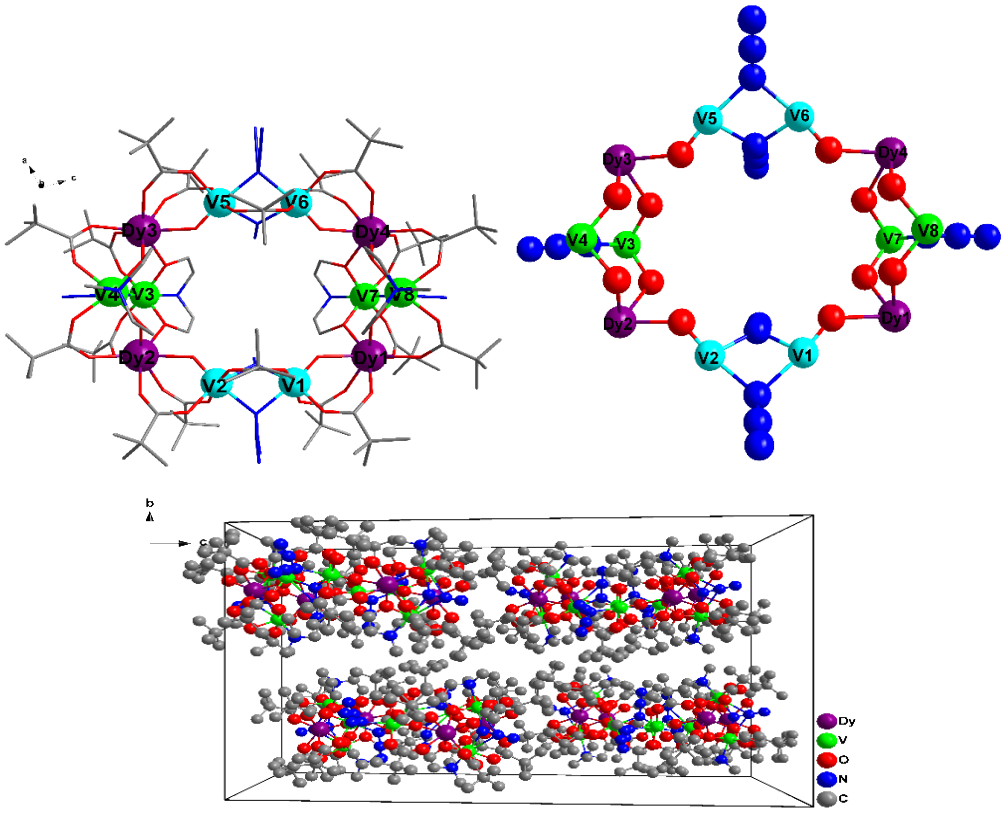

Figure 4.29: The molecular structure of $V^{III}_4V^{IV}_4Dy_4$ **4.20** (top left). the core of complex $V^{III}_4V^{IV}_4Dy_4$ **4.20** (top right). The crystal packing of complex $V^{III}_4V^{IV}_4Dy_4$ **4.20** (bottom).

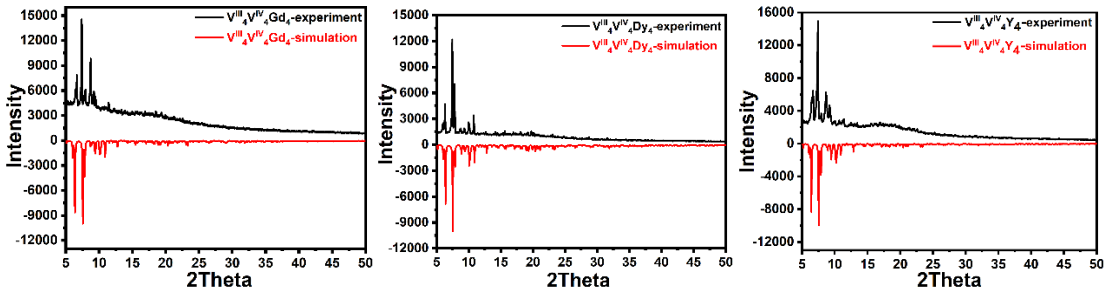

Figure 4.30: The PXRD diffractograms for $V^{III}_4V^{IV}_4Gd_4$ **4.19**, $V^{III}_4V^{IV}_4Dy_4$ **4.20** and $V^{III}_4V^{IV}_4Y_4$ **4.21**.

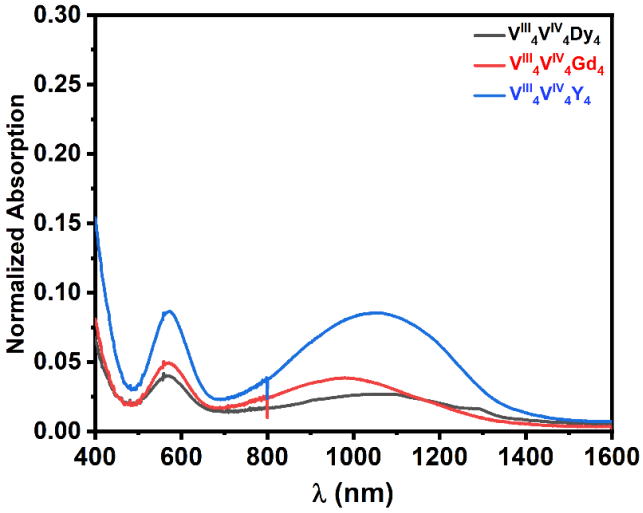

Figure 4.31: The solid-state UV/Vis spectrum for $V^{III}_4V^{IV}_4Gd_4$ **4.19**, $V^{III}_4V^{IV}_4Dy_4$ **4.20** and $V^{III}_4V^{IV}_4Y_4$ **4.21**.

4.2.5 2 Magnetic properties of complex of $V^{III}_4V^{IV}_4Dy_4$ 4.20.

Dc magnetic susceptibility studies of complex $V^{III}_4V^{IV}_4Dy_4$ **4.20** were carried out under an applied magnetic field of 1000 Oe over the temperature range 1.8-300 K. The $\chi_M T$ versus T plots for $V^{III}_4V^{IV}_4Dy_4$ **4.20** are shown in Figure **4.32**. The value of $\chi_M T$ at 300 K of 62.28 $cm^3 \cdot K \cdot mol^{-1}$ for $V^{III}_4V^{IV}_4Dy_4$ **4.20** is in very good agreement with the expected value (62.18 $cm^3 \cdot K \cdot mol^{-1}$) for four non-interacting V^{III} ions (S = 1, g = 2, and C = 1.000 $cm^3 \cdot K \cdot mol^{-1}$), four non-interacting V^{IV} ions (S = 1/2, g = 2, and C = 0.375 $cm^3 \cdot K \cdot mol^{-1}$) and four Dy^{III} ions (S = 5/2, L = 5, $^6H_{15/2}$, g = 4/3, and C = 14.17 $cm^3 \cdot K \cdot mol^{-1}$). As the temperature is decreased, the $\chi_M T$ value remains essentially constant and decreases below 50 K to reach a minimum of 45.62 $cm^3 \cdot K \cdot mol^{-1}$ at 3.0 K. This type of behavior could be the result of depopulation of the excited sub-levels and/or some antiferromagnetic interactions.

As shown in Figure **4.32**, the field dependence of magnetization of $V^{III}_4V^{IV}_4Dy_4$ **4.20** rapidly increases below 1 T and at higher fields at 2 K, increases almost linearly and to reach a maximum value of 30.32 Nβ at 7 T without true saturation, which could indicate the presence of anisotropy in the system.

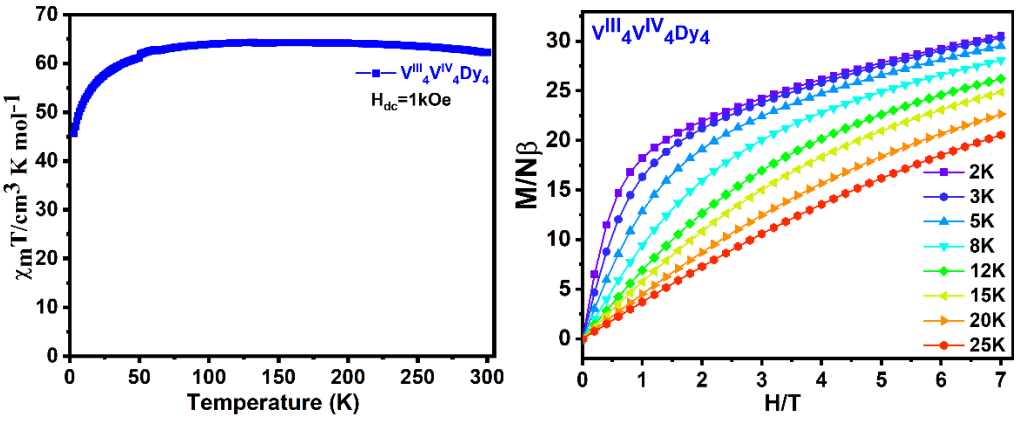

Figure 4.32: The plots of $\chi_M T$ vs T for $V^{III}_4V^{IV}_4Dy_4$ **4.20** (left) and the M vs H plot for $V^{III}_4V^{IV}_4Dy_4$ **4.20** (right).

Ac susceptibility magnetic measurements were carried out under a 3.5 Oe oscillating field at zero applied dc field. As indicated in Figure **4.33**, no out-of-phase signals (χ") could be observed. Applying a dc field did result in observable signals (Figure **4.34**).

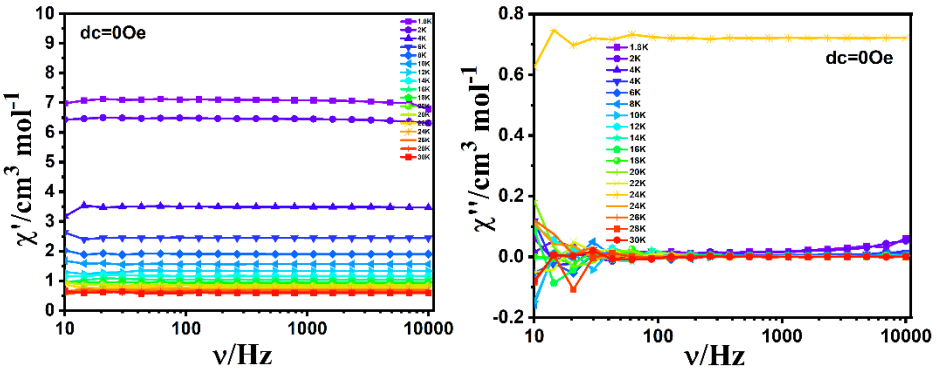

Figure 4.33: Plots of χ' (left) and χ" (right) vs frequency at different temperatures and under zero dc field for $V^{III}_4V^{IV}_4Dy_4$ **4.20**.

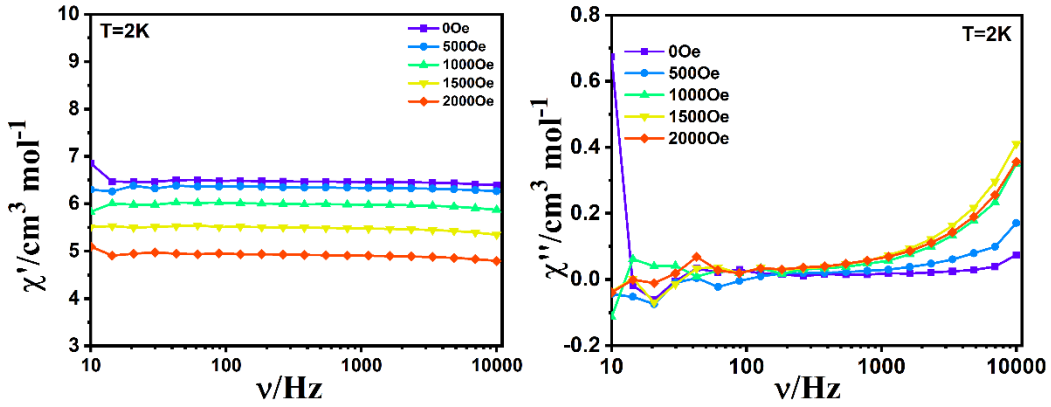

Figure 4.34: Plots of χ' (left) and χ'' (right) vs frequency range with applied dc fields from zero to 2000 Oe at 2 K for $V^{III}_4V^{IV}_4Dy_4$ **4.20**.

4.3 Discussion

In many 3d-4f complexes, there is no obvious correlation between crystal structure and magnetic properties. However, in this chapter, by summarizing the crystal structures and magnetic properties of all the ring-shape V-Ln complexes that have been obtained, it is found that there are obvious rules in the magnetic properties of this type of ring-shape V-Ln complexes, to provide predictable results for subsequent studies on the magnetic properties of similar complexes.

From Figure **4.35**, it can be seen that when the V^{III} and Dy^{III} ions are arranged in a ring-shaped structure in an alternating fashion, the susceptibility at low temperatures is consistent with ferrimagnetism. When there are adjacent V^{III} ions in the ring the magnetic properties are consistent with antiferromagnetic behavior.

To explore the influence on the magnetic properties of varying lanthanide ions in compounds with the same molecular structure as these ring-shaped V-Dy complexes, the dysprosium ions were replaced with Tb^{III}-Yb^{III} or Y^{III} (Figure **4.36**). As shown in Figure **4.36** changing the lanthanide ions affects the magnetic properties of these ring-shape V-Ln complexes. With decreasing ionic lanthanide radius and increasing number of electron pairs the trend in the magnetic interactions is from ferromagnetic to antiferromagnetic. The type **I** $V_2^{III}Dy_2$ butterfly (**2.8**) could not be obtained with other lanthanide ions but is useful to compare to isostructural compounds with different 3d metal ions.[166] Table **4.3** summarizes the relevant magnetic and structural characteristics.

The influence of changing the ligand on the magnetic behavior was also investigated. As shown in Figure **4.37** and **4.38**, the change of the ligand has little effect on the magnetic properties of ring-shape V-Ln complexes. All in all, the factors that affect the change of magnetic properties of ring-shape V-Ln complexes are the arrangement of vanadium ions and lanthanide ions and the metal- metal distances.

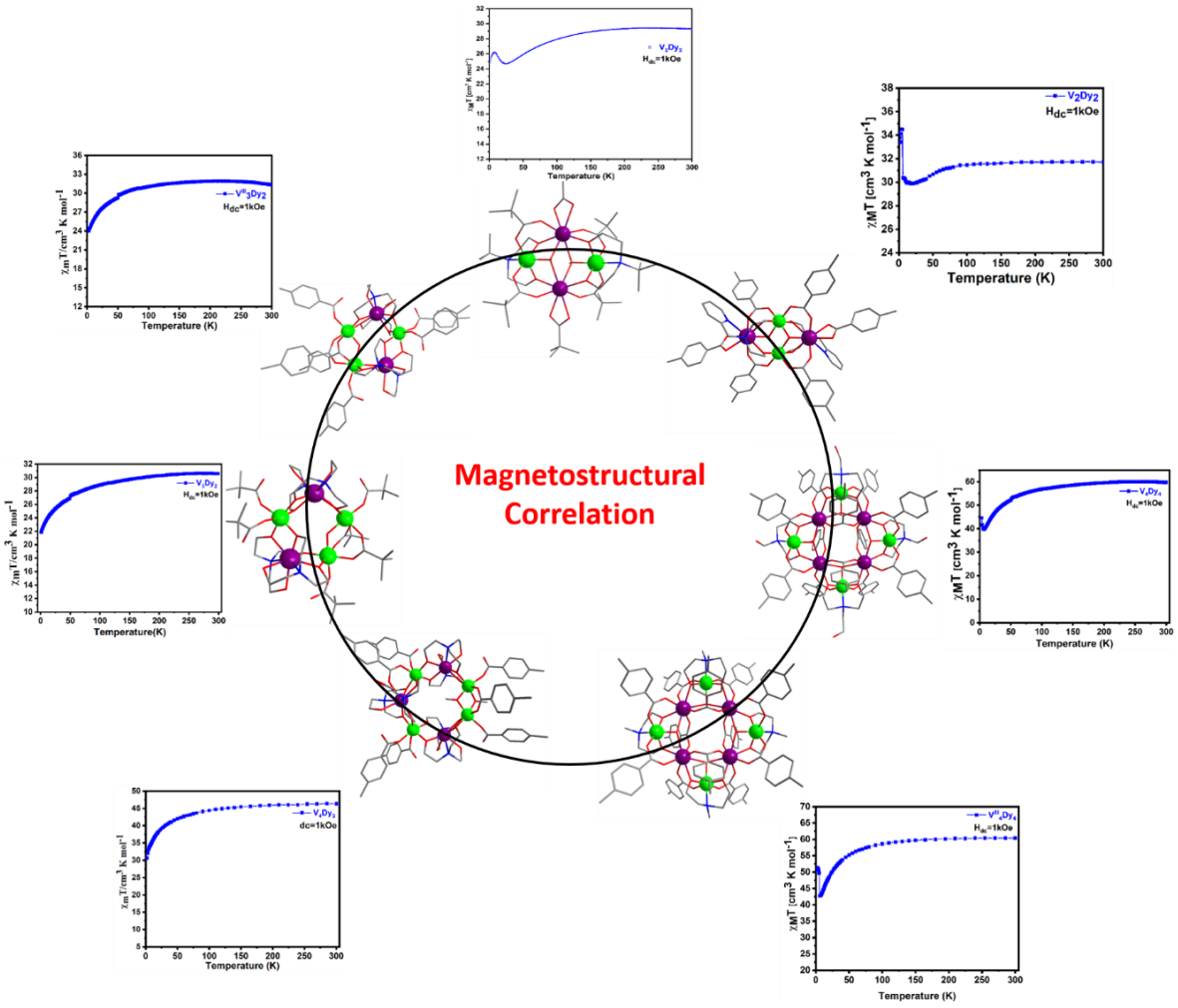

Figure 4.35: The magnetic signatures and molecular structures of a selection of ring-shaped V^{III}-Dy^{III} complexes.

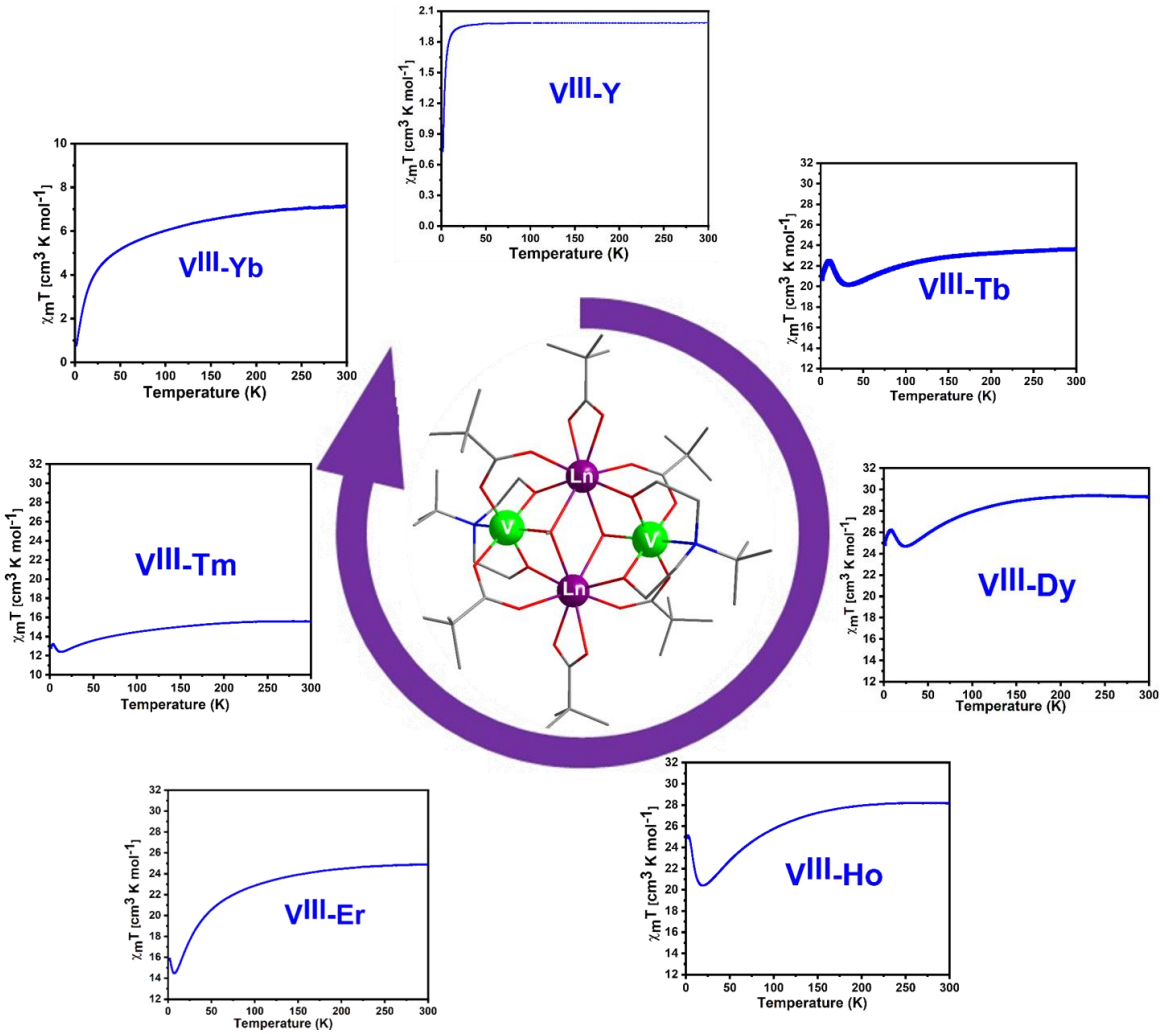

Figure 4.36: The plots of $\chi_M T$ vs T and crystal structure for a series of butterfly-type $V^{III}_2Ln_2$ complexes.

Table 4.3 The relationship between V^{III}-Ln distance and magnetism of the ring-shaped complexes $V^{III}_2Ln_2$ **2.1-2.7**.

	$V^{III}_2Tb_2$-2.1	$V^{III}_2Dy_2$-2.2	$V^{III}_2Ho_2$-2.3	$V^{III}_2Er_2$-2.4	$V^{III}_2Tm_2$-2.5	$V^{III}_2Yb_2$-2.6	$V^{III}_2Y_2$-2.7
V^{III}-Ln^{III}	**V^{III}-Tb^{III}**	**V^{III}-Dy^{III}**	**V^{III}-Ho^{III}**	**V^{III}-Er^{III}**	**V^{III}-Tm^{III}**	**V^{III}-Yb^{III}**	**V^{III}-Y^{III}**
Distance	3.3562 Å	3.3429 Å	3.3274 Å	3.3172 Å	3.3083 Å	3.2953 Å	3.3306 Å
Magnetism	FM	FM	FM	FM	FM	AF	AF

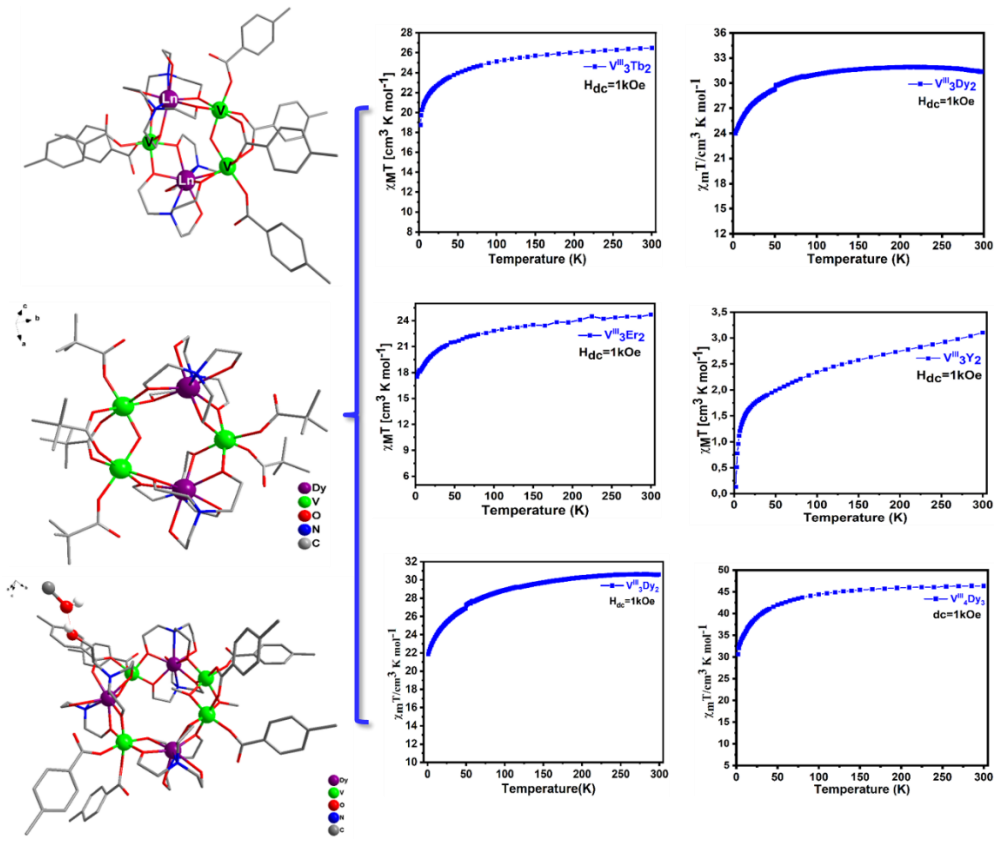

Figure 4.37: The plots of $\chi_M T$ vs T and the crystal structure of a series of ring-shape $V^{III}_3Ln_2$ and $V^{III}_4Dy_3$ complexes.

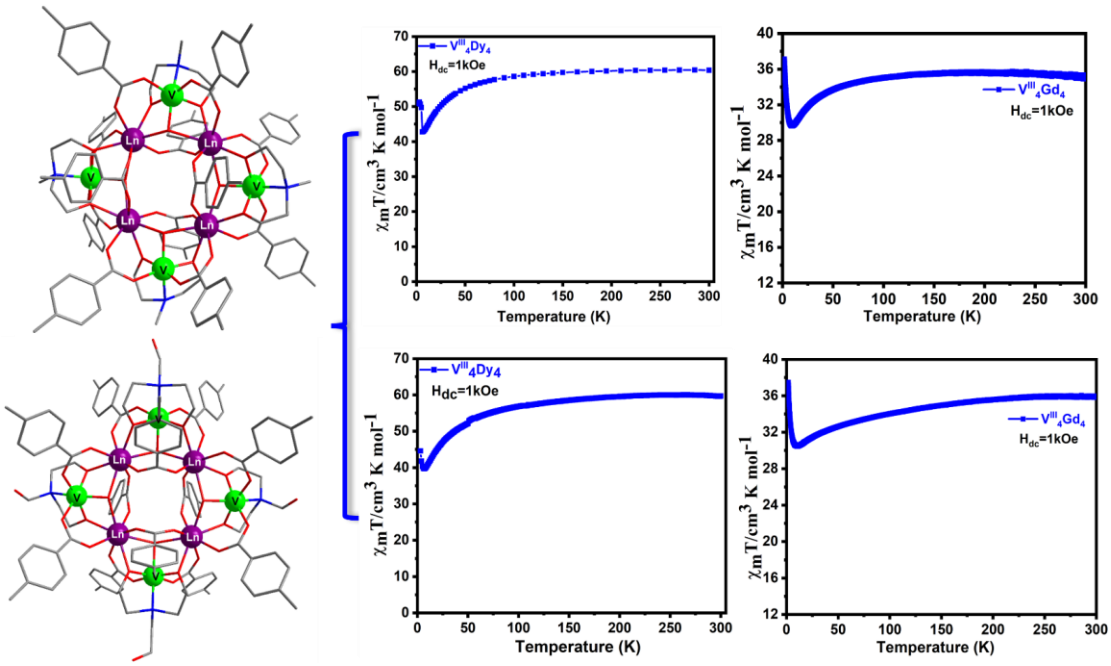

Figure 4.38: The plots of $\chi_M T$ vs T and the crystal structure of a series of ring-shape $V^{III}_4Ln_4$ complexes.

4.4 Conclusion

In this chapter, a series of ring-shape V-Ln complexes were characterized, both structurally and magnetically. The compounds presented in this chapter provide possible insights into magneto-structural relationships in ring-shaped V-Ln complexes. The focus is on the relationship between the metal-metal distances and the relative positions of the vanadium ions and lanthanide ions. In additions the influence of ligand changes of ring-shape V-Ln complexes on the magnetic properties was also monitored and found to be negligible.

The most important conclusion of this chapter is that in the ring-shaped V-Ln systems, when the vanadium ions and lanthanide ions are alternating the compounds show ferrimagnetic behavior. When there are neighboring vanadium ions ring-shaped V-Ln complexes is antiferromagnetic. In addition, with the decrease of the V-Ln distance in ring-shape V-Ln complexes, its magnetic properties are transformed from ferromagnetism to antiferromagnetism. Meanwhile, we also studied that the change of the ligand does not affect the magnetic properties of the ring-shaped V-Ln complexes.

Finally, we understand the relationship between the crystal structure and magnetic properties of ring-shaped V-Ln complexes through this chapter, and explore the influence of different factors of ring-shaped V-Ln complexes on the magnetic properties. These studies provided some predictable results for the latecomers to study the same type of ring-shaped V-Ln complexes system, which further attracted researchers' interest in this kind of system.

5. Conclusion and Outlook

This thesis mainly discusses the synthesis and magnetic properties of SMMs and magnetic refrigerants based on V-Ln complexes, and studies magnetostructural correlation between ring-shape complexes of vanadium and lanthanide ions, such as ferromagnetism and antiferromagnetism. Each chapter is classified and discussed according to their respective research fields of magnetism. Some basic measurements are carried out on V-Ln complexes, such as single-crystal X-ray diffraction, Infrared Spectroscopy, Powder X-ray diffraction, UV-Vis Spectroscopy, and most importantly, through SQUID and micro-SQUID measurements to get direct-current magnetic susceptibility, magnetization and alternating current magnetic susceptibility data for these V-Ln complexes. A total of forty-five V-Ln complexes were synthesized ranging from binuclear to tridecanuclear V-Ln complexes. Some of these complexes may result in mixed valence states of vanadium ions due to different reaction conditions. Of course, most of the vanadium ions are trivalent.

Chapter 2 details the characterization of the crystal structures and magnetic properties of two different types of V-Ln complexes. The butterfly type **II** $V^{III}_2Dy_2$ complex behaves as an SMM under an external magnetic field of 250 Oe. According to the fitting of the Arrhenius equation, τ_0 = 1.518×10^{-5} s, τ_{QTM} = 1.15×10^{-3} s, U_{eff} = 14.3(1.58) K. This extends the scope of 3d-4f butterfly systems to those containing V^{III} ions for the first time.

Much larger $V^{III}_5Dy_8$ **2.9** and $V^{III}_3V^{IV}Dy_5$ **2.10** complexes show SMM behavior in the absence of an applied external dc field but only at low temperatures. The $V^{III}_5Dy_8$ **2.9** and $V^{III}_3V^{IV}Dy_5$ **2.10** complexes required micro-SQUID measurements to demonstrate their SMM behavior. The results show that the hysteresis loops close above 0.3 K, which proves that there is an SMM phenomenon below this temperature. Fitting the relaxation data to the Arrhenius equation shows that the $V^{III}_5Dy_8$ **2.9** complex has an energy barrier

of 8.0 K and a relaxation time of 10^{-13} s. This chapter confirms that V-Ln type complexes are interesting candidates for further magnetic studies and expand the scope of the field of 3d-4f SMMs.

In Chapter 3, fourteen square-in-square $V^{III}_4Ln_4$ complexes were characterized both structurally and magnetically. The difference between these complexes lies in the ligands (exchanging pivalate with *p*-Me-$PhCO_2^-$ and $mDea^{2-}$ with $tBuDea^{2-}$ and $teaH^{2-}$, respectively) and the Ln ions (La, Gd, Dy and Y). The magnetic measurements show that these $V^{III}_4Ln_4$ complexes exhibit ferromagnetic interactions. This section also discusses the magnetocaloric properties of two isostructural $V^{III}_4Gd_4$ **3.3** and $V^{III}_4Gd_4$ **3.7** complexes with different ligands. The entropy change was calculated from the isothermal magnetization data of $V^{III}_4Gd_4$ **3.3** and $V^{III}_4Gd_4$ **3.7** using the Maxwell relation. The value of $-\Delta S_m$ for $V^{III}_4Gd_4$ **3.3** is 16.08 J kg^{-1} K^{-1} at 3 K for H = 7 T, and the value of $-\Delta S_m$ is 19.53 J kg^{-1} K^{-1} at 3 K for H = 7 T for $V^{III}_4Gd_4$ **3.7**.

Chapter 4 first discusses the structures of a series of ring-shaped vanadium-lanthanide complexes, some of which are analogues of previously reported Fe^{III}-Ln rings. In addition, the structures of hepta- to decanuclear V-Ln clusters with the vanadium ions sometimes in higher oxidation states to give mixed-valence vanadium clusters such as an azido-bridged $V^{III}_4V^{IV}_4Dy_4$ cluster with pairs of valences localized V^{III} and V^{IV} ions alternating with the Dy^{III} ions.

This chapter concludes with a magnetostructural correlation revealing the influence of ligand and metal-metal distances on the magnetic signatures. It can be concluded that a decrease in V-Ln distance as a result of the lanthanide contraction leads to a change from ferromagnetic to antiferromagnetic behavior. Changes in the ligand appear to have little influence on the magnetic properties of these ring-shaped V-Ln complexes.

Overall, this thesis presents a survey of a previously unexplored area V-Ln chemistry. One of the big successes is the ability to retain the V^{III} oxidation state in many of the compounds reported allowing to extend some already reported

structural motifs for 3d-4f compounds containing trivalent 3d metal ions to the left of Cr^{III}.

6. Materials and Equipment

Commercially available chemicals were used as received without further purification. Column chromatography was performed with Merck silica gel 60 (230-400 mesh). Elemental analyses for C, H, N were performed using an Elementar Vario EL analyzer and carried out at the Institute of Inorganic Chemistry, Karlsruhe Institute of Technology. The X-ray powder diffraction patterns were measured at room temperature using a Stoe STADI-P diffractometer with a Cu-Kα radiation at the Institute of Inorganic Chemistry, Karlsruhe Institute of Technology.

Fourier-transform infrared spectroscopy is a useful technique for identifying organic ligands and thus helps to verify the presence of organic ligands in the metal-ligand complexes. ligand complexes. In addition, it provides a unique fingerprint of the molecule and enables id entification of similar structures involving the same ligand. A small amount of the sample to be measured was ground into a fine powder together with absolutely dry KBr. Fourier-transform infrared spectroscopy were collected using a Nicolet Is50 FTIR (Fourier-transform infrared) spectrometer with ATR (attenuated total reflection) technology in the region of 4000-400 cm^{-1}.

Magnetic susceptibility measurements were performed using Quantum Design MPMS-XL SQUID magnetometers on polycrystalline material in the temperature range of 1.8-300 K under an applied DC magnetic field (H_{DC}) of 1 kOe. AC data were collected using an oscillating magnetic field of 3.5 Oe and frequencies between 1 and 1512 kHz. Magnetization data was collected with a Quantum Design MPMS3 SQUID magnetometer equipped with a 7 T magnet. The samples were embedded in solid eicosane to prevent the torque. DC data were corrected for diamagnetic contributions from the eicosane and core diamagnetism employing Pascal's constants. Low temperature (0.03–5 K) magnetization measurements were performed on single crystals using a μ-

SQUID apparatus at different sweep rates between 0.128 and 0.005 T s^{-1}. The time resolution is approximately 1 ms. The magnetic field can be applied in any direction of the micro-SQUID plane with precision much better than 0.1° by separately driving three orthogonal coils. In order to ensure good thermalisation, each sample was fixed with apiezon grease.

Suitable crystals were covered in polyfluorether oil and mounted on a MiTeGen Loop. The single-crystal X-ray diffraction data of these complexes were collected using STOE StadiVari 25 diffractometer with a Pilatus300 K detector using GeniX 3D HF micro focus with MoKα radiation (λ= 0.71073 Å) and a STOE StadiVari diffractometer, with a Ga radiation source from EXCILIUM (λ(GaKα) = 1.34143 Å) and an Eiger4M Dectris detector. The structures were solved using direct methods and were refined by full-matrix least square methods and using SHELX-2014 inbuilt in Olex2. All non-hydrogen atoms were refined anisotropically, whereas the hydrogen atoms were calculated geometrically, riding on their parent atoms. Continuous SHAPE analysis was used to determine the most probable coordination geometry around Ln(III) centers and V ions discussed in this thesis. The lowest possible values suggest the most probable coordination geometry.

7. Syntheses of ligands and complexes

7.1 General procedures

Most of the chemicals and all the solvents were obtained from commercial sources and were used without further purification. All the reactions were carried out under aerobic conditions. The ligand of N-(2-Pyridylmethyl)iminodiethanol were prepared according to literature procedures.

7.2 Preparation of organic ligands

7.2.1 N-(2-Pyridylmethyl)iminodiethanol (H_2L1)

A mixture of 2-amino-1,3-propanediol (6.31 g, 60 mmol) and 2-picolyl chloride hydrochloride (10 g, >60 mmol) in acetonitrile (250 ml) in flask was refluxed under a nitrogen gas atmosphere for 48 hours in the presence of K_2CO_3 (13.8 g, 120 mmol) and KI (1.5 g). After half an hour of reflux reaction, the solution turned orange, and then continued to reflux for 48 hours. The resulting orange solution was filtered, and the solvent was removed under reduced pressure, and the pale-yellow oil obtained by concentration was the desired ligand. The obtained pale-yellow oil was purified by chromatography using MeOH/ethylacetate (v/v = 1/3) as eluent. N-(2-Pyridylmethyl)iminodiethanol was obtained as a pale yellow oil (12.94 g, 71.2 %). ^{1}H-NMR (300 MHz, $CDCl_3$): δ(ppm) = 3.35-3.48 (m, 1 H, N-C*H*), 3.57 (d, 4H, ^{3}J=7.7 Hz, CH_2OH), 4.08 (s, 4 H, NCH_2), 6.91-6.98 (m, 2 H, H_{Ar}), 7.23 (m, 2 H, H_{Ar}), 7.61 (td, 2 H, ^{3}J=7.7 Hz, 1.8 Hz, H_{Ar}) 8.56-8.60 (m, 2 H, H_{Ar}). Anal. Calcd (Found) % for $C_{16}H_{21}N_3O_3$: C, 65.91 (65.72); H, 7.01 (7.08); N, 15.37 (15.53).

7.3 Preparation of Complexes

7.3.1 Synthesis of $[V^{III}_2Ln_2(\mu_3\text{-}OH)_2(^tBuDea)_2(piv)_6]\cdot 2MeOH$ [Ln = Tb-Yb (2.1-2.6) and Y (2.7)

Synthesis of $[V^{III}_2Tb_2(\mu_3\text{-}OH)_2(^tBuDea)_2(piv)_6]\cdot 2MeOH$ (**2.1**).

A solution of N-*tert*-butyldiethanolamine ($H_3{}^tBuDea$) (162 mg, 1 mmol) in MeCN (5 mL) was added to a solution of VCl_3 (79 mg, 0.5 mmol), $TbCl_3\cdot 6H_2O$ (187 mg, 0.5 mmol), and pivalic acid (400 mg) in mixture of MeOH and MeCN (8 mL/8 mL) in a Schlenk tube. After 10 min of stirring, Et_3N (1 mL) was added, and the solution stirred for a further 24 h. The solution was then filtered under anhydrous and oxygen-free conditions and left undisturbed for crystallization. Yield: 54% (198.60 mg, based on Tb). Anal. Calc (found)% for $V_2Tb_2C_{48}H_{94}N_2O_{18}$, $2CH_3OH$: C, 40.82 (40.73); H, 6.99 (7.03); N, 1.90 (1.87). Selected IR data (KBr, cm^{-1}): 2960 (m), 2925 (w), 1563 (m), 1524 (w), 1481 (m), 1458 (w), 1409 (m), 1375 (m), 1359 (m), 1260 (w), 1225 (m), 1086 (m), 1049 (w), 1018 (w), 894 (w), 793 (m), 598 (w), 494 (w), 457 (w), 422 (w).

Synthesis of $[V^{III}_2Dy_2(\mu_3\text{-}OH)_2(^tBuDea)_2(piv)_6]\cdot 2MeOH$ (**2.2**).

In place of $DyCl_3\cdot 6H_2O$ was used with the same procedure as above the complex **2.1** was obtained $V^{III}_2Dy_2(\mu_3\text{-}OH)_2(^tBuDea)_2(piv)_6\cdot 2MeOH$ (**2.2**). Yield: 62% (114.56 mg, based on Dy). Anal. Calc (found) % for $V_2Dy_2C_{48}H_{94}N_2O_{18}$, $2CH_3OH$: C, 40.63 (40.59); H, 6.95 (6.70); N, 1.90 (1.83). Selected IR data (KBr, cm^{-1}): 2960 (w), 2925 (w), 2870 (w), 1561 (m), 1527 (w), 1482 (m), 1409 (m), 1375 (w), 1359 (w), 1226 (w), 1088 (w), 1019 (w), 895 (w), 895 (w), 753 (w), 598 (w).

Synthesis of $[V^{III}_2Ho_2(\mu_3\text{-}OH)_2(^tBuDea)_2(piv)_6]\cdot 2MeOH$ (**2.3**).

In place of $HoCl_3\cdot 6H_2O$ was used with the same procedure as above the compound **2.1** was obtained $V^{III}_2Ho_2(\mu_3\text{-}OH)_2(^tBuDea)_2(piv)_6\cdot 2MeOH$ (**2.3**). Yield: 45% (1.67 mg, based on Ho). Anal. Calc (found) % for $V_2Ho_2C_{48}H_{94}N_2O_{18}$, $2CH_3OH$: C, 40.49 (40.38); H, 6.93 (6.87); N, 1.89 (1.82). Selected IR data (KBr,

cm^{-1}): 2956 (m), 2926 (w), 2867 (w), 1591 (m), 1569 (s), 1533 (w), 1481 (m), 1428 (m), 1407 (s), 1374 (m), 1358 (m), 1225 (m), 1097 (m), 1082 (w), 1021 (m), 909 (w), 896 (w), 794 (w), 601 (w), 580 (w), 497 (w), 462 (w), 427 (w).

Synthesis of $[V^{III}_2Er_2(\mu_3\text{-}OH)_2(^tBuDea)_2(piv)_6]\cdot 2MeOH$ (**2.4**).

In place of $ErCl_3\cdot 6H_2O$ was used with the same procedure as above the complex **2.1** was obtained $V^{III}_2Er_2(\mu_3\text{-}OH)_2(^tBuDea)_2(piv)_6\cdot 2MeOH$ (**2.4**). Yield: 43% (160 mg, based on Er). Anal. Calc (found) % for $V_2Er_2C_{48}H_{94}N_2O_{18}$, $2CH_3OH$: C, 40.37 (40.31); H, 6.91 (6.84); N, 1.88 (1.84).). Selected IR data (KBr, cm^{-1}): 2962 (m), 2928 (w), 2871 (w), 1591 (m), 1571 (s), 1531 (w), 1481 (m), 1429 (m), 1409 (s), 1374 (m), 1359 (m), 1229 (m), 1099 (m), 1084 (w), 1027 (m), 909 (w), 899 (w), 798 (w), 601 (w), 585 (w), 497 (w), 466 (w), 427 (w).

Synthesis of $[V^{III}_2Tm_2(\mu_3\text{-}OH)_2(^tBuDea)_2(piv)_6]\cdot 2MeOH$ (**2.5**).

In place of $TmCl_3\cdot 6H_2O$ was used with the same procedure as above the complex **2.1** was obtained $V^{III}_2Tm_2(\mu_3\text{-}OH)_2(^tBuDea)_2(piv)_6\cdot 2MeOH$ (**2.5**). Yield: 49% (182.6 mg, based on Tm). Anal. Calc (found) % for $V_2Tm_2C_{48}H_{94}N_2O_{18}$, $2CH_3OH$: C, 40.24 (40.15); H, 6.89 (6.74); N, 1.88 (1.74). Selected IR data (KBr, cm^{-1}): 2959 (w), 2926 (w), 1562 (m), 1530 (w), 1481 (m), 1410 (m), 1375 (w), 1359 (w), 1226 (w), 1090 (w), 896 (w), 601 (w).

Synthesis of $[V^{III}_2Yb_2(\mu_3\text{-}OH)_2(^tBuDea)_2(piv)_6]\cdot 2MeOH$ (**2.6**).

In place of $YbCl_3\cdot 6H_2O$ was used with the same procedure as above the complex **2.1** was obtained $V^{III}_2Yb_2(\mu_3\text{-}OH)_2(^tBuDea)_2(piv)_6\cdot 2MeOH$ (**2.6**). Yield: 32% (120 mg, based on Yb). Anal. Calc (found) % for $V_2Yb_2C_{48}H_{94}N_2O_{18}$, $2CH_3OH$: C, 40.05 (39.41); H, 6.85 (6.75); N, 1.87 (1.76). Selected IR data (KBr, cm^{-1}): 2961 (w), 2927 (w), 1563 (m), 1532 (w), 1482 (m), 1410 (m), 1375 (w), 1359 (w), 1225 (w), 1091 (w), 1020 (w), 603 (w).

Synthesis of $[V =V^{III}_2Y_2(\mu_3\text{-}OH)_2(^tBuDea)_2(piv)_6]\cdot 2MeOH$ (**2.7**).

In place of $YbCl_3\cdot 6H_2O$ was used with the same procedure as above the complex **2.1** was obtained $V^{III}_2Y_2(\mu_3\text{-}OH)_2(^tBuDea)_2(piv)_6\cdot 2MeOH$ (**2.7**). Yield:

29% (96.5 mg, based on Y). Anal. Calc (found) % for $V_2Y_2C_{48}H_{94}N_2O_{18}$, $2CH_3OH$: C, 45.11 (44.87); H, 7.72 (7.55); N, 2.10 (2.01). Selected IR data (KBr, cm^{-1}): 2960 (m), 2926 (w), 2871 (w), 1560 (m), 1528 (w), 1481 (m), 1411 (m), 1375 (m), 1359 (m), 1226 (m), 1089 (w), 1089 (w), 1026 (w), 896 (w), 600 (w), 495 (w), 459 (w), 427 (w).

7.3.2 Synthesis of $[V^{III}_2Dy_2(\mu_3\text{-}OH)_2(L)_2(p\text{-}Me\text{-}PhCO_2)_6]\cdot 2MeOH$ (L=N-(2-Pyridylmethyl)iminodiethanol) (2.8)

Synthesis of $[V^{III}_2Dy_2(\mu_3\text{-}OH)_2(L)_2(p\text{-}Me\text{-}PhCO_2)_6]\cdot 2MeOH$ (**2.8**).

A solution of H_2L (H_2L=N-(2-Pyridylmethyl)iminodiethanol) (100 mg, 0,5 mmol) in MeCN (5 mL) was added to a solution of VCl_3 (79 mg, 0.5 mmol), $DyCl_3\cdot 6H_2O$ (189 mg, 0.5 mmol), and 4-methylbenzoic acid (136 mg, 1mmol) in mixture of MeOH and MeCN (10 mL/8 mL) in a Schlenk tube. After 10 min stirring, Et_3N (1 mL) was added, and the solution stirred for a further 24 h. The solution was then filtered under anhydrous and oxygen-free conditions and left undisturbed for crystallization. Yield: 32% (143.06 mg, based on Dy). Anal. Calc (found)% for $V_2Dy_2C_{70}H_{80}N_4O_{20}\cdot 2CH_3OH$: C, 48.35 (47.56); H, 4.96 (5.01); N, 3.13 (3.08). Selected IR data (KBr, cm^{-1}): 2970 (w), 2915 (w), 1560 (m), 1530 (w), 1485 (m), 1411 (m), 1226 (w), 1088 (w), 1019 (w), 897 (w), 894 (w), 756 (w), 598 (w).

7.3.3 Synthesis of $(Et_3NH)[V^{III}_5Dy_8(\mu_3\text{-}OH)_{12}(Bu^tDea)_4(NCC_6H_4CO_2)_{20}]\cdot 15MeCN$ (2.9)

A mixture of N-*tert*-butyldiethanolamine ($H_3{}^tBuDea$) (162 mg, 1 mmol) was added to a solution of VCl_3 (157 mg, 1 mmol), $DyCl_3\cdot 6H_2O$ (377 mg, 1 mmol), and 4-cyanbenzic acid (441 mg) in mixture of MeCN and MeCN (7 mL/ 7 mL) in a Schlenk tube. After 10 min stirring, Et_3N (1 mL) was added, and the solution stirred for a further 24 h. The solution was then filtered under anhydrous and oxygen-free conditions and left undisturbed for crystallization. Yield: 23% (173.54 mg, based on Dy). Anal. Calc (found)% for $V_5Dy_8C_{228}H_{221}N_{40}O_{60}$: C,

46.02 (46.12); H, 3.57 (3.47); N, 7.01 (6.62). IR data (KBr, cm^{-1}): 2228 (w), 1589 (m), 1548 (m), 1404 (s), 1303 (w), 1291 (w), 1095 (w), 864 (w), 776 (m), 692 (w), 570 (w), 541 (w).

7.3.5 Synthesis of $[V^{III}_4Ln^{III}_4(u_3\text{-}OH)_4(mDea)_4(p\text{-}Me\text{-}PhCO_2)_{12}]\cdot xMeCN\ y\ CH_2Cl_2$ [Ln= La, Nd, Gd, Dy and Y (3.1-4.5)]

Synthesis of $[V^{III}_4La_4(u_3\text{-}OH)_4(mDea)_4(p\text{-}Me\text{-}PhCO_2)_{12}]\cdot 4MeCN$ (**3.1**)

A mixture of N-methyldiethanolamine (966 mg, 6.6 mmol) in MeCN (5 mL) was added to a solution of VCl_3 (314 mg, 2 mmol), $LaCl_3$ (490 mg, 2 mmol), and 4-methylbenzoic acid (532 mg) in MeCN (14 mL) in a Schlenk tube. After 10 min stirring, Et_3N (1 mL) was added, and the solution stirred for a further 24 h. The solution was then filtered under anhydrous and oxygen-free conditions and left undisturbed for crystallization. Yield: 28% (343.77 mg, based on La). Anal. Calc (found)% for $V^{III}_4La_4C_{116}H_{134}N_4O_{37}\ 4CH_3CN$: C, 48.90 (48.14); H, 4.90 (4.81); N, 3.54 (3.44). Selected IR data (KBr, cm^{-1}): 2860 (w), 1591 (m), 1546 (s), 1383 (s), 1289 (w), 1175 (w), 1081 (m), 1070 (m), 996 (w), 764 (m), 691 (w), 615 (w), 593 (w), 528 (w), 496 (w), 469 (w), 423 (w).

Synthesis of $[V^{III}_4Nd_4(u_3\text{-}OH)_4(mDea)_4(p\text{-}Me\text{-}PhCO_2)_{12}]$ (**3.2**)

In place of $NdCl_3$ was used with the same procedure as above the complex **3.1** was obtained $[V^{III}_4Nd_4(u_3\text{-}OH)_4(mDea)_4(p\text{-}Me\text{-}PhCO_2)_{12}]$ (**3.2**). Yield: 42% (310.5 mg, based on V). Anal. Calc (found)% for $V^{III}_4Nd_4C_{116}H_{134}N_4O_{37}$: C, 48.58 (48.49); H, 4.87 (4.61); N, 3.51 (3.45 Selected IR data (KBr, cm^{-1}): 3560 (w), 1590 (m), 1547 (s), 1388 (s), 1289 (w), 1176 (w), 1083 (m), 1070 (m), 996 (w), 768 (m), 691 (w), 614 (w), 594 (w), 528 (w), 497 (w), 469 (w), 425 (w).

Synthesis of $[V^{III}_4Gd_4(u_3\text{-}OH)_4(mDea)_4(p\text{-}Me\text{-}PhCO_2)_{12}]\cdot 5MeCN\ 5CH_2Cl_2$ (**3.3**)

In place of $GdCl_3$ was used with the same procedure as above the complex **3.1** was obtained $[V^{III}_4Gd_4(u_3\text{-}OH)_4(mDea)_4(p\text{-}Me\text{-}PhCO_2)_{12}]\ 5MeCN\ 5CH_2Cl_2$ (**3.3**). Yield: 11% (162.6 mg, based on V). Anal. Calc (found)% for

$V^{III}_4Gd_4C_{116}H_{132}N_4O_{36}$ 5MeCN $5CH_2Cl_2$: C, 48.17 (48.09); H, 4.84 (4.81); N, 3.85 (3.75). Selected IR data (KBr, cm^{-1}): 3562 (w), 1592 (m), 1551 (m), 1458 (w), 1392 (s), 1177 (w), 1085 (w), 1071 (m), 996 (w), 763 (m), 692 (w), 620 (w), 601 (w), 507 (w), 470 (w), 429 (w).

Synthesis of $[V^{III}_4Dy_4(u_3\text{-}OH)_4(mDea)_4(p\text{-}Me\text{-}PhCO_2)_{12}]\cdot 5MeCN\ 5CH_2Cl_2$ (**3.4**) In place of $NdCl_3$ was used with the same procedure as above the complex **3.1** was obtained $[V^{III}_4Dy_4(u_3\text{-}OH)_4(mDea)_4(p\text{-}Me\text{-}PhCO_2)_{12}]\cdot 5MeCN\ 5CH_2Cl_2$ (**3.4**).Yield: 19% (193 mg, based on V). Anal. Calc (found)% for $V^{III}_4Dy_4C_{116}H_{134}N_4O_{37}$ 5MeCN $5CH_2Cl_2$: C, 43.20 (43.49); H, 4.34 (4.29); N, 3.46 (3.42). Selected IR data (KBr, cm^{-1}): 470 (w), 517 (w), 604 (w), 692 (w), 761 (m), 850 (w), 1020 (w), 1087 (w), 1176 (w), 1290 (w), 1395 (s), 1545 (m), 1591 (m), 2860 (w).

Synthesis of $[V^{III}_4Y_4(u_3\text{-}OH)_4(mDea)_4(p\text{-}Me\text{-}PhCO_2)_{12}]\cdot 5MeCN\ 3CH_2Cl_2$ (**3.5**) In place of $NdCl_3$ was used with the same procedure as above the complex **3.1** was obtained $[V^{III}_4Y_4(u_3\text{-}OH)_4(mDea)_4(p\text{-}Me\text{-}PhCO_2)_{12}]\cdot 5MeCN\ 3CH_2Cl_2$ (**3.5**). Yield: 11% (162.6 mg, based on V). Anal. Calc (found)% for $V^{III}_4Y_4C_{116}H_{134}N_4O_{37}$ 5MeCN $3CH_2Cl_2$: C, 48.76 (48.79); H, 4.85 (4.81); N, 3.97 (3.95). Selected IR data (KBr, cm^{-1}): 3563 (w), 2901 (w), 2859 (w), 1595 (s), 1553 (s), 1394 (s), 1289 (w), 1176 (w), 1088 (m), 1020 (w), 998 (w), 893 (w), 761 (m), 693 (w), 603 (w), 572 (w), 517 (w), 469 (w), 431 (w).

7.3.6 Synthesis of $[V^{III}_4Ln^{III}_4(u_3\text{-}O)_4(teaH)_4(p\text{-}Me\text{-}PhCO_2)_{12}]\cdot xMeCN\ yCH_2Cl_2$ [Ln = La^{III}, Gd^{III}, Dy^{III} and Y^{III} (3.6-3.9)]

Synthesis of $[V^{III}_4Gd_4(u_3\text{-}OH)_4(teaH)_4(p\text{-}Me\text{-}PhCO_2)_{12}]$ 4MeCN $4CH_2Cl_2$ (**3.7**)

A mixture of triethanolamine (966 mg, 6.6 mmol) in MeCN (5 mL) was added to a solution of VCl_3 (314 mg, 2 mmol), $GdCl_3$ (316 mg, 1.2 mmol), and 4-methylbenzoic acid (531 mg) in MeCN and MeOH (10 mL/10 mL) in a Schlenk tube. After 10 min stirring, Et_3N (1 mL) was added, and the solution stirred for

a further 24 h. The solution was then filtered under anhydrous and oxygen-free conditions and left undisturbed for crystallization. Yield: 26% (282 mg, based on Gd). Anal. Calc (found)% for $V^{III}_4Gd_4C_{120}H_{140}N_4O_{40}$ 4MeCN $4CH_2Cl_2$: C, 43.86 (43.74); H, 4.46 (4.41); N, 3.10 (3.14). Selected IR data (KBr, cm^{-1}): 1592 (m), 1550 (s), 1392 (s), 1177 (w), 1095 (w), 1072 (w), 764 (m), 691 (w), 620 (w), 600 (w), 572 (w), 513 (w), 470 (w).

Synthesis of $[V^{III}_4La_4(u_3\text{-}OH)_4(teaH)_4(p\text{-}Me\text{-}PhCO_2)_{12}]$ $xMeCN$ yCH_2Cl_2 (**3.6**)

In place of $LaCl_3$ was used with the same procedure as above the complex **3.7** was obtained $[V^{III}_4La_4(u_3\text{-}OH)_4(mdea)_4(p\text{-}Me\text{-}PhCO_2)_{12}]$ (**3.6**). Yield: 42% (310.5 mg, based on V). Anal. Calc (found)% for $V^{III}_4La_4C_{116}H_{134}N_4O_{37}$: C, 48.58 (48.49); H, 4.87 (4.61); N, 3.51 (3.45). Selected IR data (KBr, cm^{-1}): 3344 (w), 2896 (w), 2862 (w), 1590 (m), 1545 (s), 1458 (w), 1381 (s), 1290 (w), 1176 (w), 1082 (w), 1070 (w), 1020 (m), 995 (w), 891 (w), 764 (m), 690 (w), 615 (w), 593 (w), 526 (w), 494 (w), 425 (w).

Synthesis of $[V^{III}_4Dy_4(u_3\text{-}OH)_4(teaH)_4(p\text{-}Me\text{-}PhCO_2)_{12}]$ $2MeCN$ $5CH_2Cl_2$ (**3.8**)

In place of $DyCl_3$ $6H_2O$ was used with the same procedure as above the complex **3.7** was obtained $[V^{III}_4Dy_4(u_3\text{-}OH)_4(teaH)_4(p\text{-}Me\text{-}PhCO_2)_{12}]$ $2MeCN$ $5CH_2Cl_2$ (**3.8**). Yield: 49% (532.6 mg, based on V). Anal. Calc (found)% for $V^{III}_4Dy_4C_{120}H_{138}N_4O_{40}$ 2MeCN $5CH_2Cl_2$: C, 42.60 (42.49); H, 4.27 (4.21); N, 2.31 (2.27). Selected IR data (KBr, cm^{-1}): 430 (w), 518 (w), 604 (w), 694 (w), 764 (m), 911 (w), 1020 (w), 1072 (w), 1098 (w), 1177 (w), 1389 (s), 1552 (m), 1591 (m), 2903 (w), 3306 (w), 3551 (w).

Synthesis of $[V^{III}_4Y_4(u_3\text{-}OH)_4(teaH)_4(p\text{-}Me\text{-}PhCO_2)_{12}]$ 8MeCN (**3.9**)

In place of YCl_3 was used with the same procedure as above the compound **3.13** was obtained $[V^{III}_4Y_4(u_3\text{-}OH)_4(teaH)_4(p\text{-}Me\text{-}PhCO_2)_{12}]$ 8MeCN (**3.16**). Yield: 27% (256 mg, based on V). Anal. Calc (found)% for $V^{III}_4Y_4C_{120}H_{140}N_4O_{40}$ 8MeCN: C, 51.59 (51.49); H, 5.22 (5.21); N, 5.30 (5.27). Selected IR data (KBr, cm^{-1}): 3550 (w), 2900 (w), 1593 (m), 1555 (m), 1387 (s) 1179 (w), 1072 (w), 1022 (w), 915 (w), 766 (m), 696 (w), 604 (w), 518 (w), 430 (w).

7.3.7 Synthesis of $[V^{III}_4La^{III}_4(u_3\text{-}OH)_4(mdea)_4(piv)_{12}]\cdot 8MeCN$ (3.10)

Synthesis of $[V^{III}_4La_4(u_3\text{-}OH)_4(mdea)_4(piv)_{12}]\cdot 8MeCN$ (**3.10**)

A mixture of N-methyldiethanolamine (966 mg, 6.6 mmol) in MeCN (5 mL) was added to a solution of VCl_3 (314 mg, 2 mmol), $LaCl_3$ (490 mg, 2 mmol), and pivalic acid (400 mg) in MeCN and CH_2Cl_2 (10 mL /10 mL) in a Schlenk tube. After 10 min stirring, Et_3N (1 mL) was added, and the solution stirred for a further 24 h. The solution was then filtered under anhydrous and oxygen-free conditions and left undisturbed for crystallization. Yield: 24% (171.36 mg, based on La). Anal. Calc (found)% for $V^{III}_4La_4C_{80}H_{158}N_4O_{37}$ $8CH_3CN$: C, 48.90 (48.14); H, 4.90 (4.81); N, 3.54 (3.44). Selected IR data (KBr, cm^{-1}): 2957 (w), 2898 (w), 2861 (w), 1558 (s), 1484 (m), 1458 (w), 1406 (s), 1375 (m), 1354 (m), 1228 (m), 1085 (m), 1069 (m), 998 (w), 888 (w), 589 (w), 498 (w).

7.3.8 Synthesis of $[V^{III}_4Gd_4(u_3\text{-}O)_4(L_1)_4(L_2)_{12}]\cdot 8MeCN$ (3.11-13)

Synthesis of $[V^{III}_4Gd_4(u_3\text{-}OH)_4(tea)_4(piv)_{12}]\cdot 8MeCN$ (**3.11**)

A mixture of triethanolamine (966 mg, 6.6 mmol) in MeCN (5 mL) was added to a solution of VCl_3 (314 mg, 2 mmol), $GdCl_3$ (527.2 mg, 2 mmol), and pivalic acid (400 mg) in MeCN and CH_2Cl_2 (10 mL /10 mL) in a Schlenk tube. After 10 min stirring, Et_3N (1 mL) was added, and the solution stirred for a further 24 h. The solution was then filtered under anhydrous and oxygen-free conditions and left undisturbed for crystallization. Yield: 31% (410 mg, based on Gd). Anal. Calc (found)% for $V^{III}_4Gd_4C_{78}H_{145}N_6O_{36}$: C, 34.87 (35.40); H, 5.40 (5.52); N, 3.12 (3.18). Selected IR data (KBr, cm^{-1}): 2965 (w), 2891 (w), 2858 (w), 1557 (s), 1483 (m), 1462 (w), 1411 (s), 1371 (m), 1354 (m), 1224 (m), 1085 (m), 1061 (m), 996 (w), 883 (w), 582 (w), 487 (w).

Synthesis of $[V^{III}_4Gd_4(u_3\text{-}OH)_4(mdea)_4(piv)_{12}]\cdot 5MeCN$ $5CH_2Cl_2$ (**3.12**)

Ligand $teaH_3$ is place of ligand $meaH_3$ and was used with the same procedure as above the complex **3.11** was obtained $[V^{III}_4Gd_4(u_3\text{-}O)_4(mdea)_4(piv)_{12}]$ x$MeCN$ yCH_2Cl_2 (**3.12**).

Synthesis of $[V^{III}_4Gd_4(u_3\text{-}OH)_4(^tBuDea)_4(p\text{-}Me\text{-}PhCO_2)_{12}]\cdot 5MeCN$ $5CH_2Cl_2$ (**3.13**)

Ligand $teaH_3$ is place of ligand $H_2{}^tBuDea$ and was used with the same procedure as above the complex **3.7** was obtained $[V^{III}_4Gd_4(u_3\text{-}O)_4(^tBuDea)_4(p\text{-}Me\text{-}PhCO_2)_{12}]$ x$MeCN$ yCH_2Cl_2 (**3.13**). Yield: 18% (341 mg, based on V). Anal. Calc (found)% for $V^{III}_4Gd_4C_{143}H_{181}N_9O_{36}$: C, 45.27 (45.33); H, 4.70 (4.81); N, 3.20 (3.33). Selected IR data (KBr, cm^{-1}): 2955 (w), 2893 (w), 2854 (w), 1548 (s), 1489 (m), 1464 (w), 1412 (s), 1370 (m), 1354 (m), 1224 (m), 1089 (m), 1067 (m), 996 (w), 887 (w), 572 (w), 481 (w).

7.3.9 Synthesis of $[V^{III}_3Ln_2(\mu_3\text{-}OH)(tea)_4(p\text{-}Me\text{-}PhCO_2)_2(p\text{-}Me\text{-}PhCOOH)_4]\cdot 2MeCN$ [Ln = Tb-Er, Yb and Y (4.1-4.6)

Synthesis of $[V^{III}_3Tb_2(\mu_3\text{-}OH)(tea)_4(p\text{-}Me\text{-}PhCO_2)_6]\cdot 2MeCN$ (**4.1**).

A mixture of triethanolamine (483 mg, 3.3 mmol) in MeCN (5 mL) was added to a solution of VCl_3 (157 mg, 1 mmol), $TbCl_3\cdot 6H_2O$ (187 mg, 0.5 mmol), and 4-methylbenzoic acid (531 mg) in mixture of CH_2Cl_2 and MeCN (10 mL/10 mL) in a Schlenk tube. After 10 min stirring, Et_3N (1 mL) was added, and the solution stirred for a further 24 h The solution was then filtered under anhydrous and oxygen-free conditions and left undisturbed for crystallization. Yield: 41% (201.86 mg, based on Tb). Anal. Calc (found)% for $V_3Tb_2C_{72}H_{95}N_4O_{25}\cdot 2CH_3CN$: C, 46.35 (45.69); H, 5.17 (5.10); N, 4.27 (4.29). Selected IR data (KBr, cm^{-1}): 3308 (w), 2859 (w), 1588 (m), 1530 (m), 1398 (m), 1177 (w), 1068 (w), 901 (w), 850 (w), 764 (m), 693 (w), 610 (w), 471 (w).

Synthesis of $[V^{III}_3Dy_2(\mu_3\text{-}OH)(tea)_4(p\text{-}Me\text{-}PhCO_2)_6]\cdot 2MeCN$ (**4.2**).

In place of $DyCl_3\cdot 6H_2O$ (226 mg, 0.6 mmol) was used with the same

procedure as above the complex **4.1** was obtained [$V^{III}_3Dy_2(\mu_3\text{-}OH)(tea)_4(p\text{-}Me\text{-}PhCO_2)_6$]·2MeCN (**4.2**). Yield: 21% (124.5 mg, based on Dy). Anal. Calc (found) % for $V_3Dy_2C_{72}H_{95}N_4O_{25}\cdot 2CH_3CN$: C, 46.18 (46.08); H, 5.15 (5.10); N, 4.25 (4.20). Selected IR data (KBr, cm^{-1}): 3311 (w), 2868 (w), 1588 (m), 1534 (m), 1398 (s), 1261 (w), 1177 (w), 1061 (m), 1021 (w), 956 (w), 898 (w), 861 (w), 764 (m), 693 (w), 619 (w), 470(w).

Synthesis of [$V^{III}_3Ho_2(\mu_3\text{-}OH)(tea)_4(p\text{-}Me\text{-}PhCO_2)_6$]·2MeCN (**4.3**).

In place of $HoCl_3\cdot 6H_2O$ (190 mg, 0.5 mmol) was used with the same procedure as above the complex **4.1** was obtained [$V^{III}_3Ho_2(\mu_3\text{-}OH)(tea)_4(p\text{-}Me\text{-}PhCO_2)_6$]·2MeCN (**4.3**). Yield: 17% (84.2 mg, based on Ho). Anal. Calc (found) % for $V_3Ho_2C_{72}H_{95}N_4O_{25}\cdot 2CH_3CN$: C, 46.07 (46.08); H, 5.14 (5.17); N, 4.24 (4.32). Selected IR data (KBr, cm^{-1}): 2848 (m), 1586 (m), 1533 (m), 1441 (w), 1389 (s), 1370 (s), 1284 (w), 1266 (m), 1228 (w), 1174 (w), 1095 (m), 1076 (m), 1065 (m), 1019 (m), 914 (w), 896 (m), 849 (w), 762 (m), 647 (w), 609 (w), 554 (w), 486 (w), 415 (w).

Synthesis of [$V^{III}_3Er_2(\mu_3\text{-}OH)(tea)_4(p\text{-}Me\text{-}PhCO_2)_6$]·2MeCN (**4.4**).

In place of $ErCl_3\cdot 6H_2O$ (191mg, 0.5 mmol) was used with the same procedure as above the complex **4.1** was obtained [$V^{III}_3Er_2(\mu_3\text{-}OH)(tea)_4(p\text{-}Me\text{-}PhCO_2)_6$]·2MeCN (**4.4**). Yield: 47% (496.5 mg, based on Er). Anal. Calc (found) % for $V_3Er_2C_{72}H_{95}N_4O_{25}\cdot 2CH_3CN$: C, 45.96 (46.01); H, 5.13 (5.11); N, 4.23 (4.33). Selected IR data (KBr, cm^{-1}): 3358 (m), 2864 (m), 1588 (m), 1529 (m), 1409 (s), 1178 (w), 1070 (w), 1020 (w), 946 (m), 850 (w), 765 (m), 692 (w), 609 (w), 462 (w).

Synthesis of [$V^{III}_3Yb_2(\mu_3\text{-}OH)(tea)_4(p\text{-}Me\text{-}PhCO_2)_6$]·2MeCN (**4.5**).

In place of $YbCl_3$ (140 mg, 0.5 mmol) was used with the same procedure as above the complex **4.1** was obtained [$V^{III}_3Yb_2(\mu_3\text{-}OH)(tea)_4(p\text{-}Me\text{-}PhCO_2)_6$]·2MeCN (**4.5**). Yield: 32% (159.8 mg, based on Yb). Anal. Calc (found) % for $V_3Yb_2C_{72}H_{95}N_4O_{25}\cdot 2CH_3CN$: C, 45.69 (46.03); H, 5.10 (5.14); N, 4.20 (4.23). Selected IR data (KBr, cm^{-1}): 2850 (w), 1587 (w), 1534 (m), 1397

(m), 1284 (w), 1175 (w), 1096 (w), 1065 (m), 1020 (w), 917 (w), 898 (w), 762 (m), 609 (w), 556 (w), 498 (w), 469 (w).

Synthesis of $[V^{III}_3Y_2(\mu_3\text{-}OH)(tea)_4(p\text{-}Me\text{-}PhCO_2)_6]\cdot 2MeCN$ (**4.6**).

In place of YCl_3 (98mg, 0.5 mmol) was used with the same procedure as above the complex **4.1** was obtained $[V^{III}_3Y_2(\mu_3\text{-}OH)(tea)_4(p\text{-}Me\text{-}PhCO_2)_6]\cdot 2MeCN$ (**4.6**). Yield: 27% (123.5 mg, based on Y). Anal. Calc (found) % for $V_3Y_2C_{72}H_{95}N_4O_{25}\cdot 2CH_3CN$: C, 49.90 (48.01); H, 5.56 (5.61); N, 4.59 (4.37). Selected IR data (KBr, cm^{-1}): 3308 (m), 3158 (m), 1588 (m), 1529 (m), 1408 (s), 1178 (w), 1067 (w), 1033 (w), 956 (w), 851 (w), 765 (m), 693 (w), 609 (w), 471 (w).

7.3.10 Synthesis of $[V^{III}_3Ln_2(\mu_3\text{-}OH)(tea)_4(piv)_6]\cdot xMeCN\ yCH_2Cl_2$ [Ln = Tb-Tm (4.7-4.11)

Synthesis of $[V^{III}_3Tb_2(\mu_3\text{-}OH)(tea)_4(piv)_6]\cdot MeCN$ (**4.7**).

A mixture of triethanolamine (483 mg, 3.3 mmol) in MeCN (5 mL) was added to a solution of VCl_3 (236 mg, 1.5 mmol), $TbCl_3$ (133 mg, 0.5 mmol), and pivalic acid (400 mg) in mixture of CH_2Cl_2 and MeCN (10 mL/10 mL) in a Schlenk tube. After 10 min stirring, Et_3N (1 mL) was added, and the solution stirred for a further 24 h. The solution was then filtered under anhydrous and oxygen-free conditions and left undisturbed for crystallization. Anal. Calc (found) % for $V^{III}_3Tb_2C_{54}H_{107}N_4O_{25}\cdot 2CH_2Cl_2$: C, 37.65 (37.74); H, 6.27 (6.28); N, 3.19 (3.14). Selected IR data (KBr, cm^{-1}): 2960 (m), 2848 (m), 1530 (m), 1483 (m), 1457 (w), 1425 (m), 1410 (m), 1367 (m), 1358 (m), 1225 (w), 1110 (m), 1077 (w), 1068 (m), 1028 (w), 915 (w), 899 (w), 734 (w), 647 (w), 615 (w), 558 (w), 499 (w).

Synthesis of $[V^{III}_3Dy_2(\mu_3\text{-}OH)(tea)_4(piv)_6]\cdot 2CH_2Cl_2$ (**4.8**).

In place of $DyCl_3\ 6H_2O$ (189 mg, 0.5 mmol) was used with the same procedure as above the complex **4.7** was obtained $[V^{III}_3Dy_2(\mu_3\text{-}OH)(tea)_4(piv)_6]\cdot 2CH_2Cl_2$ (**4.8**). Yield: 27% (120.8 mg, based on Dy). Anal. Calc

(found) % for $V^{III}_3Dy_2C_{54}H_{107}N_4O_{25}\cdot 2CH_2Cl_2$: C, 37.59 (37.64); H, 6.25 (6.17); N, 3.13 (3.10). Selected IR data (KBr, cm^{-1}): 3315 (w), 2961 (m), 2929 (w), 2871 (m), 1536 (m), 1483 (m), 1458 (w), 1421 (m), 1376 (m), 1360 (m), 1261 (w), 1225 (w), 1055 (m), 1024 (w), 955 (m), 925 (w), 897 (w), 809 (w), 792 (w), 744 (w), 630 (w), 603 (w), 431 (w).

Synthesis of $[V^{III}_3Ho_2(\mu_3\text{-}OH)(tea)_4(piv)_6]\cdot 2CH_2Cl_2$ MeCN (**4.9**).

In place of $HoCl_3$ (136 mg, 0.5 mmol) was used with the same procedure as above the complex **4.7** was obtained $[V^{III}_3Ho_2(\mu_3\text{-}OH)(tea)_4(piv)_6]\cdot 2CH_2Cl_2$ MeCN (**4.9**). Yield: 19% (90.54 mg, based on Ho). Anal. Calc (found) % for $V^{III}_3Ho_2C_{54}H_{107}N_4O_{25}\cdot 2CH_2Cl_2$ CH_3CN: C, 36.55 (37.14); H, 6.02 (6.12); N, 3.67 (3.18). Selected IR data (KBr, cm^{-1}): 2955 (m), 2847 (m), 1530 (m), 1480 (m), 1457 (w), 1420 (m), 1407 (m), 1367 (m), 1353 (m), 1225 (w), 1102 (m), 1077 (w), 1068 (m), 1020 (w), 915 (w), 897 (w), 734 (w), 647 (w), 603 (w), 558 (w), 491 (w).

Synthesis of $[V^{III}_3Er_2(\mu_3\text{-}OH)(tea)_4(piv)_6]\cdot 2CH_2Cl_2$ MeCN (**4.10**).

In place of $ErCl_3\cdot 6H_2O$ (191 mg, 0.5 mmol) was used with the same procedure as above the complex **4.7** was obtained $[V^{III}_3Er_2(\mu_3\text{-}OH)(tea)_4(piv)_6]\cdot 2CH_2Cl_2$ MeCN (**4.10**). Yield: 19% (133.8 mg, based on Er). Anal. Calc (found) % for $V^{III}_3Er_2C_{54}H_{107}N_4O_{25}\cdot 2CH_2Cl_2$ CH_3CN: C, 36.46 (36.44); H, 6.01 (6.04); N, 3.66 (3.58). Selected IR data (KBr, cm^{-1}): 2958 (m), 2847 (m), 1530 (m), 1480 (m), 1457 (w), 1422 (m), 1407 (m), 1367 (m), 1354 (m), 1225 (w), 1102 (m), 1081 (w), 1068 (m), 1020 (w), 915 (m), 897 (w), 738 (w), 647 (w), 603 (w), 558 (w), 495 (w).

Synthesis of $[V^{III}_3Tm_2(\mu_3\text{-}OH)(tea)_4(Piv)_6]\cdot 2CH_2Cl_2$ MeCN (**4.11**).

In place of $TmCl_3\cdot 6H_2O$ (197 mg, 0.5 mmol) was used with the same procedure as above the complex **4.7** was obtained $[V^{III}_3Tm_2(\mu_3\text{-}OH)(tea)_4(Piv)_6]\cdot 2CH_2Cl_2$ MeCN (**4.11**). Yield: 64% (306 mg, based on Tm). Anal. Calc (found) % for $V^{III}_3Tm_2C_{54}H_{107}N_4O_{25}\cdot 2CH_2Cl_2$ CH_3CN: C, 36.39 (36.41); H, 6.00 (6.07); N, 3.66 (3.54). Selected IR data (KBr, cm^{-1}): 2955 (m),

2847 (m), 1530 (m), 1480 (m), 1420 (m), 1407 (m), 1367 (m), 1225 (w), 1102 (m), 1077 (w), 1068 (m), 915 (w), 897 (w), 734 (w), 647 (w), 603 (w), 562 (w), 498 (w).

7.3.11 $[V^{III}_4Ln_3(\mu_2\text{-}OMe)_2(teaH)_6(p\text{-}Me\text{-}PhCO_2)_7]\cdot MeOH\ 3MeCN$ [Ln = Dy and Y (4.12-4.13)]

Synthesis of $[V^{III}_4Dy_3(\mu_2\text{-}OMe)_2(teaH)_6(p\text{-}Me\text{-}PhCO_2)_7]\cdot MeOH\ 3MeCN$ (**4.12**)

A mixture of triethanolamine (483 mg, 3.3 mmol) in MeCN (5 mL) was added to a solution of VCl_3 (314 mg, 2 mmol), $DyCl_3\ 6H_2O$ (566 mg, 1.5 mmol), and pivalic acid (400 mg) in mixture of CH_2Cl_2 and MeCN (10 mL/10 mL) in a Schlenk tube. After 10 min stirring, Et_3N (1 mL) was added, and the solution stirred for a further 24 h. The solution was then filtered under anhydrous and oxygen-free conditions and left undisturbed for crystallization. Yield: 31% (423.5 mg, based on Dy). Anal. Calc (found)% for $V^{III}_4Dy_3C_{94}H_{127}N_4O_{34}\cdot CH_3OH\ 3CH_3CN$: C, 44.39 (44.14); H, 5.20 (5.11); N, 4.13 (4.20). Selected IR data (KBr, cm^{-1}): 3308 (w), 2920 (w), 2855 (w), 1589 (w), 1534 (m), 1400 (m), 1262 (w), 1177 (w), 1066 (w), 898 (w), 861 (w), 764 (w), 619 (w), 472 (w).

Synthesis of $[V^{III}_4Y_3(\mu_2\text{-}OMe)_2(teaH)_6(p\text{-}Me\text{-}PhCO_2)_7]\cdot MeOH\ 3MeCN$ (**4.13**)

In place of YCl_3 (293.25mg, 1.5 mmol) was used with the same procedure as above the complex **4.12** was obtained $[V^{III}_4Y_3(\mu_2\text{-}OMe)_2(tea)_6(p\text{-}Me\text{-}PhCO_2)_7]\cdot MeOH\ 3MeCN$ (**4.13**).Yield: 26% (326.5 mg, based on Y). Anal. Calc (found)% for $V^{III}_4Y_3C_{94}H_{127}N_4O_{34}\cdot CH_3OH\ 3CH_3CN$: C, 48.29 (48.19); H, 5.66 (5.61); N, 5.02 (5.10). Selected IR data (KBr, cm^{-1}): 3315 (w), 2924 (w), 2858 (w), 1590 (w), 1539 (m), 1402 (m), 1268 (w), 1179 (w), 1069 (w), 898 (w), 861 (w), 768 (w), 619 (w), 478 (w).

7.3.12 Synthesis of $(Et_3NH)[V^{IV}_4Gd_3(O)_3(\mu_3\text{-}O)(\mu_3\text{-}OH)_5(teaH)_3(piv)_6](piv)\cdot MeCN\cdot CH_2Cl_2\cdot H_2O$ (4.14)

Synthesis of $(Et_3NH)[V^{IV}_4Gd_3(O)_3(\mu_3\text{-}O)(\mu_3\text{-}OH)_5(teaH)_3(piv)_6](piv)\cdot MeCN\cdot CH_2Cl_2\cdot H_2O$ (**4.14**)

A mixture of triethanolamine (786 mg, 6.6 mmol) in MeCN (5 mL) was added to a solution of VCl_3 (314 mg, 2 mmol), $GdCl_3$ (526 mg, 2 mmol), and pivalic acid (400 mg) in mixture of CH_2Cl_2 and MeCN (5 mL/5 mL) in a Schlenk tube. After 10 min stirring, Et_3N (1 mL) was added, and the solution stirred for a further 24 h. The solution was then filtered under anhydrous and oxygen-free conditions and left undisturbed for crystallization. Yield: 24% (266 mg, based on V). Anal. Calc (found)% for $V^{III}_4Gd_3C_{62}H_{130}N_5O_{33}$: C, 33.54 (33.51); H, 5.90 (5.91); N, 3.15 (3.20). Selected IR data (KBr, cm^{-1}): 2958 (w), 2899 (w), 2862 (w), 1601 (m), 1576 (m), 1543 (m), 1480 (m), 1460 (w), 1425 (w), 1413 (w), 1395 (m), 1374 (w), 1356 (m), 1344 (m), 1395 (m), 1218 (w), 1097 (m), 999 (w), 925 (w), 901 (w), 875 (w), 788 (w), 644 (w), 617 (w), 563 (w), 507 (w).

7.3.13 Synthesis of $[V^{III}_4Gd_5(\mu_3\text{-}OH)_7(teaH)_3(piv)_{12}]\cdot 4MeCN$ (4.15)

Synthesis of $[V^{III}_4Gd_5(\mu_3\text{-}OH)_7(teaH)_3(piv)_{12}]\cdot 4MeCN$ (**4.15**)

A mixture of triethanolamine (483 mg, 3.3 mmol) in MeCN (5 mL) was added to a solution of VCl_3 (314 mg, 2 mmol), $GdCl_3$ (526 mg, 2 mmol), and pivalic acid (400 mg) in mixture of CH_2Cl_2 and MeCN (8 mL/12 mL) in a Schlenk tube. After 10 min stirring, Et_3N (1 mL) was added, and the solution stirred for a further 24 h. The solution was then filtered under anhydrous and oxygen-free conditions and left undisturbed for crystallization. Yield: 28% (343.77 mg, based on Gd). Anal. Calc (found)% for $V^{III}_4Gd_5C_{84}H_{161}N_4O_{43}\ 4CH_3CN$: C, 36.00 (36.14); H, 5.68 (5.61); N, 3.65 (3.64).

7.3.14 Synthesis of $[V^{IV}_4V^{III}Dy_6(\mu_4\text{-}O)_4(\mu_2\text{-}O)_4(\mu_3\text{-}OH)_4(Bu^tDea)_4(NCCH_2COO)_8(MeOH)_6]Cl\cdot 8MeCN$ (4.16)

Synthesis of $[V^{IV}_4V^{III}Dy_6(\mu_4\text{-}O)_4(\mu_2\text{-}O)_4(\mu_3\text{-}OH)_4(Bu^tDea)_4(NCCH_2COO)_8(MeOH)_6]Cl\cdot 8MeCN$ (**4.16**)

A mixture of N-tert-butyldiethanolamine (532 mg, 3.3 mmol) was added to a solution of VCl_3 (157 mg, 1 mmol), $DyCl_3$ (377 mg, 1.0 mmol), and cyanoacetic acid (255 mg) in MeOH (12 mL) in a Schlenk tube. After 10 min stirring, Et_3N (1 mL) was added, and the solution stirred for a further 24 h. The solution was then filtered under anhydrous and oxygen-free conditions and left undisturbed for crystallization. Yield: 41% (222.5 mg, based on Dy). Anal. Calc (found)% for $V^{IV}_4V^{III}Dy_6C_{62}H_{112}N_{12}O_{42}$ 8MeCN: C, 28.86 (28.78); H, 4.16 (4.21); N, 8.45 (8.60). Selected IR data (KBr, cm^{-1}): 3334 (w), 1596 (m), 1409 (w), 1374 (m), 1082 (w), 904 (w), 629 (w), 575 (w).

7.3.15 Synthesis of $[V^{III}_2V^{IV}_4Dy_4(\mu_2\text{-}O)_4(\mu_3\text{-}OH)_2(\mu_2\text{-}OMe)_2(\mu\text{-}N_3)(\mu\text{-}Cl)(mDea)_2(mDeaH)(piv)_{14}(H_2O)_4]^{3+}$ (4.17)

Synthesis of $[V^{III}_2V^{IV}_4Dy_4(\mu_2\text{-}O)_4(\mu_3\text{-}OH)_2(\mu_2\text{-}OMe)_2(\mu\text{-}N_3)(\mu\text{-}Cl)(mDea)_2(mDeaH)(piv)_{14}(H_2O)_4]^{3+}$ (**4.17**)

A mixture of N-methyldiethanolamine (393 mg, 3.3 mmol) in MeCN (5 mL) was added to a solution of VCl_3 (220 mg, 1.4 mmol), $DyCl_3$ $6H_2O$ (264 mg, 0.7 mmol), and pivalic acid (400 mg) in mixture of CH_2Cl_2 and MeCN (10 mL/10 mL) in Schlenk tube. After 10 min stirring, Et_3N (1 mL) was added, and the solution stirred for a further 24 h. The solution was then filtered under anhydrous and oxygen-free conditions and left undisturbed for crystallization. Yield: 36% (226.4 mg, based on Dy). Anal. Calc (found)% for $V^{III}_2V^{IV}_4Dy_4C_{87}H_{172}N_9O_{46}$ Cl_3 11MeCN: C, 36.25 (36.43); H, 5.46 (5.75); N, 8.10 (7.79).

7.3.16 Synthesis of $[(V^{IV}=O)_4\{V^{V}O_3(OMe)\}_2Dy_4(\mu_4\text{-}O)_2(\mu_2\text{-}OMe)_4(OMe)_2(MeOH)_2(teaH)_2(piv)_4]$ (4.18)

Synthesis of $[(V^{IV}=O)_4\{V^{V}O_3(OMe)\}_2Dy_4(\mu_4\text{-}O)_2(\mu_2\text{-}OMe)_4(OMe)_2(MeOH)_2(teaH)_2(piv)_4]$ (**4.18**)

A mixture of triethanolamine (483 mg, 3.3 mmol) in MeCN (5 mL) was added to a solution of VCl_3 (157 mg, 1 mmol), $DyCl_3$ $6H_2O$ (226 mg, 0.6 mmol), Sodium azide (110mg, 1.69mmol) and pivalic acid (400 mg) in MeCN and MeOH (10 mL/10 mL) in a Schlenk tube. After 10 min stirring, Et_3N (1 mL) was added, and the solution stirred for a further 24 h. The solution was then filtered under anhydrous and oxygen-free conditions and left undisturbed for crystallization. Yield: 46% (148.8 mg, based on Dy). Anal. Calc (found)% for $V^{IV}_6Dy_4C_{42}H_{92}N_2O_{36}$: C, 23.54 (23.39); H, 4.41 (4.30); N, 1.31 (1.30).

7.3.17 $[V^{III}_4V^{IV}_4Ln_4(\mu_2\text{-}O)_4(mDea)_4(piv)_{18}(N_3)_6]\cdot nCH_2Cl_2$ MeCN (Ln = Gd (4.19), Dy (4.20) and Y (4.21))

Synthesis of $[V^{III}_4V^{IV}_4Gd_4(\mu_2\text{-}O)_4(mDea)_4(Piv)_{18}(N_3)_6]\cdot 4CH_2Cl_2$ MeCN (**4.19**)

A mixture of N-methyldiethanolamine (393 mg, 3.3 mmol) in MeCN (5 mL) was added to a solution of VCl_3 (157 mg, 1 mmol), $GdCl_3$ (116 mg, 0.44 mmol), and pivalic acid (400 mg) in MeCN and CH_2Cl_2 (5 mL/10 mL) in a Schlenk tube. After 10 min stirring, Et_3N (1 mL) was added, and the solution stirred for a further 24 h. The solution was then filtered under anhydrous and oxygen-free conditions and left undisturbed for crystallization. Yield: 38% (168 mg, based on Gd). Anal. Calc (found)% for $V^{III}_4V^{IV}_4Gd_4C_{110}H_{206}N_{22}O_{48}$ MeCN $4CH_2Cl_2$: C, 34.25 (34.64); H, 5.31 (5.44); N, 7.89 (8.01). Selected IR data (KBr, cm^{-1}): 2959 (m), 2927 (w), 2084 (s), 1550 (s), 1482 (s), 1457 (w), 1418 (s), 1378 (m), 1361 (m), 1226 (m), 1061 (w), 937 (w), 889 (w), 601 (w), 582 (w), 439 (w).

Synthesis of $[V^{III}_4V^{IV}_4Dy_4(\mu_2\text{-}O)_4(mDea)_4(Piv)_{18}(N_3)_6]\cdot 5CH_2Cl_2$ MeCN (**4.20**)

In place of $DyCl_3$ (165 mg, 0.44 mmol) was used with the same procedure as above the complex **4.19** was obtained $[V^{III}_4V^{IV}_4Dy_4(\mu_2\text{-}$

$O)_4(mDea)_4(Piv)_{18}(N_3)_6]\cdot 5CH_2Cl_2$ MeCN (**4.20**).Yield: 26% (326.5 mg, based on Y). Anal. Calc (found)% for $V^{III}_4V^{IV}_4Dy_4C_{109}H_{199}N_{22}O_{48}\cdot 5CH_2Cl_2$ CH_3CN: C, 34.01 (34.04); H, 5.10 (5.35); N, 7.64 (7.80). Selected IR data (KBr, cm^{-1}): 2961 (w), 2927 (w), 2086 (m), 1549 (s), 1482 (m), 1457 (w), 1418 (s), 1378 (m), 1361 (m), 1228 (m), 1059 (w), 934 (w), 889 (w), 600 (w), 581 (w), 439 (w).

Synthesis of $[V^{III}_4V^{IV}_4Y_4(\mu_2\text{-}O)_4(mDea)_4(Piv)_{18}(N_3)_6]\cdot 4CH_2Cl_2$ MeCN (**4.21**)

In place of YCl_3 (85.9 mg, 0.44 mmol) was used with the same procedure as above the complex **4.19** was obtained $[V^{III}_4V^{IV}_4Y_4(\mu_2\text{-}O)_4(mDea)_4(Piv)_{18}(N_3)_6]\cdot 5CH_2Cl_2$ MeCN (**4.21**).Yield: 56% (230.9 mg, based on Y). Anal. Calc (found)% for $V^{III}_4V^{IV}_4Dy_4C_{109}H_{199}N_{22}O_{48}\cdot 5CH_2Cl_2$ CH_3CN: C, 37.01 (37.16); H, 5.75 (5.83); N, 8.64 (8.59). Selected IR data (KBr, cm^{-1}): 2959 (w), 2927 (w), 2096 (m), 2084 (s), 1551 (s), 1482 (s), 1456 (w), 1417 (s), 1378 (m), 1360 (m), 1229 (m), 1060 (w), 934 (w), 890 (w), 602 (w), 581 (w), 439 (w).

8. Crystallographic Data

Complex	**2.1**	**2.2**
Formula	$V^{III}_2Tb_2C_{50}H_{102}N_2O_{20}$	$V^{III}_2Dy_2C_{50}H_{102}N_2O_{20}$
M_r(g/mol)	1471.08	1478.210
Colour	violette	violette
Crystal system	triclinic	triclinic
Space group	*P*-1 (No. 2)	*P*-1 (No. 2)
T[K]	150	180
a [Å]	9.7942(5)	9.7345(3)
b [Å]	13.5453(7)	13.6421(4)
c [Å]	14.6650(8)	14.4772(4)
α [°]	108.846(4)	115.179(2)
β [°]	107.528(4)	97.400(2)
γ [°]	105.723(4)	104.700(2)
V [$Å^3$]	1602.90(16)	1620.2(1)
Z	1	1
ρ calcd [g cm^{-3}]	1.522	1.515
μ (Ga-Ka) [g cm^{-1}]	1.34143	0.71073
F (000)	752	754
Reflns collected	7556	10816
Unique data	7079	654
R_{int}	0.0520	0.0677
Data with I>2σ(I)	18150	9027
Parameters/restraints	408/37	338/0
S on F^2	1.031	1.065
R_1 [I>2σ(I)]	0.0496	0.0630
wR_2 （all data）	0.1316	0.1803

Complex	**2.3**	**2.4**
Formula	$V^{III}_2Ho_2C_{50}H_{102}N_2O_{20}$	$V^{III}_2Er_2C_{50}H_{102}N_2O_{20}$
M_r(g/mol)	1483.07	1487.73
Colour	violette	violette
Crystal system	triclinic	triclinic
Space group	*P*-1 (No. 2)	*P*-1 (No. 2)
T[K]	150	180
a [Å]	9.8591(4)	9.7136(2)
b [Å]	13.3931(5)	13.5673(3)
c [Å]	14.5563(6)	14.3884(4)
α [°]	108.191(3)	115.124(2)
β [°]	107.516(3)	97.487(2)
γ [°]	106.344(3)	104.676(2)
V [Å^3]	1584.85(12)	1598.37(7)
Z	1	1
ρ calcd [g cm^{-3}]	1.554	1.546
μ (Ga-Ka) [g cm^{-1}]	1.34143	1.34143
F (000)	756	758
Reflns collected	7484	7538
Unique data	7085	7043
R_{int}	0.0577	0.0329
Data with I>2σ(I)	17316	18607
Parameters/restraints	358/1	437/109
S on F^2	1.047	1.056
R_1 [I>2σ(I)]	0.0556	0.0304
wR_2 （all data）	0.1566	0.0815

Complex	**2.5**	**2.6**
Formula	$V^{III}_2Tm_2C_{50}H_{102}N_2O_{20}$	$V^{III}_2Yb_2C_{50}H_{102}N_2O_{20}$
M_r(g/mol)	1491.0978	1499.290
Colour	violette	violette
Crystal system	triclinic	triclinic
Space group	*P*-1 (No. 2)	*P*-1 (No. 2)
T[K]	180	180
a [Å]	9.6975(3)	9.6989(8)
b [Å]	13.5481(4)	13.5245(16)
c [Å]	14.7270(4)	14.3722(12)
α [°]	109.939(2)	114.983(8)
β [°]	107.402(2)	97.693(7)
γ [°]	104.511(2)	104.490(8)
V [Å^3]	1595.97(9)	1591.7(3)
Z	1	1
ρ calcd [g cm^{-3}]	1.543	1.398
μ (Ga-Ka) [g cm^{-1}]	1.34143	1.34143
F (000)	752	632
Reflns collected	7489	16924
Unique data	6987	11912
R_{int}	0.0270	0.064
Data with I>2σ(I)	18954	16924
Parameters/restraints	427/ 63	352/0
S on F^2	1.071	1.116
R_1 [I>2σ(I)]	0.0247	0.0625
wR_2 （all data）	0.0642	0.1777

Complex	**2.7**	**2.8**
Formula	$V^{III}_2Y_2C_{50}H_{102}N_2O_{20}$	$V^{III}_2Dy_2C_{72}H_{88}N_4O_{22}$
M_r(g/mol)	1331.03	1788.340
Colour	violette	light yellow
Crystal system	triclinic	monoclinic
Space group	*P*-1 (No. 2)	*P2₁/c* (No. 14)
T[K]	180	180
a [Å]	9.7025(3)	15.8116(2)
b [Å]	13.5515(4)	10.1581(2)
c [Å]	14.4081(5)	24.3056(4)
α [°]	115.388(3)	90.000
β [°]	97.040(3)	100.619(1)
γ [°]	104.724(3)	90.000
V [Å^3]	1596.10(10)	3837.0(1)
Z	1	2
ρ calcd [g cm^{-3}]	1.385	1.547
μ (Ga-Ka) [g cm^{-1}]	1.54178	1.34143
F (000)	700	1800
Reflns collected	5950	32999
Unique data	5816	26299
R_{int}	0.0403	0.0384
Data with I>2σ(I)	13782	32999
Parameters/restraints	425/85	572/0
S on F^2	1.103	1.048
R_1 [I>2σ(I)]	0.0393	0.0353
wR_2 （all data）	0.1095	0.0955

Complex	**2.9**	**2.10**
Formula	$V^{III}_5Dy_8C_{228}H_{221}N_{40}O_{60}$	$V^{III}_4V^{IV}Dy_5C_{92}H_{176}N_7O_{40}$
M_r(g/mol)	6036.13	3028.65
Colour	yellow	blue
Crystal system	triclinic	monoclinic
Space group	*P*-1 (No. 2)	*P2₁/c* (No. 14)
T[K]	180	150
a [Å]	18.3907(8)	19.6751(3)
b [Å]	18.5825(8)	17.5398(2)
c [Å]	21.4659(11)	38.4949(7)
α [°]	66.947(4)	90
β [°]	67.510(4)	101.438(1)
γ [°]	79.134(3)	90
V [Å^3]	6230.2(6)	13020.7(3)
Z	1	4
ρ calcd [g cm^{-3}]	1.609	1.545
μ (Ga-Ka) [g cm^{-1}]	1.34143	1.34143
F (000)	2992	6060
Reflns collected	24780	29579
Unique data	17179	22012
R_{int}	0.0716	0.1276
Data with I>2σ(I)	76861	130744
Parameters/restraints	1379/11	1198/323
S on F^2	0.949	1.014
R_1 [I>2σ(I)]	0.0467	0.1011
wR_2 （all data）	0.1167	0.2690

Complex	**3.1**	**3.2**
Formula	$V^{III}_4La_4C_{124}H_{146}N_8O_{37}$	$V^{III}_4Nd_4C_{116}H_{134}N_4O_{37}$
M_r(g/mol)	3099.88	2956.98
Colour	red	pink
Crystal system	triclinic	monoclinic
Space group	*P*-1 (No. 2)	*P2₁/c* (No. 14)
T[K]	150	180
a [Å]	18.6536(8)	25.2503(8)
b [Å]	19.8007(7)	39.994(2)
c [Å]	22.7295(6)	35.5714(12)
α [°]	76.542(3)	90
β [°]	73.164(3)	101.567(3)
γ [°]	62.530(3)	90
V [Å^3]	7080.7(5)	35192(3)
Z	2	8
ρ calcd [g cm^{-3}]	1.454	1.116
μ (Ga-Ka) [g cm^{-1}]	1.34143	1.34143
F (000)	3124	11888
Reflns collected	32769	52577
Unique data	29646	22332
R_{int}	0.0724	0.1726
Data with I>2σ(I)	75332	163693
Parameters/restraints	1657/37	2944/374
S on F^2	1.101	0.936
R_1 [I>2σ(I)]	0.0678	0.0942
wR_2 （all data）	0.1599	0.2561

Complex	**3.3**	**3.4**
Formula	$V^{III}_4Gd_4C_{131}H_{157}N_9O_{36}Cl_{10}$	$V^{III}_4Dy_4C_{131}H_{157}N_9O_{36}Cl_{10}$
M_r(g/mol)	3620.91	2956.98
Colour	pink	violet
Crystal system	triclinic	triclinic
Space group	*P*-1 (No. 2)	*P*-1 (No. 2)
T[K]	150	150
a [Å]	20.1102(5)	19.9941(4)
b [Å]	20.8198(5)	20.7351(4)
c [Å]	22.4392(7)	22.3570(4)
α [°]	70.213(2)	70.115(1)
β [°]	66.988(2)	66.995(1)
γ [°]	66.988(2)	70.535(1)
V [Å^3]	7904.2(4)	7805.2(3)
Z	2	2
ρ calcd [g cm^{-3}]	1.521	1.550
μ (Ga-Ka) [g cm^{-1}]	1.34143	1.34143
F (000)	3624	3640
Reflns collected	36853	36565
Unique data	27166	26958
R_{int}	0.0573	0.0514
Data with I>2σ(I)	91011	99951
Parameters/restraints	1543/79	1582/4
S on F^2	1.043	1.000
R_1 [I>2σ(I)]	0.0400	0.0336
wR_2 （all data）	0.1040	0.0822

Complex	**3.5**	**3.6**
Formula	$V^{III}_4Y_4C_{129}H_{153}N_9O_{36}Cl_6$	$V^{III}_4La_4C_{132}H_{160}N_8O_{40}Cl_8$
M_r(g/mol)	3177.69	3541.72
Colour	pink	pink
Crystal system	triclinic	monoclinic
Space group	P-1 (No. 2)	$P2_1/c$ (No. 14)
T[K]	150	180
a [Å]	20.1139(3)	25.2852(11)
b [Å]	20.8423(3)	34.0806(17)
c [Å]	22.4394(3)	35.1536(17)
α [°]	70.8810(10)	90
β [°]	67.5130(10)	100.857(4)
γ [°]	70.7820(10)	90
V [Å^3]	7985.2(2)	29751(2)
Z	2	8
ρ calcd [g cm^{-3}]	1.322	1.169
μ (Ga-Ka) [g cm^{-1}]	1.34143	1.34143
F (000)	3256	10144
Reflns collected	32654	57232
Unique data	23521	13756
R_{int}	0.0699	0.3141
Data with I>2σ(I)	106253	57232
Parameters/restraints	1543/79	1417/0
S on F^2	1.015	1.029
R_1 [I>2σ(I)]	0.0519	0.2900
wR_2 （all data）	0.1420	0.3282

Complex	**3.7**	**3.8**
Formula	$V^{III}_4Gd_4C_{132}H_{160}N_8O_{40}Cl_8$	$V^{III}_4Dy_4C_{129}H_{154}N_6O_{40}Cl_{10}$
M_r(g/mol)	3615.03	3636.83
Colour	pink	pink
Crystal system	triclinic	monoclinic
Space group	*P*-1 (No. 2)	$P2_1/m$ (No. 11)
T[K]	150	180
a [Å]	19.6913(6)	14.2290(4)
b [Å]	20.2766(9)	28.8514(6)
c [Å]	22.2055(8)	19.2962(6)
α [°]	70.879(3)	90
β [°]	68.447(3)	110.994(2)
γ [°]	73.413(3)	90
V [Å^3]	7652.4(5)	7395.7(4)
Z	2	2
ρ calcd [g cm^{-3}]	1.569	1.633
μ (Ga-Ka) [g cm^{-1}]	1.34143	0.71073
F (000)	3624	3632
Reflns collected	35548	19839
Unique data	29058	13477
R_{int}	0.0510	0.1067
Data with I>2σ(I)	83413	49245
Parameters/restraints	1571/45	936/59
S on F^2	1.058	1.059
R_1 [I>2σ(I)]	0.0414	0.0772
wR_2 （all data）	0.1097	0.2146

Complex	**3.9**	**3.10**
Formula	$V^{III}_4Y_4C_{136}H_{164}N_{12}O_{40}$	$V^{III}_4La_4C_{96}H_{182}N_{12}O_{37}$
M_r(g/mol)	3166.18	2855.93
Colour	pink	pink
Crystal system	monoclinic	monoclinic
Space group	*C*2/c (No. 15)	*C*2/c (No. 15)
T[K]	150	150
a [Å]	34.7545(9)	14.6417(4)
b [Å]	21.3118(6)	33.0365(9)
c [Å]	24.2599(6)	26.9149(6)
α [°]	90	90
β [°]	124.520(2)	104.285(2)
γ [°]	90	90
V [Å^3]	14805.0(7)	12616.5(6)
Z	4	4
ρ calcd [g cm^{-3}]	1.420	1.504
μ (Ga-Ka) [g cm^{-1}]	1.34143	1.34143
F (000)	6528	5832
Reflns collected	16944	15213
Unique data	12579	11901
R_{int}	0.0585	0.0500
Data with I>2σ(I)	124977	118472
Parameters/restraints	891/74	642/23
S on F^2	1.056	1.075
R_1 [I>2σ(I)]	0.0435	0.0402
wR_2 （all data）	0.1206	0.1128

Complex	**3.11**	**3.12**
Formula	$V^{III}_4Gd_4C_{74}H_{128}N_4O_{35}$	$V^{III}_4Gd_4C_{96}H_{182}N_{12}O_{37}$
M_r(g/mol)	2408.69	2855.93
Colour	pink	pink
Crystal system	monoclinic	monoclinic
Space group	*P2₁/c* (No. 14)	*C*2/c (No. 15)
T[K]	180	150
a [Å]	16.3483(2)	14.6417(4)
b [Å]	31.5544(4)	33.0365(9)
c [Å]	22.3198(3)	26.9149(6)
α [°]	90	90
β [°]	93.2370(10)	104.285(2)
γ [°]	90	90
V [Å^3]	11495.5(3)	12616.5(6)
Z	4	4
ρ calcd [g cm^{-3}]	1.552	1.504
μ (Ga-Ka) [g cm^{-1}]	1.34143	1.34143
F (000)	5363	5832
Reflns collected	26549	15213
Unique data	20053	11901
R_{int}	0.0817	0.0500
Data with I>2σ(I)	63672	118472
Parameters/restraints	1131/136	642/23
S on F^2	1.038	1.075
R_1 [I>2σ(I)]	0.0639	0.0402
wR_2 （all data）	0.2014	0.1128

Complex	**3.13**	**3.14**
Formula	$V^{III}_4Gd_4C_{143}H_{181}N_9O_{36}$	$V^{III}_4Dy_4C_{110}H_{100}N_4O_{32}$
M_r(g/mol)	3789.22	2532.56
Colour	Block	pink
Crystal system	triclinic	monoclinic
Space group	*P*-1 (No. 2)	$P2_1/c$ (No. 14)
T[K]	150	150
a [Å]	19.8110(6)	13.8344(3)
b [Å]	20.4391(5)	50.5403(15)
c [Å]	22.2354(6)	16.6265(4)
α [°]	70.662(2)	90
β [°]	68.813(2)	97.988(2)
γ [°]	75.127(2)	90
V [Å^3]	7824.7(4)	11512.4(5)
Z	2	4
ρ calcd [g cm^{-3}]	1.392	1.461
μ (Ga-Ka) [g cm^{-1}]	1.34143	1.34143
F (000)	3816	4977
Reflns collected	36239	145497
Unique data	31358	53817
R_{int}	0.0428	0.1758
Data with I>2σ(I)	86781	145497
Parameters/restraints	1611/32	561/0
S on F^2	1.013	1.498
R_1 [I>2σ(I)]	0.0361	0.1487
wR_2 （all data）	0.0913	0.3924

Compound	**4.1**	**4.2**
Formula	$V^{III}_3Tb_2C_{76}H_{101}N_6O_{25}$	$V^{III}_3Dy_2C_{76}H_{101}N_6O_{25}$
M_r(g/mol)	1969.28	1976.44
Colour	green	green
Crystal system	triclinic	triclinic
Space group	*P*-1 (No. 2)	*P*-1 (No. 2)
T[K]	180	150
a [Å]	14.7356(4)	14.6519(6)
b [Å]	16.2294(4)	16.2078(10)
c [Å]	18.5289(5)	18.5253(8)
α [°]	97.054(2)	97.089(4)
β [°]	107.599(2)	107.293(3)
γ [°]	99.017(2)	99.429(4)
V [Å^3]	4102.85(19)	4073.9(4)
Z	2	2
ρ calcd [g cm^{-3}]	1.594	1.611
μ (Ga-Ka) [g cm^{-1}]	1.34143	1.34143
F (000)	1996	2000
Reflns collected	19079	18101
Unique data	14022	12610
R_{int}	0.0517	0.0663
Data with I>2σ(I)	55780	47796
Parameters/restraints	956/42	971/22
S on F^2	0.940	0.927
R_1 [I>2σ(I)]	0.0320	0.0377
wR_2 （all data）	0.0750	0.0822

Compound	**4.3**	**4.4**
Formula	$V^{III}_3Ho_2C_{76}H_{101}N_6O_{25}$	$V^{III}_3Er_2C_{76}H_{101}N_6O_{25}$
M_r(g/mol)	1981.30	1985.96
Colour	green	green
Crystal system	triclinic	triclinic
Space group	*P*-1 (No. 2)	*P*-1 (No. 2)
T[K]	180	180
a [Å]	14.7054(9)	14.5992(4)
b [Å]	16.2054(9)	16.2087(4)
c [Å]	18.4710(9)	18.5051(4)
α [°]	97.116(4)	97.710(2)
β [°]	107.266(4)	107.503(2)
γ [°]	99.024(5)	99.521(2)
V [Å^3]	4083.0(4)	4039.17(18)
Z	2	2
ρ calcd [g cm^{-3}]	1.612	1.633
μ (Ga-Ka) [g cm^{-1}]	1.34143	1.34143
F (000)	2004	2008
Reflns collected	14022	18814
Unique data	7241	13733
R_{int}	0.1022	0.0609
Data with I>2σ(I)	11557	49004
Parameters/restraints	966/43	975/50
S on F^2	0.953	1.010
R_1 [I>2σ(I)]	0.0568	0.0399
wR_2 （all data）	0.1343	0.0982

Compound	**4.5**	**4.6**
Formula	$V^{III}_3Yb_2C_{76}H_{101}N_6O_{25}$	$V^{III}_3Y_2C_{76}H_{101}N_6O_{25}$
M_r(g/mol)	1997.52	1829.26
Colour	green	green
Crystal system	triclinic	triclinic
Space group	*P*-1 (No. 2)	*P*-1 (No. 2)
T[K]	200	180
a [Å]	14.8376(5)	14.7482(7)
b [Å]	16.1841(7)	16.1901(7)
c [Å]	18.4268(7)	18.4676(10)
α [°]	96.832(3)	96.956(4)
β [°]	107.310(3)	107.534(4)
γ [°]	98.583(3)	98.770(3)
V [$Å^3$]	4114.1(3)	4089.8(4)
Z	2	2
ρ calcd [g cm^{-3}]	1.612	1.485
μ (Ga-Ka) [g cm^{-1}]	1.34143	1.34143
F (000)	2016	1892
Reflns collected	13304	16141
Unique data	9935	9772
R_{int}	0.0931	0.0860
Data with I>2σ(I)	31052	46726
Parameters/restraints	954/44	979/44
S on F^2	0.995	0.888
R_1 [I>2σ(I)]	0.0711	0.0410
wR_2 （all data）	0.1912	0.0824

Compound	**4.7**	**4.8**
Formula	$V^{III}_3Tb_2C_{58}H_{114}N_5O_{25}Cl_4$	$V^{III}_3Dy_2C_{58}H_{114}N_5O_{25}Cl_4$
M_r(g/mol)	1897.96	1901.18
Colour	blue	green
Crystal system	triclinic	triclinic
Space group	*P*-1 (No. 2)	*P*-1 (No. 2)
T[K]	180	180
a [Å]	14.2426(3)	14.2475(3)
b [Å]	16.1704(3)	16.1692(4)
c [Å]	19.0224(4)	19.0226(4)
α [°]	98.156(2)	98.031(2)
β [°]	105.045(2)	105.311(2)
γ [°]	103.925(2)	103.943(2)
V [Å^3]	4007.75(15)	4004.22(16)
Z	2	2
ρ calcd [g cm^{-3}]	1.573	1.595
μ (Ga-Ka) [g cm^{-1}]	1.34143	0.71073
F (000)	1903	1952
Reflns collected	62877	30258
Unique data	41598	24550
R_{int}	0.0734	0.0452
Data with I>2σ(I)	62877	74929
Parameters/restraints	793/0	907/68
S on F^2	1.132	1.064
R_1 [I>2σ(I)]	0.0671	0.0331
wR_2 （all data）	0.1969	0.0865

Compound	**4.9**	**4.10**
Formula	$V^{III}_3Ho_2C_{58}H_{114}N_5O_{25}Cl_4$	$V^{III}_3Er_2C_{58}H_{114}N_5O_{25}Cl_4$
M_r(g/mol)	1906.02	1910.68
Colour	green	green
Crystal system	triclinic	triclinic
Space group	*P*-1 (No. 2)	*P*-1 (No. 2)
T[K]	180	180
a [Å]	14.2423(2)	14.2530(3)
b [Å]	16.1438(2)	16.0945(4)
c [Å]	19.0200(3)	19.0426(4)
α [°]	98.081(1)	98.016(2)
β [°]	105.289(1)	105.329(2)
γ [°]	103.888(1)	103.775(2)
V [Å^3]	3996.85(10)	3995.04(16)
Z	2	2
ρ calcd [g cm^{-3}]	1.584	1.588
μ (Ga-Ka) [g cm^{-1}]	1.34143	1.34143
F (000)	1936	1940
Reflns collected	19319	18943
Unique data	17214	15890
R_{int}	0.0724	0.0525
Data with I>2σ(I)	54500	56774
Parameters/restraints	902/69	848/49
S on F^2	1.091	1.099
R_1 [I>2σ(I)]	0.0674	0.0436
wR_2 （all data）	0.1847	0.1189

Compound	**4.11**	**4.12**
Formula	$V^{III}_3Tm_2C_{58}H_{114}N_5O_{25}Cl_4$	$V^{III}_4Dy_3C_{101}H_{140}N_9O_{35}$
M_r(g/mol)	1914.02	2731.47
Colour	green	green
Crystal system	triclinic	triclinic
Space group	*P*-1 (No. 2)	*P*-1 (No. 2)
T[K]	180	180
a [Å]	14.2448(5)	17.6874(5)
b [Å]	16.0998(6)	18.8677(5)
c [Å]	19.0185(7)	19.5565(6)
α [°]	98.063(3)	86.263(2)
β [°]	105.298(3)	72.918(2)
γ [°]	103.806(3)	69.130(2)
V [Å^3]	3988.3(3)	5823.5(3)
Z	2	2
ρ calcd [g cm^{-3}]	1.594	1.558
μ (Ga-Ka) [g cm^{-1}]	1.34143	1.34143
F (000)	1944	2758
Reflns collected	16784	21494
Unique data	14458	13231
R_{int}	0.0699	0.0884
Data with I>2σ(I)	59789	59580
Parameters/restraints	887/46	1314/6
S on F^2	1.121	0.907
R_1 [I>2σ(I)]	0.0614	0.0499
wR_2 （all data）	0.1738	0.1159

Compound	**4.13**	**4.14**
Formula	$V^{III}_4Y_3C_{101}H_{140}N_9O_{35}$	$V^{IV}_4Gd_3C_{62}H_{130}N_5O_{33}Cl_2$
M_r(g/mol)	2510.72	2220.13
Colour	green	blue
Crystal system	triclinic	monoclinic
Space group	*P*-1 (No. 2)	*P2₁/c* (No. 14)
T[K]	180	180
a [Å]	17.6044(7)	19.7138(3)
b [Å]	18.8449(7)	17.4362(3)
c [Å]	19.4832(8)	25.8981(4)
α [°]	86.258(3)	90
β [°]	73.838(3)	92.1590(10)
γ [°]	69.029(3)	90
V [Å^3]	5792.7(4)	8895.7(2)
Z	2	4
ρ calcd [g cm^{-3}]	1.442	1.658
μ (Ga-Ka) [g cm^{-1}]	1.34143	1.34143
F (000)	2606	4476
Reflns collected	23955	20903
Unique data	17419	17964
R_{int}	0.0687	0.0553
Data with I>2σ(I)	63798	52925
Parameters/restraints	1340/14	1136/174
S on F^2	1.056	1.067
R_1 [I>2σ(I)]	0.0482	0.0473
wR_2 （all data）	0.1304	0.1285

Compound	**4.15**	**4.16**
Formula	$V^{III}_4Gd_5C_{92}H_{173}N_8O_{43}$	$V^{IV}_4V^{III}Dy_6C_{78}H_{136}N_{20}O_{42}$
M_r(g/mol)	3069.38	3255.76
Colour	blue	brown
Crystal system	monoclinic	monoclinic
Space group	*P2₁/c* (No. 14)	*P2₁/c* (No. 14)
T[K]	180	180
a [Å]	16.6601(13)	25.3732(6)
b [Å]	24.078(2)	16.3900(3)
c [Å]	32.567(3)	26.6658(7)
α [°]	90	90
β [°]	104.232(6)	92.351(2)
γ [°]	90	90
V [Å^3]	12663.0(18)	11080.1(4)
Z	4	4
ρ calcd [g cm^{-3}]	1.610	1.952
μ (Ga-Ka) [g cm^{-1}]	0.71073	1.34143
F (000)	6148	6364
Reflns collected	12551	25991
Unique data	6794	20212
R_{int}	0.1002	0.0826
Data with I>2σ(I)	27262	64424
Parameters/restraints	1203/183	1187/118
S on F^2	0.864	1.043
R_1 [I>2σ(I)]	0.0532	0.0684
wR_2 （all data）	0.1195	0.1873

Compound	**4.17**	**4.18**
Formula	$V^{III}_2V^{IV}_4Dy_4C_{109}H_{205}N_{20}O_{46}Cl_3$	$V^{IV}_6Dy_4C_{42}H_{92}N_2O_{36}$
M_r(g/mol)	3593.91	2156.81
Colour	pink	orange
Crystal system	monoclinic	monoclinic
Space group	*P2₁/c* (No. 14)	*P2₁/c* (No. 14)
T[K]	180	180
a [Å]	18.4556(2)	12.4336(3)
b [Å]	25.0485(2)	20.3983(3)
c [Å]	34.5293(3)	13.7690(3)
α [°]	90	90
β [°]	91.307(1)	90.790(2)
γ [°]	90	90
V [Å^3]	15958.2(3)	3491.82(12)
Z	4	2
ρ calcd [g cm^{-3}]	1.496	2.051
μ (Ga-Ka) [g cm^{-1}]	1.34143	1.34143
F (000)	7280	2096
Reflns collected	32879	8377
Unique data	23635	6524
R_{int}	0.0916	0.0614
Data with I>2σ(I)	143512	38371
Parameters/restraints	1477/262	420/1
S on F^2	1.030	0.981
R_1 [I>2σ(I)]	0.0683	0.0465
wR_2 （all data）	0.1866	0.1206

Compound	**4.19**	**4.20**
Formula	$V^{III}_4V^{IV}_4Gd_4C_{116}H_{217}N_{23}O_{48}Cl_8$	$V^{III}_4V^{IV}_4Dy_4C_{117}H_{219}N_{23}O_{48}Cl_{10}$
M_r(g/mol)	4022.23	4128.16
Colour	violet	violet
Crystal system	monoclinic	monoclinic
Space group	*P2₁/c* (No. 14)	*P2₁/c* (No. 14)
T[K]	180	180
a [Å]	20.4026(3)	20.2322(5)
b [Å]	23.3591(3)	23.4775(10)
c [Å]	38.0067(5)	37.9990(9)
α [°]	90	90
β [°]	95.846(1)	95.966(2)
γ [°]	90	90
V [Å^3]	18019.3(4)	17951.8(10)
Z	4	4
ρ calcd [g cm^{-3}]	1.483	1.527
μ (Ga-Ka) [g cm^{-1}]	0.71073	0.71073
F (000)	8136	8336
Reflns collected	37185	25546
Unique data	25485	13498
R_{int}	0.0905	0.1167
Data with I>2σ(I)	69986	75144
Parameters/restraints	1813/250	1831/255
S on F^2	1.069	0.935
R_1 [I>2σ(I)]	0.0640	0.0556
wR_2 （all data）	0.1831	0.1328

Compound	**4.21**
Formula	$V^{III}_4V^{IV}_4Y_4C_{116}H_{217}N_{23}O_{48}Cl_8$
M_r(g/mol)	3748.87
Colour	violet
Crystal system	monoclinic
Space group	*P2₁/c* (No. 14)
T[K]	150
a [Å]	20.1785(2)
b [Å]	23.4164(2)
c [Å]	37.8904(4)
α [°]	90
β [°]	95.9770(10)
γ [°]	90
V [Å^3]	17806.2(3)
Z	4
ρ calcd [g cm^{-3}]	1.398
μ (Ga-Ka) [g cm^{-1}]	1.34143
F (000)	7736
Reflns collected	41006
Unique data	30677
R_{int}	0.1066
Data with I>2σ(I)	101390
Parameters/restraints	1792/261
S on F^2	1.041
R_1 [I>2σ(I)]	0.0878
wR_2 （all data）	0.2548

9. Bibliography

1. Mattis D. C. *The Theory of Magnetism Made Simple*. Utah: World Scientific, 2006.
2. N. Jones, *Nature.*, 2011, **472**, 22-24.
3. Pointillart F., Cador O., Le Guennic B., et al. *Uncommon lanthanide ions in purely 4f Single Molecule Magnets*. Coord. Chem. Rev., 2017, **346**, 150-175.
4. Sessoli R., Powell A. K. *Strategies towards single molecule magnets based on lanthanide ions*. Coord. Chem. Rev., 2009, **253**, 2328-2341.
5. Kahn O, *Molecular Magnetism*, VCH, 1993.
6. Miller J. S., Drillon M. *Magnetism: Molecules to Materials*, Vol. I-V, Wiley-VCH, 2002-2005.
7. Zhang P., Guo Y. N., Tang J. *Recent advances in dysprosium-based single molecule magnets: Structural overview and synthetic strategies*. Coord. Chem. Rev., 2013, **257**, 1728-1763.
8. Woodruff D. N., Winpenny R. E., Layfield R. A.. *Lanthanide single-molecule magnets*. Chem. Rev., 2013, **113**, 5110-5148.
9. Sorace L., Benelli C., Gatteschi D. *Lanthanides in molecular magnetism: old tools in a new field*. Chem. Soc. Rev., 2011, **40**, 3092-104.
10. Tuna F., Smith C. A., Bodensteiner M, et al. *A high anisotropy barrier in a sulfur-bridged organodysprosium single-molecule magnet*. Angew. Chem. Int. Ed., 2012, **51**, 6976-6980.
11. Gould C. A., Darago L. E., Gonzalez M. I., et al. *A Trinuclear Radical-Bridged Lanthanide Single-Molecule Magnet*. Angew. Chem. Int. Ed., 2017, **56**, 10103-10107.
12. Meng Y. S., Jiang S. D., Wang B. W., et al. *Understanding the Magnetic Anisotropy toward Single-Ion Magnets*. Accounts Chem. Res., 2016, **49**, 2381-2389.
13. Rinehart J. D., Long J. R.. *Exploiting single-ion anisotropy in the design of f-element single-molecule magnets*. Chem. Sci., 2011, **2**, 2078-2085.
14. Gatteschi D., Sessoli R., Villain J. *Molecular Nanomagnets*: New York Oxford University Press, 2006.
15. Domingo N., Bellido E., Ruiz-Molina D. *Advances on structuring, integration and magnetic characterization of molecular nanomagnets on surfaces and devices*. Coord. Chem. Rev., 2012, **41**, 258-302.
16. Coronado E. *Molecular magnetism: from chemical design to spin control in molecules, materials and devices*. Nat. Rev. Mater., 2020, **5**, 87-104.

17. Sessoli R., Gatteschi D., Caneschi A., et al. *Magnetic bistability in a metal-ion cluster*. Nature, 1993, **365**, 141-143.

18. Urdampilleta M., Klyatskaya S., Cleuziou J. P., et al. *Supramolecular spin valves*. Nat. Mater., 2011, **10**, 502-506.

19. Miller J. S. *Magnetically ordered molecule-based materials*. Coord. Chem. Rev., 2011, **40**, 3266-3296.

20. Aromi G., Aguila D., Gamez P., et al. *Design of magnetic coordination complexes for quantum computing*. Chem. Soc. Rev., 2012, **41**, 537-546.

21. Candini A., Klyatskaya S., Ruben M., et al. *Graphene Spintronic Devices with Molecular Nanomagnets*. Nano Lett., 2011, **11**, 2634-2639.

22. Bogani L., Wernsdorfer W. *Molecular spintronics using single-molecule magnets*. Nat. Mater., 2008, **7**, 179-186.

23. Ren M., Zheng L. M. *Lanthanide-based Single Molecule Magnets*. Acta Chim. Sinica, 2015, **73**, 1091-1113.

24. Ako A. M., Hewitt I. J., Mereacre V., et al. *A Ferromagnetically Coupled Mn_{19} Aggregate with a Record S=83/2 Ground Spin State*. Angew. Chem. Int. Ed.,2006, **45**, 4926-4929.

25. Stamatatos T. C., Abboud K. A., Wernsdorfer W., et al. *"Spin Tweaking" of a High-Spin Molecule: An Mn_{25} Single-Molecule Magnet with an S = 61/2 Ground State*. Angew. Chem. Int. Ed., 2007, **46**, 884-888.

26. Kang S., Zheng H., Liu T., et al. *A ferromagnetically coupled Fe_{42} cyanide-bridged nanocage.* Nat. Commun., 2015, **6**, 5955.

27. Murugesu M, Habrych M, Wernsdorfer W, et al. *Single-Molecule Magnets: A Mn_{25} Complex with a Record S = 51/2 Spin for a Molecular Species*. J. Am. Chem. Soc., 2004, **126**, 4766-4767.

28. Abbasi, Parisa, et al. *Transition metal single-molecule magnets: a {Mn_{31}} nanosized cluster with a large energy barrier of∼ 60 K and magnetic hysteresis at∼ 5 K.* J. Am. Chem. Soc. 2017, **139**, 15644-15647.

29. Tasiopoulos, Anastasios J., et al. Giant single-molecule magnets: a Mn_{84} torus and its supramolecular nanotubes. Angew. Chem. Int. Ed. 2004, **116**, 2169-2173.

30. Oliver W. *A Criterion for the Anisotropy Barrier in Single Molecule Magnets*. Inorg. Chem., 2007, **46**, 10035-10037.

31. Neese F., Pantazis D. A. *What is not required to make a single molecule magnet*. Faraday Discuss., 2011, **148**, 229-38.

32. Ruiz E., Cirera J., Cano J., et al. *Can large magnetic anisotropy and high spin really coexist*. Chem. Commun., 2008, **50**, 52-54.

33. Zadrozny, J. M., Xiao, D. J., Atanasov, M., Long, G. J., et al. *Magnetic*

blocking in a linear iron (I) complex. Nat. Chem., 2013, **5**, 577-581.

34. Xiang, J., Liu, J. J., Chen, X. X., Jia, L. H., Yu, F., Wang, B. W., et al. *Slow magnetic relaxation in a mononuclear 8-coordinate Fe(II) complex*. Chem. Commun., 2017, **53**, 1474-1477.

35. Li, G. L., Wu, S. Q., Zhang, L. F., Wang, Z., Ouyang, Z. W., et al. *Field-Induced Slow Magnetic Relaxation in an Octacoordinated Fe(II) Complex with Pseudo-D_{2d} Symmetry: Magnetic, HF-EPR, and Theoretical Investigations*. Inorg. Chem., 2017, **56**, 8018-8025.

36. Zadrozny, Joseph M., and Jeffrey R. Long. *Slow magnetic relaxation at zero field in the tetrahedral complex $[Co(SPh)_4]^{2-}$*. J. Am. Chem. Soc., 2011, **133**, 20732-20734.

37. Yao, X. N., Du, J. Z., Zhang, Y. Q., Leng, X. B., Yang, M. W., Jiang, S. D., et al. *Two-coordinate Co (II) imido complexes as outstanding single-molecule magnets*. J. Am. Chem. Soc., 2017, **139**, 373-380.

38. Rechkemmer, Y., Breitgoff, F. D., Van Der Meer, M., Atanasov, M., Hakl, M., et al. *A four-coordinate cobalt (II) single-ion magnet with coercivity and a very high energy barrier*. Nat. Commun., 2016, **7**, 10467.

39. Bunting, P. C., Atanasov, M., Damgaard-Møller, E., Perfetti, M., Crassee, I., et al. *A linear cobalt (II) complex with maximal orbital angular momentum from a non-Aufbau ground state*. Science, 2018, **362**, 7319.

40. Poulten, R. C., Page, M. J., Algarra, A. G., Le Roy, J. J., López, I., et al. Synthesis, electronic structure, and magnetism of $[Ni(6\text{-}Mes)_2]^+$: A two-coordinate nickel (I) complex stabilized by bulky N-heterocyclic carbenes. J. Am. Chem. Soc., 2013, **135**, 13640-13643.

41. Miklovič, J., Valigura, D., Boča, R., & Titiš, J. *A mononuclear Ni (II) complex: a field induced single-molecule magnet showing two slow relaxation processes*. Dalton Trans., 2015, **44**, 12484-12487.

42. Lomjanský, D., Moncol, J., Rajnák, C., et al. *Field effects to slow magnetic relaxation in a mononuclear Ni (II) complex.* Chem. Commun., 2017, **53**, 6930-6932.

43. Barra, A. L., Caneschi, A., Cornia, A., Fabrizi De Biani, F., Gatteschi, D., et al. *Single-molecule magnet behavior of a tetranuclear iron (III) complex. The origin of slow magnetic relaxation in iron (III) clusters*. J. Am. Chem. Soc., 1999, **121**, 5302-5310.

44. Murrie, Mark. *Cobalt (II) single-molecule magnets*. Chem. Soc. Rev., 2010, **39**, 1986-1995.

45. Yang, E. C., Wernsdorfer, W., et al. *Fast magnetization tunneling in tetranickel (II) single-molecule magnets*. Inorg. Chem., 2006, **45**, 529-546.

46. Castro, S. L., Sun, Z., Bollinger, J. C., Hendrickson, D. N., et al. *Tetranuclear vanadium (III) carboxylate chemistry, and a new example of a metal butterfly complex exhibiting spin frustration: structure and properties of* $[V_4O_2(O_2CEt)_7(bpy)_2](ClO_4)$. J. Chem. Soc., Chem. Commun.1995, **24**, 2517-2518.

47. Hendrickson, DavidáN, CraigáM Grant, and StephanieáL Castro. *Single-molecule magnets: out-of-phase ac susceptibility signals from tetranuclear vanadium (III) complexes with an S=3 ground state*. Chem. Commun., 1998, **6**, 721-722.

48. Single-Molecule Magnets and Related Phenomena, Springer-Verlag Berlin Heidelberg, 2006.

49. Demir S., Zadrozny J. M., Nippe M., et al. *Exchange coupling and magnetic blocking in bipyrimidyl radical-bridged dilanthanide complexes*. J. Am. Chem. Soc., 2012, **134**, 18546-18549.

50. Dolinar B. S., Alexandropoulos D. I., Vignesh K R, et al. *Lanthanide Triangles Supported by Radical Bridging Ligands*. J. Am. Chem. Soc., 2018, **140**, 908-911.

51. Meihaus K. R., Corbey J. F., Fang M., et al. *Influence of an inner-sphere K+ ion on the magnetic behavior of* N_2^{3-} *radical-bridged dilanthanide complexes isolated using an external magnetic field*. Inorg. Chem., 2014, **53**, 3099-30107.

52. Bar A. K., Kalita P.., Singh M. K., et al. *Low-coordinate mononuclear lanthanide complexes as molecular nanomagnets*. Coord. Chem. Rev., 2018, **367**,163-216.

53. Ishikawa, N., Sugita, M., Ishikawa, T., et al. Lanthanide double-decker complexes functioning as magnets at the single-molecular level. J. Am. Chem. Soc., 2003, **125**, 8694-8695.

54. Domingo N., Luis F., Nakano M., et al. *Particle-size dependence of magnetization relaxation in* Mn_{12} *crystals*. Phys. Rev. B., 2009, **79**, 214404.

55. Gatteschi D., Sessoli R., Villain J.. *Molecular Nanomagnets*, Oxford University Press, Oxford, 2006.

56. Pinkowicz D., Ren M., Zheng L. M., et al. *Control of the Single-Molecule Magnet Behavior of Lanthanide-Diarylethene Photochromic Assemblies by Irradiation with Light*. Chem. Eur. J., 2014, **20**, 12502-12513.

57. Chen Y. C., Liu J. L., Ungur L., et al. *Symmetry-Supported Magnetic Blocking at 20 K in Pentagonal Bipyramidal Dy(III) Single-Ion Magnets*. J. Am. Chem. Soc., 2016, **138**, 2829-2837.

58. Liu, J., Chen, Y. C., Liu, J. L., Vieru, V., Ungur, L., Jia, J. H., et al. *A Stable Pentagonal Bipyramidal Dy(III) Single-Ion Magnet with a Record*

Magnetization Reversal Barrier over 1000 K. J. Am. Chem. Soc., 2016, **138**, 5441-5450.

59. Gupta S. K., Rajeshkumar T., Rajaraman G., et al. *An air-stable Dy(iii) single-ion magnet with high anisotropy barrier and blocking temperature*. Chem. Sci., 2016, **7**, 5181-5191.

60. Ding Y. S., Chilton N. F., Winpenny R. E. P., et al. *On Approaching the Limit of Molecular Magnetic Anisotropy: A Near-Perfect Pentagonal Bipyramidal Dysprosium Single-Molecule Magnet*. Angew. Chem. Int. Ed., 2016, **55**, 16071-16074.

61. Guo F. S., Day B. M., Chen Y. C., et al. *A Dysprosium Metallocene Single-Molecule Magnet Functioning at the Axial Limit*. Angew. Chem. Int. Ed., 2017, **56**, 11445-11449.

62. Goodwin C. a P., Ortu F., Reta D., et al. *Molecular magnetic hysteresis at 60 kelvin in dysprosocenium*. Nature, 2017, **548**, 439-442.57.

63. Guo F. S., Day B. M., Chen Y. C., et al. *Magnetic hysteresis up to 80 kelvin in a dysprosium metallocene single-molecule magnet*. Science, 2018, **362**, 1400-1403.

64. Wu, J., Zhao, L., Zhang, L., Li, X. L., et al. *Metallosupramolecular Coordination Complexes: The Design of Heterometallic 3d-4f Gridlike Structures*. Inorg. Chem., 2016, **55**, 5514-5519.

65. Yao, M. X., Zhu, Z. X., Lu, X. Y., et al. *Rare single-molecule magnets with six-coordinate Ln^{III} ion exhibiting trigonal antiprism configuration*. Dalton Trans., 2016, **45**, 10689-10695.

66. Yin J. J., Chen C., Zhuang G. L., et al. *Anion-Dependent Assembly of 3d-4f Heterometallic Clusters Ln_5Cr_2 and Ln_8Cr_4*. Inorg. Chem., 2020, **59**, 1959-1966.

67. Singh S. K., Beg M. F., Rajaraman G. *Role of Magnetic Exchange Interactions in the Magnetization Relaxation of 3d-4f Single-Molecule Magnets: A Theoretical Perspective.* Chem. Eur. J., 2016, **22**, 672-680.

68. Xiong G., You L. X., Ren B. Y., et al. *Structure and Magnetocaloric Effect of Two Kinds of Ln-MnII Heterometallic Coordination Polymers Produced by Fractional Crystallization.* Eur. J. Inorg. Chem., 2016, **2016**, 3969-3977.

69. Li X. L., Min F. Y., Wang C., et al. *Ln(III)-Mn(II)-Ln(III) heterometallic compounds: rare linear SMMs with divalent manganese ions.* Dalton Trans., 2015, **44**, 3430-3438.

70. Zhang H. G., Du Y. C., Yang H., et al. *A new family of Co_4Ln_8 metallacrowns with a butterfly-shaped structure*. Inorg. Chem. Front., 2019, **6**, 1904-1908.

71. Oyarzabal I., Artetxe B., Rodriguez-Dieguez A., et al. *A family of acetato-diphenoxo triply bridged dimetallic $Zn^{II}Ln^{III}$ complexes: SMM behavior and luminescent properties.* Dalton Trans., 2016, **45**, 9712-9726.

72. Song X., Liu P., Wang C.,et al. *Three sandwich-type zinc(ii)–lanthanide(iii) clusters: structures, luminescence and magnetic properties*. RSC Adv., 2017, **7**, 22692-22698.

73. Dey A., Acharya J., Chandra sekhar V. *Heterometallic 3d–4f Complexes as Single-Molecule Magnets*. Chem. Asian. J., 2019, **14**, 4433-4453.

74. Sun W. B., Yan P. F., Jiang S. D., et al. *High symmetry or low symmetry, that is the question-high performance Dy(iii) single-ion magnets by electrostatic potential design*. Chem. Sci., 2016, **7**, 684-691.

75. Langley S. K., Wielechowski D. P., Vieru V., et al. *A $Cr^{III}_2Dy^{III}_2$ Single-Molecule Magnet: Enhancing the Blocking Temperature through 3d Magnetic Exchange*. Angew. Chem. Int. Ed., 2013, **52**, 12014-12019.

76. Langley S. K., Chilton N. F., Moubaraki B., et al*. Anisotropy barrier enhancement via ligand substitution in tetranuclear $Co^{III}_2Ln^{III}_2$ single molecule magnets.* Chem. Commun., 2013, **49**, 6965-6967.

77. Langley S. K., Wielechowski D. P., Vieru V., et al. *The first 4d/4f single-molecule magnet containing a $Ru^{III}_2Dy^{III}_2$ core*. Chem. Commun., 2015, **51**, 2044-2047.

78. Liu, J. L., Wu, J. Y., Chen, Y. C., Mereacre, V., Powell, A. K., Ungur, L., et al. *A heterometallic Fe^{II}–Dy^{III} single-molecule magnet with a record anisotropy barrier.* Angew. Chem. Int. Ed., 2014, **53**, 12966-12970.

79. Andruh M. *Heterotrimetallic complexes in molecular magnetism*. Chem. Commun., 2018, **54**, 3559-3577.

80. Wang, J., Li, Q. W., Wu, S. G., Chen, Y. C., Wan, R. C., et al. *Opening magnetic hysteresis by axial ferromagnetic coupling: from mono-decker to double-decker metallacrown*. Angew. Chem. Int. Ed., 2021, **133**, 5359-5366.

81. Evangelisti, M., Candini, A., Ghirri, A., Affronte, M., et al. *Spin-enhanced magnetocaloric effect in molecular nanomagnets.* Appl. Phys. Lett. 2005, **87**, 072504.

82. Manoli, M., Johnstone, R. D. L., Parsons, S., et al. *A Ferromagnetic Mixed-Valent Mn Supertetrahedron: Towards Low-Temperature Magnetic Refrigeration with Molecular Clusters*. Angew. Chem. Int. Ed. 2007, **46**, 4456-4460.

83. Karotsis, G.; Evangelisti, M.; Dalgarno, S. J.; Brechin, E. K. *A calix [4] arene 3d/4f magnetic cooler.* Angew. Chem. Int. Ed. 2009, **52**, 10112-10115.

84. Evangelisti, M.; Brechin, E. K. Recipes for enhanced molecular cooling. Dalton Trans. 2010, **39**, 4672-4676.

85. R. Shaw, R. H. Laye, L. F. Jones, D. M. Low, C. Talbot-Eeckelaers, Q. Wei, C. J. Milios, S. Teat, M. Helliwell, et al. 1,2,3-Triazolate-bridged tetradecametallic transition metal clusters $[M_{14}(L)_6O_6(OMe)_{18}X_6]$(M= Fe^{III}, Cr^{III} and $V^{III/IV}$) and related compounds: Ground-state spins ranging from S= 0 to S= 25 and spin-enhanced magnetocaloric effect, Inorg. Chem., 2007, **46**, 4968-4978.

86. M. Evangelisti, F. Luis, et al. *Magnetothermal properties of molecule-based materials.* J. Mater. Chem., 2006, **16**, 2534–2549.

87. E. Warburg, Ann. Phys., 1881, **249**, 141.

88. Debye, Peter. *Einige bemerkungen zur magnetisierung bei tiefer temperatur*. Annalen der Physik., 1926, **386**, 1154-1160.

89. Giauque, W. F. *A thermodynamic treatment of certain magnetic effects. A proposed method of producing temperatures considerably below 1 absolute.* J. Am. Chem. Soc., 1927, **49**, 1864-1870.

90. Giauque, W. F., and D. P. MacDougall. *The production of temperatures below one degree absolute by adiabatic demagnetization of gadolinium sulfate*. J. Am. Chem. Soc., 1935, **57**, 1175-1185.

91. M. Evangelisti, O. Roubeau, E. Palacios, A. Camo´n, T. N. Hooper, E. K. Brechin and J. J. Alonso, Cryogenic magnetocaloric effect in a ferromagnetic molecular dimer., Angew. Chem., Int. Ed., 2011, **50**, 6606–6609.

92. J. Bartolome, F. Luis, J.F. Fernandez, Molecular Magnets: Physics andApplications, Springer-Verlag, Berlin Heidelberg, 2014.

93. Yu.I. Spichkin, A.K. Zvezdin, S.P. Gubin, A.S. Mischenko, et al. *Magnetic molecular clusters as promising materials for refrigeration in low-temperature regions.* J. Phys. D:Appl. Phys. 2001, **34**, 1162.

94. O. Gutfleisch, M.A. Willard, E. Brück, C.H. Chen, et al. *Magnetic materials and devices for the 21st century: stronger, lighter, and more energy efficient*. Adv. Mater., 2011, **23**, 821-842.

95. Sessoli, Roberta. *Chilling with magnetic molecules*. Angew. Chem., Int. Ed., 2012, **51**, 43-45.

96. Zheng, Y. Z., Zhou, G. J., Zheng, Z. and Winpenny, R. E. *Molecule-based magnetic coolers*. Chem. Soc. Rev., 2014, **43**, 1462-1475.

97. Sharples, Joseph W., and David Collison. *Reprint of "Coordination compounds and the magnetocaloric effect"*. Polyhedron. 2013, **66**, 15-27.

98. Pecharsky, Vitalij K., and Karl A. Gschneidner Jr. *Magnetocaloric effect*

and magnetic refrigeration. J. Magn. Magn. Mater., 1999, **200**, 44-56.

99. A.M. Tishin, Y.I. Spichkin, *The Magnetocaloric Effect and Its Applications*, Taylor & Francis, London, 2003.

100. R.L. Carlin, *Magnetochemistry*, Springer-Verlag, Berlin, 1986.

101. Zhang, X. X., Wei, H. L., Zhang, Z. Q., Zhang, L. *Anisotropic magnetocaloric effect in nanostructured magnetic clusters*. Phys. Rev. Lett., 2001, **87**, 157203.

102. H. Chen, C.-B. Ma, M.-Q. Hu, H.-M. Wen, H.-H. Cui, et al. *Octanuclear $Mn^{III}_6Mn^{II}Ln$ (Ln= Gd, Dy and Er) clusters with a novel core topology: syntheses, structures, and magnetic properties.* Dalton. Trans. 2013, **42**, 4908-4914.

103. Rinck, J., Novitchi, G., Van den Heuvel, et al. *An Octanuclear $[Cr^{III}_4Dy^{III}_4]$ 3d–4f Single-Molecule Magnet*. Angew. Chem. Int. Ed., 2010, **49**, 7583-7587.

104. Mereacre, V., Ako, A. M., Clérac, R., Wernsdorfer, W et al. *Heterometallic $[Mn_5$-$Ln_4]$ Single-Molecule Magnets with High Anisotropy Barriers.* Chem. Eur. J., 2008, **14**, 3577-3584.

105. Abbas, G., Lan, Y., Mereacre, V., Buth, G., Sougrati, M. T et al. *Synthesis, magnetism, and ^{57}Fe Mossbauer spectroscopic study of a family of $[Ln_3Fe_7]$ coordination clusters (Ln= Gd, Tb, and Er).* Inorg. Chem., 2013, **52**, 11767-11777.

106. Warner, M., Din, S., Tupitsyn, I. S., Morley, G. W., Stoneham, A. M., Gardener, J. A. and Aeppli, G. *Potential for spin-based information processing in a thin-film molecular semiconductor*. Nature, 2013, **503**, 504-508.

107. Roch, N., Florens, S., Bouchiat, V., Wernsdorfer, W., and Balestro, F.. *Quantum phase transition in a single-molecule quantum dot*. Nature, 2008, **453**, 633-637.

108. Corradini, V., Ghirri, A., Candini, A., Biagi, R., del Pennino, U., Dotti, G., and Affronte, M. *Magnetic cooling at a single molecule level: a spectroscopic investigation of isolated molecules on a surface*. Adv. Mater., 2013, **25**, 2816-2820.

109. Lee, C. F., Leigh, D. A., Pritchard, R. G., Schultz, D., Teat, S. J., Timco, G. A., and Winpenny, R. E. *Hybrid organic–inorganic rotaxanes and molecular shuttles*. Nature, 2009, **458**, 314-318.

110. R. Sessoli, H.L. Tsai, A.R. Schake, S.Y. Wang, J.B. Vincent, K. Folting, D. Gat-teschi, et al. High-spin molecules:$[Mn_{12}O_{12}(O_2CR)_{16}(H_2O)_4]$. J. Am. Chem. Soc. 1993, **115**, 1804-1816.

111. A. Caneschi, D. Gatteschi, R. Sessoli, A.L. Barra, et al., *Alternating*

current susceptibility, high field magnetization, and millimeter band EPR evidence for a ground S= 10 state in $[Mn_{12}O_{12}(CH_3COO)_{16}(H_2O)_4]$ $2CH_3COOH$ $4H_2O$. J. Am. Chem. Soc. 1991, **113**, 5873-5874.

112. Sessoli, R., Gatteschi, D., Caneschi, A., and Novak, M. A. *Magnetic bistability in a metal-ion cluster*. Nature, 1993, **365**, 141-143.

113. Clérac, R., Miyasaka, H., Yamashita, M., and Coulon, C. *Evidence for single-chain magnet behavior in a* Mn^{III}*−*Ni^{II} *chain designed with high spin magnetic units: a route to high temperature metastable magnets*. J. Am. Chem. Soc., 2002, **124**, 12837-12844.

114. Kostakis, G. E.; Hewitt, I. J.; Ako, A. M.; Mereacre, V.; Powell, A. K., *Magnetic coordination clusters and networks: synthesis and topological description*. Philos. Trans. R. Soc. A., 2010, **368**, 1509-1536.

115. S. Piligkos, G. Rjaraman, M. Soler, N. Kirchner, J. van Slageren, R. Bircher,S. Parsons, H.-U. Güdel, K. Kortus, W. Wernsdorfer, G. Christou, E.K. Brechin. *Studies of an enneanuclear manganese single-molecule magnet*. J. Am. Chem. Soc. 2005, **127**, 5572.

116. C. Boskovic, E.K. Brechin, W.E. Streib, K. Folting, J.C. Bollinger, D.N. Hen-drickson, G. Christou. *Single-molecule magnets: a new family of Mn12 clusters of formula* $[Mn_{12}O_8X_4(O_2CPh)_8L_6]$. J. Am. Chem. Soc. 2002, **124**, 3725.

117. M. Soler, W. Wernsdorfer, K. Folting, M. Pink, G. Christou. *Single-molecule magnets: a large* Mn_{30} *molecular nanomagnet exhibiting quantum tunneling of magnetization*. J. Am. Chem. Soc. 2004, **126**, 2156-2165.

118. M. Soler, W. Wernsdorfer, K.A. Abboud, J.C. Huffman, E.R. Davidson, D.N.Hendrickson, G. Christou. *Single-molecule magnets: two-electron reduced version of a* Mn_{12} *complex and environmental influences on the magnetization relaxation of* $(PPh_4)_2[Mn_{12}O_{12}(O_2CCHCl_2)_{16}(H_2O)_4]$. J. Am. Chem. Soc. 2003, **125**, 3576-3588.

119. G.G. Condorelli, A. Motta, I.L. Fragala, F. Giannazzo, V. Raineri, A. Caneschi,D. Gatteschi. *Anchoring molecular magnets on the Si (100) surface*. Angew. Chem. Int. Ed. 2004, **43**, 4081-4084.

120. E. Coronado, A. Torment-Aliga, A. Gaita-Arino, C. Giminez-Saiz, F.M.Romero, W. Wernsdorfer. *Polycationic* Mn_{12} *Single-Molecule Magnets as Electron Reservoirs with S>10 Ground States*. Angew. Chem. Int. Ed. 2004, **43**, 6152-6282.

121. Andruh, Marius. *Compartmental Schiff-base ligands—a rich library of tectons in designing magnetic and luminescent materials*. Chem. Commun. 2011, **47**, 3025-3042.

122. C.J. Milios, P.A. Wood, S. Parsons, D. Foguet-Albiol, C. Lampropoulos,

et al. *The use of methylsalicyloxime in manganese chemistry: A [Mn_3^{III}] triangle and its oxidation to a [$Mn_4^{IV}Ce_2^{III}$] rod.* Inorg. Chim. Acta., 2007, **13**, 3932-3940.

123. Osa, S., Kido, T., Matsumoto, N., Re, N., Pochaba, A., & Mrozinski, J. *A tetranuclear 3d− 4f single molecule magnet:[$Cu^{II}LTb^{III}(hfac)_2]_2$.* J. Am. Chem. Soc., 2004, **126**, 420-421.

124. Costes, Jean-Pierre, Françoise Dahan, and Wolfgang Wernsdorfer. *Heterodinuclear Cu−Tb single-molecule magnet*. Inorg. Chem., 2006, **45**, 5-7.

125. V. Chandrasekhar, B.M. Pandian, R. Boomishankar, A. Steiner, et al. *Trinuclear Heterobimetallic Ni_2Ln complexes [L_2Ni_2Ln][ClO_4](Ln=La, Ce, Pr, Nd, Sm, Eu, Gd, Tb, Dy, Ho, and Er; LH_3=(S)P[N(Me)N=CH−C_6H_3-2-OH-3-OMe]$_3$): From Simple Paramagnetic Complexes to Single-Molecule Magnet Behavior.* Inorg. Chem., 2008, **47**, 4918-4929.

126. T. Yamaguchi, J.-P. Costes, Y. Kisima, M. Kojima, Y. Sunatsuki, et al *Face-Sharing Heterotrinuclear M^{II}−Ln^{III}−M^{II} (M= Mn, Fe, Co, Zn; Ln= La, Gd, Tb, Dy) Complexes: Synthesis, Structures, and Magnetic Properties*. Inorg. Chem. 2010, **49**, 9125-9135.

127. Chandrasekhar, V., Pandian, B. M., et al. Synthesis, Structure, and Magnetism of Heterobimetallic Trinuclear Complexes {[L_2Co_2Ln][X]}[Ln=Eu, X=Cl; Ln=Tb, Dy, Ho, X= NO_3; LH_3=(S)P[N(Me)N=CH−C_6H_3-2-OH-3-OMe]$_3$]: A 3d−4f Family of Single-Molecule Magnets. Inorg. Chem., 2009, **48**, 1148-1157.

128. Feltham, H. L., Clérac, R., Ungur, L., et al. *By design: a macrocyclic 3d–4f single-molecule magnet with quantifiable zero-field slow relaxation of magnetization*. Inorg. Chem., 2013, **52**, 3236-3240.

129. Mondal, K. C., Kostakis, G. E., Lan, Y., Wernsdorfer, W., et al. *Defect-Dicubane Ni_2Ln_2(Ln=Dy, Tb) Single Molecule Magnets*. Inorg. Chem., 2011, **50**, 11604-11611.

130. Mori, F., Ishida, T., and Nogami, T. *Structure and magnetic properties of 3d–4f heterometallic complexes containing di-2-pyridyl ketoximate: An approach to single-molecule magnets*. Polyhedron, 2005, **24**, 2588-2592.

131. Khan, A., Akhtar, M. N., Lan, Y., Anson, C. E., et al. *Linear shaped hetero-metallic [Zn_2Ln_4] clusters with Schiff base ligand: Synthesis, characterization and magnetic properties*. Inorg. Chim. Acta., 2021, **524**, 120437.

132. Colacio, E., Ruiz, J., Mota, A. J., Palacios, M. A., Cremades, E., Ruiz, E., et al. *Family of carboxylate-and nitrate-diphenoxo triply bridged dinuclear $Ni^{II}Ln^{III}$ complexes (Ln= Eu, Gd, Tb, Ho, Er, Y): Synthesis, experimental and theoretical magneto-structural studies, and single-*

molecule magnet behavior. Inorg. Chem., 2012, **51**, 5857-5868.

133. Thuesen, C. A., Pedersen, K. S., Schau-Magnussen, M., Evangelisti, M., Vibenholt, et al. *Fluoride-bridged {Ln_2Cr_2} polynuclear complexes from semi-labile mer-[$CrF_3(py)_3$] and [Ln (hfac)(H_2O)$_2$]*. Dalton Trans., 2012, **41**, 11284-11292.

134. Liu, C. M., Zhang, D. Q., Hao, X., et al. *Trinuclear [Co^{III}_2–Ln^{III}](Ln= Tb, Dy) Single-Ion Magnets with Mixed 6-Chloro-2-Hydroxypyridine and Schiff Base Ligands*. Chem. Asian. J., 2014, **9**, 1847-1853.

135. Baniodeh, A., Lan, Y., Novitchi, G., Mereacre, V., et al. *Magnetic anisotropy and exchange coupling in a family of isostructural $Fe^{III}_2Ln^{III}_2$ complexes*. Dalton Trans., 2013, **42**, 8926-8938.

136. Pointillart, F., Bernot, K., et al. *Effects of 3d–4f Magnetic Exchange Interactions on the Dynamics of the Magnetization of Dy^{III}-M^{II}-Dy^{III} Trinuclear Clusters.* Chem. Eur. J., 2007, **13**, 1602-160.

137. Xu, G. F., Gamez, P., Tang, J., Clerac, et al. *$M^{III}Dy^{III}_3$ (M= Fe^{III}, Co^{III}) complexes: three-blade propellers exhibiting slow relaxation of magnetization.* Inorg. Chem., 2012, **51**, 5693-5698.

138. Abtab, S. M. T., Majee, M. C., Maity, M., et al. *Tetranuclear Hetero-Metal [$Co^{II}_2Ln^{III}_2$](Ln= Gd, Tb, Dy, Ho, La) Complexes Involving Carboxylato Bridges in a Rare μ4–η2: η2 Mode: Synthesis, Crystal Structures, and Magnetic Properties*. Inorg. Chem., 2014, **53**, 1295-1306.

139. J. Rinck, G. Novitchi, W.V. den Heuvel, L. Ungur, Y. Lan, et al. An *Octanuclear [$Cr^{III}_4Dy^{III}_4$] 3d–4f Single-Molecule Magnet*. Angew. Chem. Int. Ed. 2010, **49**, 7583.

140. Li, M., Lan, Y., Ako, A. M., Wernsdorfer, W., et al. *A family of 3d-4f octa-nuclear [$Mn^{III}_4Ln^{III}_4$] wheels (Ln= Sm, Gd, Tb, Dy, Ho, Er, and Y): synthesis, structure, and magnetism*. Inorg. Chem., 2010, **49**, 11587-11594.

141. Li, M., Ako, A. M., Lan, Y., Wernsdorfer, W., et al, *New heterometallic [$Mn^{III}_4Ln^{III}_4$] wheels incorporating formate ligands.* Dalton Trans., 2010, **39**, 3375-3377.

142. V. Mereacre, A.M. Ako, R. Clérac, W. Wernsdorfer, et al. *Heterometallic [Mn_5-Ln_4] Single-Molecule Magnets with High Anisotropy Barriers*. Chem. Eur. J., 2008, **14**, 3577-3584.

143. M. Hoły´nska, D. Premuˇzi´c, I.-R. Jeon, W. Wernsdorfer, et al. *[$Mn^{III}_6O_3Ln_2$] Single-Molecule Magnets: Increasing the Energy Barrier Above 100K.* Chem. Eur. J. 2011, **17**, 9605-9610.

144. C. Papatriantafyllopoulou, M. Estrader, C.G. Efthymiou, et al. *In search for mixed transition metal/lanthanide single-molecule magnets: Synthetic routes to Ni^{II}/Tb^{III} and Ni^{II}/Dy^{III} clusters featuring a 2-pyridyl*

oximate ligand, Polyhedron, 2009, **28**, 1652-1655.

145. C. Aronica, G. Pilet, G. Chastanet, W. Wernsdorfer, et al. *A nonanuclear dysprosium (III)–copper (II) complex exhibiting single-molecule magnet behavior with very slow zero-field relaxation*. Angew. Chem. Int. Ed. 2006, **45**, 4659.

146. Liu, J. L., Chen, Y. C., Li, Q. W., Gómez-Coca, S., Aravena, et al. *Two 3d–4f nanomagnets formed via a two-step in situ reaction of picolinaldehyde.* Chem. Commun., 2013, **49**, 6549-6551.

147. C. M. Zaleski, E. C. Depperman, J. W. Kampf, et al. *Synthesis, structure, and magnetic properties of a large lanthanide–transition-metal single-molecule magnet*. Angew. Chem., Int. Ed., 2004, **43**, 3912–3914.

148. S. Xue, Y. Guo, L. Zhao, et al. *Molecular Magnetic Investigation of a Family of Octanuclear [Cu_6Ln_2] Nanoclusters*. Inorg. Chem., 2014, **53**, 8165–8171.

149. S. Ghosh, Y. Ida, T. Ishida and A. Ghosh. Linker stoichiometry-controlled stepwise supramolecular growth of a flexible Cu_2Tb single molecule magnet from monomer to dimer to one-dimensional chain. Cryst. Growth Des., 2014, **14**, 2588–2598.

150. L. Zhao, J. Wu, H. Ke and J. Tang. *Family of Defect-Dicubane Ni_4Ln_2 (Ln = Gd, Tb, Dy, Ho) and Ni_4Y_2 Complexes: Rare Tb(III) and Ho(III) Examples Showing SMM Behavior*. Inorg. Chem., 2014, **53**, 3519–3525.

151. K.-Q. Hu, S.-Q. Wu, A.-L. Cui and H.-Z. Kou. *Synthesis, structure, and magnetic properties of heterotrimetallic tetranuclear complexes*. Transition Met. Chem., 2014, **39**, 713–718.

152. Y.-F. Zeng, G.-C. Xu, X. Hu, Z. Chen, X.-H. Bu, S. Gao and E. C. Sañudo. *Single-Molecule-Magnet Behavior in a $Fe_{12}Sm_4$ Cluster*. Inorg. Chem., 2010, **49**, 9734–9736.

153. J. Ruiz, G. Lorusso, M. Evangelisti, E. K. Brechin, S. J. A. Pope and E. Colacio. *Closely-Related $Zn^{II}_2Ln^{III}_2$ Complexes (Ln^{III} = Gd, Yb) with Either Magnetic Refrigerant or Luminescent Single-Molecule Magnet Properties.* Inorg. Chem., 2014, **53**, 3586–3594.

154. Y.-N. Guo, G.-F. Xu, Y. Guo and J. Tang, Relaxation dynamics of dysprosium (III) single molecule magnets. Dalton Trans., 2011, **40**, 9953–9963.

155. Sañudo, E. C., Smith, A. A., Mason, P. V., et al. *Polynuclear vanadium complexes from thermal decomposition of [$V_3O(O_2CPh)_6(H_2O)_3$]Cl*. Dalton Trans., 2006, **16**, 1981-1987.

156. Sorolla, M. G., Wang, X., Makarenko, T., & Jacobson, A. J. *A large spin, magnetically anisotropic, octanuclear vanadium (iii) wheel*. Chem. Commun., 2019, **55**, 342-344.

157. Aronica, C., Chastanet, G., Zueva, E., Borshch, S. A., et al. *A Mixed-Valence Polyoxovanadate(III, IV) Cluster with a Calixarene Cap Exhibiting Ferromagnetic V(III)−V(IV) Interactions.* J. Am. Chem. Soc., 2008, **130**, 2365-2371.

158. Westrup, K. C. M., Boulon, M. E., Totaro, P., Nunes, G. G., et al. *Adding Remnant Magnetization and Anisotropic Exchange to Propeller-like Single-Molecule Magnets through Chemical Design.* Chem. Eur. J., 2014, **20**, 13681-13691.

159. Cao, J. P., Xue, Y. S., Hu, Z. B., Luo, X. M., Cui, C. H., et al. *Exploring the Magnetic Interaction of Asymmetric Structures Based on Chiral V^{III}_8 Clusters*. Inorg. Chem., 2019, **58**, 2645-2651.

160. Tidmarsh, I. S., Batchelor, L. J., Scales, E., Laye, et al. *Tri-, tetra-and octa-metallic vanadium (III) clusters from new, simple starting materials: interplay of exchange and anisotropy effects.* Dalton Trans., 2009, **43**, 9402-9409.

161. Saber, M. R., Thirunavukkuarasu, K., Greer, S. M., et al. *Magnetostructural and EPR studies of anisotropic vanadium trans-dicyanide molecules*. Inorg. Chem., **59**, 13262-13269.

162. Laye, R. H., Murrie, M., Ochsenbein, S., Bell, A. R., Teat, S. J., et al. *Solvothermal Syntheses of High-Nuclearity Vanadium (iii) Clusters.* Chem. Eur. J., **9**, 6215-6220.

163. Khanra, S., Kloth, M., Mansaray, H., Muryn, C. A., et al. *Synthesis of molecular vanadium (III) phosphonates.* Angew. Chem., Int. Ed., **119**, 5664-5667.

164. Tidmarsh, I. S., Scales, E., Brearley, P. R., et al. *Synthesis, structural, and magnetic studies on a redox family of tetrametallic vanadium clusters:$\{V^{IV}_4\}$,$\{V^{III}_2V^{IV}_2\}$, and $\{V^{III}_4\}$ butterfly complexes*. Inorg. Chem., 2007, **46**, 9743-9753.

165. Rinck, J., Lan, Y., Anson, C. E., Powell, A. K. *Coordination Cluster Nuclearity Decreases with Decreasing Rare Earth Ionic Radius in 1: 1 Cr/Ln N-Butyldiethanolamine Compounds: A Journey across the Lanthanide Series from $Cr_4^{III}La_4$–$Cr_4^{III}Tb_4$ via $Cr_3^{III}Dy_3$ and $Cr_3^{III}Ho_3$ to $Cr_2^{III}Er_2$–$Cr_2^{III}Lu_2$*. Inorg. Chem., 2015, **7**, 3107-3117.

166. Peng, Y., Singh, M. K., Mereacre, V., Anson, C. E., Rajaraman, G., Powell, A. K. *Mechanism of magnetisation relaxation in $\{M^{III}_2Dy^{III}_2\}$(M= Cr, Mn, Fe, Al)"Butterfly" complexes: how important are the transition metal ions here?*. Chem. Sci., 2019, **21**, 5528-5538.

167. Peng, Y., Mereacre, V., Anson, C. E., Powell, A. K. *Butterfly $M_2^{III}Er_2$ (M^{III}= Fe and Al) SMMs: Synthesis, Characterization, and Magnetic Properties*. ACS Omega, 2018, **6**, 6360-6368.

168. Mondal, Sourav, and Alessandro Lunghi. *Unraveling the Contributions to Spin–Lattice Relaxation in Kramers Single-Molecule Magnets*. J. Am. Chem. Soc., 2022, **50**, 22965-22975.

169. Gu L, Wu R. *Origins of slow magnetic relaxation in single-molecule magnets*. Phys.Rev.Lett., 2020, **11**, 117203.

170. Gu L, Wu R. *Origin of the anomalously low Raman exponents in single molecule magnets*. Phys. Rev. B, 2021, **1**, 014401.

171. Pfleger R F, Schlittenhardt S, Merkel M P, et al. *Terminal ligand and packing effects on slow relaxation in an isostructural set of $[Dy(H_2dapp)X_2]^+$ single molecule magnets*. Chem. Eur. J., 2021, **61**, 15086-15095.

172. Ako, A. M., Mereacre, V., Clérac, R., Hewitt, I. J., Lan, Y., Anson, C. E., Powell, A. K. *High-nuclearity 3d–4f $[Fe^{III}_5Ln^{III}_8]$ complexes: synthesis, structure and magnetic properties*. Dalton Trans., 2007, **45**, 5245-5247.

173. Ako, A. M., Mereacre, V., Clérac, R., Hewitt, I. J., Lan, Y., Buth, G., Powell, A. K. *Tridecanuclear $[Mn^{III}_5Ln^{III}_8]$ Complexes Derived from N-^{t}Butyl-diethanolamine: Synthesis, Structures, and Magnetic Properties*. Inorg. Chem., 2009, **14**, 6713-6723.

174. Chilton N F, Collison D, McInnes E J L, et al. *An electrostatic model for the determination of magnetic anisotropy in dysprosium complexes*. Nat. Commun., 2013, **1**, 2551.

175. Kaemmerer H, Baniodeh A, Peng Y, et al. *Inorganic approach to stabilizing nanoscale toroidicity in a tetraicosanuclear $Fe_{18}Dy_6$ single molecule magnet*. J. Am. Chem. Soc., 2020, 35, 14838-14842.

176. Woodruff, D. N., Winpenny, R. E. and Layfield, R. A. *Lanthanide single-molecule magnets*. Chem. Rev. 2013, **113**, 5110-5148.

177. Zhang, P., Zhang, L. and Tang, J. *Lanthanide single molecule magnets: progress and perspective*. Dalton Trans., 2015, **44**, 3923-3929.

178. Sun, H. L., Wang, Z. M. and Gao, S. *Strategies towards single-chain magnets.* Coord. Chem. Rev., 2010, **254**, 1081-1100.

179. A. M. Tishin and Y. I. Spichkin, *The Magnetocaloric Effect and its Application*, IOP Publishing, Bristol and Philadelphia, 2003.

180. E. Warburg, *Magnetic investigations*. Ann. Phys., 1881, **249**, 141.

181. Giauque, W. F. and MacDougall, D. P.. *The production of temperatures below one degree absolute by adiabatic demagnetization of gadolinium sulfate*. J. Am. Chem. Soc., 1935, **7**, 1175-1185.

182. Zheng, Y. Z., Evangelisti, M. and Winpenny, R. E. *Co–Gd phosphonate complexes as magnetic refrigerants*. *Chem. Sci.*, 2011, **1**, 99-102.

183. M. Evangelisti, F. Luis, L. J. de Jongh and M. Affronte.. *Magnetothermal properties of molecule-based materials*. J. Mater. Chem., 2006, **16**, 2534-2549.

184. M. Evangelisti and E. K. Brechin., *Recipes for enhanced molecular cooling*. Dalton Trans., 2010, **39**, 4672-4676.

185. F. Torres, J. M. Herna´ndez, X. Bohigas and J. Tejada. *Giant and time-dependent magnetocaloric effect in high-spin molecular magnets*. Appl. Phys. Lett., 2000, **77**, 3248-3250.

186. X. X. Zhang, H. L. Wei, Z. Q. Zhang and L. Zhang. Anisotropic magnetocaloric effect in nanostructured magnetic clusters. Phys. Rev. Lett., 2001, **87**, 157203.

187. M. Affronte, A. Ghirri, S. Carretta, G. Amoretti, S. Piligkos, G. A. Timco and R. E. P. Winpenny. *Engineering molecular rings for magnetocaloric effect*. Appl. Phys. Lett., 2004, **84**, 3468-3470.

188. S. Ma, W. B. Cui, D. Li, N. K. Sun, D. Y. Geng, X. Jiang and Z. D. Zhang. *Large cryogenic magnetocaloric effect of $DyCo_2$ nanoparticles without encapsulation*. Appl. Phys. Lett., 2008, **92**, 173113.

189. K. Matsumoto, A. Matsuzaki, K. Kamiya and T. Numazawa. *Magnetocaloric effect, specific heat, and entropy of iron-substituted Gadolinium Gallium Garnets $Gd_3(Ga_{1-x}Fe_x)_5O_{12}$*. Jpn. J. Appl. Phys., 2009, **48**, 113002.

190. Peng, J. B., Zhang, Q. C., Kong, X. J., Ren, Y. P., Long, L. S., Huang, R. B. and Zheng, Z. *A 48-Metal Cluster Exhibiting a Large Magnetocaloric Effect.* Angew. Chem. Int. Ed., 2011, **123**, 10837-10840.

191. Lorusso, G., Sharples, J. W., Palacios, E., Roubeau, O., Brechin, E. K., Sessoli, R. and Evangelisti, M. *A dense metal–organic framework for enhanced magnetic refrigeration*. Adv. Mater., 2013, **25**, 4653-4656.

192. Karotsis, G., Evangelisti, M., Dalgarno, S. J. and Brechin, E. K. *A calix [4] arene 3d/4f magnetic cooler.* Angew. Chem. Int. Ed. 2009, **121**, 10112-10115.

193. Karotsis, G., Evangelisti, M., Dalgarno, S. J. and Brechin, E. K. *A calix [4] arene 3d/4f magnetic cooler.* Angew. Chem. Int. Ed. 2009, **121**, 10112-10115.

194. Schray D, Westerbeck D, Braun J, et al. *Fe–Gd Ferromagnetic Cyclic Coordination Cluster $[Fe^{III}_4Gd^{III}_4(teaH)_8(N_3)8(H_2O)]$ with Magnetic Anisotropy─ Theory and Experiment*. Inorg. Chem., 2023, **17**, 6642-6648.

195. C. Papatriantafyllopoulou, E. E. Moushi, G. Christou, A. J. Tasiopoulos. *Filling the gap between the quantum and classical worlds of nanoscale magnetism: giant molecular aggregates based on paramagnetic 3d*

metal ions. Chem. Soc. Rev. 2016, **45**, 1597-1628.

196. X.-Y. Zheng, X.-J. Kong, Z. Zheng, L.-S. Long, L.-S. Zheng. *High-nuclearity lanthanide-containing clusters as potential molecular magnetic coolers.* Acc. Chem. Res. 2018. **51**, 517-525.

197. Dinca, A. S., Ghirri, A., Madalan, A. M., Affronte, M., Andruh, M. *Dodecanuclear [$Cu^{II}_6Gd^{III}_6$] nanoclusters as magnetic refrigerants*. Inorg. Chem., 2012, **7**, 3935-3937.

198. Dermitzaki, D., Lorusso, G., Raptopoulou, C. P., Psycharis, V., Escuer, A., Evangelisti, M., Stamatatos, T. C. *Molecular Nanoscale Magnetic Refrigerants: A Ferrimagnetic {$Cu^{II}_{15}Gd^{III}_7$} Cagelike Cluster from the Use of Pyridine-2, 6-dimethanol.* Inorg. Chem., 2013, **18**, 10235-10237.

199. Li, Z. Y., Wang, Y. X., Zhu, J., Liu, S. Q., Xin, G., Zhang, J. J., Duan, C. Y. *Three series of 3d–4f heterometallic polymers based on [$LnCu_6$] or [Ln_6Cu_{24}] clusters and formate bridges: Displaying significant magnetocaloric effect.* Cryst. Growth. Des., 2013, **8**, 3429-3437.

200. Liu, J. L., Lin, W. Q., Chen, Y. C., Gómez-Coca, S., Aravena, D., Ruiz, E., Tong, M. L. *Cu^{II}-Gd^{III} Cryogenic Magnetic Refrigerants and Cu_8Dy_9 Single-Molecule Magnet Generated by In Situ Reactions of Picolinaldehyde and Acetylpyridine: Experimental and Theoretical Study*. Chem. Eur. J., 2013, **51**, 17567-17577.

201. Leng, J. D., Liu, J. L., Tong, M. L. *Unique nanoscale {$Cu^{II}_{36}Ln^{III}_{24}$}(Ln= Dy and Gd) metallo-rings*. Chem. Comm., 2012, **43**, 5286-5288.

202. Pineda, E. M., Tuna, F., Zheng, Y. Z., Winpenny, R. E., McInnes, E. J. *Wells–Dawson Cages as Molecular Refrigerants*. Inorg. Chem., 2013, **23**, 13702-13707.

203. Hosoi, A., Yukawa, Y., Igarashi, S., Teat, S. J., Roubeau, O., Evangelisti, M., Aromí, G. *A molecular pair of [$GdNi_3$] tetrahedra bridged by water molecules.* Chem. Eur. J., 2011, **30**, 8264-8268.

204. Li, Z. Y., Zhu, J., Wang, X. Q., Ni, J., Zhang, J. J., Liu, S. Q., Duan, C. Y. *New 3d–4f heterometallic clusters built from mixed glycine and iminodiacetate acid: dioctahedron {La_2Ni_9} and onion-like {Gd_5}⊂{Ni_{12}} with interesting magnetocaloric effect*. Dalton Trans., 2013, **16**, 5711-5717.

205. Wang, P., Shannigrahi, S., Yakovlev, N. L., Hor, T. A. *General One-Step Self-Assembly of Isostructural Intermetallic $Co^{II}_3Ln^{III}$ Cubane Aggregates.* Inorg. Chem., 2012, **22**, 12059-12061.

206. Pineda, E. M., Tuna, F., Pritchard, R. G., Regan, A. C., Winpenny, R. E., McInnes, E. J. *Molecular amino-phosphonate cobalt–lanthanide clusters*. Chem. Comm., 2013, **34**, 3522-3524.

207. Zhang, Z. M., Pan, L. Y., Lin, W. Q., Leng, J. D., Guo, F. S., Chen, Y. C.,

Tong, M. L. *Wheel-shaped nanoscale 3d–4f {$Co^{II}_{16}Ln^{III}_{24}$} clusters (Ln= Dy and Gd)*. Chem. Comm., 2013, **73**, 8081-8083.

208. Zheng, Y. Z., Pineda, E. M., Helliwell, M., Winpenny, R. E. *Mn^{II}–Gd^{III} phosphonate cages with a large magnetocaloric effect*. Chem. Eur. J., 2012, **14**, 4161-4165.

209. Liu, J. L., Lin, W. Q., Chen, Y. C., Leng, J. D., Guo, F. S., Tong, M. L. *Symmetry-related [$Ln^{III}_6Mn^{III}_{12}$] clusters toward single-molecule magnets and cryogenic magnetic refrigerants*. Inorg. Chem., 2013, **1**, 457-463.

210. Pedersen, K. S., Lorusso, G., Morales, J. J., Weyhermüller, T., Piligkos, S., Singh, S. K., Bendix, J. *Fluoride-Bridged {$Gd^{III}_3M^{III}_2$}(M= Cr, Fe, Ga) Molecular Magnetic Refrigerants*. Angew. Chem. Int. Ed., 2014, **9**, 2394-2397.

211. Langley, S. K., Ungur, L., Chilton, N. F., Moubaraki, B., Chibotaru, L. F., Murray, K. S. *Structure, Magnetism and Theory of a Family of Nonanuclear $Cu^{II}_5Ln^{III}_4$–Triethanolamine Clusters Displaying Single-Molecule Magnet Behaviour*. Chem. Eur. J., 2011, **33**, 9209-9218.

212. Zheng, Y. Z., Evangelisti, M., Tuna, F., Winpenny, R. E. *Co–Ln mixed-metal phosphonate grids and cages as molecular magnetic refrigerants*. J. Am. Chem. Soc., 2012, **2**, 1057-1065.

213. Guo, F. S., Chen, Y. C., Liu, J. L., Leng, J. D., Meng, Z. S., Vrabel, P., Tong, M. L. *A large cryogenic magnetocaloric effect exhibited at low field by a 3D ferromagnetically coupled Mn (II)–Gd (III) framework material.* Chem. Comm., 2012, **100**, 12219-12221.

214. Mereacre, V., Akhtar, M. N., Lan, Y., Ako, A. M., Clérac, R., Anson, C. E., Powell, A. K. *Structures and magnetic properties of $Mn^{III}_4Ln^{III}_4$ aggregates with a "square-in-square" topology*. Dalton Trans., 2010, **20**, 4918-4927.

215. Chen, S., Mereacre, V., Prodius, D., Kostakis, G. E., Powell, A. K. *Developing a "highway code" to steer the structural and electronic properties of Fe^{III}/Dy^{III} coordination clusters*. Inorg. Chem., 2015, **7**, 3218-3227.

216. Wu, C., Feng, F., Xie, Y. *Design of vanadium oxide structures with controllable electrical properties for energy applications*. Chem. Soc. Rev., 2013, **12**, 5157-5183.

217. Benelli, C., Blake, A. J., Milne, P. E., Rawson, J. M., Winpenny, R. E. *Magnetic and Structural Studies of Copper–Lanthanoid Complexes; the Synthesis and Structures of New Cu_3Ln Complexes of 6-chloro-2-Pyridone (Ln= Gd, Dy and Er) and Magnetic Studies on Cu_2Gd_2, Cu_4Gd_2 and Cu_3Gd Complexes*. Chem. Eur. J., 1995, **9**, 614-618.

218. Goswami, D., Patra, S. G., Ray, D. *Magneto-Structural Analysis of*

Hydroxido-Bridged Cu^{II}_2 Complexes: Density Functional Theory and Other Treatments. Magnetochemistry, 2023, **6**, 154.

219. Iasco, O., Novitchi, G., Jeanneau, E., Luneau, D. *Lanthanide triangles sandwiched by tetranuclear copper complexes afford a family of hendecanuclear heterometallic complexes $[Ln^{III}_3Cu^{II}_8]$(Ln= La–Lu): synthesis and magnetostructural studies.* Inorg. Chem., 2013, **15**, 8723-8731.

220. Aronica, C., Chastanet, G., Pilet, G., Le Guennic, B., Robert, V., Wernsdorfer, W., Luneau, D. *Cubane Variations: Syntheses, Structures, and Magnetic Property Analyses of Lanthanide (III)− Copper (II) Architectures with Controlled Nuclearities*. Inorg. Chem., 2007, **15**, 6108-6119.

221. Li, Y. T., Liao, D. Z., Jiang, Z. H., Wang, G. L. *Synthesis and magnetic studies of copper (II)-lanthanide (III) complexes with N, N'-bis (2-aminopropyl) oxamidocopper (II)*. Polyhedron, 1995, **14**, 2209-2213.

222. Castro, I., Calatayud, M. L., Yuste, C., Castellano, M., Ruiz-Garcia, R., Cano, J., Lloret, F. *Dinuclear copper (II) complexes as testing ground for molecular magnetism theory*. Polyhedron, 2019, **169**, 66-77.

223. Baniodeh A, Anson C E, Powell A K. *Ringing the changes in Fe^{III}/Yb^{III} cyclic coordination clusters*. Chem. Sci., 2013, **12**, 4354-4361.

224. Vignesh K R, Soncini A, Langley S K, et al. *Ferrotoroidic ground state in a heterometallic ($Cr^{III}Dy^{III}6$) complex displaying slow magnetic relaxation*. Nature communications, 2017, **1**, 1023.

10. Appendix

10.1. Acknowledgements

First and foremost, I would like to extend my heartfelt appreciation to all the individuals who have accompanied and supported me throughout this long yet brief journey of my Ph.D. life.

My deepest gratitude goes to Prof. Annie K Powell, my supervisor, for graciously allowing me to join her research group and providing invaluable feedback and suggestions with unparalleled patience. Her unwavering encouragement and guidance have been instrumental in shaping my studies, and I am grateful for her continuous support.

I would also like to express my thanks to Dr. Christopher E Anson, Dr. Yan Peng, Dr. Masooma Ibrahim, Dr. Hagen Kämmerer, Dr. Thomas Ruppert, Dr. Rouven Pfleger, Dr. Krisana Peewasan, Dr. Marcel Merkel and Dr. Ghulam Abbas for their mentorship and for imparting their expertise in instruments, experiments, and fundamental knowledge during my initial work in the lab. They have consistently taken the time to answer my questions and have offered me much advice, insightful discussions, ideas, and guidance throughout my studies.

I am profoundly grateful to Prof. Dr. Dieter Fenske and Dr. Olaf Fuhr for their exceptional help and guidance in crystal structure testing and crystal structure analysis. Their unwavering commitment to their work has not only provided me with invaluable knowledge but has also served as a powerful source of inspiration for my future scientific research career. Moreover, I am deeply inspired by Prof. Dr. Dieter Fenske's unwavering passion for scientific exploration, even at the remarkable age of 80. His commitment to advancing the frontiers of knowledge and his continuous pursuit of excellence have been a true revelation. Witnessing his enthusiasm for research has reinforced my belief in the lifelong pursuit of learning and discovery. I extend my heartfelt appreciation to Prof. Dr. Dieter Fenske and Dr. Olaf Fuhr for their mentorship, encouragement, and the profound impact they have had on my academic and professional growth.

A special appreciation goes to Dr. Umaira Shuaib and Dr. Jonas Braun for their ongoing study advice, patience, and meticulous proofreading of my Ph.D. thesis and publication drafts. Their assistance has been invaluable in refining my work.

I am immensely grateful to all my lab mates for their invaluable contributions to my Ph.D. journey. I would like to express my sincere thanks to Dr. Luis Basche for his strictness in guiding my experimental procedures. His attention to detail and insistence on precision have been instrumental in ensuring the accuracy and reliability of my research. Furthermore, I extend my heartfelt appreciation to Aiswarya Chalikunnath Venu, Aravind Raveendranathan, Vanikrishna Ajithkumar Njayappallil, Yangxin Chen, Daniel Seufert, Prashant Anand, Yannik Schneider, and Sarah Rockenfeller for fostering a motivating and collaborative work environment. The camaraderie and spirit of teamwork within our group have been pivotal in pushing the boundaries of scientific exploration and in tackling complex challenges. I consider myself incredibly fortunate to have had the opportunity to work with such an exceptional team. Their diverse perspectives, expertise, and dedication have enriched my research experience and shaped my growth as a researcher.

My sincere gratitude extends to Mr. Nikolai Bartnick for his assistance and for supplying the lab with necessary supplies and or his help with elemental analysis.

I would also like to express my appreciation to our collaborators - Prof. Wolfgang Wernsdorfer's group from Physikalisches Institut, especially Michael Schulze and Dr. Paul Sagar, for conducting μ-SQUID experiments on the samples provided. I would like to extend my heartfelt gratitude to Dr. Senthil Kumar Kuppusamy, Dr. Tingting Ruan, and Sören Schlittenhardt from Prof. Dr. Mario Ruben's research group for their invaluable assistance in magnetic performance testing. Their expertise and willingness to lend a helping hand have been instrumental in advancing my research and understanding of

magnetic properties.

I am deeply grateful for the invaluable assistance provided by external universities and research groups during my Ph.D. journey. Their collaboration and expertise have been crucial in enhancing the scope and depth of my research. Firstly, I extend my sincere thanks to Jan Victor Arneth and Dr. Changhyun Koo from the research group of Prof. Dr. Rüdiger Klinger at Heidelberg University for their support in magnetic properties and Electron Paramagnetic Resonance (EPR) testing. Their proficiency in these areas has significantly enriched my understanding of magnetic materials and contributed to the comprehensive analysis of my experimental data. I am also thankful to Tanu Sharma from the research group of Prof. Dr. Gopalan Rajaraman in Indian Institute of Technology Bombay and Dennis Westerbeck from the research group of Prof. Dr. Jürgen Schnack in Bielefeld University for their help with magnetic calculations. Their expertise and insights have been instrumental in interpreting the complex magnetic phenomena observed in my research, and their contributions have strengthened the theoretical framework of my work. The willingness of these external schools and research groups to offer their expertise and collaborate with me has been a testament to the spirit of scientific cooperation and knowledge-sharing. Their support has allowed me to tackle complex research questions from various angles, leading to a more comprehensive and robust Ph.D. study.

I want to express my gratitude to my friends Zhongkai Mei, Xi Chen, da Jin, Hengheng Zhang, Jun Li, Zihan Xia, Yanxin Chen, Zhiyun Xu for their friendship, kindness, and unwavering support.

I am deeply thankful to the China Scholarship Council (CSC) for funding my entire Ph.D. period and providing me with this wonderful opportunity to study in Germany.

Lastly, I want to convey my heartfelt gratitude to my beloved family for their unyielding love, support, and encouragement throughout my Ph.D. journey. My

parents' tireless efforts in providing me with the best education and opportunities, their unconditional love, and belief in me have given me the confidence and resilience to overcome challenges and persist in achieving my goals. I must thank my brother for his unwavering support and care for our parents, as well as his support to me. I could not have accomplished this without them; their understanding, tolerance, and faith in me have been an unwavering source of courage.